Dynamic triggering: The effects of remote earthquakes on volcanoes, hydrothermal systems and tectonics

Dissertation

zur

Erlangung des Doktorgrades (Dr. rer. nat.)

der

Mathematisch-Naturwissenschaftlichen Fakultät

der

Rheinischen Friedrich-Wilhelms-Universität Bonn

vorgelegt von

Florian Fuchs

aus

Herdecke

Bonn 2014

Angefertigt mit Genehmigung der Mathematisch-Naturwissenschaftlichen Fakultät
der Rheinischen Friedrich-Wilhelms-Universität Bonn
am Steinmann-Institut für Geologie, Mineralogie und Paläontologie

1. Gutachter: Prof. Dr. Stephen A. Miller
2. Gutachter: Prof. Dr. Andreas Kemna

Tag der Promotion: 15.01.2015
Erscheinungsjahr: 2015

Abstract

Dynamic stresses induced by seismic waves from large earthquakes can trigger a variety of geologic phenomena. This thesis focuses on observational evidence of dynamically triggered seismic activity in hydrothermal, volcanic and mud-volcanic systems.

During summer 2011 and 2013 we discovered microseismic activity under the Snæfellsjökull volcano, Iceland. Earthquakes with magnitudes $M_l < 1.5$ are located around 5–13 km below sea level. Seismicity likely reflects hybrid events that involve brittle failure in combination with fluid-related processes in deep sections of the crust. Additional Synthetic Aperture Radar Interferometry shows no vertical surface deformation between years 2004 and 2008, indicating negligible inflation/deflation within the inferred magma reservoir.

We analyze the triggering of seismic activity at the Irazú-Turrialba volcanic complex, Costa Rica, following the 2012 M_w 7.6 Nicoya earthquake. After the passage of seismic waves we observe a sudden increase in seismicity lasting approximately 36 hours with a maximum rate of 75 events/hour. We point out that $M_w < 4.5$ aftershocks are also followed by increased seismicity. We propose the combined action of dynamic stress and short-lived coseismic relaxation triggered seismic activity in this near-critical system. Additionally, we show similar earthquake triggering by teleseismic surface waves in the Larderello-Travale geothermal field, Italy.

Furthermore, we present evidence for triggered tremor beneath the island of Sumbawa, Indonesia. We show tremor in response to three teleseismic earthquakes and constrain a triggering threshold of 8 kPa dynamic stress. Triggered tremor amplitudes scale with induced ground velocity. Tremor responds to 45–65 s period surface waves and predominantly correlates with Rayleigh waves. We could not locate the tremor but data indicates potential source volumes such as the Flores Thrust, the Java subduction zone, or Tambora volcano.

Using numerical wave propagation we investigate the trigger of the 2006 Lusi mud eruption, Indonesia. We show that the parabolic-shaped lithology at Lusi could have reflected and focused incoming seismic energy from the 2006 M_w 6.3 Yogyakarta earthquake. Our simulations show that energy concentrations in the mud layer could have been sufficient to liquefy the mud source. We conclude that the Lusi mud eruption was a natural occurrence and suggest that parabolic lithologies with varying acoustic impedance can focus and amplify incoming seismic energy and trigger a response in various volcanic and hydrothermal systems.

Results from this thesis suggest that dynamic stresses in the low Kilopascal range can trigger a variety of geologic responses. The dynamic interaction during triggering is more complex than can be covered in established basic magnitude-distance relations which should be reformulated or enhanced.

Zusammenfassung

Seismische Wellen starker Erdbeben induzieren dynamische Spannungen und können eine Vielzahl geologischer Phänomene auslösen. Der Schwerpunkt dieser Arbeit liegt auf Beobachtungen von ausgelöster seismischer Aktivität in hydrothermalen, vulkanischen und schlammvulkanischen Systemen.

In den Jahren 2011 und 2013 haben wir mikroseismische Aktivität unter dem Snæfellsjökull Vulkan auf Island gemessen. Erdbeben mit Magnituden $M_l < 1.5$ befinden sich 5–13 km unter dem Meeresspiegel und sind möglicherweise auf eine Kombination von sprödem Bruch unter Fluid-Einfluss in tiefen Teilen der Kruste zurückzuführen. InSAR Messungen zeigen keine Oberflächenverformung zwischen 2004 und 2008, woraus wir schließen, dass es keine Volumenänderung in einem Magma Reservoir gegeben hat.

Wir analysieren ansteigende seismische Aktivität im Irazú-Turrialba Vulkankomplex, Costa Rica, nach dem 2012 M_w 7.6 Nicoya Erdbeben. Nach Passage der seismischen Wellen konnten wir einen abrupten Anstieg der Erdbebenrate beobachten, welcher ungefähr 36 Stunden anhielt. Bemerkenswert ist, dass Nachbeben mit $M_w < 4.5$ das System ebenfalls beinflussten. Eine Kombination aus dynamischen Spannungen und koseismischer Relaxion kann den Anstieg der Erdbebenrate ausgelöst haben. In einer vergleichbaren Studie stellen wir Erdbeben vor, die durch teleseismische Wellen im italienischen Geothermalgebiet Larderello-Travale ausgelöst wurden.

Desweiteren präsentieren wir Daten, die tektonischen Tremor unter der Insel Sumbawa in Indonesien belegen. Wir zeigen Tremor als Reaktion auf drei teleseismische Erdbeben und bestimmen eine Auslöseschwelle von 8 kPa seismischer Spannung. Tremor Amplituden skalieren mit der induzierten Bodenbewegung. Zudem reagiert Tremor auf Oberflächenwellen mit einer Periode zwischen 45–65 s und korreliert insbesondere mit Rayleigh Wellen. Der Ursprung dieser Tremor-Signale kann nicht bestimmt werden, die Daten sprechen jedoch für die Flores Verwerfung, die Java Subduktionszone oder den Tambora Vulkan.

Mittels numerischer Simulation untersuchen wir den Lusi Schlammausbruch in Indonesien aus dem Jahr 2006. Wir zeigen, dass eine kuppelförmige Lithologie die seismischen Wellen des M_w 6.3 Yogyakarta Erdbebens reflektiert und fokussiert haben kann. So konnte sich Energie in der schlammführenden Schicht konzentrieren und den Schlamm verflüssigen. Wir schlussfolgern, dass der Lusi Ausbruch natürlichen Ursprungs ist und generell kuppelförmige Gesteinsschichtungen einfallende seismische Wellen verstärken können und somit Reaktionen in vulkanischen oder hydrothermalen Systemen auslösen.

Die Ergebnisse dieser Arbeit zeigen, dass dynamische Spannungen von wenigen Kilopascal eine Vielzahl an geologischen Reaktionen auslösen können. Etablierte Magnitude-Entfernungs-Relationen können diese komplexe Interaktion nicht erfassen und sollten daher umformuliert oder erweitert werden.

Contents

1 Introduction

We live on a solid earth. Every now and then we are reminded by a catastrophic event that what we so naturally assume is not entirely correct. The solid 20–30 km thick crust we live on is just the very outer skin of our planet earth. Deep inside the earth, many hundreds to thousands kilometers below this surface hot material is in constant viscous flow. It is this motion of the earth's interior that by convection inside the outer core creates the earth magnetic field which shields life on earth from destructive cosmic radiation. It is also the viscous characteristics of the earth's mantle that allows hot material to flow in convective cells which is the mechanism that eventually drives crustal plate tectonics [Tackley, 2000].

Especially along the boundaries of tectonic plates we come to realize that the earth is not only solid. Formation of volcanoes and their ongoing eruptions along subduction zones are a consequence of tectonic plate motion. Earthquakes shatter the crust, cause great damage and pose a major hazard to human population. Most famous are the boundaries of the Pacific Plate and the neighboring Filipino, Juan de Fuca, Cocos and Nazca Plate which form the so called Pacific Ring of Fire. Active arc volcanism [Dickinson and Hatherton, 1967] and frequent earthquakes [Tobin and Sykes, 1968] threaten the coastal population of the Philippines, Japan, New Zealand and the entire western coastline of North and South America. The devastating 2010 M_w 8.8 Chile and 2011 M_w 9.0 Japan earthquakes are just the two most recent catastrophic events to remind us that the earth's crust is not at rest.

It is one of the major goals of geology and seismology in particular to mitigate the earthquake related hazards on human population, with the ultimate ambition of predicting or forecasting earthquakes. Yet, more than eighty years of earthquake research led to the general acceptance that earthquakes are unpredictable. The Gutenberg-Richter law on earthquake magnitudes [Gutenberg and Richter, 2010] and the Omori law of aftershocks [Utsu et al., 1995] are essentially the two statistical tools for present day calculation of earthquake risks. Modified and adopted since their original formulation, these laws have been verified by nature. However, both are based on empirical observations and a stringent physical explanation has yet to be found. Thus, the statistics of earthquake occurrence are well understood but do not provide the smoking gun for earthquake prediction.

Efforts have been made and are being made to substantiate e.g. the Omori law of aftershocks by means of physical mechanisms for earthquake nucleation. One of the most investigated of such mechanisms is the elaborate principle of rate and state dependent friction. Originally formulated by Dieterich [1994] it is still subject of ongoing research [Bar-Sinai et al., 2013; Foster et al., 2013] and aims to explain both earthquake initiation and complex slip distributions. Alternative approaches utilize the effects of fluid pressure

in the crust as an important parameter for earthquake initiation and explanation of the earthquake cycle. Miller [2013] provides a comprehensive review of the role of fluids in tectonic and earthquake processes.

While the timing of earthquakes cannot be predicted or forecasted, efforts are still being made to exploit the well-known empirical laws or establish new geophysical observables to provide insight into the nucleation of earthquakes for early earthquake warning. Among the suggested techniques for earthquake forecasting are statistical physics [Main, 1996], analysis of earthquake recurrence time [Nishenko and Buland, 1987; Visini and Pace, 2014] and attempts for 24-hour forecast systems in very densely instrumented regions, such as California, USA [Gerstenberger et al., 2005]. Proposed geophysical observables include gas geochemistry [King, 1986], hydrogeodeformation [Vartanyan et al., 2014] or electrotellurics [Varostos and Lazaridou, 1991]. Yet, none of this efforts has gained general acceptance among the scientific community. Lately, the discovery of slow earthquakes and tectonic tremor [Shelly et al., 2006] promises insights into the earthquake cycle and may lead to better understanding of long term earthquake formation.

Under certain circumstances earthquakes can, however, be triggered or induced by external influences. For example, Miller [2008] comments on various effects of heavy rainfall as a trigger for earthquakes through increased pore pressure at depth. In Enhanced Geothermal Systems small earthquakes are deliberately induced by fluid injection to increase the permeability at depth for geothermal power plants [Terakawa et al., 2012]. While most of such earthquakes have magnitudes $M_w < 2$ and are barely felt, an induced M_w 3.4 earthquake in 2006 lead to the termination of the Basel Deep Heat Mining geothermal project. Gupta [2002] reviews earthquakes triggered by filling of artificial water reservoirs at dams. In 1983 a magnitude M_w 5.9 earthquake struck in the vicinity of the Srinagarind Dam, Thailand, and was attributed to the filling of the barrier lake. The exploitation of oil and gas reservoirs can lead to substantial pressure drops and stress changes, resulting in earthquakes as described by Segall and Fitzgerald [1998]. In turn, oil-production-induced microseismicity can be used for reservoir characterization [Rutledge et al., 1998]. Recently, Gonzalez et al. [2012] reported an earthquake controlled by draining of an aquifer by groundwater extraction in Spain. Earthquakes may even be triggered by the solid earth tides [Cochran et al., 2004]. While most of the aforementioned examples are man-made, earthquakes are also triggered by other earthquakes.

King et al. [1994] suggested that slip during earthquakes changes the regional stress field and thus may lead to triggering of subsequent earthquakes if the stress changes promote Coulomb failure. Using this approach, Stein et al. [1997] present an impressive earthquake prediction study, demonstrating in retrospective the progressive failure of the North Anatolian fault, Turkey, since 1939 by static stress transfer. Similarly, Toda et al. [2005] explain the evolution of seismicity in Southern California by static stress transfer. Static stress transfer by one earthquake on the surrounding crust which may lead to a follow-up earthquake is a promising and well understood mechanism to constrain possible areas of future earthquakes. Static stress transfer was among the first principles to suggest that one earthquake may be triggered by another and is further

introduced in Section 2.2. Static stress change also explains hydrological effects such as stream flow or water level changes after earthquakes [Miller, 2012, and references therein]. The mechanism also applies to volcanic systems, where the static reduction of normal stress may trigger magma ascent which eventually results in a volcanic eruption [Bonali, 2013; Diez et al., 2005; Nostro et al., 1998].

Plenty of observations prove static stress transfer, yet it is only effective within regional distances, that is up to approximately one fault length from the triggering earthquake [Toda et al., 2011]. This limits the range of static stress triggering to several hundred kilometers even for large $M_w > 8$ earthquakes. The 1992 M_w 7.3 Landers, California earthquake demonstrated that the triggering capability of earthquakes can extend far beyond regional distances as expected from static stress triggering. Hill et al. [1993] reported a sudden and widespread increase in earthquake activity across much of the western United States following the 1992 Landers earthquake. Triggered earthquakes occured up to 1250 km from the mainshock and could not be explained by static stress transfer. Hill et al. [1993] argued that the increase of seismicity was remotely triggered by the dynamic stresses accompanying transient seismic waves. During the passage of seismic waves the ground is temporarily subject to additional stresses which under critical conditions may result in failure of rock, slip on existing faults or pore pressure driven reactions in fluid related systems. Seismic surface waves in particular seem capable of triggering a secondary event and thus the range of dynamic stress triggering greatly exceeds that of static stress triggering and can extend many thousands of kilometers from the epicenter. [Jousset and Rohmer, 2012] report earthquakes triggered in a salt cavern 12,000 km distant from a triggering M_w 7.2 earthquake and Peng et al. [2011] show repeated earthquake triggering by surface waves that circle the earth multiple times.

Studies show that seismic waves can remotely trigger a variety of geodynamic events, both immediately during the passage of the waves or delayed by hours to days [Brodsky, 2006]. Ishihara [1993] discusses the effects of earthquake induced liquefaction and Berberian et al. [2001] and Mazzini et al. [2009] show that even distant earthquakes may re-activate movement on faults. Keefer [2002] reviews earthquake-triggered landslides and Dadson et al. [2004] report over 20,000 landslides triggered all over Taiwan by the 1999 M_w 7.7 Chi-Chi earthquake. Dynamic triggering also affects volcanoes by means of increased seismic activity [Power et al., 2001], elevated heat flow [Delle Donne et al., 2010; Harris and Ripepe, 2007] or eruption of long dormant volcanoes after subduction zone earthquakes [Marzocchi, 2002a]. In fact, dynamic triggering is most commonly observed in volcanic or hydro- and geothermal areas [Brodsky and Prejean, 2005; Hill et al., 1993; Husen et al., 2004b; Saccorotti et al., 2013]. Geysers respond to distant earthquakes [Manga and Brodsky, 2006] and the devastating 2006 Lusi mud eruption in Sidoarjo district, Java may have been initiated by dynamic triggering [Davies et al., 2008; Lupi et al., 2013]. Teleseismic surface waves repeatedly trigger tectonic tremor along the Pacific Ocean subduction zones and on the San Andreas Fault [Gomberg et al., 2008]. Likely connected to slow-slip earthquakes, better understanding of tectonic tremor can provide insight into stages of the earthquake cycle and thus triggered tremor is currently of great interest. Yet, despite the observational abundance of dynamic triggering, stringent physical mechanisms to explain the different manifestations of

remote triggering have yet to be found. Section 2.3 summarizes various mechanisms proposed for the physics of dynamic earthquake triggering and volcanic excitation by seismic waves.

Chapter 2 lays ground for the work presented in Chapters 3–6 and introduces basic physical concepts for earthquake generation and both static as well as dynamic triggering. Chapter 3 treats the seismological observation of the currently dormant Snæfellsjökull volcano in western Iceland to allow for a better understanding of seismic signals in a volcanic environment at rest. Results are backed up by Interferometric Synthetic Aperture Radar (InSAR) measurements. Subsequently, Chapter 4 reports dynamic triggering of an earthquake swarm within the Irazú-Turrialba volcanic complex, Costa Rica by the 200 km distant 2012 M_{w} 7.6 Nicoya earthquake and instances of triggered earthquakes in the Larderello-Travale geothermal field, Italy, by the 2011 M_{w} 9.0 Tohoku earthquake. Presented in Chapter 5 are first-time observations of triggered tectonic tremor in the Sunda Arc, Indonesia, near the Java subduction zone. Finally, Chapter 6 treats triggering of mud volcanoes with examples from Lusi, Indonesia and the Salse di Nirano mud volcanic field, Italy and concludes this thesis with a numerical simulation that suggests a key geologic feature for the triggering of the 2006 Lusi mud eruption. Results point toward a general mechanism of seismic wave focusing in dome-shaped lithologies which may promote dynamic triggering on intermediate distances.

2 Theoretical background

2.1 Coulomb failure and earthquakes

The concept of both static and dynamic earthquake triggering is based on the Mohr-Coulomb failure criterion. The findings of Coulomb [1776] and Mohr [1900] lay ground for the one basic principle to describe the mechanism of earthquake generation by means of brittle rock failure which is introduced in the following (based on Zoporowski [2011]).

In mechanics, stress $\sigma = F/A$ defines as the ratio of a force F applied to a body over an area A. Any stress can be decomposed into perpendicular and tangential forces to the body's surface, called normal stress σ and shear stress τ, respectively. In a three-dimensional Cartesian coordinate frame (x,y,z) normal and shear stresses define as depicted in Figure 2.1 such that at any point of the body an arbitrarily oriented stress σ is generally given by the second order tensor

$$\sigma = \begin{pmatrix} \sigma_{xx} & \tau_{xy} & \tau_{xz} \\ \tau_{yx} & \sigma_{yy} & \tau_{yz} \\ \tau_{zx} & \tau_{zy} & \sigma_{zz} \end{pmatrix} \tag{2.1}$$

with normal stresses $\sigma_{\mathrm{n}} = \sigma_{ij}, i = j$ and shear stresses $\tau_{ij}, i \neq j\,[i,j \in (x,y,z)]$. In static equilibrium, stresses on opposite faces of the body must equal, hence the shear components $\tau_{ij} = \tau_{ji}$ of the stress tensor are symmetric.

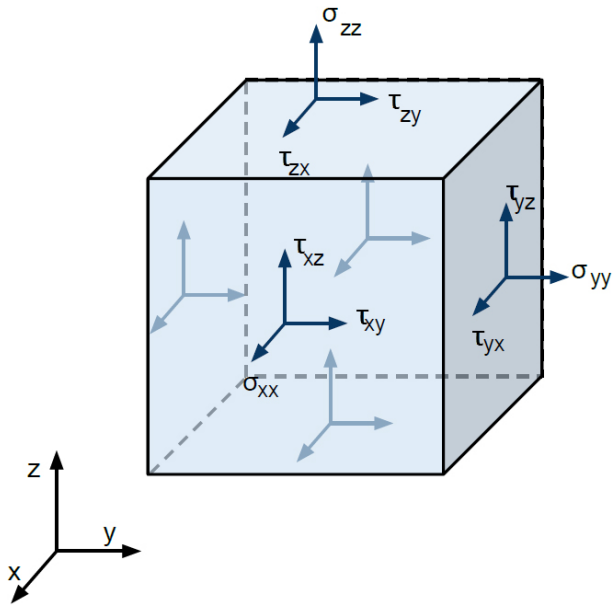

Figure 2.1: Definition of normal stresses $\sigma_{ij}, i = j$ and shear stresses $\tau_{ij}, i \neq j$ acting on the surfaces of a sample body in a three-dimensional Cartesian frame [Zoporowski, 2011].

Assuming a body under stress σ, for any point of that body one can find three specific planes, set by normal vectors $\vec{n}_1$, $\vec{n}_2$, $\vec{n}_3$, that experience no shear stresses but solely normal stresses. These normal stresses, being parallel to $\vec{n}_1$ or $\vec{n}_2$ or $\vec{n}_3$, respectively, are called principal stresses σ_1, σ_2 and σ_3 (with $\sigma_1 \geq \sigma_2 \geq \sigma_3$) and are the eigenvalues of the stress tensor.

The Mohr circle, as shown in Figure 2.2, illustrates normal stresses σ_n and shear stresses τ acting on any given plane of a stressed body. In a frame defined by the principal stresses σ_1, σ_2 and σ_3, any point on the circumference of a Mohr circle connecting σ_1 and σ_3 represents planes perpendicular to both σ_1 and σ_3 with orientation θ to the normal of the major principal stress σ_1. Likewise, the Mohr circle that connects σ_2 and σ_3 (or σ_1 and σ_2) represents planes perpendicular to both σ_2 and σ_3 (or σ_1 and σ_2) inclined to the normal of σ_2 (or σ_1). Hence, a plane that is oriented normal to σ_1 ($\theta = 0°$) will experience only normal stress $\sigma_\mathrm{n} = \sigma_1$ and no shear stress. Since, by definition, all principal stresses are perpendicular to each other, a plane parallel to σ_1 ($\theta = 90°$) will likewise experience no shear stress but normal stress σ_n equal to σ_2 or σ_3. Generally, for a plane oriented at an angle θ to the normal of the major principal stress σ_1, shear stress τ and normal stress σ_n read

$$\tau = \frac{1}{2}\left(\sigma_1 - \sigma_3\right)\sin 2\theta \tag{2.2}$$

$$\sigma_\mathrm{n} = \frac{1}{2}\left(\left(\sigma_1 + \sigma_3\right) - \left(\sigma_1 - \sigma_3\right)\cos 2\theta\right) \tag{2.3}$$

with σ_3 being the least principal stress, σ_1 the maximum principal stress and σ_2 the intermediate principle stress.

In geodynamics, the relative motion of tectonic plates is responsible for the build-up of stresses in the Lithosphere and the direction of motion defines the orientation of the principal stresses. In compressional settings such as subduction zones (Figure 2.3a) the increasing maximum principal stress σ_1 acts horizontally and parallel to the direction of motion of the subducted plate. In this scenario the least principal stress $\sigma_3 = \rho z g$ is the constant, vertical lithospheric load (rock density ρ, depth z, $g = 9.81$ m/s^2). This stress configuration favors thrust faulting. Extensional settings (Figure 2.3b) are defined by strong constant lithospheric load $\sigma_1 = \rho z g$ and decreasing minimum principal stress σ_3 and will lead to normal faulting. Strike-slip regimes (Figure 2.3c) occur where the lithospheric load is $\sigma_2 = \rho z g$ and differs only slightly from both σ_1 and σ_3 Strike-slip faulting will occur for when the differential stress $1/2(\sigma_1 - \sigma_3)$ is small. Eventually, the tectonic forces lead to build-up of a critical stress state that exceeds the strength of the Lithosphere. The rock breaks and fractures are created or faults begin to slip and the accompanying rapid motion is the origin of earthquakes.

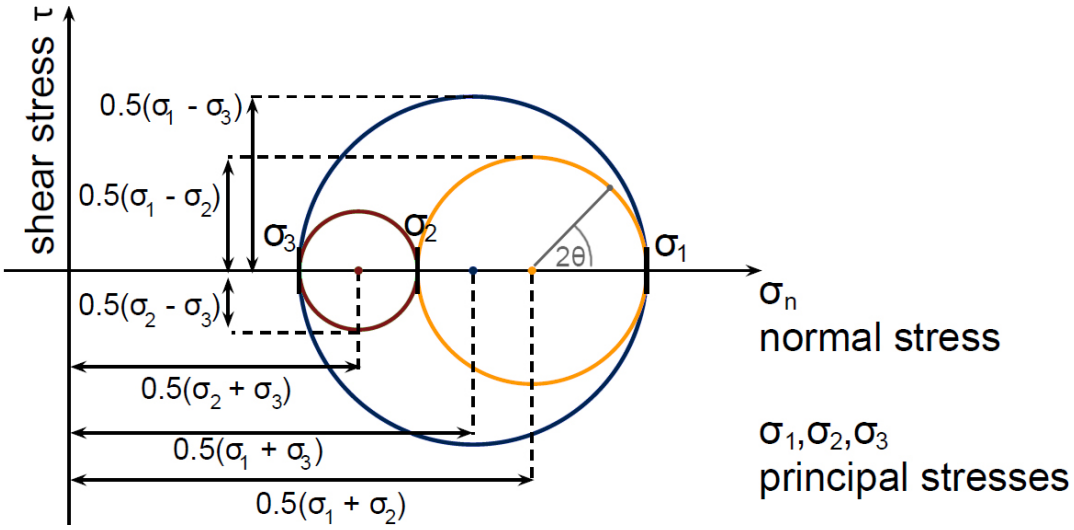

Figure 2.2: Mohr circle representation of stresses. In a diagram spanned by shear stress τ versus normal stress σ_n any point on a circle spanned by the principal stresses σ_i and σ_j represents a plane perpendicular to both σ_i and σ_j. The orientation of the respective plane is given by the angle θ with respect to the normal of σ_1, as indicated. In three dimensions there exist three circles for planes normal to each one of the principal stresses $\sigma_1 > \sigma_2 > \sigma_3$ [Zoporowski, 2011].

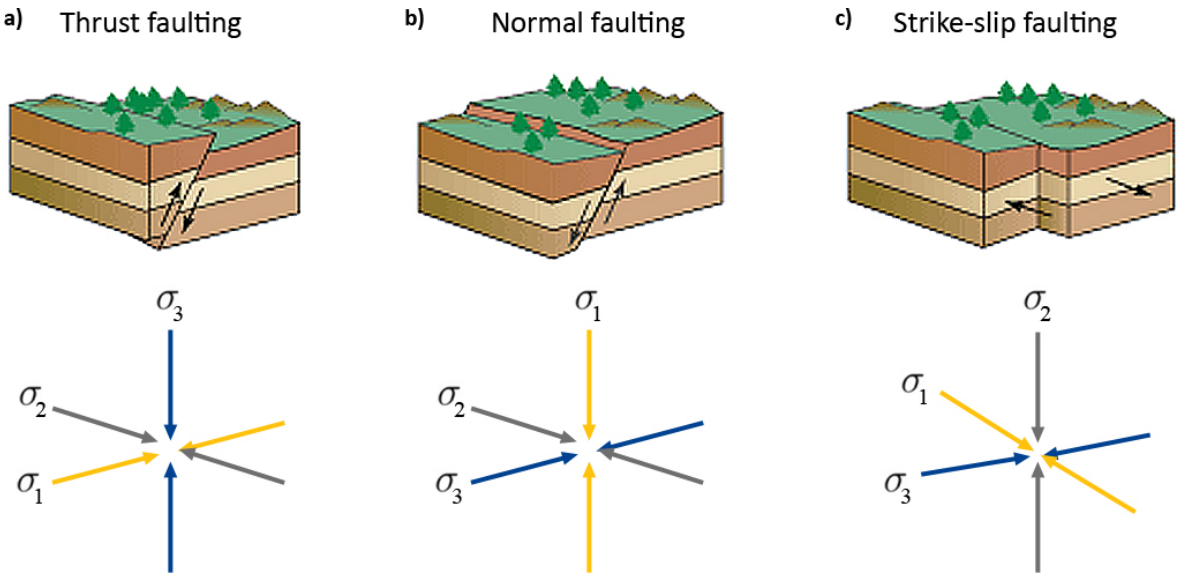

Figure 2.3: Tectonic settings and corresponding principal stress orientations. **a)** For compressional settings such as subduction zones, horizontal orientation of σ_1 caused by plate collision and comparably little lithospheric load $\sigma_3 = \rho z g$ will result in thrust faulting. **b)** Normal faulting will occur in extensional settings such as Grabens and Mid-Ocean ridges, where the vertical lithospheric load $\sigma_1 = \rho z g$ is the strongest of the acting tectonic stresses and the confining horizontal stress σ_3 is small **c)** Strike-slip faulting will occur for σ_2 as lithospheric load, small differential stress $1/2(\sigma_1 - \sigma_3)$ and if the local stress field is rotated with respect to the fault strike, in contrast to the perpendicular orientation for normal and thrust faulting.

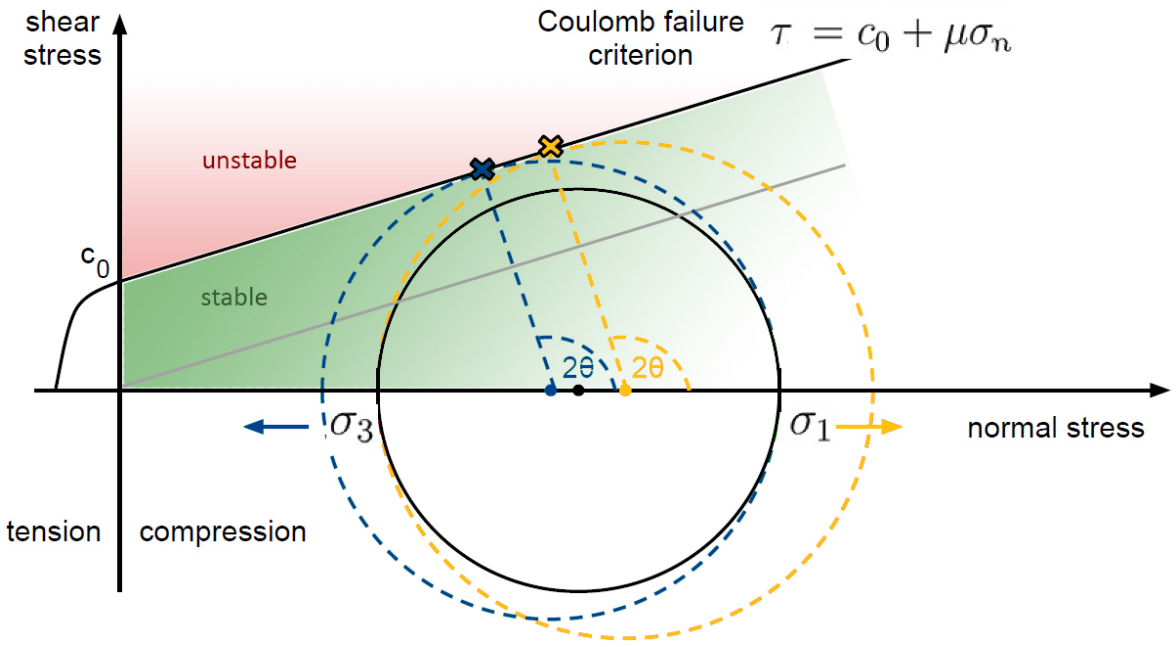

Figure 2.4: Mohr-Coulomb brittle rock failure. In a shear stress versus normal stress diagram, the Coulomb failure line for brittle rock failure is a line with slope given by the friction coefficient μ. The black line is valid for intact rocks with non-zero cohesion c_0, while the gray line holds for pre-existing faults with negligible cohesion. Stable and unstable regimes are marked with respect to the non-zero cohesion case. Any point below the failure line represents a stable stress state while any point above the line is unstable and leads to slipping. Increasing the maximum principal stress σ_1 (such as in compressional tectonics) from an initially stable stress state (black circle in Figure 2.4 will expand the radius of the Mohr circle and eventually put one point on the Coulomb failure line (orange circle)and result in rock failure and thrust faulting. Similarly, decreasing σ_3 (such as in extensional tectonics) will increase the Mohr circle radius (blue circle) and eventually result in normal faulting. Note that in this diagram and for the drawn Mohr circles, for pre-existing faults any point above the gray line would be unstable and slip would occur on any of such planes if there exist a fault with the respective orientation θ.

The Coulomb failure criterion [Handin, 1969] describes the ability of rock or faults to oppose stress with internal shearing. In terms of the Mohr diagram, the Coulomb failure criterion reads

$$\tau = c_0 + \mu\sigma_\mathrm{n} \tag{2.4}$$

with the cohesion c_0 and the friction coefficient $\mu = \tan\vartheta$ given by the angle of internal friction ϑ (see Figure 2.4). Since pre-existing faults have negligible cohesion, their Coulomb failure threshold is lower than that of intact rock and they can withstand less stress before slipping. In the Mohr diagram the Coulomb failure criterion shows as a line (Figure 2.4) for positive compression. The regime of negative stresses (tension) is described by Griffith failure [Berry, 1960]. Rocks or faults are stable for any point below the Coulomb failure line and will break or slip for any point on or above. Thus, the Mohr circle representation of stresses can illustrate the different stress regimes that lead to the generation of earthquakes. Assuming a stable stress state given by σ_1 and

σ_3, there are two possibilities to bring intact rock to failure or a locked fault to slip: As in compressional regimes, increasing σ_1 over time while keeping σ_3 constant will enlarge the Mohr circle radius and eventually put one point on the Coulomb failure line. The rock will break, or a fault will slip and a thrust earthquake occurs. Breaking the rock will create a fracture that is oriented at θ with respect to the normal of σ_1. For lithospheric rocks, $\mu = 0.6$ and thus $\theta = 60°$. Slip on pre-existing faults will likewise occur if the failure criterion is reached and there exists a fault that is oriented at $\theta = 60°$ to the normal of σ_1. Analogously, in extensional settings, reduction of σ_3 under constant σ_1 will result in normal faulting.

Note that the orientation θ of newly created fractures (with respect to the normal plane of σ_1) is determined by the slope of the Coulomb failure line and thus by the angle of internal friction ϑ. For lithospheric rocks the internal friction angle is approximately $\vartheta \approx 30°$ ($\mu \approx 0.6$) such that new fracture are oriented at $\theta = 60°$ [Schön, 2011]. Since the failure criterion for pre-existing faults (because of negligible cohesion) allows for significantly less stress before failure (see gray line in Figures 2.4 and 2.5) it is more common for earthquake generation that slip occurs on pre-existing faults rather than intact rock is fractured and new faults are created. Pre-existing faults that are oriented at $\theta = 60°$ to σ_1 (for a failure slope of $\mu = 0.6$) are termed optimally oriented faults since for any originally stable stress state they will be the first to fail and slip if stresses change towards Coulomb failure.

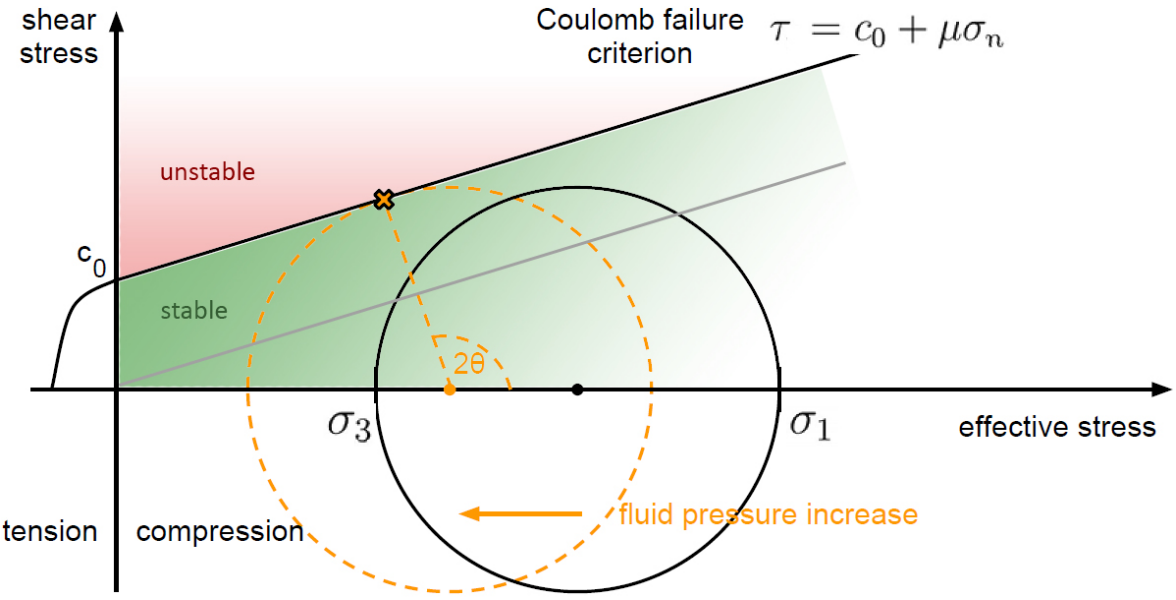

Figure 2.5: Mohr-Coulomb brittle rock failure under high fluid pore pressure. In the presence of fluids with pore pressure p the normal stress on any plane is reduced to an effective stress $\sigma_{\text{eff}} = \sigma_n - p$. Hence, an otherwise stable stress state can be brought to failure by increasing the pore pressure p as the Mohr circle is shifted leftwards and the Coulomb failure criterion is eventually matched. The orientation of fractures or faults is still given by the friction coefficient μ and thus same as in Figure 2.4 for dry conditions.

Crustal fluids are of great importance for earthquake generation. The presence of fluids with pore pressure p can significantly reduce the effective strength of rocks and faults by diminishing the normal stress to an effective normal stress [Terzaghi, 1943]

$$\sigma_{\text{eff}} = \sigma_{\text{n}} - p \tag{2.5}$$

Replacing the normal stress with the effective stress σ_{eff} in a Mohr-Coulomb diagram (see Figure 2.5) shows how a previously stable rock (black circle) can be brought to failure by increasing fluid pressure (orange circle). Thus, the presence of crustal fluids is an essential parameter for earthquake generation. Even for very uncritical stress states (e.g. small differential stress; the Mohr circle radius is small) high fluid pore pressure p can result in rock failure. Note that instead of using an effective normal stress, the effect of fluid pressure can also be included in an apparent friction coefficient μ^* that is lower than the friction coefficient for dry conditions [Beeler et al., 2000, and references therein].

2.2 Static stress transfer

During an earthquake the slip along the fault plane changes the crustal stresses in the vicinity of the fault. These stress changes may bring adjacent faults closer to Coulomb failure by e.g. enhancing the maximum principal stress σ_1 or reducing the least principal stress σ_3. For a given fault the post-seismic changes in shear stress $\Delta\tau$ and normal stress $\Delta\sigma_{\text{n}}$ induced by a nearby earthquake determine the change in Coulomb failure stress

$$\Delta\text{CFS} = \Delta\tau + \mu\Delta\sigma_{\text{n}} \tag{2.6}$$

that states if the stress state on the fault changed towards Coulomb failure (positive ΔCFS) or away from Coulomb failure (negative ΔCFS). The change in Coulomb failure stress ΔCFS strongly depends on the orientation and type of the receiving fault and the spatial pattern of the main shock slip distribution [Toda et al., 2011, and references therein]. Coulomb failure stress change is the basic principle of static stress triggering that has been successfully applied to explain both the triggering of earthquakes and aftershocks and the response of volcanic systems to nearby earthquakes. Faults that experience positive ΔCFS will be more likely to fail and slip while a negative ΔCFS on faults will reduce the risk of earthquakes. Figure 2.6 shows an application of static Coulomb stress change by King et al. [1994] after the 1992 M_{w} 7.3 Landers earthquake. Aftershocks fall almost exclusively into areas of positive Coulomb failure stress change and the fault of the 1999 M_{w} 7.1 Hector Mine earthquake is put closer to failure. Similarly, Stein et al. [1997] apply Coulomb failure stress changes to demonstrate the subsequent failure of sections of the North Anatolian Fault, Turkey by static stress triggering.

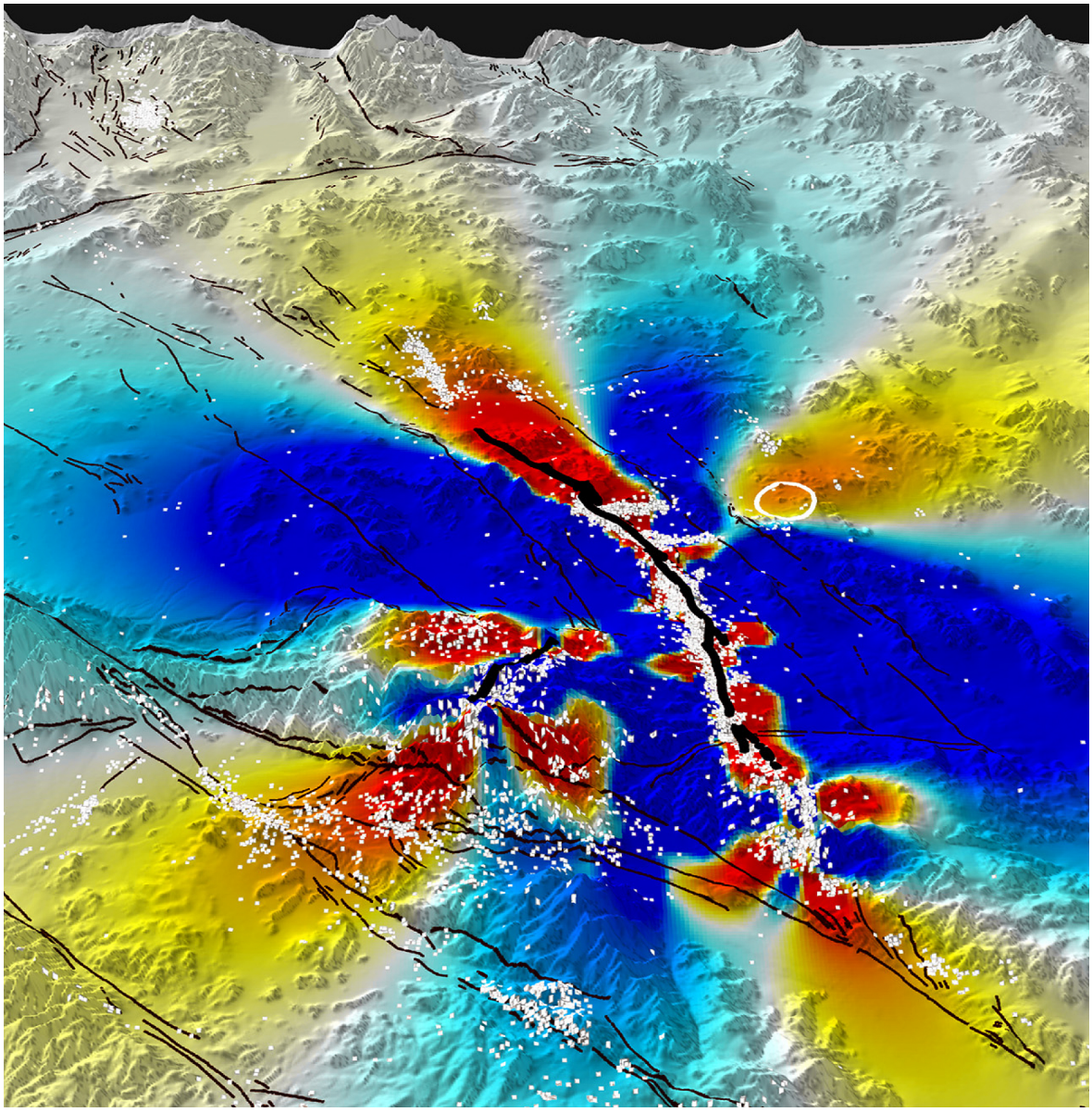

Figure 2.6: Static Coulomb stress change at 7.5 km depth imparted by the 1992 M_w 7.3 Landers, California, earthquake to the surrounding crust, together with the next 7 years of $M_w \geq 2$ aftershocks (white dots) [King et al., 1994]. Red and blue colors denote positive and negative ΔCFS, respectively. The white circle denotes the epicenter of the 1999 M_w 7.1 Hector Mine earthquake.

The static stress change mechanism also applies to volcanic systems. For open conduit systems, such as volcanoes during an ongoing eruption or active phase, Nostro et al. [1998] suggest that magma may be pushed out of the reservoir chamber by raised confining pressure if the volcano is located and oriented such that the magma reservoir experiences increased normal stresses. More commonly observed is increased activity along volcanic arcs after preceding subduction zone earthquakes [Bonali, 2013; Diez et al., 2005; Marzocchi, 2002a]. In this scenario, confining stresses onto the volcanic system are reduced by slip on the plate interface, thus making it easier for magma at

depth to rise and fracture surrounding rock, eventually resulting in an eruption of an otherwise uncritical volcano. As for earthquake triggering, these effects of static stress change range only approximately one fault length from the epicenter.

2.3 Dynamic stress triggering

2.3.1 Coulomb failure under dynamic stresses

Dynamic stress triggering denotes the concept that transient stresses carried by seismic waves may bring a system closer to Coulomb failure. Since at distance surface waves induce the strongest ground motion and thus the highest dynamic stresses, they are most commonly responsible for dynamic triggering. The range of dynamic triggering thus greatly exceeds that of static stress triggering. The following simplified descriptions are based on the work of Hill [2008, 2010, 2012a,b] on triggering potential of seismic surface waves.

Dynamic stresses σ_d of seismic waves can be estimated through the relationship

$$\sigma_\mathrm{d} = G \cdot \frac{\mathrm{PGV}}{v_\mathrm{s}} \tag{2.7}$$

with the crusts shear modulus $G \approx 30$ GPa, the peak ground velocity PGV induced by the seismic waves and the S-wave velocity v_s at the respective depth. Under the assumption that peak dynamic stresses are small compared to the local stress difference $|R| = (\sigma_1 - \sigma_3)/2$ one can derive a triggering potential P that describes the ability of seismic surface waves to trigger reactions on a pre-existing fault for different incident angles. This assumption is consistent with reported dynamic triggering stresses in the low Kilopascal to low Megapascal range compared to the order of 100 MPa near-critical tectonic stress states in the seismogenic crust.

During the passage of surface waves, the local stress field will fluctuate in both amplitude and orientation, resulting in an oscillatory motion of the tip $\vec{R}$ that follows the stress state of an optimally oriented fault in the Mohr circle representation (see Figure 2.7). Analogous to the definition of the static change in Coulomb failure stress ΔCFS one defines a time-dependent dynamic change in Coulomb failure stress $\delta\mathrm{CFS}(t)$ that acts only during the passage of seismic waves:

$$\delta\mathrm{CFS}(\gamma,t) = \delta\tau(\gamma,t) - \mu\delta\sigma_\mathrm{n}(\gamma,t) \tag{2.8}$$

with $\tau(\gamma,t)$ and $\sigma_\mathrm{n}(\gamma,t)$ being the time-dependent shear stress and normal stress, respectively, imposed on a given fault by seismic waves incident at an angle γ from a remote earthquake. Figure 2.7 illustrates these additional stresses within a Mohr-Coulomb diagram for a Rayleigh wave acting on an optimally oriented fault. Note that $\delta\mathrm{CFS}(t)$ is the one-dimensional projection of the two-dimensional seismic wave stress orbit onto the normal of the Coulomb failure criterion. While both Love and Rayleigh waves generally cause distortional stresses (decomposed into shear stress τ and normal stress σ_n) only

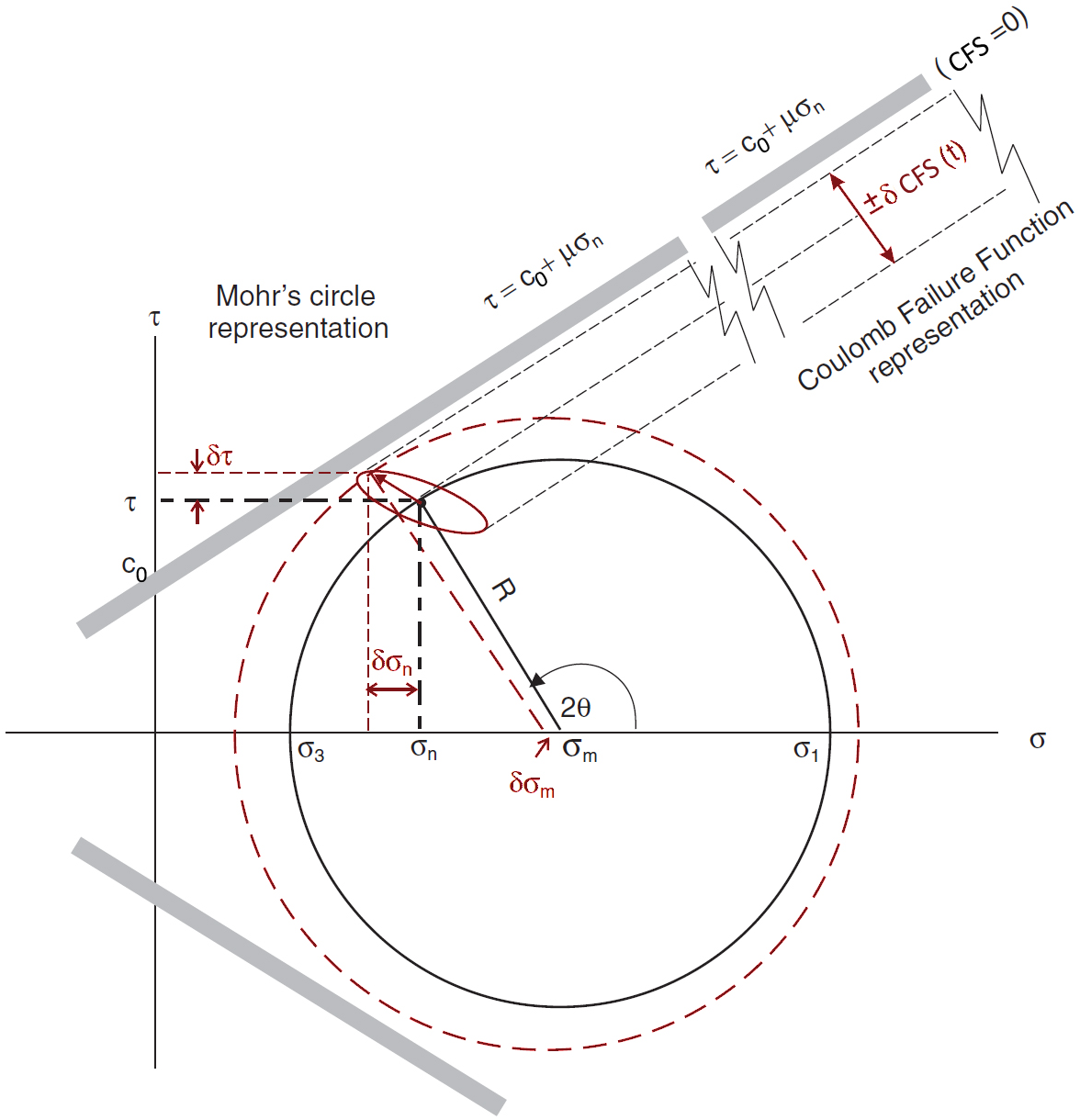

Figure 2.7: Mohr circle representation of the Rayleigh wave induced perturbation of the local stress field on an optimally oriented fault. Dashed red lines show the total stress state at a time t. The solid red ellipse is the dynamic stress orbit of the Rayleigh wave acting on the fault as traced by the tip of $\vec{R}(t)$ [Hill, 2012a].

Rayleigh waves additionally induce or dilatational stresses. The latter are represented by a perturbation of the mean stress $\delta\sigma_{\mathrm{m}}$ in a Mohr diagram.

For a given fault, the dynamic stress orbits $\tau(\gamma,t)$ and $\sigma_{\mathrm{n}}(\gamma,t)$ induced by Love or Rayleigh waves depend only on the direction of wave propagation γ with respect to the fault strike. For example, Love waves arriving strike-perpendicular on a thrust or normal fault will neither induce additional dip-parallel shear stress $\delta\tau_{\mathrm{d}}$ nor additional normal stress $\delta\sigma_{\mathrm{n}}$. In contrast, Love waves propagating strike-parallel will cause both dynamic shear and normal stress change, with the amplitudes depending on the dip

δ of the fault (see Figure 2.8). Rayleigh wave stresses are anti-correlated with Love wave stresses and show strongest effects when arriving strike-perpendicular. Note that particle motion of both Rayleigh and Love waves is depth-dependent and thus the amplitude of both $\tau(\gamma,t)$ and $\sigma_n(\gamma,t)$ changes with depth, as depicted in Figure 2.9. Consequently, stress orbits of Love and Rayleigh waves as shown in Figure 2.8 will look different for another depth.

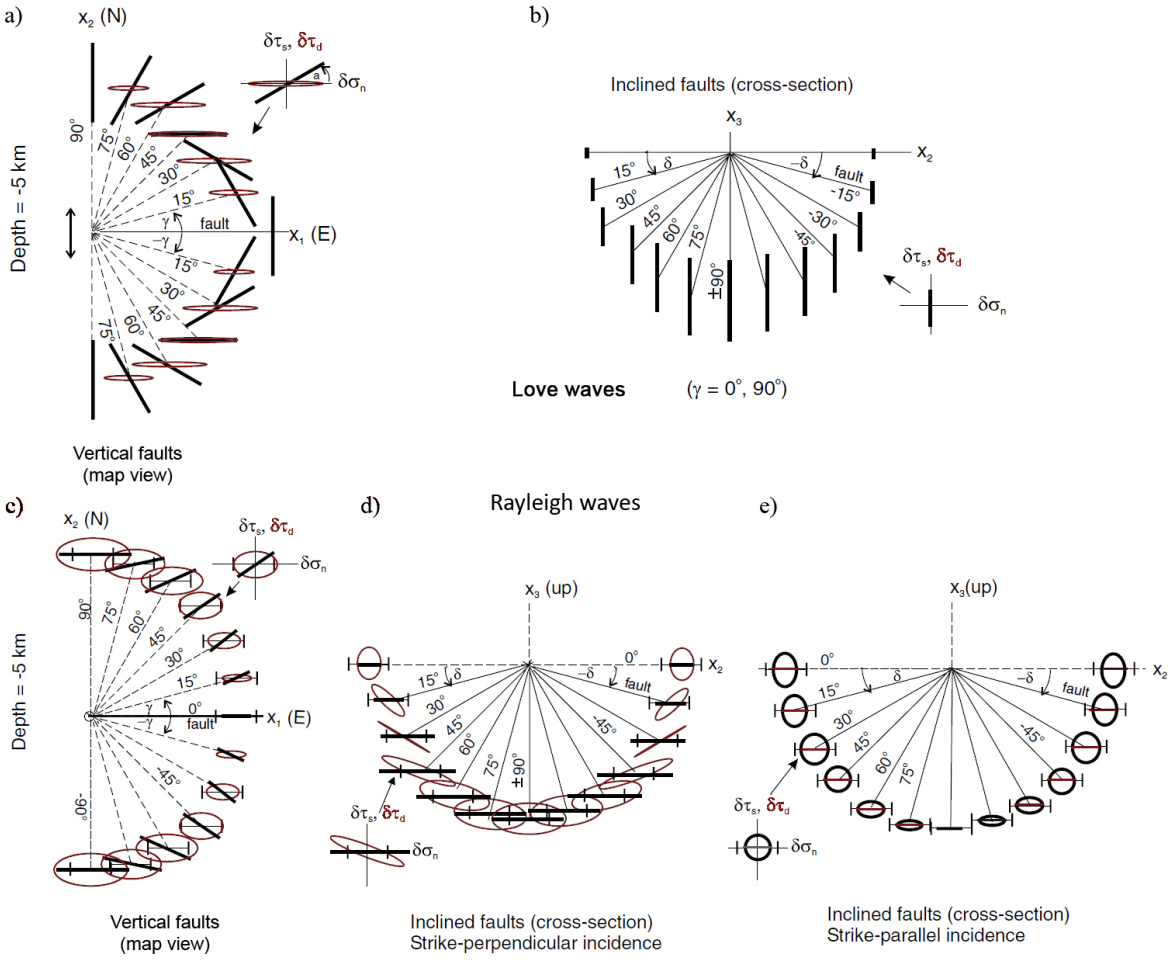

Figure 2.8: Dynamic stress orbits of Love (top) and Rayleigh waves (bottom) at 5 km depth. Strike-parallel stress orbits ($\delta\tau_s$ vs. $\delta\sigma_n$) and dip-parallel orbits ($\delta\tau_d$ vs. $\delta\sigma_n$) are indicated by black and red solid lines, respectively (see insets). **a)** and **b)** Map view of east-striking, vertical fault planes with incidence angles $-90° \leq \gamma \leq 90°$ in 15° increments (dashed lines). **b)**, **d)** and **e)** Cross section of dipping fault planes over the dip range $-90° \leq \delta \leq 90°$ for strike-parallel and strike-perpendicular incidence. Note that for Love waves at this shallow depth, stress orbits for strike-parallel and strike-perpendicular incidence are essentially coincident and no normal stress change $\delta\sigma_n$ is imposed. For strike-parallel incidence, Love waves impose normal stress changes only at greater depth (see Figure 2.9). For Rayleigh waves, the short vertical bars indicate the relative amplitude of the dilatational stress component $\delta\sigma_m$ which is isotropic (independent of γ). Modified after Hill [2012a].

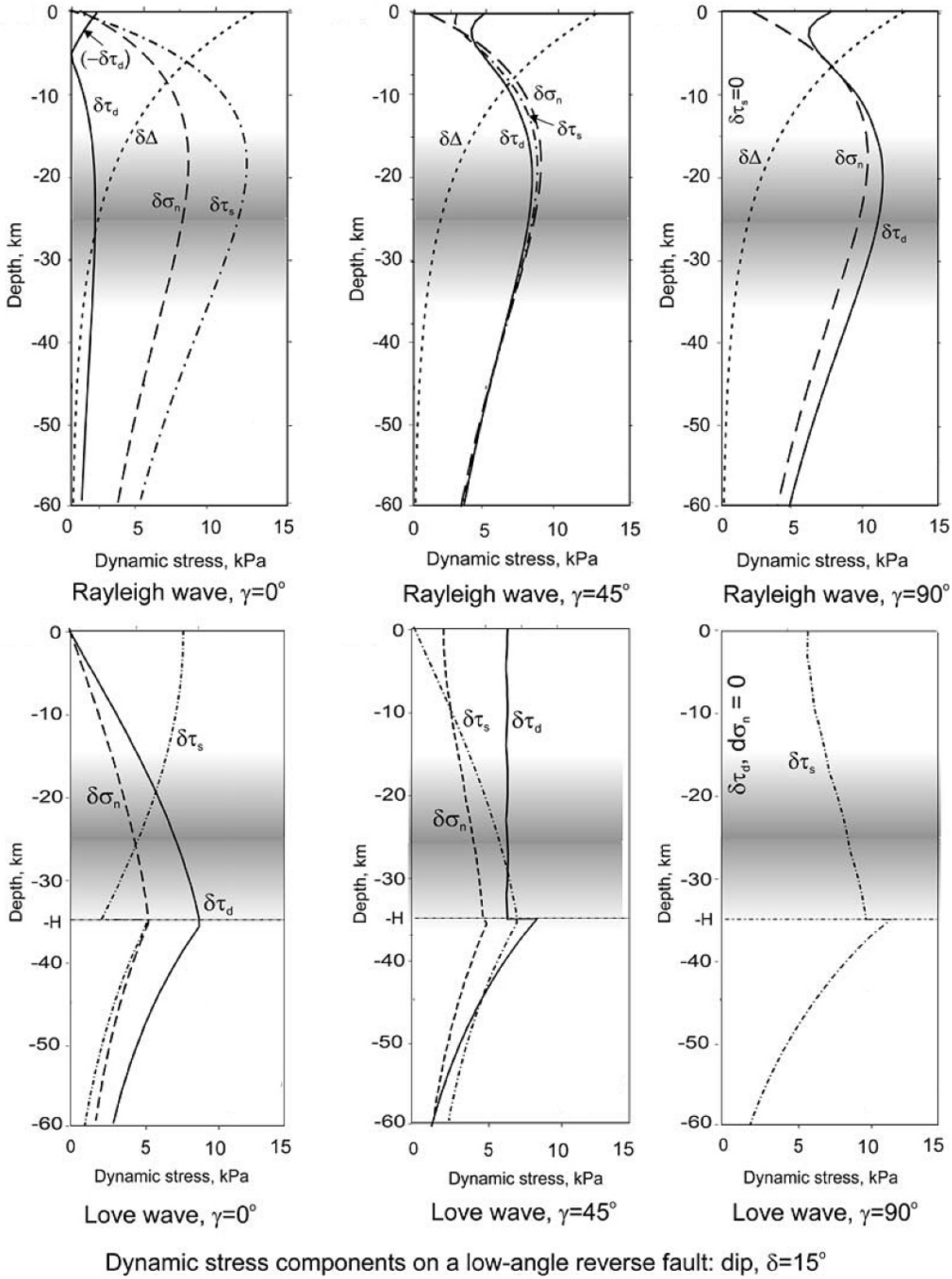

Figure 2.9: Surface wave stresses as a function of depth. Shown are the peak absolute values for dynamic stress components of Rayleigh (top) and Love waves (bottom) incident on a low-angle thrust fault at different incidence angles γ. Plotted are dynamic normal stress $\delta\sigma_n$ and both dynamic dip-parallel shear stress $\delta\tau_d$ and dynamic strike-parallel shear stress $\delta\tau_s$. The gray bands indicate the common approximate depth range of tectonic tremor. The line at $z = -H$ marks the boundary between two layers of the Love wave velocity model [Hill, 2012b].

The triggering capability of surface waves is expressed by the triggering potential $P(\gamma)$ that depends solely on the incident angle γ for a given fault and depth.

$$P(\gamma) = |(L/L_{\max}) \sin[\vartheta - a(\gamma)]| \tag{2.9}$$

where $\vartheta = \tan^{-1}\mu$ is the angle of internal friction and $a(\gamma) = \tan^{-1}[\delta\tau(\gamma)/\delta\sigma_{\mathrm{n}}(\gamma)]$ reflects the inclination of $\vec{L}$ for a given incidence angle γ [Hill, 2012a,b].

$$L = \sqrt{[\delta\sigma_{\mathrm{n}}(\gamma)]^2 + [\delta\tau(\gamma)]^2} \tag{2.10}$$

is the length of the stress orbit extending beyond the background Mohr circle and $L_{\max}$ is the maximum value of L. Thus, the triggering potential $0 \leq P(\gamma) \leq 1$ represents the normalized length of the stress orbit extending beyond the Mohr cirle, projected onto the normal to the Coulomb failure line. Note that this is analogous to the equation 2.8 definition of the dynamic Coulomb failure stress δCFS(γ,t). Figure 2.10 illustrates all of the above definitions in the Mohr-Coulomb representation.

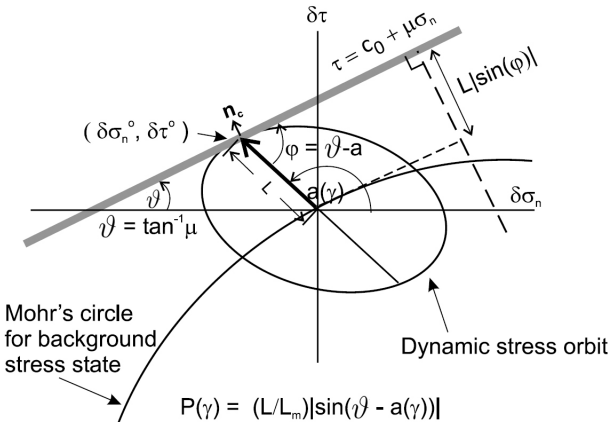

Figure 2.10: Diagram illustrating the geometric significance of the triggering potential $P(\gamma)$ for an elliptical stress orbit tangent to the Coulomb failure line. Modified after Hill [2012b].

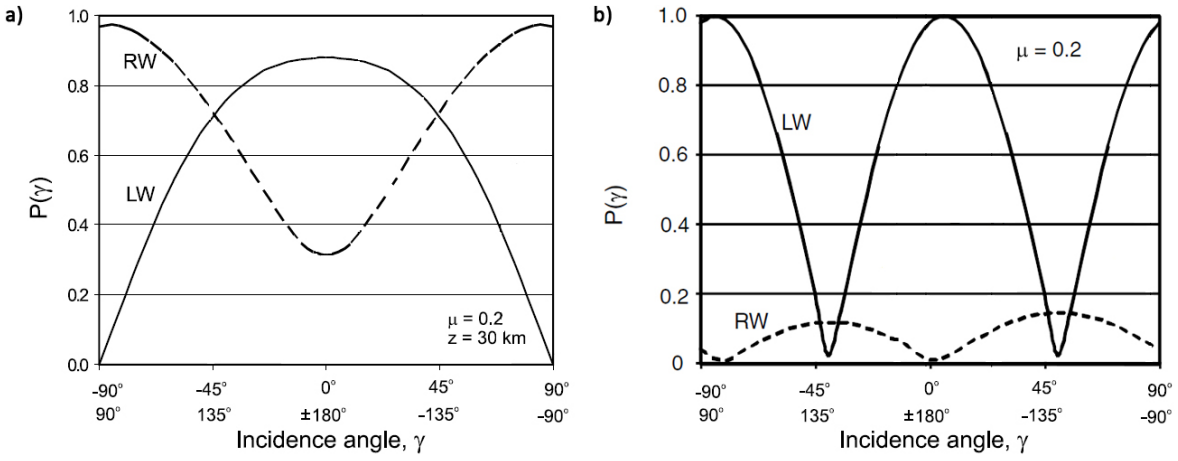

Figure 2.11: Triggering potential on **a)** low-angle megathrust ($\delta = 15°$) and **b)** vertical strike slip fault. Solid lines show Love wave triggering potential and dashed lines represent Rayleigh wave triggering potential on a weak fault ($\mu = 0.2$). Values are scaled for a common $L_{\max}$ at $z = 0$ km. Note the anti-correlation of Love and Rayleigh wave potential and the reduced Rayleigh wave potential on strike-slip faults (right). Modified after Hill [2012b].

The value of the triggering potential is determined by how the surface wave particle motion splits into normal stress $\delta\sigma_n$ and dip-parallel $\delta\tau_d$ or strike-parallel $\delta\tau_s$ shear stresses. Thus, the triggering potential $P(\gamma)$ differs for Love and Rayleigh waves and strongly depends on the type of the receiving fault and its dip, as well as the angle of incidence of the seismic waves with respect to the fault strike. Because of the different particle motion, Love wave and Rayleigh wave triggering potential are anti-correlated as exemplary shown in Figure 2.11 for a low-angle (dip $\delta = 15°$) megathrust and a strike-slip fault.

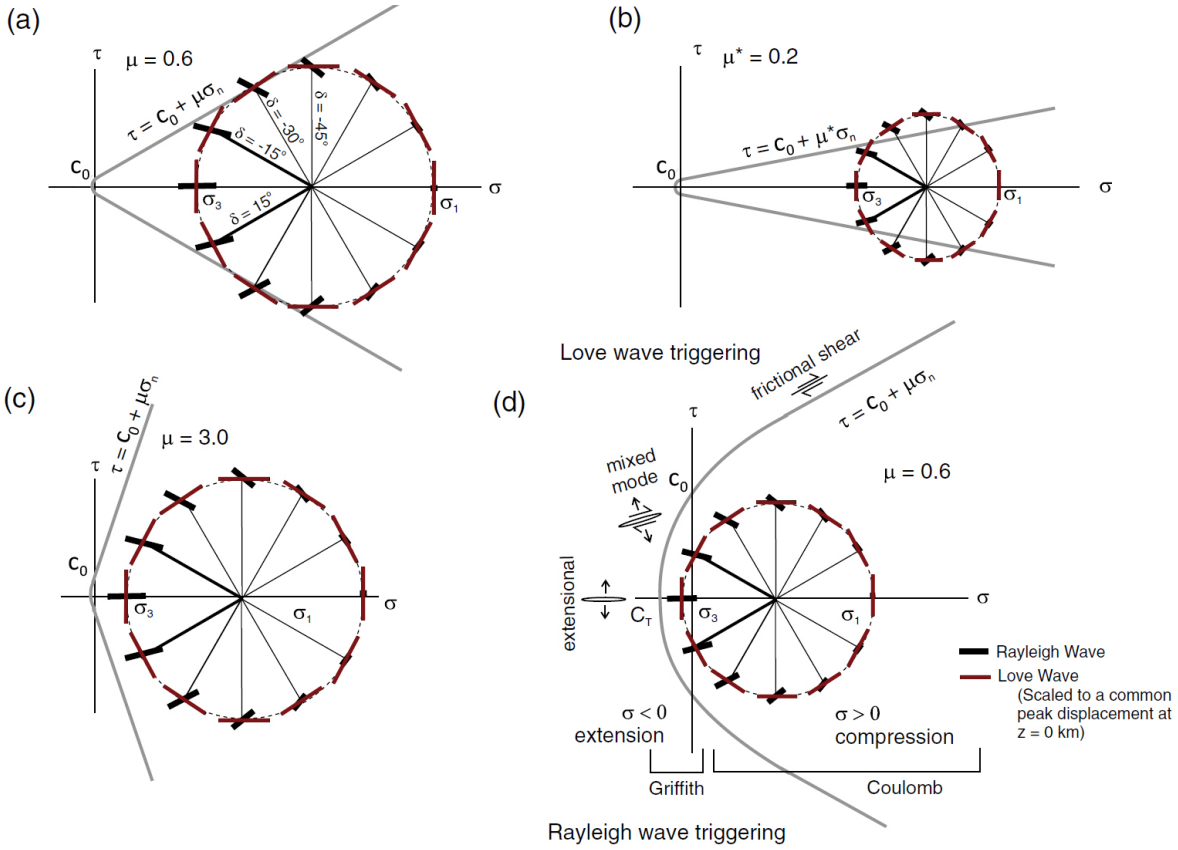

Figure 2.12: Scenarios for Love or Rayleigh wave favored triggering. Black and red bars show the maximum amplitude of stress orbits for Rayleigh and Love waves, respectively, at 30 km depth. Stress orbits are calculated for strike-parallel incidence on a thrust fault with different dips δ. **(a)** Large ambient differential stress $[1/2(\sigma_1 - \sigma_3) \gg C]$ and mean stress σ_m, with $\mu = 0.6$ admit both Love and Rayleigh wave triggering. **(b)** Moderate ambient differential and mean stresses with a high fault-confined pore pressure ($\mu^* = 0.2$) in the megathrust favors Love wave triggering. **(c)** Large differential and mean stresses with a high friction coefficient and **(d)** small differential and mean apparent stresses under a near-lithostatic ambient pore pressure both favor Rayleigh-wave triggering [Hill, 2012b].

Figure 2.12 illustrates different stress scenarios which preferably allow for Love or Rayleigh wave triggering for strike-parallel incidence on megathrust faults with different dip δ. For large ambient differential stress $(1/2[\sigma_1 - \sigma_3] \gg C)$ and moderate intrinsic friction $(\mu = 0.6)$ the fault is equally sensitive to both Love and Rayleigh wave triggering such that the dip δ determines which type of surface wave is more likely to trigger

failure on such faults. For moderate ambient differential stress and faults weakened by high pore pressures (here expressed by a reduced apparent friction coefficient μ^*) Love wave generally carry greater triggering potential. In turn, Rayleigh wave triggering is favored for large differential stresses and high friction coefficients or for small differential stresses under near-lithostatic ambient pore pressure.

While Love waves induce deviatoric stresses only, Rayleigh waves additionally cause dilatational stress changes which the above formulation of the triggering potential does not include. Yet, Rayleigh wave dilatational stresses influence the fluid pore pressure and thus play a role in the Rayleigh wave interaction with faults through fluid pressure related fault weakening. This concept may be of particular importance for triggering within volcanic and geothermal areas. Miyazawa and Brodsky [2008] suggest that dilatational stresses change the aperture of pre-existing fractures. Thus, permeability is locally increased for extensional stress and reduced for compressional stress of Rayleigh waves. The resulting temporary oscillation of permeability may lead to fluid flow which eventually weakens sections of the fault by increased pore pressure. However, the interplay of deviatoric and dilatational stresses induced by Rayleigh waves is complex. Depending on the relative phase between dilatational stress and the normal component of the deviatoric stress, elevated pore pressure may be offset by increased normal stress. However, the phase shift between dilatational and deviatoric normal stress changes with both depth and angle of incidence such that dilatational stresses have to be individually evaluated for each triggering scenario. Additionally, Lockner and Beeler [2003] point out that in anisotropic media deviatoric stresses from both Love and Rayleigh waves can contribute to dilatational strain. Still, the role of Rayleigh wave dilatational stress in triggering phenomena is yet to be settled.

The above introduction of the surface wave triggering potential applies to triggering of crustal brittle-failure earthquakes and tectonic tremor. Surface wave interaction with volcanic or geothermal systems requires additional mechanisms which are introduced in the following.

2.3.2 Dynamic earthquake-volcano interaction

Volcanic and geothermal systems can be influenced by seismic waves of remote earthquakes. Responses may range from heat flow changes [Delle Donne et al., 2010] to eruptions of long dormant volcanoes [Marzocchi, 2002a]. Most commonly observed, however, are changes in seismic activity within geothermal areas or hydrothermal systems in close vicinity of volcanoes. Yet, despite more than ten years of earthquake volcano interaction observation, credible mechanisms that explain the interplay of volcanic fluids and seismic waves are still to be found [Hill and Prejean, 2014, and references therein]. Proposed models [Hill et al., 2002] either focus on crustal hydrothermal fluids that react to incoming seismic waves or interactions within the magmatic body. The following descriptions are based on reviews of Hill et al. [2002] and Hill and Prejean [2014].

Crustal fluids

One physical explanation for earthquake triggering within volcanic or geothermal systems is the unclogging of small fractures by seismic wave induced shaking [Brodsky et al., 2003; Elkhoury et al., 2011]. Pre-existing fractures within the hydrothermal system are clogged by accumulating detritus over time. The shaking that accompanies seismic waves may flush fractures open and thus locally increase the permeability of the fracture network. The resulting redistribution of pressure leads to fluid flow which eventually is the cause of locally enhanced seismicity. Such models should be viable in areas where isolated pockets of high pressure fluids develop, such as active geothermal areas where high pressure compartments may form over short time scales. Additionally, the subsequent clogging of fractures after they were flushed by seismic waves may explain the observed recovery time in which geothermal systems are relatively insensitive to external stimuli after a dynamic triggering event took place.

The hydraulic surge model proposed by Fournier [1999] follows a similar approach. In the plastic low-permeability zone that usually shields magma bodies from the brittle part of the crust, hydrous magmatic fluids can reach near-lithostatic pressure. Dynamic stresses from remote earthquakes may rupture this otherwise impermeable zone, allowing high pressure fluids to surge into the brittle crust and cause earthquakes or even volcanic eruptions if the reduced confining stress on the magma initiates bubble formation, ascent and growth. Since fluids move through the fractured low-permeability zone and crust by diffusion, this mechanism could as well apply to delayed triggering, where seismicity starts after the wavetrain has passed.

Magmatic fluids

Dynamic stresses of remote earthquakes are capable of perturbing the state of crustal or upper mantle magma bodies. Models that try to explain such reaction are usually based on internal pressure changes in the magma chamber which cause deformation of the magma body or intrusions into the surrounding material. Triggered seismic activity is then only a secondary response to this local deformation. Since such models predict distinct ground deformation, high-resolution deformation monitoring such as radar interferometry InSAR can test their validity [Hill and Prejean, 2014].

In the rectified diffusion model [Brodsky et al., 1998] volatiles in saturated magmatic fluids are selectively pumped into bubbles during the dilatational phase of Rayleigh waves. Over several pumping cycles during the wavetrain this mechanism may lead to increased bubble pressure. The model of advective overpressure describes that bubbles adhering to walls of magma body are shaken lose by the seismic waves and buoyantly rise to the top of the magma chamber which effectively increases the pressure in the magma chamber [Linde et al., 1994]. Both models explain triggered seismicity by pressure transmission from the magmatic body to the surrounding interstitial fluids. Yet, both highly idealized models appear unrealistic under natural conditions [Ichihara and Brodsky, 2006].

Hill et al. [2002] nicely summarizes two other mechanisms of volcano excitation that are not bubble driven. The following is cited from [Hill et al., 2002]:

As it evolves, a magma chamber in the crust can reach a partially crystallized state either by the gradual cooling of a previously molten volume or by the partial melting of a previously solid volume. The resulting interconnected solid matrix will sustain stress differences that accumulate in the region. Strong seismic waves from a distant earthquake might disrupt the integrity of the solid matrix and release any accumulated stress differences, thereby deforming the surrounding crust and triggering local earthquakes [Hill et al., 1995].

Relatively dense, loosely held masses of crystals can accumulate on the ceiling and sides of a crystallizing magma body and might be dislodged by passing seismic waves. As crystal-rich plumes sink, less dense and crystal-poor magma is forced upward, producing convection. Magma that is forced upward will contain volatiles, and the ascent can trigger bubble formation. Further ascent of the bubbles will induce advective overpressure. Calculations specific to dynamic triggering have yet to be carried out [...], but measurements suggest that magma can convect at a rate of 0.01 to 10 cm/s. At 1 cm/s, gas-rich magma in a preexisting conduit can be pushed upward from subvolcanic storage to eruption in less than a week [Manga and Brodsky, 2006].

Each of the aforementioned models requires time for the respective systems to return to a near-critical state after a triggering episode. The recharge time may vary from days to weeks for the bubble-based models in a hydrothermal system and from decades to centuries for the relaxing magma body model. In principle, volcanic unrest triggered by each of these interaction modes has the potential for evolving to a volcanic eruption, provided the associated magmatic system is sufficiently close to a critical state. [Hill et al., 2002, end of citation].

Prejean and Hill [2013] and Hill and Prejean [2014] point out that the susceptibility of volcanic systems to dynamic triggering does not necessarily correlate with volcanic unrest. Additionally, volcanic response to remote earthquakes is more commonly observed within the hydrothermal system rather than the magmatic section of volcanic systems.

2.4 Volcano seismology

Many results within this thesis are based on the analysis of seismic waveforms measured in volcanic areas. In the following, the most common manifestations of seismicity in volcanic systems are introduced. Sample waveforms and spectra are taken from Wassermann [2012]. The indicated waveform amplitudes are normalized to the amplitude of the deep volcano-tectonic event (Figure 2.13). For each spectrum, color is scaled to the dominant frequency.

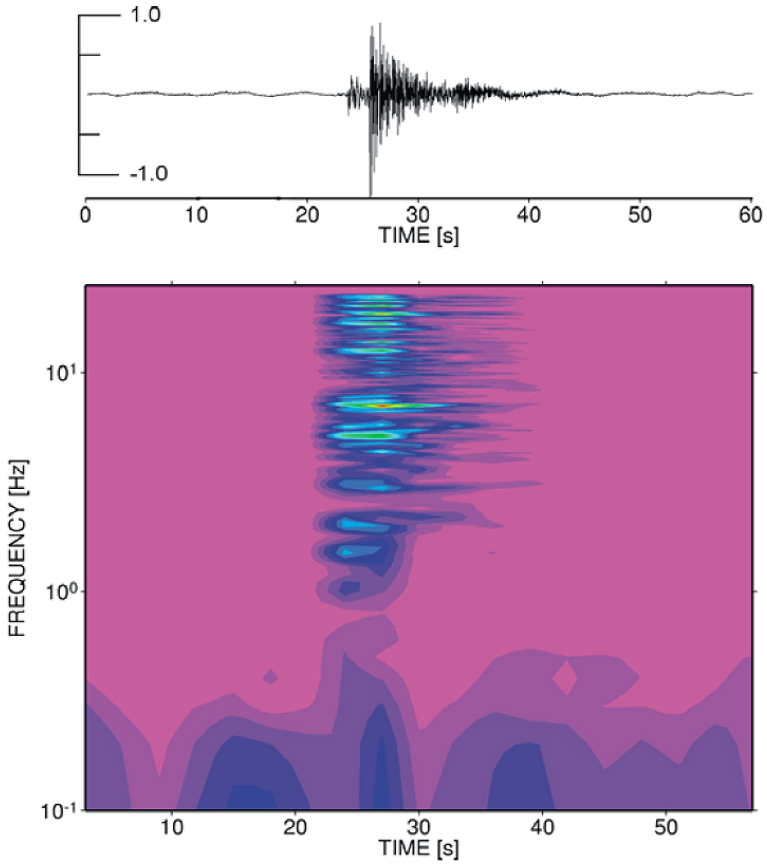

Figure 2.13: Deep volcano-tectonic (VT) earthquake. Brittle shear failure earthquakes originating from 2 km depth and below. Deep volcano-tectonic events show distinct and clear onsets of P and S wave arrivals and their frequency content is higher than 5 Hz [Wassermann, 2012].

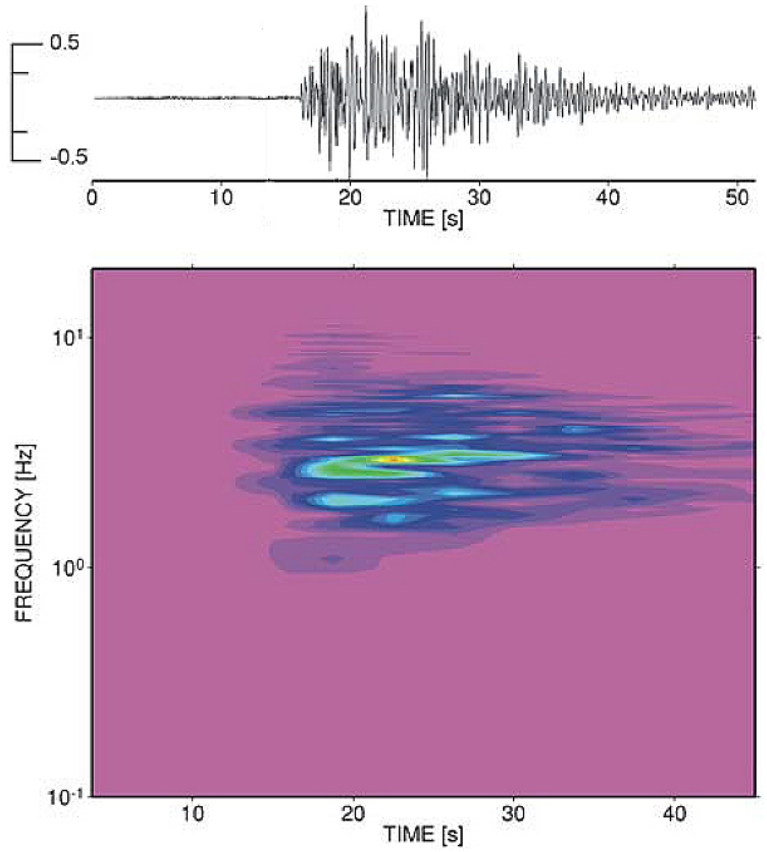

Figure 2.14: Shallow volcano-tectonic (VT) earthquake. Brittle shear failure earthquakes originating from above 2 km depth. Shallow volcano-tectonic events usually originate from within the volcanic cone and experience larger amount of scattering. Hence, P-wave onsets are very emergent, S-wave onsets can hardly be identified and the frequency content is in the lower 1–5 Hz range [Wassermann, 2012].

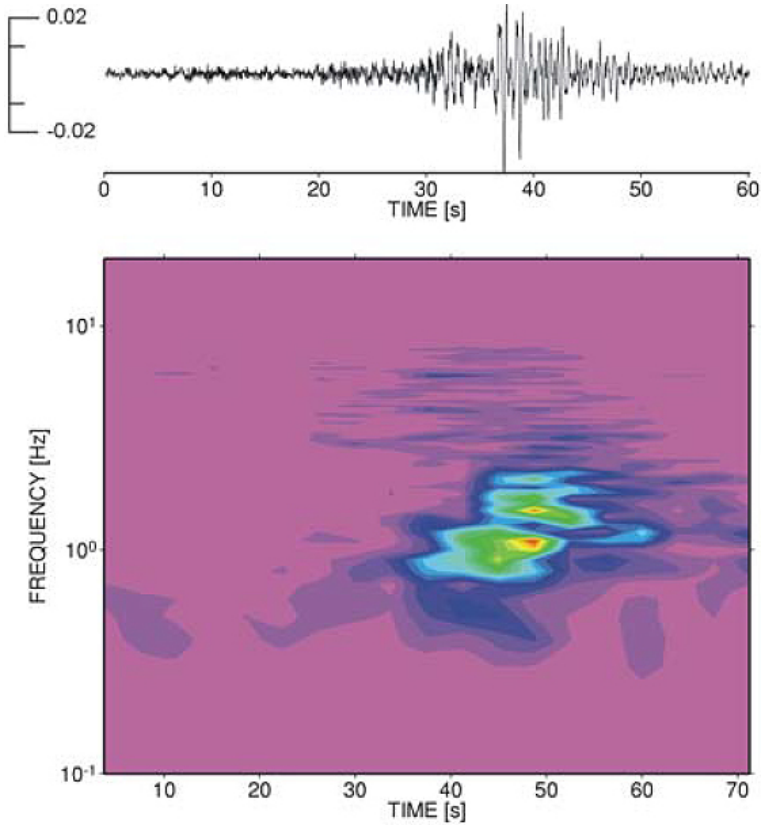

Figure 2.15: Low-frequency earthquake (LFE). Low-frequency or long-period events usually show no S-wave arrival and a very emergent onset. Their name is due to the comparably low frequency content in between 0.2–5 Hz. LFEs can be procuded at both shallow (<2 km [Kawakatsu et al., 2000]) and great (30–40 km [Shaw and Chouet, 1991]) depth. Low-frequency events are likely connected to ascending low viscous magma such as in opening and resonating cracks or oscillations of fluids in feeding channels or dikes [Wassermann, 2012].

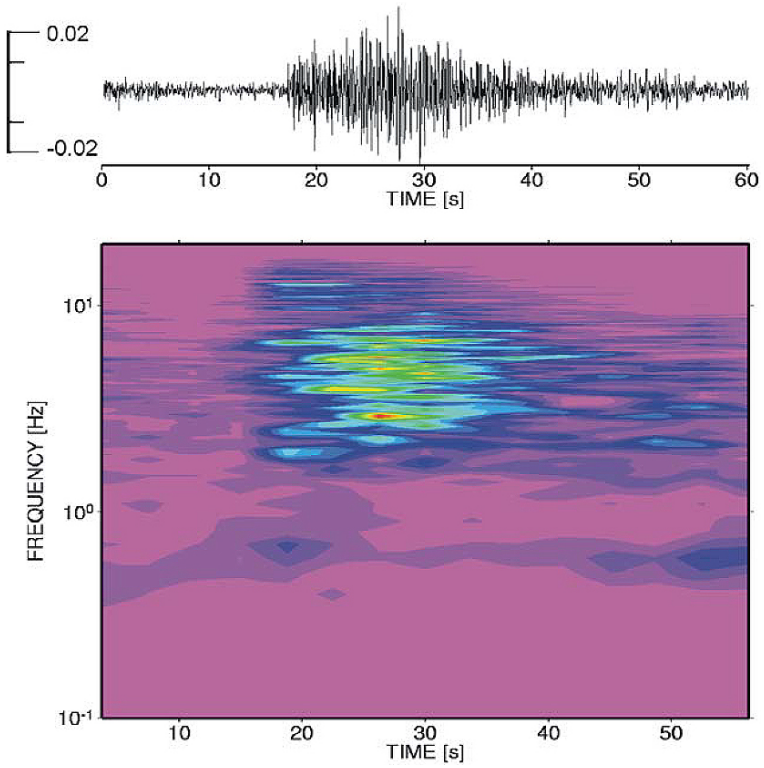

Figure 2.16: Hybrid or multiphase event. Hybrid events reflect the apparent waveforms and frequency content of shallow VT events, but are much weaker in amplitude and of longer duration. The source mechanism is still a topic of research but likely is a mixture of VT and LF events, yet of much shallower depth [Wassermann, 2012].

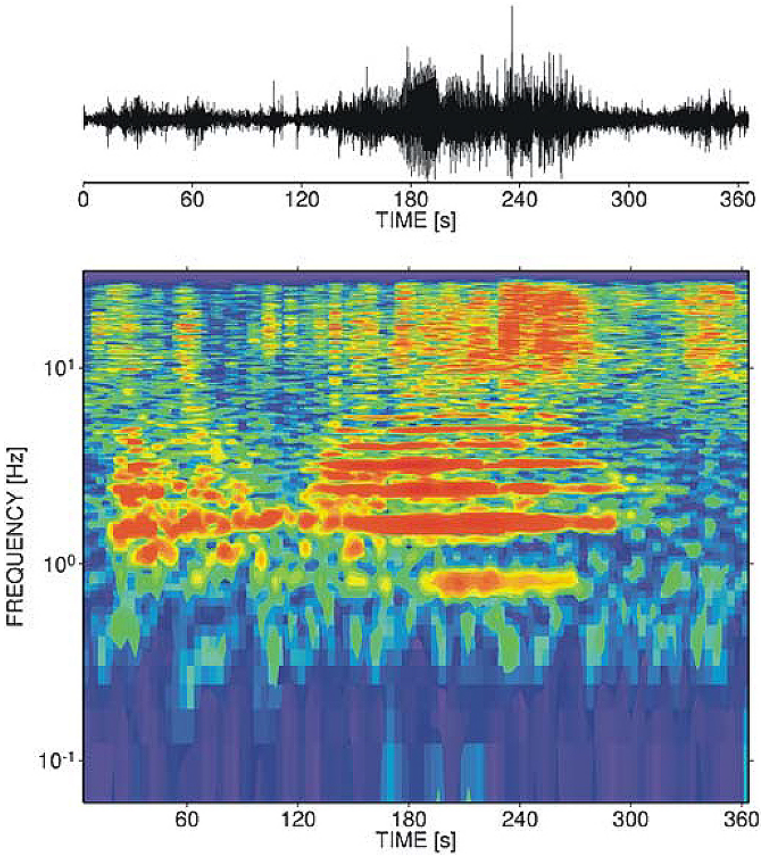

Figure 2.17: Volcanic tremor. This long-lasting, emergent and irregular signal is termed volcanic tremor. The outstanding feature is the characteristic overtone spectrum that may contain distinct frequency bands with up to 30 overtones [Hellweg, 2000]. Occurence of volcanic tremor is a sign of strong volcanic activity and future eruptions. Yet, the process of its generation is not well understood but is supposed to involve a feedback mechanism of resonating gases in high-viscous magma. Volcanic tremor likely consist of repeating hybrid or multi-phase events [Wassermann, 2012].

3 The microseismic signature of dormant volcanoes

Prejean and Hill [2013] state that volcanoes showing a response to remote dynamic triggering quite often are not in a state of unrest. Yet, unless being in populated areas or in regions of broader scientific interest, inactive volcanoes are if at all not extensively monitored. This chapter describes the seismic monitoring of the Snæfellsjökull volcano in western Iceland over two periods in 2011 and 2013. The volcano is generally considered active although it is dormant since 1750 BP. Originally aiming to explain the origin of rejuvenated volcanism along the Snæfellsnes peninsula in western Iceland, the following study revealed seismic activity below the long dormant Snæfellsjökull volcano. Hence, the Snæfellsjökull allows for insights into seismic activity of resting volcanoes which may help to evaluate instances of triggered volcanic seismicity as compared to regular seismic activity elsewhere. However, in contrast to many volcanic areas that were prone to remote triggering in the past the Snæfellsjökull does not have strong manifestations of hydrothermal activity at the surface such that triggering is not necessarily expected.

The Snæfellsnes study was performed in two parts. Section 3.1 deals with the first exploratory campaign that was conducted in summer 2011 utilizing five broadband seismometers. Figure 3.1 shows the equipment used during this campaign and a typical installation of a seismic station. Section 3.2 supplements the results of the first campaign with InSAR studies. Presented in section 3.3 are the preliminary results of the follow-up deployment in summer 2013 that involved a total of 21 seismic stations.

Figure 3.1: Instrument deployment during the 2011 campagin on the Snæfellsnes. Left: Broadband instruments, thermal insulation cover, data cables, GPS antennas and 12V batteries for power supply. The Snæfellsjökull volcano is seen in the background. Right: Typical installation of a seismic station. The Seismometer is on base-rock with thermal insulation. Data logger and battery are inside the metal box. The solar panel charges the battery and allows for long term operation.

3.1 Seismicity observed under Snæfellsjökull volcano

This Section is published as: F. Fuchs, M. Lupi, S. S. Jakobsdóttir, T. Thordarson and S. A. Miller (2013), Seismicity observed under the Snæfellsjökull volcano, *Jökull, 63*, 105–112.

Introduction

Volcanic and seismic activity in Iceland are driven by the interaction of the Mid-Atlantic Ridge and the Icelandic Plume [Einarsson, 2008; Jakobsdóttir, 2008; Mjelde et al., 2008]. Seismicity concentrates along the Mid-Atlantic Ridge cutting through Iceland and separating the north-American and Eurasian plates. Seismic activity is particularly intense in the South Icelandic Seismic Zone (SISZ) and in the Tjörnes Fracture Zone (TFZ) (see inset in Figure 3.2), which are two transform fracture zones that accommodate the offset of the Mid-Atlantic Ridge [Stefánsson et al., 2006, 2008]. The axial rift was located in the Western Fjords (WF) at 15 Ma and then moved east towards the Icelandic plume, intercepting the Snæfellsnes peninsula and the Skagi peninsula around 7 Ma [Martin et al., 2011].

Previous studies of the Snæfellsnes peninsula focused on constraining the evolution of the neovolcanic zone and dating volcanic activity [Hardarsson and Fitton, 1991; Jóhannesson, 1980, 1982a,b; Kokfelt et al., 2009; Martin and Sigmarsson, 2010; Martin et al., 2011]. Figure 3.2 shows the outlines of volcanic systems found on the Snæfellsnes peninsula. Sigurdsson [1970] and Jóhannesson [1982b] pointed out the existence of WNW-ESE trending en-echelon lineaments identified by the alignment of volcanic structures and vents. Interestingly, the orientation of these lineaments is perpendicular to en-echelon patterns observed in the neighboring Western Volcanic Zone and in the South Icelandic Seismic Zone.

The Snæfellsnes peninsula hosts three volcanic systems that form the Snæfellsnes Volcanic Belt (SVB). The central volcano Snæfellsjökull is located on the westernmost tip of the peninsula (Figure 3.2) and its last rhyolitic explosive eruption has been dated to 1750 BP by Steinthorsson [1967]. Located further east is the Lýsuhóll (or Helgrindur) volcanic system which was active during the Holocene while the Ljósufjöll volcanic system marks the easternmost extension of the SVB. Here the 1050 BP Raudhálsar event took place, which is the most recent volcanic eruption in the SVB [Flude et al., 2008; Jóhannesson, 1982a]. However, the reason why the Snæfellsnes peninsula features rejuvenated volcanism with the observed alignment remains unknown.

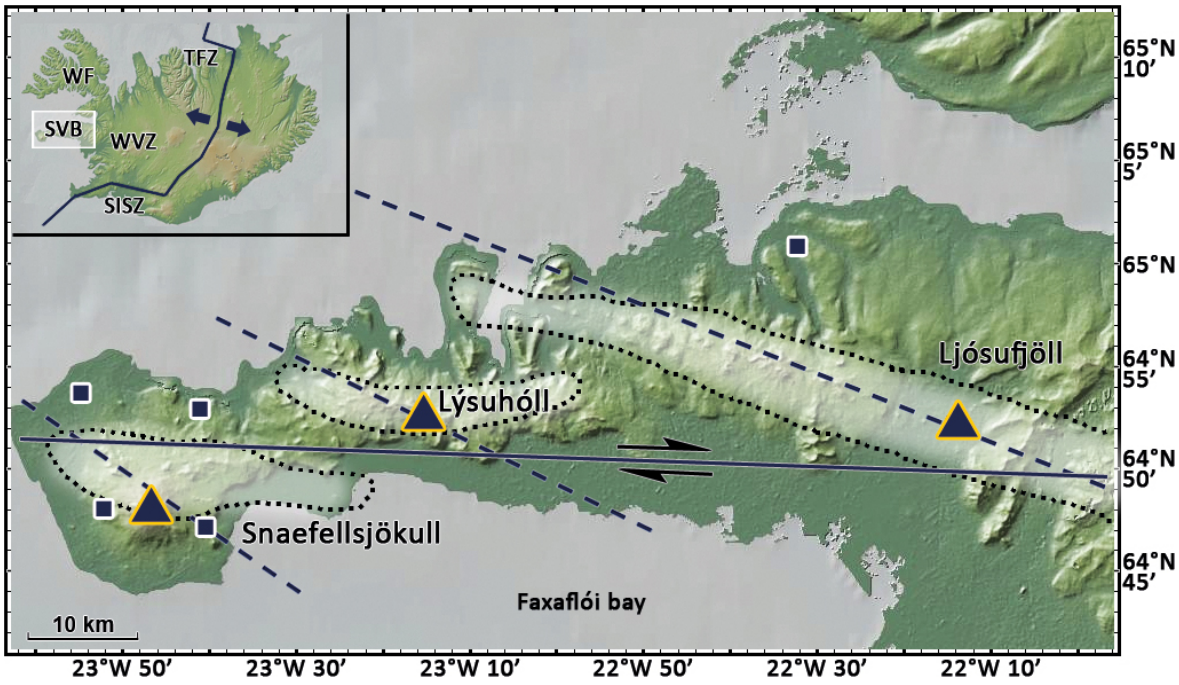

Figure 3.2: Map of the Snæfellsnes peninsula showing the Snæfellsjökull, Lýsuhóll, and Ljósufjöll volcanic centers (triangles) as well as the orientation of geological lineaments described by Sigurdsson [1970] (dashed lines). The shaded regions mark distributions of volcanic systems in the region. The location of the inferred transcurrent fault is indicated by the east-west trending solid line. The positions of our seismic stations are denoted by squares.

Geophysical data in the region are sparse when compared to geological and geochemical data. Little is known about the deep structure of the Snæfellsnes peninsula. Based on recordings from the HOTSPOT experiment both Allen et al. [2002] and Du et al. [2002] report a crustal thickness of about 15–20 km for the Snæfellsnes, which is the thinnest crust on Iceland. Darbyshire et al. [2000] estimated the Moho depth underneath the Snæfellsnes to 20–24 km. There is no record of historic seismicity on the Snæfellsnes. Also, no data are available about present day seismicity in this part of Iceland because the South Iceland Lowland (SIL) network is not designed to detect low-magnitude events occurring beneath the Snæfellsnes peninsula. Only during the HOTSPOT experiment in 1996–1998 a seismometer was placed near Snæfellsjökull. Therefore, we performed a seismic campaign to determine whether any seismicity occurs in this region near the volcanic centers.

Seismicity has previously been reported from many other central volcanoes on Iceland, e.g. Askja [Soosalu et al., 2009] and Eyjafjallajökull [Tarasewicz et al., 2012] and also from long-dormant volcanoes such as Hrómundartindur, Hofsjökull or Öræfajökull [Jakobsdóttir, 2008]. The observed seismic activity typically occurs in swarms and epicenters are densely clustered around magma reservoirs or dyking volumes. Hypocentral depths of volcano related seismicity reach down to 34 km but events are mostly clustered within 2–6 km depth [Jakobsdóttir, 2008]. This paper reports the results of our three-months field campaign and identifies for the first time the occurrence of seismic activity beneath the Snæfellsjökull volcano.

Data and Methods

We deployed five Trillium 240 broadband seismometers on the Snæfellsnes peninsula from July to September 2011, with the locations shown by squares in Figures 3.2 and 3.3. Since our primary objective was to determine the existence of seismic activity beneath the Snæfellsjökull volcano, we deployed four stations in the westernmost part of the peninsula, distributed 5 to 12 km distant from the volcano. We installed our fifth seismometer approximately 21 km northwest of the Ljósufjöll volcanic complex because our second objective was to determine if seismicity occurs between the Snæfellsjökull and the eastern parts of the peninsula. The stations around Snæfellsjökull were deployed either on lava flows or on hyaloclastic rocks. Data were recorded at a sampling rate of 100 Hz. The recordings were manually inspected for seismic events, which were located from hand-picked Pand S-wave arrivals using the HYPOCENTER code [Lienert and Havskov, 1995] and the 1D SIL velocity model introduced by Stefánsson et al. [1993] (see Table 3.1). We considered only events showing a S-wave arrival on the OLA, GLA and STA stations (see Figure 3.3; GUF recordings were dominated by large background noise and are excluded from this study) and that at least allow for one P-wave pick at any of the three stations. We used the ObsPy toolbox [Beyreuther et al., 2010] for data processing.

Table 3.1: 1D velocity model based on Stefánsson et al. [1993] with 1.74 as v_p/v_s ratio.

Depth [km]	v_p [km/s]
0	3.53
1	4.47
2	5.16
3	5.60
4	5.96
6	6.50
9	6.73
20	7.20

Results

During three months of continuous recording, we identified and located 29 seismic events that were not listed in the Icelandic seismic catalog. Numerous other micro-seismic events were also detected but are not included here because the low signal to noise ratio prevented reliable epicenter determinations. Nominal epicenter uncertainties for the reported 29 seismic events range from 0.5 km to 3.5 km in both Longitude and Latitude but are likely underestimated. However, uncertainties in the phase picking additionally contribute to scattering of the epicenter locations, since P-wave picks were not available for all stations. The respective locations are shown as red circles in Figure 3.3. The observed seismicity clusters beneath the southern and north-eastern flanks of Snæfellsjökull volcano, respectively with some additional events ranging towards

the lower lands in the North-West. Red circles in Figure 3.3 denote epicenters located by phase picks on OLA, GLA and STA recordings. Additionally, few seismic events showed clear arrivals on both GLA and STA but could not be identified at OLA due to large background noise. The respective phase arrivals on GLA and STA allow for two possible epicenter locations that are shown as grey circles (shaded and solid) in Figure 3.3. However, the potential epicenter locations towards the south (marked as grey shaded) fall outside the volcanic complex, whereas the alternative locations (grey solid) are within the cluster at the north-eastern flank of the volcano and appear more plausible. We therefore suggest that these events belong to the same seismic source volume and are located within the north-eastern flank of Snæfellsjökull as well.

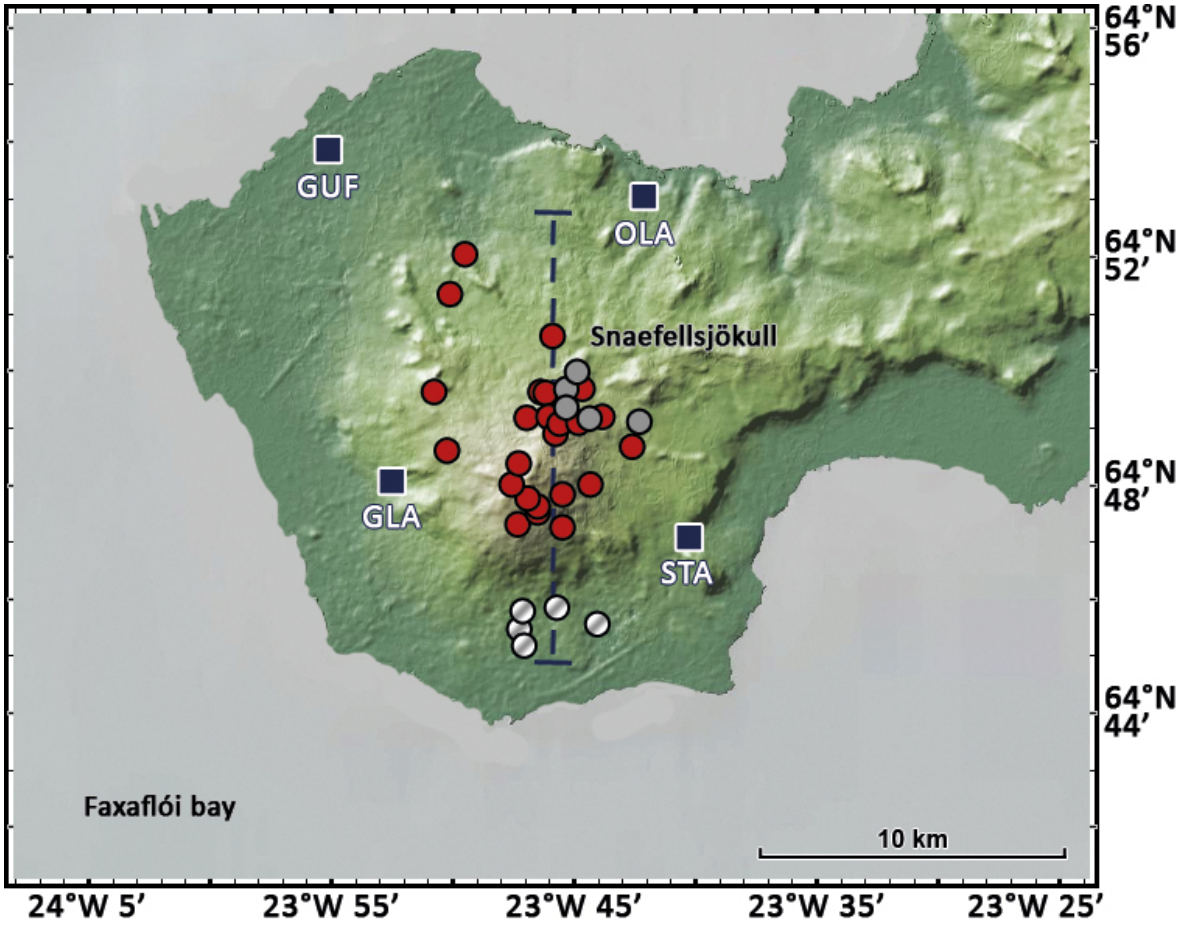

Figure 3.3: Spatial distribution of the recorded seismic events around the Snæfellsjökull volcano. The locations of the seismometers are denoted by blue squares and the dashed line marks the cross section that is used for the plot of Figure 3.4.

The dashed line in Figure 3.3 represents the trace of the profile shown in Figure 3.4. Although hypocenter depths are not well-constrained (the nominal depth error ranges from 3 km to 5 km deep) and weak P-waves complicated phase picking (see below) we observe that most of the seismic activity originates from depths of 9 to 13 km. Still, the poorly constrained hypocenter locations do not allow us to identify significant changes in depth. Note that including only three seismometers with the given geometry and unclear

P-arrivals render the resulting depths highly uncertain and thus the hypocentral depth might be much shallower than stated here [Tarasewicz et al., 2011]. The actual seismic wave velocities underneath the Snæfellsnes peninsula are likely to deviate from the 1D SIL velocity model used for this study. We therefore checked how hypocentral depths are affected by different P-wave velocities. Yang and Shen [2005] report a low velocity anomaly in the Snæfellsnes area while in the same region Allen et al. [2002] observe slightly higher wave velocities in the upper crust. Thus, we reduced and enhanced P-wave velocities by 0.25 km/s at all depths of the 1D model. Reduced wave velocities result in hypocenters raised to shallower depths by about 600–1000 m, while increased velocities would place them about 200–1000 m deeper. Thus, the effect is of the same order as the uncertainties on the depth.

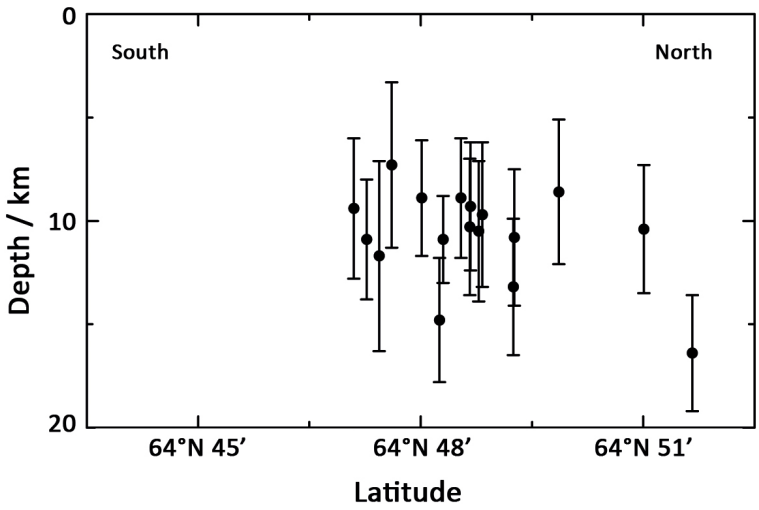

Figure 3.4: Cross section along the Snæfellsjökull volcano as marked by the dashed line in Figure 3.3, showing the depth of the seismic events as a function of latitude. Uncertainties in the determination of the depth are indicated by error bars and range from ±3 to ±5 km.

Figure 3.5 shows the waveform and the spectrogram of the strongest seismic event (M_l 1.1) recorded on July 18th 2011, located beneath the Snæfellsjökull volcano. The picks for phase arrivals of the P- and S-wave are marked by solid red lines and are identical with the theoretically calculated arrival times for the given hypocenter. Figure 3.5a shows waveforms bandpass filtered at 4–12 Hz where the signal-to-noise ratio is best, while for the same reason the spectrograms shown in Figure 3.5b were generated from frequencies $>$ 3 Hz highpassed data. The signal is dominated by frequencies between 2–12 Hz and is most prominent at 5–6 Hz. In general, waveforms of all recorded seismic events are comparable and show a similar low-frequency content. Except for the M_l 1.1 event the magnitude range of the measured seismicity is between M_l -0.5 and 0.7. Generally, S-wave arrivals were much more prominent than P-wave arrivals. The latter are often not well pronounced and pose one of the major uncertainties in the determination of the hypocentral depth.

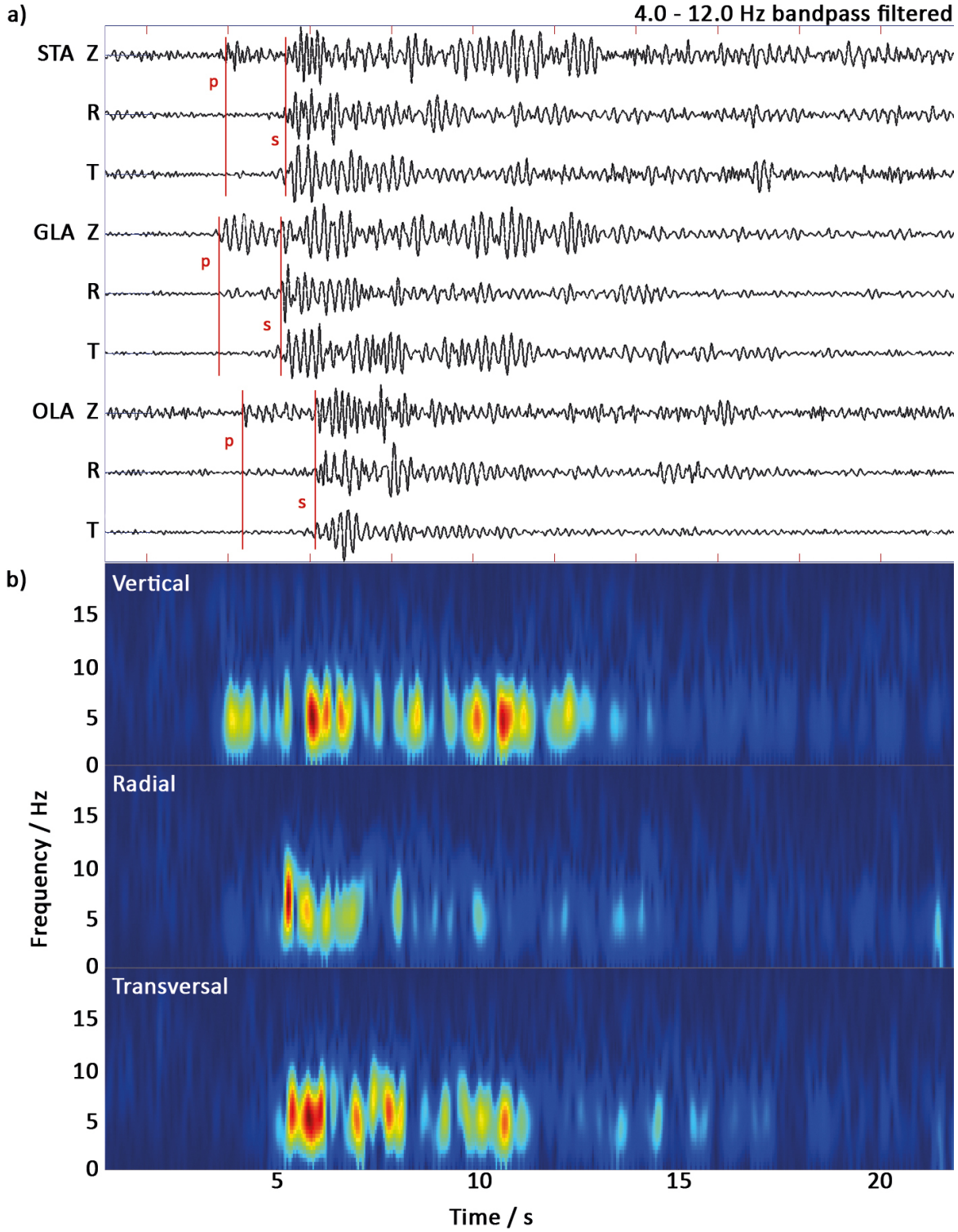

Figure 3.5: a) Seismogram of the M_l 1.1 event on 18 July 2011 showing vertical (Z), radial (R) and transversal (T) components as recorded by three different stations (see Figure 3.3 for station labeling). For a better visualization data are bandpassed with a filter between 4–12 Hz where the signal-to-noise ratio is best. Picks for the phase onsets are marked by solid red lines. **b)** Spectrogram of the same event as recorded on the GLA station after instrument correction. The data displayed in the spectrograms was highpass-filtered for frequencies > 3 Hz so the plot is not dominated by low frequency noise.

Seismicity at Snæfellsjökull tends to cluster in time and space. A total of 10 events were recorded between 19th and 22nd of August 2011 and another 9 events occurred during 12 hours on September 6th. While seismic activity in July and August is rather uniformly distributed, the September events predominantly belong to the north-eastern cluster.

The events recorded near the volcano were too small to be detected by the fifth seismometer located 60 km away near the Ljósufjöll volcanic complex. On this distant seismometer we could not identify clear signals of microseismicity like those measured with the stations close to the Snæfellsjökull volcano. However, we did record signals that could be of seismic origin but due to the lack of nearby seismic stations it is not possible to identify the nature of these events.

Discussion

We show evidence of ongoing seismic activity beneath and around the Snæfellsjökull volcano. We can not rule out seismic activity in other parts of the Snæfellsnes peninsula, because our network was specifically designed to detect seismicity around Snæfellsjökull. The similarity in waveforms for many of the measured events suggests a common source mechanism and might point to much tighter spatial clustering than observed by the epicenter distribution. The spatial distribution of the epicenters and depths of approximately 10 km indicate a magmatic origin for the seismic activity. Lava flows around the Snæfellsjökull have been mapped by Jóhannesson et al. [1981]. The southern cluster of seismic events falls into the area that was active during the most recent central caldera eruption of Snæfellsjökull which covered the southern flanks of the volcano. Similarly, seismicity in the north-eastern cluster might originate from the magma source that was active during the 4000–5000 BP eruptive phase. Few seismic events were located northwest of the volcano where young flows associated with local craters have also been found. Still, a denser seismometer network is necessary to investigate the spatial clustering of hypocenters with more detail.

Two models for the geometry of the plumbing system of the Snæfellsjökull have been proposed by Kokfelt et al. [2009] based on isotope data of volcanic rocks. The first model suggests a stratified and long-lived magma chamber of conical shape, while the second model proposes a simultaneously evolving plumbing system made of smaller and isolated magmatic bodies of at least 3–4 km^3 each. Both models have in common that older and more evolved magmas are situated at shallower depths beneath the central summit, while younger magmas are located at greater depths below the flanks of the volcano. We identify three potentially separate sources of seismicity on the Snæfellsjökull volcano, with two main clusters on the southern and north-eastern flanks, respectively and few events located in the lower lands north-west of the volcanic edifice (Figure 3.3). The origin of seismicity is in agreement with both models proposed by Kokfelt et al. [2009] and suggests that the plumbing system of the Snæfellsjökull volcano extends from about 8 to 13 km depth. However, uncertainties on epicenters and depth are too large to rule out either of the two suggested scenarios. Based on seismic and

geodetic data, magma chambers beneath active Icelandic volcanoes are confined to the upper crust [Brandsdóttir and Menke, 2008; Mitchell et al., 2013].

The absence of high frequency components in the waveforms and the swarm-like appearance of seismicity suggest that seismic activity could be associated with fluid processes. However, seismicity that has been associated with fluid-induced mechanisms at e.g. Eyjafjallajökull [Tarasewicz et al., 2012] or Upptyppingar [White et al., 2011] volcano shows higher frequencies and is termed to be of volcano-tectonic origin. Similar low-frequency bands have been observed at Askja volcano but were interpreted as a result of absorption of high frequencies by Soosalu et al. [2009]. Additionally, the frequency content of the signals we measure underneath Snæfellsjökull is too high and the signal duration too short to be purely fluid related such as long period events [Chouet, 1996]. Regarding the thin crust of approximately only 15–20 km under the Snæfellsnes, our estimated hypocentral depths may fall within the normally ductile part of the crust. White et al. [2011] argue that brittle failure within the ductile regime can be generated by high strain rates induced locally by magma movement. We therefore propose that seismic activity underneath the Snæfellsjökull volcano reflects hybrid events that involve brittle failure in combination with fluid-related processes. Although scattering and absorption of the seismic waves may contribute to the absence of higher frequency signals, we favor the scenario where seismicity is related to fluid-induced brittle failure in the deeper part of the crust.

Sigurdsson [1970] suggested that seismic and volcanic activity in the SVB could be increasing as present day spreading rates are comparable to the late Pleistocene ones which might have formed the en-echelon alignment of volcanic structures [Árnadóttir et al., 2009]. In this case one would also expect tectonic events at shallower depths that follow the orientation of the inferred transcurrent fault. However, the origin of recent volcanism and its distribution along the Snæfellsnes peninsula is poorly understood and the proposed fault remains hypothetical. The installation of continuous GPS stations associated with a larger array of permanent seismic stations could help to determine the current tectonic deformation of the Snæfellsnes peninsula and to reveal the origins of its rejuvenated volcanism.

Conclusions

We conducted a seismic campaign to ascertain whether or not the Snæfellsnes is seismically active. We found seismicity that clusters in time and space beneath the Snæfellsjökull volcano and originates from depths of 8 to 15 km. The seismic events show magnitudes from M_l -0.5 to 1.1 and are mainly located underneath the southern and north-eastern flanks. We propose that the seismic activity reflects hybrid volcanic events and is related to movement of fluids within the ductile part of the crust under Snæfellsjökull volcano.

Our results are the first to show seismic activity underneath the Snæfellsjökull volcano. However, a denser seismic network is necessary to draw more specific conclusions about the origin of the seismicity. Future investigations should include continuous seismic and

GPS measurements along the peninsula. This will allow more robust interpretations of the geology of the Snæfellsnes peninsula, the Snæfellsjökull volcano in particular, and will help to better constrain present day activity and its relationship to Icelandic tectonics.

3.2 Snæfellsjökull imaged by InSAR

Seismic activity at volcanic systems is often caused by deformation of the crust underneath the volcano [Baer et al., 2008; Pallister et al., 2010; Pedersen and Sigmundsson, 2006]. When pressure builds up inside the magma chamber due to accumulating material feeded from the mantle, the magma chamber will eventually inflate and deform the surrounding crust. While potentially causing seismicity through changing stresses, depending on the depth and size of the inflating volume this process also leads to measurable ground deformation at the surface. Similarly, intrusions of magma from a reservoir into surrounding rock will result in intense seismic activity around the intruded volume and cause surface ground deformation. By means of satellite-based Synthetic Aperture Radar Interferometry (InSAR) vertical surface deformations in the Centimeter range can be remotely measured over large areas world wide [Bamler and Hartl, 1998].

We applied this technique to the Snæfellsjökull volcano to evaluate if seismic activity may be accompanied by ground deformation. In such case, seismicity could be related to the deflation or inflation of a magmatic reservoir beneath the volcano. At the time of the study no suitable data was available for the period in 2011 when seismicity was first observed under the Snæfellsjökull and we cannot supplement seismic data of the 2011 campaign with InSAR observations. However, earthquakes might have previously occured at Snæfellsjökull without being noticed since the volcano was not seismically monitored. Hence we nevertheless analyzed older satellite data to determine any potential surface deformation episodes at Snæfellsjökull. For the interferometry we used Envisat ASAR images with baseline differences less than 200 m. From the ascending track (No. 216) we used data between May 2005 and June 2008 and images from July 2004 to October 2008 from the descending track (No. 453). Satellite data from winter month could not be used because of snow coverage.

Figure 3.6 shows the interferometry results for two image pairs from the ascending track between 2005 and 2007. While one image pair shows a small area of uplift on the southern flank of the volcano, another image pair that was taken within the time span of the first does show surface subsidence in the same area. Hence the results are not consistent among each other. Additionally, image pairs from the descending track as in Figure 3.7 cover the same date range from 2005 to 2007 but show no significant vertical ground motion at all. Stacking the vertical displacement obtained from all available image pairs yields the overall ground motion during the entire time span from 2005 to 2008. Figure 3.8 shows the stacked image for both ascending and descending track which do not show any significant vertical surface motion.

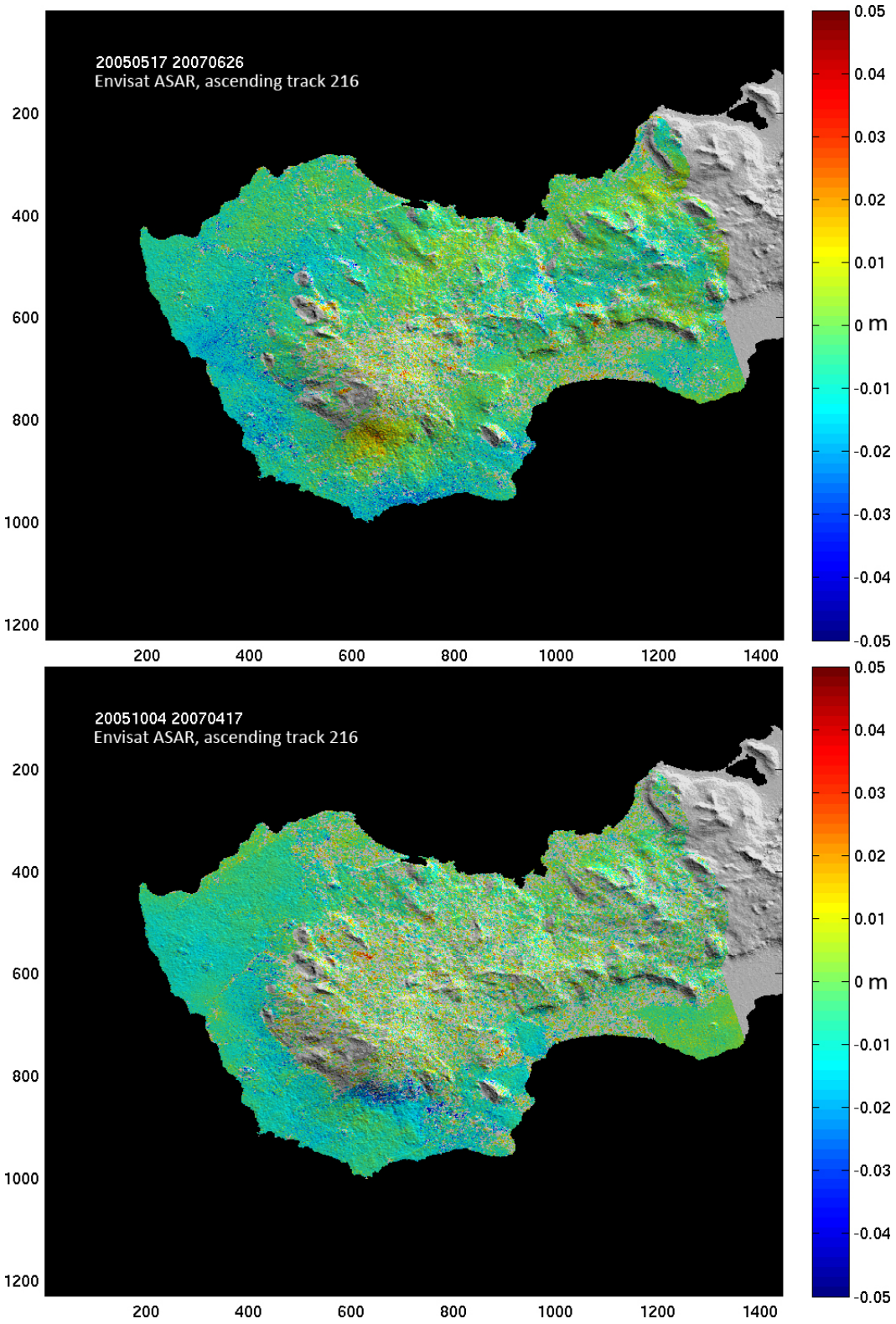

Figure 3.6: Vertical ground displacement for Envisat ASAR ascending track 216. Red and blue colors (saturating at ± 5 cm) mark uplift or subsidence, respectively. The date of the two images used for the interferometry is given in the upper left corner. While the upper image (May 2005 – June 2007) indicates a small area of uplift on the southern volcano flank, the lower image (October 2005 – April 2007) shows subsidence for the same area. Color scale is in Meters.

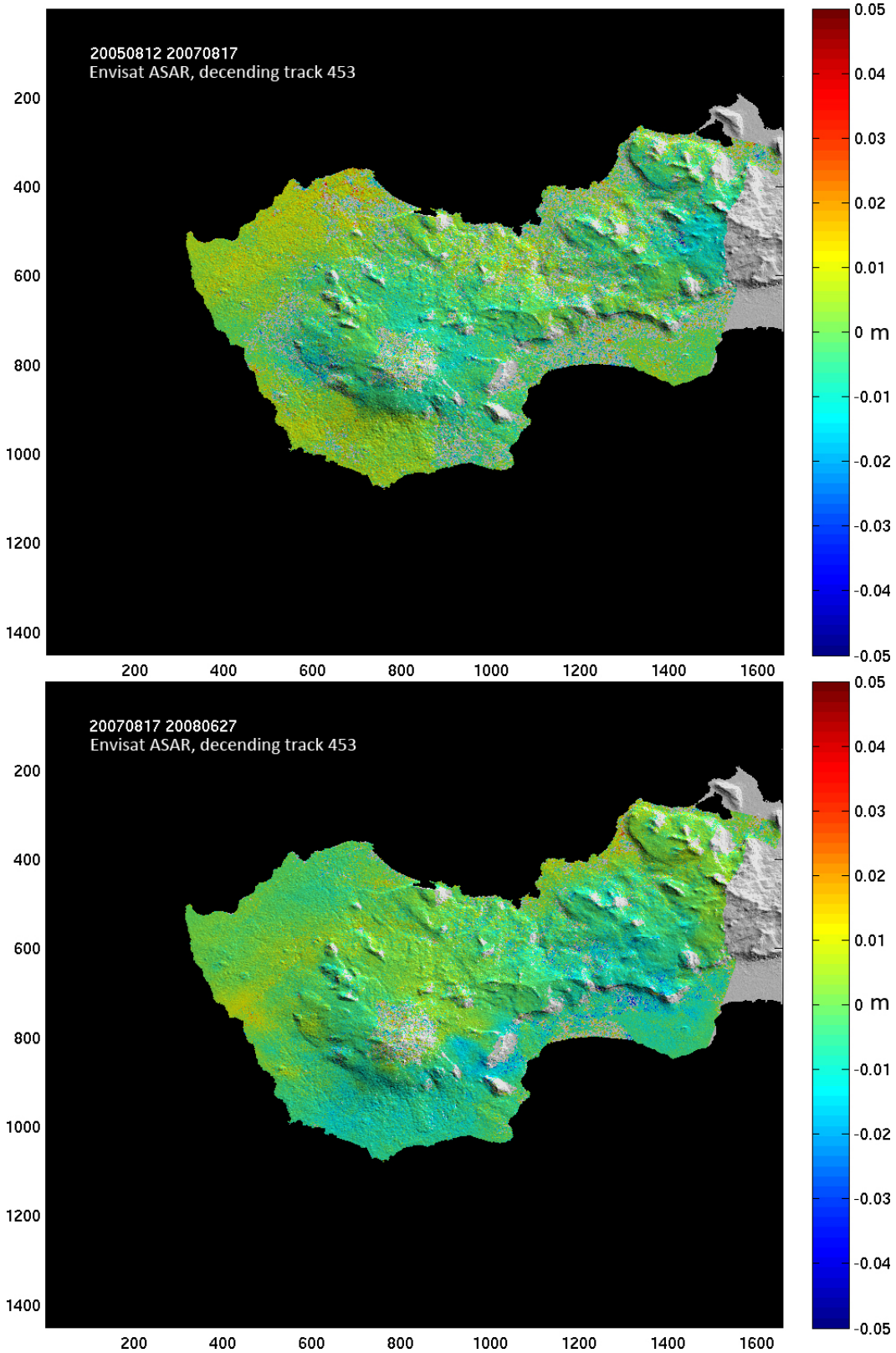

Figure 3.7: Vertical ground displacement for Envisat ASAR descending track 453. Color saturates at ± 5 cm. Neither in the August 2005 – August 2007 (top) period nor in August 2007 – June 2008 (bottom) significant ground motion is detected. This contrasts the results from the ascending track in Figure 3.6. Color scale is in Meters.

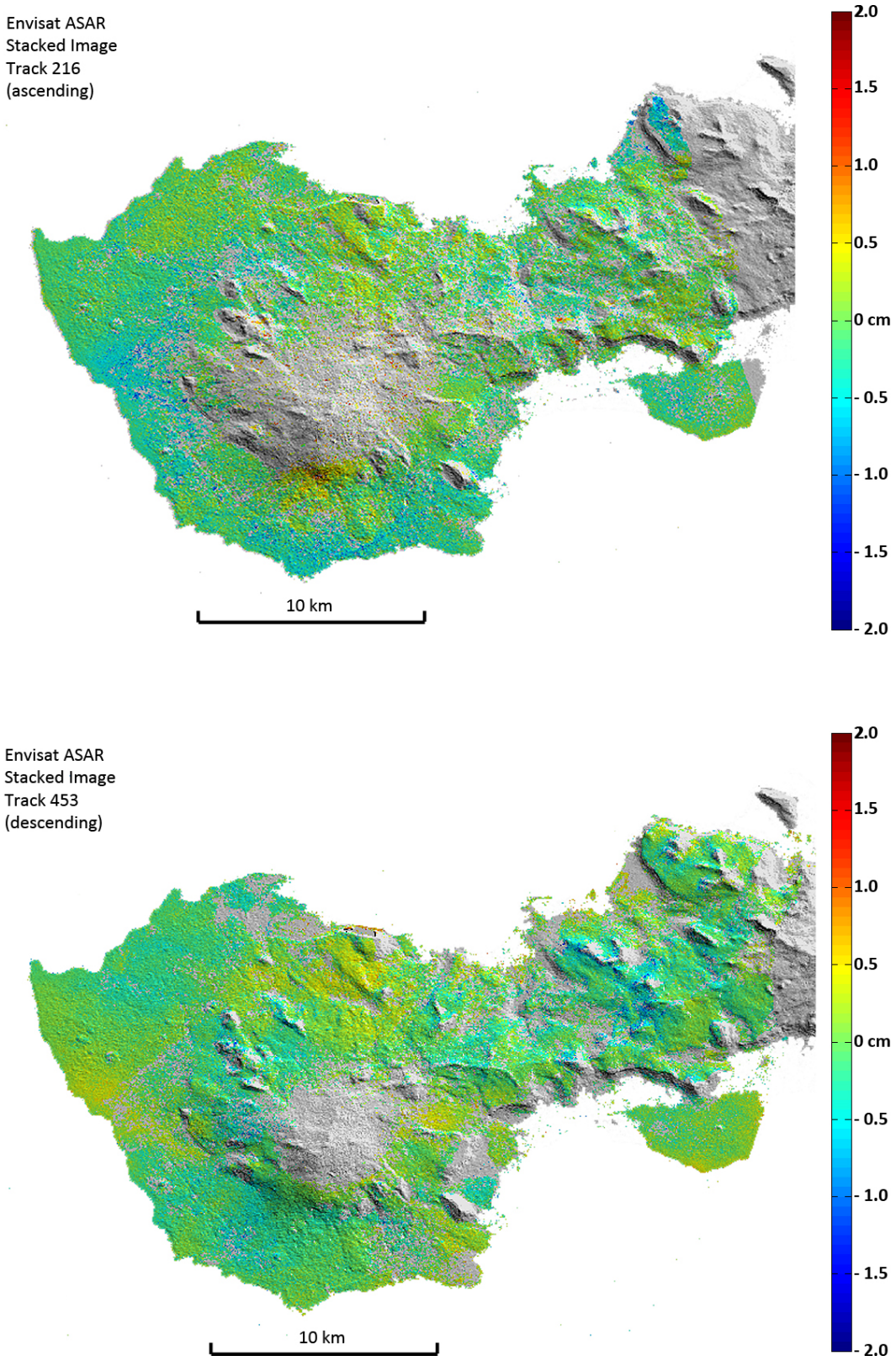

Figure 3.8: Stacked vertical ground motion of Snæfellsjökull measured with InSAR. Top image shows stacked ground motion obtained from the ascending track in 2005–2007. Bottom image shows the stacked results from the descending track in 2005–2008. Color saturates at ± 2 cm. None of the stacked images shows significant vertical surface displacement.

The results of the InSAR study on the Snæfellsjökull volcano can be interpreted as follows. Either no vertical ground motion occurred around Snæfellsjökull during the 2005–2008 period or the amplitude of ground motion was too small ($\ll 1$ cm) to be detected by InSAR methods. This leads to the conclusion that either no deflation or inflation of a magmatic reservoir took place in 2005–2008 or the deflation/inflation did not result in measurable ground displacement at the surface. Seismicity measured in 2011 concentrates at about 10 km depth which is well in the depth range for inflating/deflating bodies that would produce significant surface deformation [Dzurisin and Lu, 2006]. Since we do not measure any ground deformation at Snæfellsjökull we conclude that no inflation or deflation of the Snæfellsjökull magmatic reservoirs occurred in 2005–2008. The seismic activity during this period is unknown and the results for 2005–2008 do not allow any conclusions to be drawn about potential surface deformation during the 2011 seismically active period. Since both more recent and older satellite data is now available for the Snæfellsjökull it should be used to back up 2011 and 2013 seismic data.

3.3 The latest data from Snæfellsjökull

As shown in Section 3.1 the 2011 measurement campaign revealed seismicity around Snæfellsjökull only. Still, this was a surprising result since the volcano is considered dormant and is not seismically monitored. Thus the outcome of the 2011 campaign suggested to focus future efforts on the Snæfellsjökull and aim for a better understanding of the seismic activity and thus to improve knowledge about the plumbing system and evaluate potential hazards. During May – October 2013 a total of 21 seismic stations were installed around the Snæfellsjökull. Figure 3.11 shows the seismometer distribution of this very dense, temporary array. The setup consisted of 10 short-period and 11 broadband seismometers that were provided by the Geophysical Instrument Pool Potsdam (GIPP) of the GFZ Potsdam, Germany.

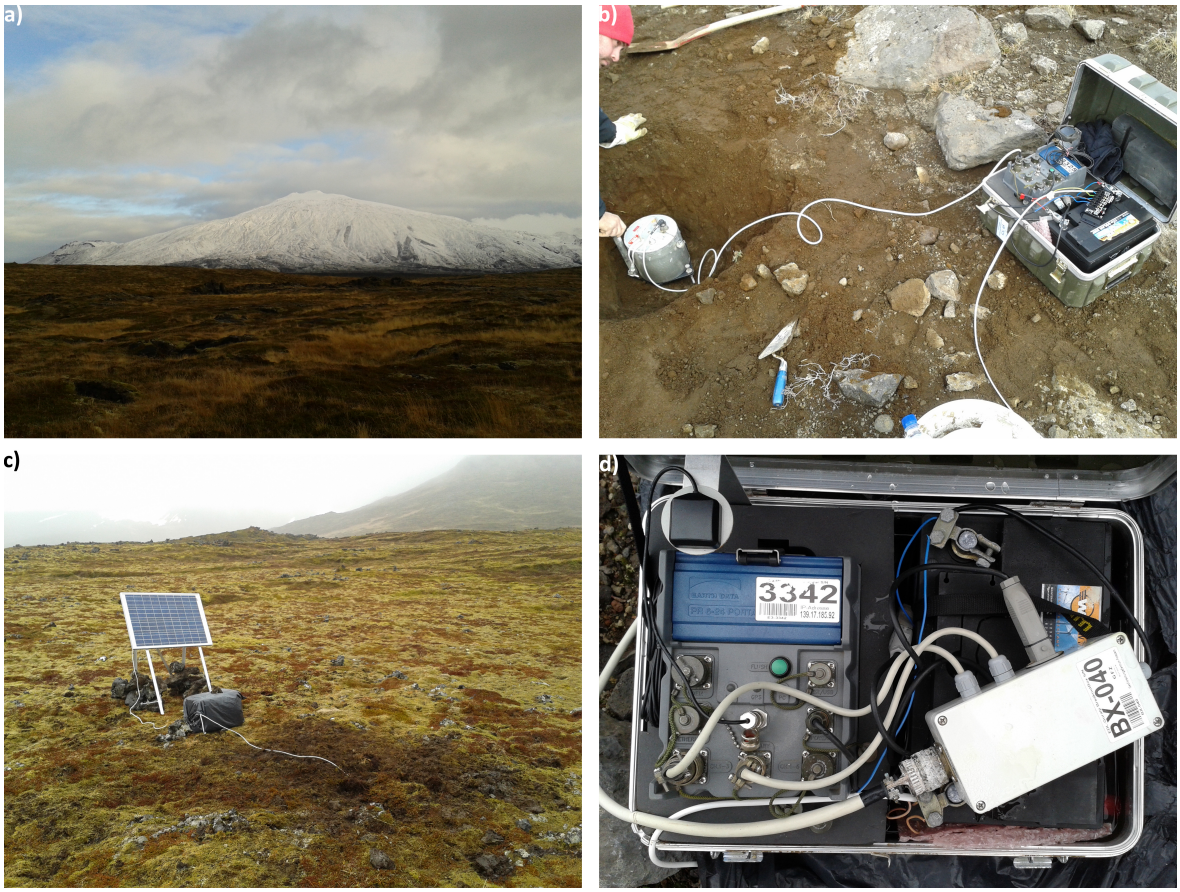

Figure 3.9: Deployment in 2013. **a)** Snæfellsjökull central volcano. **b)** Installation and leveling of a Mark short-period instrument. **c)** Typical station setup with the seismometer buried underground and a solar panel for battery recharge. **d)** Data logger with GPS antenna, 12V battery and breakout box for the Güralp broadband seismometers.

Figure 3.10: Deployment in 2013. **a)** Seismic noise testing before installation of the seismometer. **b)** Setting up the seismic station. **c)** Cementing the base of the hole for broadband installation. **d)** Broadband instrument inside hole on cemented ground.

Short-period instruments were MARK L-4C-3D three-component geophones for measuring ground velocity in the 1 Hz to >100 Hz frequency range. Broadband instruments were Güralp CMG-3ESP Compact seismometers for periods <60 seconds. Data was continuously recorded at 100 Hz sampling rate with EarthData PR6-24 digital data loggers and stored on internal, exchangeable 40 GB hard-drives in MiniSeed format. Except for one installation in an abandoned construction site (BB01), all instruments were buried underground for shelter from noise-generating wind and rain. Some sites were tested for seismic noise with a portable Lennartz LE-3D 5 seconds seismometer (see Figure 3.10a). Where possible, the seismometers were placed on solid base rock such as lava flows or hyaloclastic rocks (Figure 3.9b). If no such base could be found or the base did not allow for horizontal leveling, ground for the instruments was cemented (Figures 3.10c,d). While the short-period instruments were covered with soil only, broadband seismometers were additionally sheltered with polystyrene boxes for thermal insulation. Figures 3.9 and 3.10 show photographs taken during the installation and retrieval of the stations in May and October 2013.

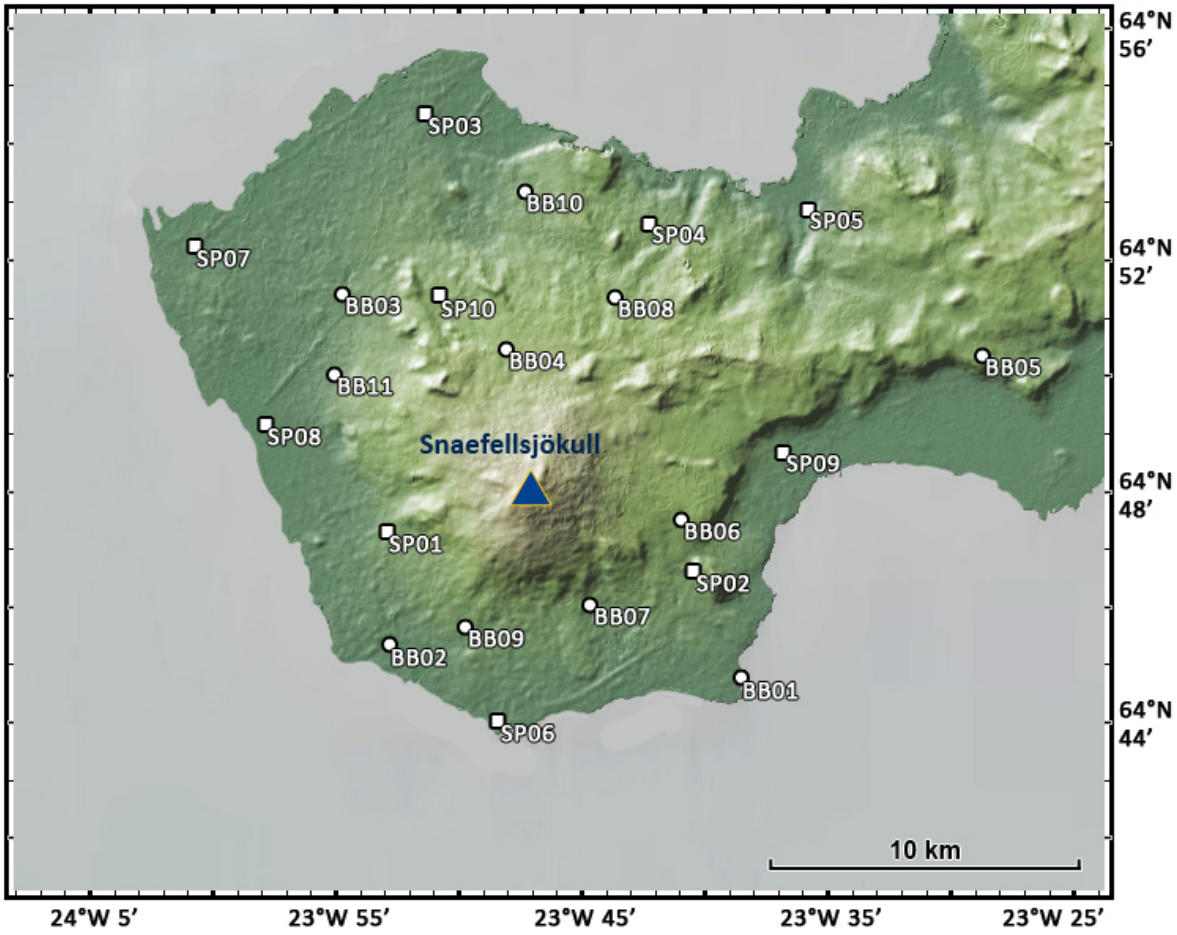

Figure 3.11: Distribution of seismometers around Snæfellsjökull volcano for the 2013 campaign. 10 short-period and 11 broadband stations were installed in accessible spots around the volcano.

For the analysis, data were bandpass filtered between 2–12 Hz and automatically scanned for earthquakes using a recursive STA/LTA algorithm [Withers et al., 1998] on

the vertical components. The corner frequencies for the bandpass filter resemble the expected frequency range of seismic events near the Snæfellsjökull as suggested from the 2011 campaign results (see Section 3.1). STA and LTA window lengths were 1.5 and 20 seconds, respectively, the event detection triggering threshold was set to 6 and the detriggering threshold to 1. We required positive detection on at least 4 of the 21 stations for the algorithm to declare a potential seismic event and store 120 minutes of waveform data around the potential earthquake into an event database.

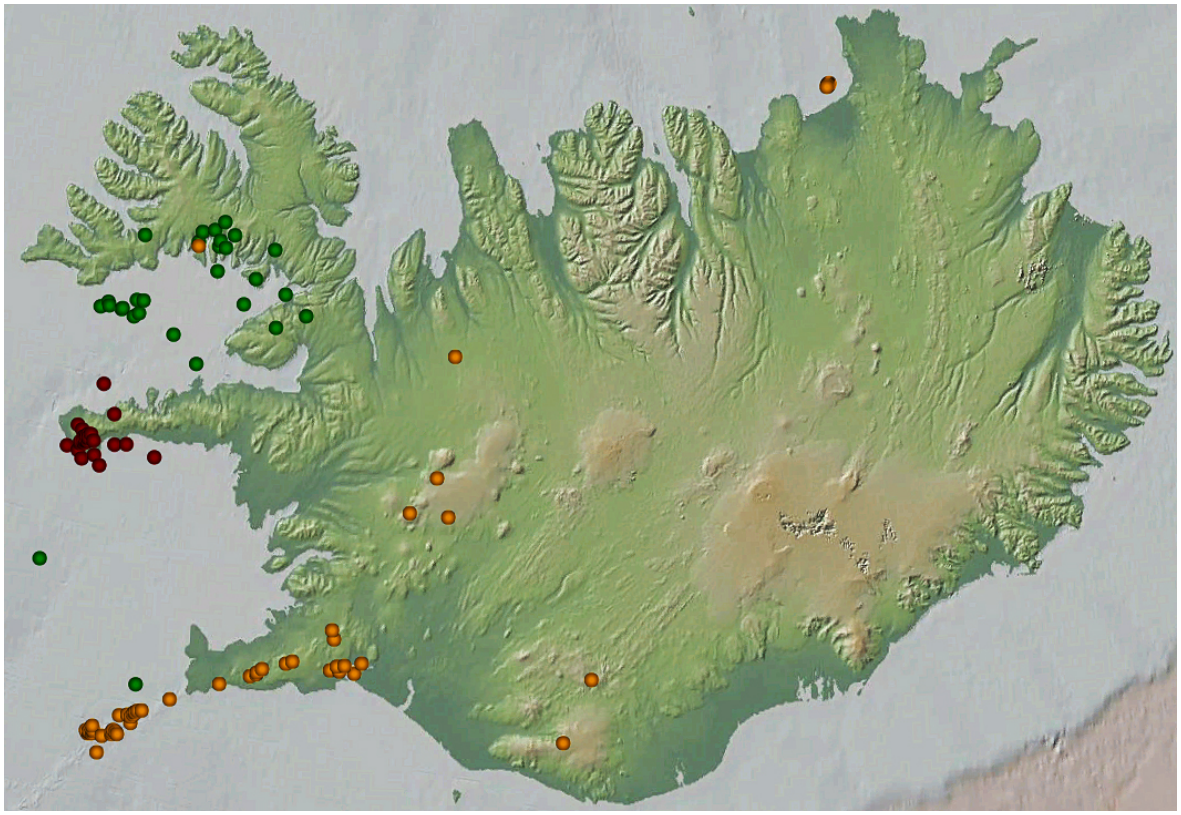

Figure 3.12: Seismic events in summer 2013 identified by the recursive STA/LTA algorithm. Earthquakes were manually located by P and S wave arrivals. Red and green markers indicate seismic activity near Snæfellsjökull volcano and in the Westfjords, respectively. Yellow markers represent earthquakes listed in the IMO seismic catalog.

The STA/LTA algorithm identified 191 potential seismic events which were manually validated and located by means of P and S wave arrivals. The velocity model used for the preliminary earthquake locations is the one referenced in Table 3.1 and that was used for the 2011 analysis as well. Note again, that the actual seismic wave velocity structure beneath the Snæfellsjökull and the Snæfellsnes peninsula is likely to differ from this model (this issue is further discussed in Section 3.4). From 191 potential seismic events, 131 were validated as individual earthquakes while 7 were identified as false alarms triggered by noise and 53 events were registered multiple times. Figure 3.12 shows all 131 events that were correctly identified by the triggering algorithm. 66 events (marked yellow in Figure 3.12) are regional earthquakes from the main seismic and volcanic zones on Iceland and are registered with time, location and magnitude in

the IMO earthquake catalog. All other 65 earthquakes have not been detected by the SIL permanent seismic network and thus reveal newly detected seismic activity on the Snæfellsnes and in the Westfjords.

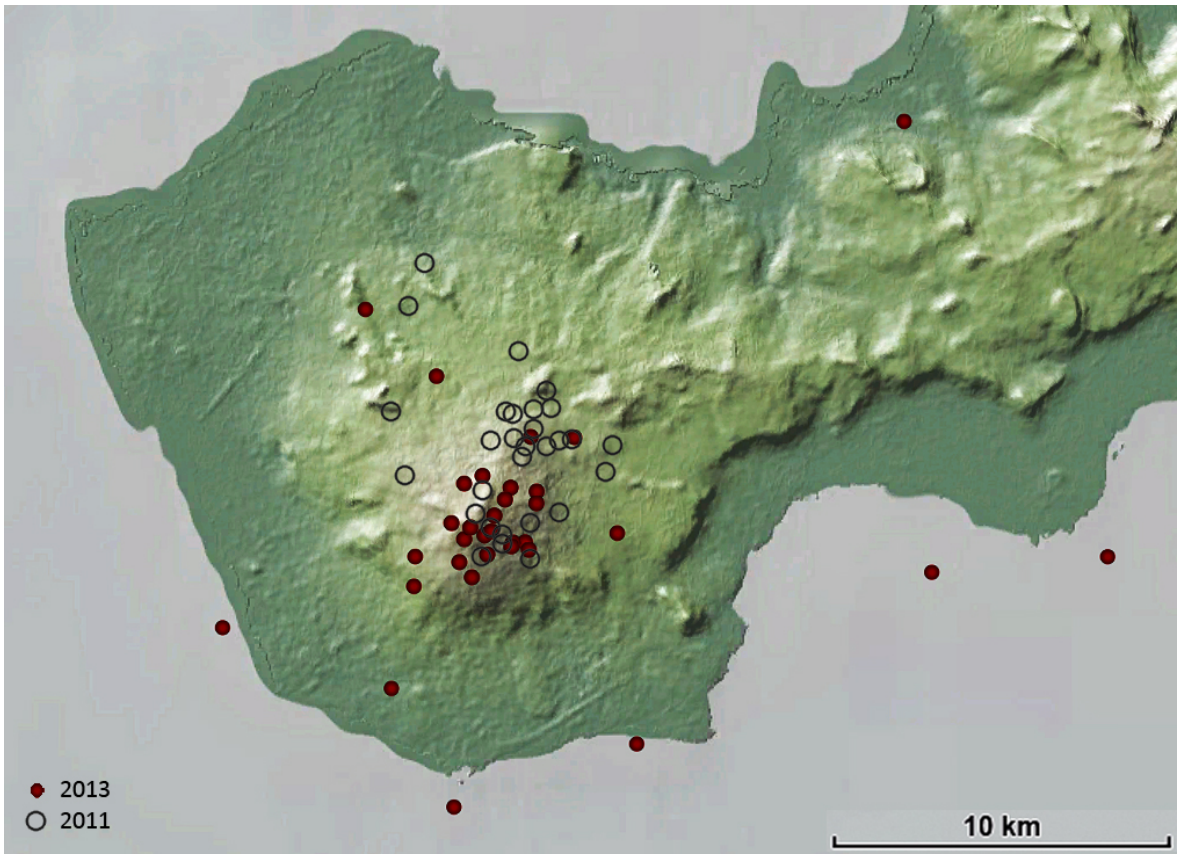

Figure 3.13: Preliminary distribution of seismicity around Snæfellsjökull in summer 2013. Epicenters mainly cluster under the southern flank of the volcano. Some events occur scattered around the central cone but may be mislocated. Note that epicenters mainly fall into the southern cluster of the summer 2011 activity.

We find 36 earthquakes near Snæfellsjökull in 2013 (see Table A.1) which confirms active seismicity within the volcanic complex as was reported in Section 3.1 from the year 2011. Earthquake locations and magnitudes are still preliminary, but similar to those found in 2011. Figure 3.13 shows the distribution of epicenters around the volcano summit. Most of the events fall right underneath the summit, slightly trending towards the southern and northern flank and thus within the same areas as during the 2011 seismic activity. Due to the dense station coverage around the volcano uncertainties on the epicenter locations are greatly reduced, however. Errors on Longitude and Latitude are less than 1.5 km for all events shown in Figure 3.13. Still, results are biased because of the likely erroneous velocity model. Some events occur scattered around the volcano where no seismicity could be observed during the 2011 deployment. Since results are preliminary these locations may, however, change upon closer inspection. Magnitudes for all earthquakes are $M_l < 1.5$. Figure 3.14 shows a North-South cross-section along the main volcanic cone for the same Latitude range used in Figure 3.4 for the 2011

results. Depths are now well constrained at ± 1.5 km and although the overall depth range is comparable to the 2011 results, it occurs that during the 2013 deployment seismicity clusters at slightly lower depth between 5–11 km.

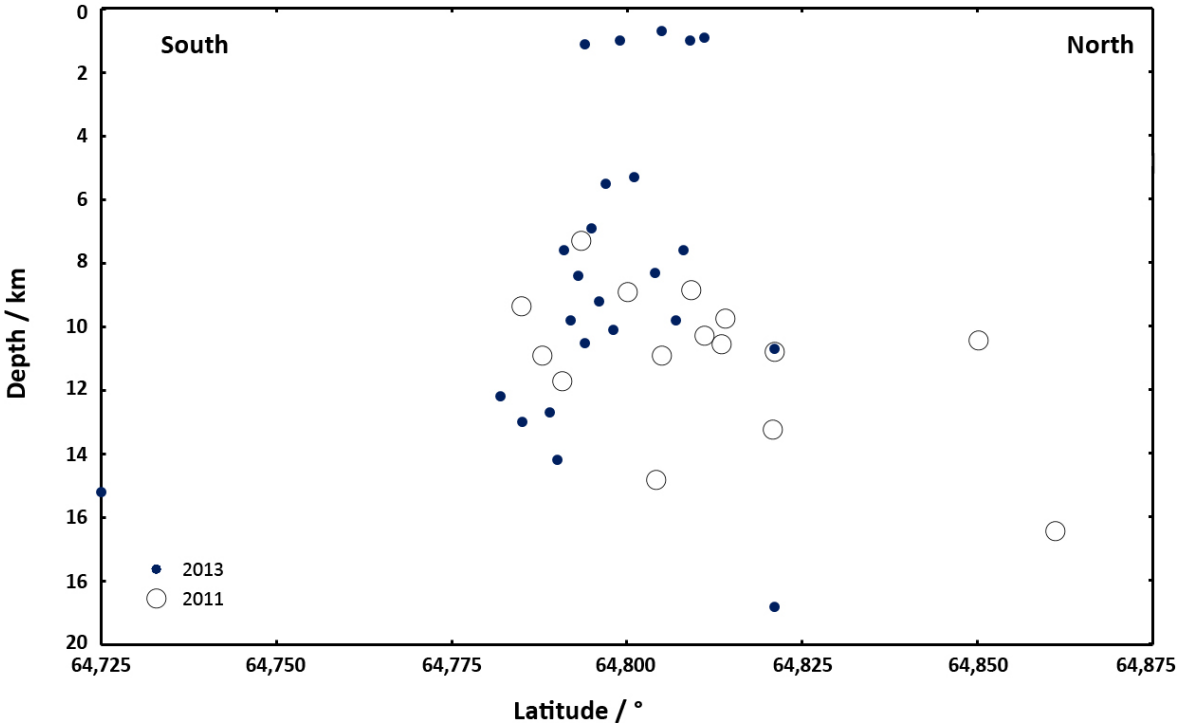

Figure 3.14: North-South cross section along the Snæfellsjökull volcano, showing the depth of the seismic events in 2013 as a function of Latitude. Depth uncertainties are around ±1.5 km. Note that as compared to the activity in summer 2011 the events now cluster at slightly lower depth between 5–11 km.

The finding of seismic activity in the Westfjords is a new discovery. During the five month deployment in 2013 we registered 29 earthquakes in the southern regimes of the Westfjords. Since all events fall far outside the seismic network the epicenters are only loosely constrained (errors on epicenter range from 5–40 km on Longitude or Latitude). However, we can verify that the locations in the Westfjords are reliable by comparison with a reference earthquake. One of the recorded earthquakes is registered in the IMO seismic catalog and is well located in the southern central Westfjords (marked yellow in Figure 3.15). Waveforms and arrival time of seismic waves among the network are very similar for all events that locate in the Westfjords, including the one registered in the IMO catalog. Additionally, several epicenters cluster near this well-constrained event. Therefore the epicenters of the newly measured events appear trustworthy, although uncertainties on the epicenter location are huge. A second apparent cluster of earthquake epicenters locates south of the Westfjords landmass inside the Breidafjördur bay. The remaining seismic events appear randomly scattered off the clusters and are likely not located properly. Thus we conclude that there are two seismically active regions within the Westfjords. Note that we cannot rule out that seismicity from the coastal Westfjord regime is man-made by construction-related explosions.

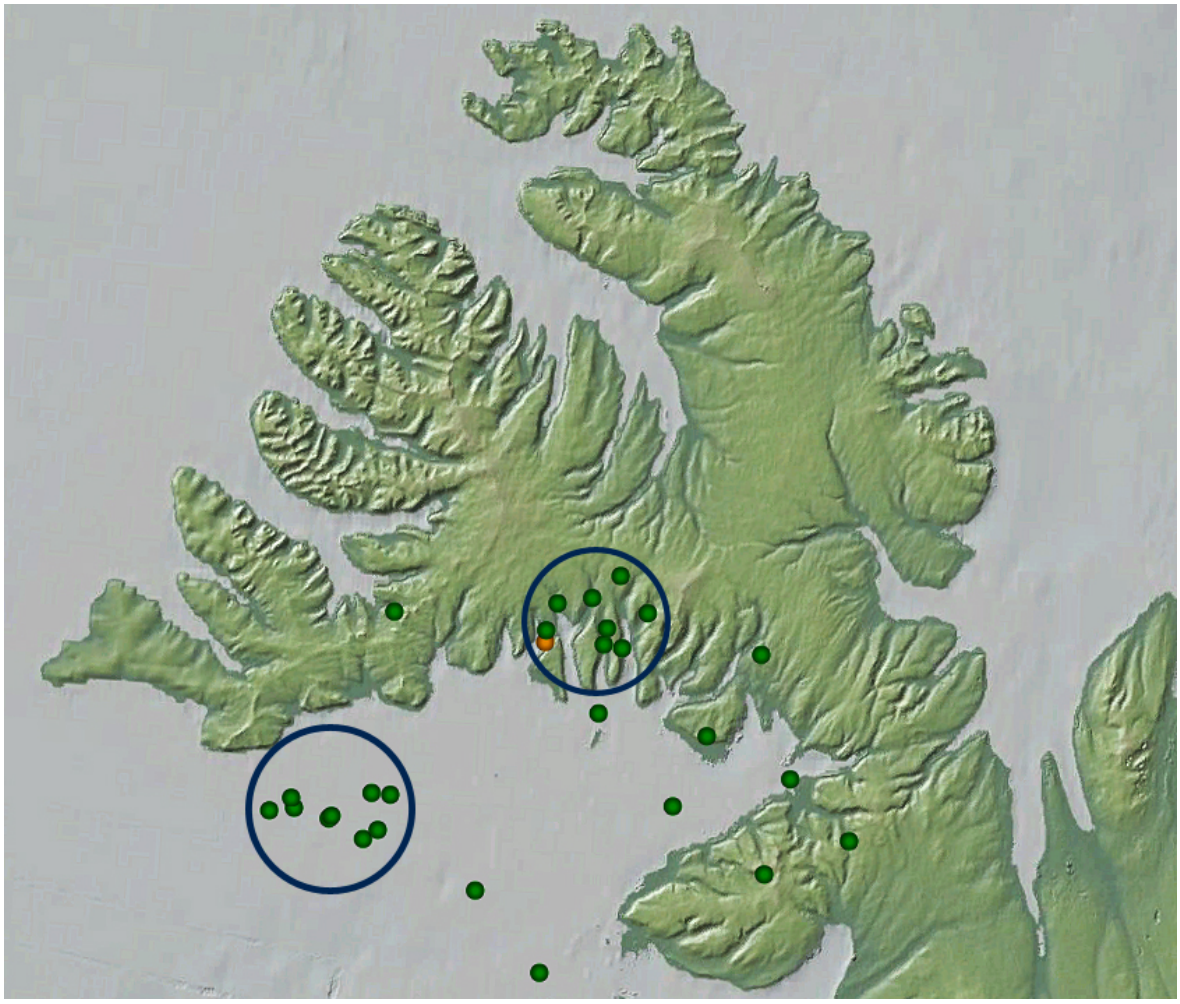

Figure 3.15: Seismicity measured in the Westfjords during summer 2013. The earthquake highlighted in yellow is listed in the IMO seismic catalog. Epicenters are preliminary and not well located but seismic activity mainly falls into two marked clusters in the south-central Westfjords and the Breidafjördur bay.

Just as the Snæfellsnes, the Westfjords are a remnant of the Mid-Atlantic-Ridge. The axial rift was located in the Westfjords at 15 Ma [Martin et al., 2011]. To our knowledge no studies exist on geodynamics or seismic activity in the Westfjords. Since all events in the Westfjords are not well constrained in epicenter and depth, we cannot draw conclusions about the origin of the seismic activity. Yet, note that many of these earthquakes seem to fall at comparably great depth around 25–60 km. The crust is about 30 km thick at the Westfjords [Bjarnason and Schmeling, 2009] so if the preliminary depth estimations hold, seismicity would fall into the usually ductile part of the Lithosphere.

3.4 Remarks & Outlook on future research

Seismic data from the 2013 deployment is still being processed and the results presented above are preliminary. It is a major goal of the 2013 campaign to improve the results from the 2011 analysis and obtain a more detailed knowledge of the interiors of the Snæfellsjökull volcano. The 21 station deployment potentially allows to locate earthquake epicenters with great accuracy. However, earthquake locations by means of P and S arrivals strongly depend on the seismic velocity model. The one-dimensional model shown in Table 3.1 is valid only for the main rift zones in Central and Southern Iceland [Stefánsson et al., 1993] and surely differs from the actual seismic velocities under the Snæfellsnes peninsula. Thus, proper improvement of earthquake locations requires a new velocity model. Ambient noise analysis can provide a detailed three-dimensional velocity model of the crust beneath the Snæfellsjökull volcano and is currently being applied to the data set. Once a new velocity model is obtained, all epicenters will be re-located and improved by cross-correlation (double difference) techniques [Waldhauser and Ellsworth, 2000].

The results from the 2011 and 2013 deployments show that the Snæfellsjökull volcano is seismically active. Upcoming results from the 2013 analysis will show if seismicity is linked to potential volcanic activity and will allow to better constrain the plumbing system of the volcanic complex. Ambient noise tomography results will significantly enhance the seismic wave velocity model for the crust and mantle under the Snæfellsnes peninsula and will be of great use for future seismic studies that may target the Ljósofjöll and Lýsuhóll volcanic systems (see Figure 3.2) or the entire peninsula. Temporary seismic networks at the aforementioned volcanic complexes may shed light on seismic activity and potentially linked volcanic activity. Since both the 2011 and 2013 deployments focused on the Snæfellsjökull volcano, the obtained results do not allow for any conclusions about the geologic setting of the Snæfellsnes peninsula in its entirety. The origin of the en-echelon alignment of volcanic centers that contrasts alignments observed elsewhere on Iceland, still remains unknown. A temporary seismic network that covers the entire peninsula along with continuous GPS stations may provide further insights into the mysterious geology of the Snæfellsnes.

4 Triggering in volcanic and hydrothermal settings

In cooperation with the Observatorio Vulcanológico y Sismológico de Costa Rica (OVSICORI) we performed the following analysis of a triggered earthquake sequence at the Irazú-Turrialba volcanic complex, Costa Rica, after the 2012 M_w 7.6 subduction zone earthquake under the Nicoya peninsula. While the Nicoya earthquake triggered widespread increased seismic activity all over Costa Rica [Linkimer et al., 2013] we focused on triggered activity at the Irazú-Turrialba volcanic complex since it provides an excellent sample to to learn more about earthquake-volcano interaction in volcanic arcs along subduction zones and to test the triggering hypothesis of Prejean and Hill [2013] that resting volcanoes are more likely to respond to remote earthquakes than those currently in eruption.

Figure 4.1: Turrialba (left) and Irazú (right) volcanoes near the city of San Jose in central Costa Rica.The photograph was taken during the 2013 active phase of the Turrialba volcano [Liechavicius, 2013].

4.1 Seismic swarm at the Irazú-Turrialba volcanoes

This Section is published as: M. Lupi, F. Fuchs and J. F. Pacheco (2014), Fault reactivation due to the M7.6 Nicoya earthquake at the Turrialba-Irazú volcanic complex, Costa Rica: effects of dynamic stress triggering, *Geophysical Research Letters, 41*, 4142–4148.

Introduction

Static and dynamic stresses generated by large magnitude earthquakes act at different time-scales and distances. Static stress variations operate over decades and relatively short distances (the stress decays according to $1/R^3$, where R is the distance from the epicentre) [Hill et al., 2002] while dynamic stress affects the near- and far-field during the propagation of the seismic waves. Effects of moderate to large magnitude earthquakes in the near- and far-field are well-documented (e.g. [Eggert and Walter, 2009; Hill et al., 2002; Marzocchi et al., 2002b; Walter et al., 2007] and include hydrogeological responses [Wang, 2007; Wang and Manga, 2010], triggered seismic activity [Hill and Prejean, 2007; Husen et al., 2004a; West et al., 2005], temperature variations at hydrothermal systems [Dziak et al., 2003; Johnson et al., 2000], variations of water-levels in boreholes [Matsumoto et al., 2003; Roeloffs, 1998; Weingarten and Ge, 2014], triggered volcanic activity [Delle Donne et al., 2010; Linde and Sacks, 1998; Manga and Brodsky, 2006; Walter et al., 2007], and triggered mud volcanism [Lupi et al., 2013; Manga and Bonini, 2012; Mazzini et al., 2007]. In addition, earthquakes may promote the co-seismic precipitation of gold deposits and induce mineral phase precipitation in hydrothermal systems [Weatherley and Henley, 2013]. Volcanic and hydrothermal environments are particularly sensitive to external perturbations because the (often) critical conditions encountered at depth (e.g. [van der Elst et al., 2013]).

The oblique subduction of the Cocos plate beneath the Caribbean plate imposes strain partitioning in the upper-plate leading to intense and shallow seismic activity along a NW-striking fault system (and the associated NE-trending antithetic faults) running through the volcanic arc [Corti et al., 2005; Lewis et al., 2008; Montero et al., 2013]. The maximum slip of the M_w 7.6 Nicoya earthquake (5^{th} of September 2012, 14:42 UTC) was approximately 2.5 m ($\sim$ 9.76° N, 85.56°W) [Yue et al., 2013]. It induced a ground acceleration greater than 4.9 m/s^2 close to the epicenter [Protti et al., 2014] and an average ground acceleration of 0.5 m/s^2 near the Irazú-Turrialba volcanic complex (ITVC) [Yue et al., 2013]. The ITVC is cut by the southernmost segment of the East Río Sucio Fault (ERSF), a right-lateral strike slip system that joins the Finca Liebres volcanic depression between the Irazú and Turrialba volcanoes (Figure 4.2b). At the surface, this area is not characterized by any strong hydrothermal activity. The only hot thermal spring is Quebrada Peña (60°C), near the Turrialba volcano, while around the Irazú volcano sparse hot springs emissions range from 30°C to 60°C.

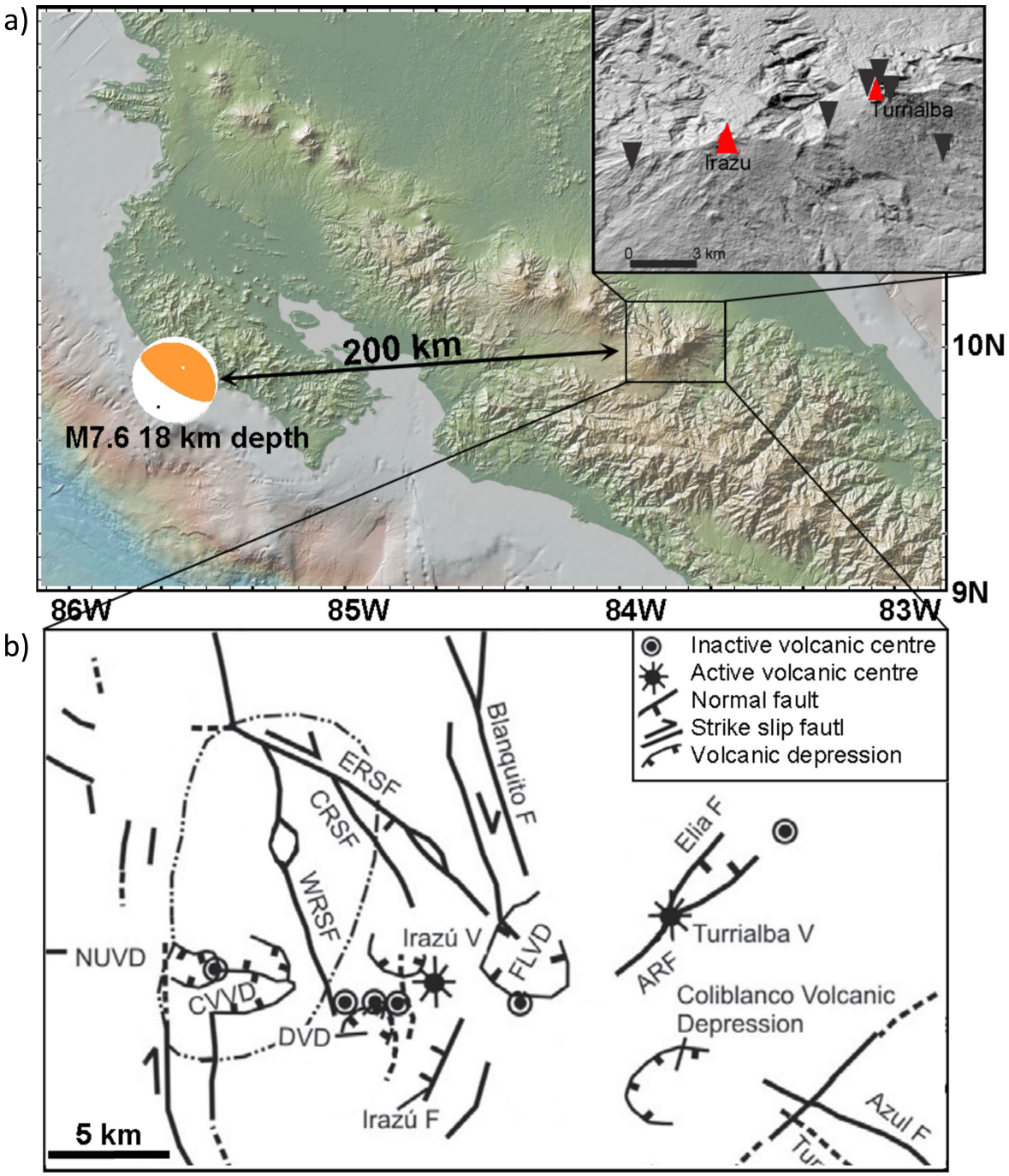

Figure 4.2: **a)** Map of Costa Rica and tectonic setting around the Irazú and Turrialba volcanoes. The Nicoya earthquake occurred at the subduction interface and the inverted fault plane solution shows almost a pure reverse-slip. The gray-shaded inset shows the Irazú-Turrialba volcanic complex (red triangles show the main craters) and the distribution of the seismic stations (black triangles). The stations are deployed on volcanoclastic deposits due to the lack of suitable sites on bedrocks. However, the site amplification effect for the seismic stations around the ITVC affects the higher frequencies only (i.e. above 15 Hz). **b)** The map (modified after Montero et al. [2013]) represents the tectonic features of this region including the East Río Sucio Fault (ERSF). Other abbreviations are for the Central Río Sucio Fault (CRSF), the West Río Sucio Fault (WRSF) and Finca Liebres Volcanic Depression (FLVD).

The last major eruption of the Irazú volcano occurred in 1963 (VEI=3) while the most recent volcanic activity took place on the NW flank in 1994 and consisted of a small magnitude phreatic explosion [Alvarado et al., 2006]. The Turrialba volcano was quiescent during the last century until the 5th of January 2010 when a VEI=2 eruption occurred at the SW crater. Activity at Turrialba continued with repeating explosions (VEI from 1 to 2) until May 2013 and returned to a dormant state in June 2013.

The Observatorio Vulcanológico y Sismológico de Costa Rica (OVSICORI) maintains a network of six seismic stations around the ITVC (inset of Figure 4.2a and Figure 4.3) to monitor the volcanic activity of the area. After the 2012 M_w 7.6 Nicoya earthquake the network recorded more than 300 locatable seismic events occurring in swarm sequences during the twenty-four hours following the main slip (Figure 4.3a). In this occasion, the Irazú and Turrialba volcanoes behaved differently. Several events occurred around the Irazú volcano while almost no seismic activity was recorded beneath the Turrialba volcano. We use data from the OVSICORI seismic network to shed light on the interaction between dynamic stresses and critically stressed geologic environments and to describe the occurrence of seismic activity along the ERSF after the 2012 M_w 7.6 Nicoya, Costa Rica, earthquake.

Data

Before the M_w 7.6 Nicoya earthquake, the seismic activity at the ITVC was mostly located beneath the NW flank of the Turrialba volcano with hybrid seismic events characterized by dominant frequencies between 4 Hz and 12 Hz, from 1 km to 8 km depth (purple events in Figure 4.3). After the main-shock of the Nicoya earthquake a swarm sequence took place beneath the E flank of the Irazú volcano (see Figure A.1 for sample waveforms). Based on a spectrogram analysis the first local event occurred 40 s after the arrival of the P-waves, which corresponds to the arrival of the S-waves. We could not constrain this first motion further as it overlaps with the signal generated by the Nicoya main-shock. The second local event (M_l 3.8), the largest of the seismic sequence, occurred after the coda of the surface waves at 14:48 UTC. However, the swarm sequence only accelerated significantly after 14:57 UTC with seventy-five (locatable) seismic events occurred during the first hour (Figure 4.4). Non-locatable events increase the total number of event occurrences to more than 110 events per hour.

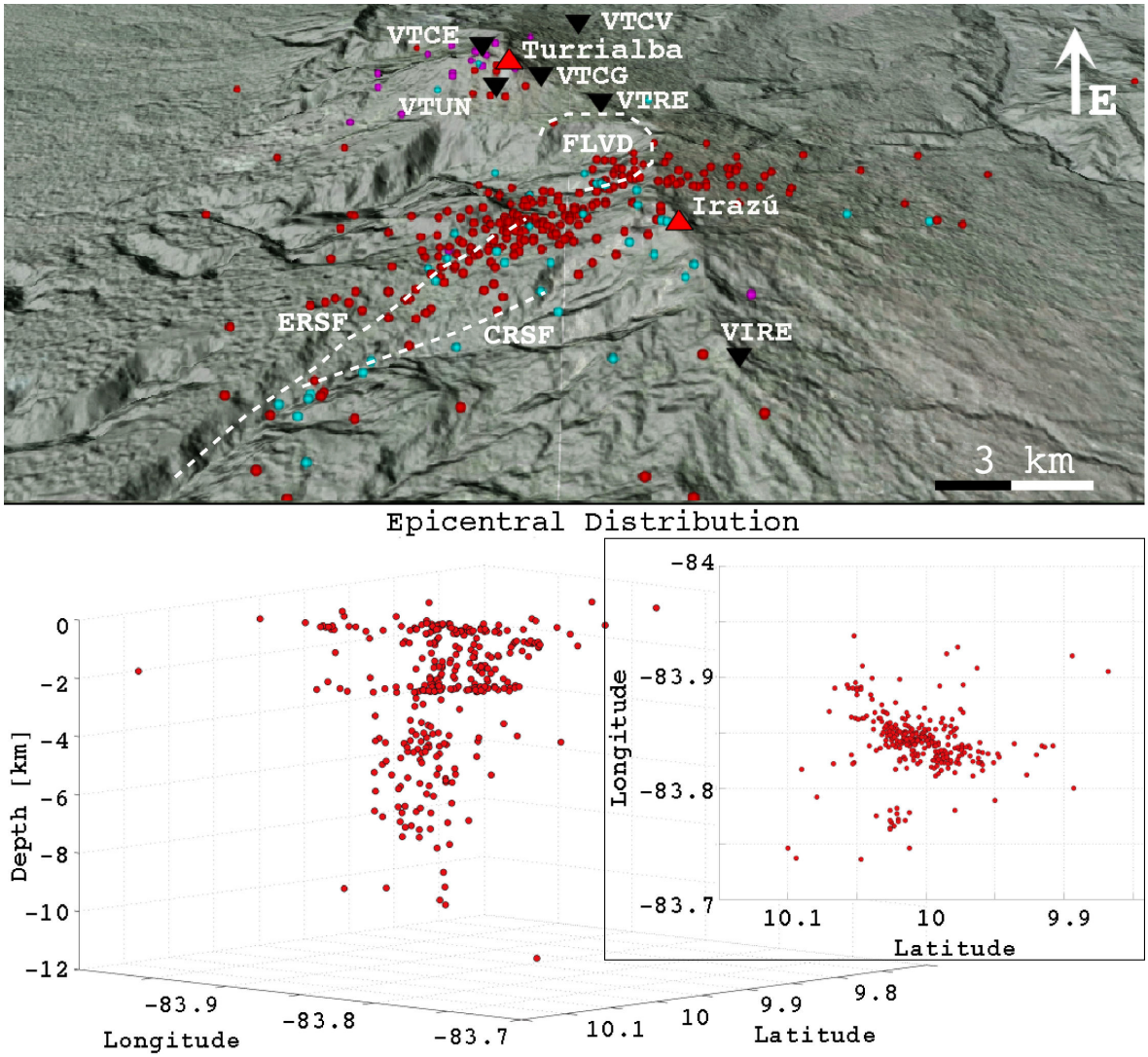

Figure 4.3: Epicentral distribution of seismic events at the Irazú Turrialba volcanic complex after the M_w 7.6 Nicoya earthquake. Depth 0 refers to the sea level (i.e. $\sim$ 3 km below the ground surface). Pink and red circles show the location of the seismic events before and after the M_w 7.6 Nicoya earthquake, respectively. Turquoise circles represent the location of the seismic events the day after the Nicoya earthquake. Body wave arrivals were manually picked and located with SEISAN [Havskov and Ottemoller, 1999]. However, due to the limited number of stations, and their sub-aligned distribution, location accuracy is affected by up to $\sim$ 3 km errors laterally and vertically. The velocity model used is taken from Quintero and Kissling [2001].

Three pairs of aftershocks followed the main slip of the Nicoya earthquake approximately 1 hour, 8 hours and 14 hours after the main slip, respectively (Figure 4.4). The first pair of aftershocks (M_w 4.4 and M_w 4.5) struck during the peak of seismicity triggered by the main slip. Hence, we could not decouple seismic activity promoted by the main-slip from the one promoted by the first pair of aftershocks. However, the following aftershocks triggered swarm activity along the fault plane inducing two peaks of 30 events per hour and 20 events per hour, respectively (Figure 4.4). Local earthquakes continued throughout the day and returned to normal levels after approximately 30

hours. A similar, but ambiguous, behavior was recorded in the same region on the 27th of August 2012 (04:37 UTC) after the M_w 7.3 El Salvador earthquake. The dynamic stress

$$\sigma_d \approx G \cdot \frac{PGV}{v_s} \tag{4.1}$$

imposed by the M_w 7.3 El Salvador earthquake was $\sim$ 0.5 kPa (using v_s of 5300 m/s^2). Yet, the local earthquake rate along the ERSF increased from an average of four events per hour to twelve events per hour after the earthquake. After the El Salvador earthquake the first seismic event at the ITVC occurred several hours (09:25 UTC) after the main-shock. The number of local earthquakes grew to seven events per hour from 10:00 to 11:00 UTC reaching the peak of thirteen events per hour from 10:00 UTC to 12:00 UTC. Then the seismic rate decreased back to seven, four, and two events per hour from 12:00 UTC to 13:00 UTC, 13:00 UTC to 14:00 UTC, and 14:00 UTC to 15:00 UTC, respectively.

The magnitude of the seismic events triggered by the Nicoya earthquake varies from M_l 0.5 to M_l 3.5, with a clear dominance of events between M_l 0.5 and M_l 1.0. Magnitude 0.5 is the magnitude threshold of detection for our array. Hypocentral depths vary from 10 km to 0 km (Figure 4.3), with the vast majority of the earthquakes being shallower than 5 km depth. The epicenters are distributed along a NW-NE region stretching from the southernmost part of the ERSF to the easternmost part of the Irazú volcanic edifice. This region showed a similar behavior after the 1983 M_w 7.3, the 1990 M_w 7.0, and the 1991 M_w 7.6 earthquakes offshore Costa Rica.

Discussion

We performed a Coulomb stress analysis [Toda et al., 2011] to calculate the static stress imposed by the Nicoya earthquake on the ERSF. Due to the poor signal to noise ratio we could not invert for moment tensor solutions for the largest events of the seismic sequence presented here. Hence, we used as receiver fault sub-parallel to the arc the plane identified by the M_w 6.1 earthquake that occurred on the 8th of January 2009 near the volcano Poás (strike, dip, and rake of 306, 86, and 150, respectively), with a friction coefficient of 0.6 and a depth of 10 km. The resulting Coulomb stress change imposed on the ITVC by the Nicoya earthquake is $\sim$ 1 kPa. However, the dynamic stress σ_d imposed at the ITVC by the passing S-waves is 0.3 MPa (assuming a shear modulus of G = 30 GPa, an average shear wave velocity of 5300 m/s according to Quintero and Kissling [2001] and a measured PGV of 0.05 m/s at the ITVC). Despite the specific values used for the shear modulus and for the velocity of the shear waves, the dynamic stress associated with the passing seismic waves does not exceed 1 MPa. This suggests that the seismicity triggered along the ERSF was not principally induced by static stress variations but rather by dynamic stress triggering.

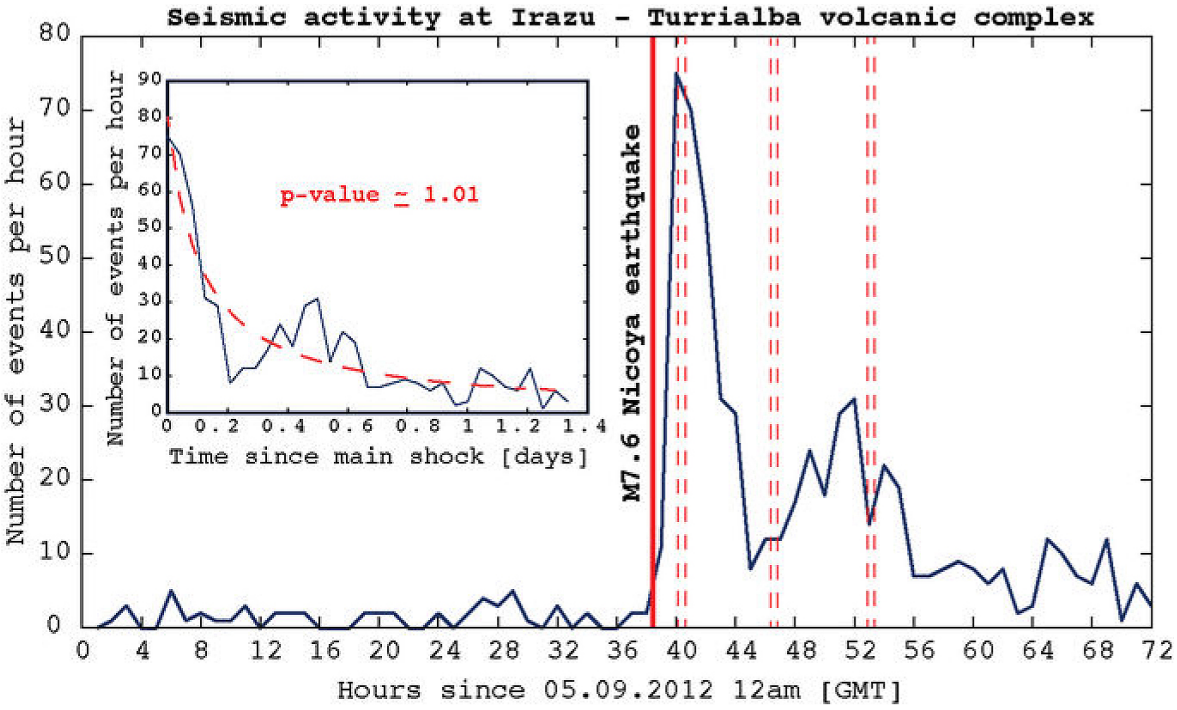

Figure 4.4: Seismicity rate along the East Río Sucio Fault by the M7.6 Nicoya earthquake and its aftershocks (red dashed lines). The only M≥M4 earthquake that shows a local earthquake within the waveform is the M7.6 earthquake (within the S-waves). We could not recognize any local seismic event within any of the waveforms of the aftershocks. The increase of seismic activity that follows each pair of aftershocks is smooth, except for the first pair that is followed 11 minutes after by a sharp increase of local events. After the second and third pair of aftershocks the increase of local seismicity is less marked. Overall, the aftershock decay versus time fits an Omori's decay [Utsu, 1961], with k, c, and p of 8.5, 0.1, 1.0173, respectively.

The portion of the ERSF affected by the triggered seismic activity corresponds to the easternmost part of the Irazú volcanic edifice. In critically stressed volcanic environments, small variations of confining pressure may promote shear failure on optimally oriented fractures. Additionally, under such conditions the reduction of confining pressure may lead to an increase of the fluid pressure at depth (i.e. via gas phase exsolution) promoting hydro-fracturing [Sibson, 1981] and vertical migration of hydrothermal fluids along the fault plane [Lupi et al., 2011]. Violay et al. [2014] show that the presence of pore fluids strongly affects the initial frictional weakening promoting slip conditions at depth, particularly for small magnitude events (slip less than 0.5 m). Hence, variations as small as 0.3 MPa may have been sufficient to perturb this part of the ERSF that crosscuts the volcanic edifice of the Irazú volcano. Our findings are in agreement with recent conclusions of Prejean and Hill [2013] who points out that response of volcanic systems to incoming seismic energy is often observed on the sides of the volcanic edifice (i.e. in the hydrothermal systems or in groundwater reservoirs) rather than above the magmatic plumbing system.

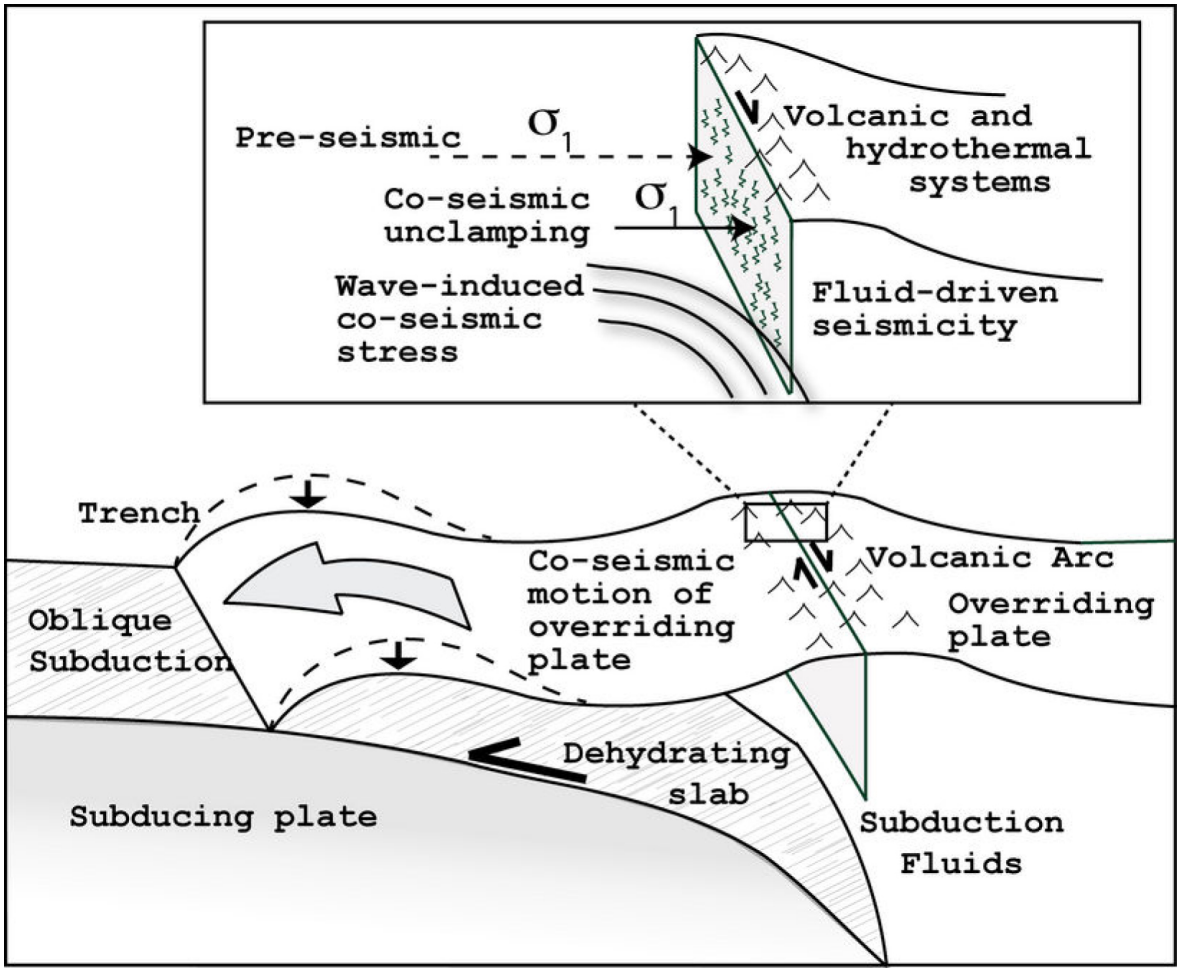

Figure 4.5: Coupled effects of elastic unloading and dynamic stress propagation. The reduction of the principal stress $\sigma_1 = \sigma_n$ from pre-seismic (dashed line) to co-seismic (solid line) times translates into a reduction of the confining pressure on the fault plane. This promotes the reduction of the effective normal stress σ_{eff} and facilitate the reactivation of the fault.

Super-imposed on the seismic dynamic trigger we also propose an effect due to the co-seismic elastic deformation caused by the main-slip. This mechanism would correspond to the *tectonic pull* described after mega-thrust earthquakes by recent authors. In fact, Pritchard et al. [2013] and Takada and Fukushima [2013] highlight that volcanic systems residing in volcanic arcs at convergent margins undergo a rapid subsidence (from days to months) immediately after the occurrence of a large magnitude subduction earthquake. This is also supported by cGPS measurements [Vigny et al., 2011] that show uplift and subsidence of few centimeters at different regions in the volcanic arc during the Maule earthquake. A similar behavior was also observed by Ikuta et al. [2012] in Japan during the M_w 9.0 Tohoku-Oki earthquake. Lupi and Miller [2014] suggest that at obliquely convergent margins lateral motion in the volcanic arc is promoted after part of the confining stress is removed by the mega-thrust slip. In oblique subduction zones, the shear stress is then accommodated in the overriding plate by trench-parallel, regional-scale, strike-slip faults that may be reactivated when the effective normal stress σ_{eff} along the fault planes is reduced. However, contrary to the Chilean and the

Japanese cases, the Nicoya earthquake did not impose long-term Coulomb variations on the volcanic arc. Figure 4.5 suggests that over a short time window (i.e less than a year), ignoring visco-elastic effects and assuming an elastic upper crust, the co-seismic reduction of the normal stress σ_n imposed by the earthquake slip at the subduction interface may also affect distant faults facing the region of main slip of the earthquake. In this case fault unclamping may not be large magnitude (i.e. 1 kPa) but may still facilitate shear failure. In addition, upwelling fluids can ultimately reduce the effective normal stress σ_{eff} along the fault plane further. This would support the observation of peaks of seismic activity following the major aftershocks of the Nicoya earthquake (Figure 4.4). The effects of $\sim M_w$ 4.5 earthquakes have been suggested to be negligible for distances larger than 30 km from the epicenter [Manga et al., 2009]. Yet, Figure 4.4 shows two clear peaks of increased seismic activity after the major aftershocks of the Nicoya earthquake. Recent laboratory experiments at elevated slip rates show that friction may reduce as low as 0.05 once the fault plane is reactivated [Di Toro et al., 2011]. Hence, in fault systems where friction is reduced, less seismic energy may be required to trigger seismic activity remotely.

Conclusion

Examining the seismic records from the OVSCORI seismic network around the Irazú-Turrialba volcanic complex before, during, and after the M_w 7.6 Nicoya earthquake we find evidence of triggered seismic activity. The seismicity is remarkably higher (more than 300 locatable earthquakes within 24 hours) if compared to the normal seismic rate of five to six events per day normally occurring at the ITVC. The seismic rate triggered by the Nicoya mega-thrust earthquake is also larger than the peaks of seismicity sometimes observed at the ITVC that reach a maximum of 150 of events during the entire seismic series that may last few days. The epicenters of the events triggered by the Nicoya earthquake are distributed along the southernmost part of the East Rio Sucío Fault system, a right lateral strike slip fault that joins the Finca Liebres Volcanic Depression between the Irazú and Turrialba volcanic edifices. The calculated static stress imposed by the M7.6 Nicoya earthquake on a fault plane sub-parallel to the southernmost end of the East Rio Sucío Fault was smaller than the dynamic stress imposed by the passing seismic waves. The maximum dynamic stress was in the order of 0.3 MPa and may have been the principal factor that determined the reactivation of the fault. However, we suggest that under the assumption of an elastic upper crust, the co-seismic reduction of the normal stress σ_n imposed by the main slip at the subduction interface may also have affected this part of the fault system. Due to the swarm-like character of the seismic sequence and the likely presence of a fluid circulation system maintained by the elevated geothermal gradient of the area, we suggest that the triggered seismic activity may have involved fluid mobilization.

The decay of the number of seismic events along the East Rio Sucío Fault follows an Omori's decay. However, we point out that powerful aftershocks of the Nicoya earthquake (i.e. $\sim M_w$ 4.5) also affected and enhanced seismic activity along the fault as suggested by peaks of seismic activity up to 14 hours after the main shock. This

may be favored by the coupled effects of a reduced friction of the reactivated East Rio Sucío Fault and the result of shear failure due to increased fluid pressure.

4.2 Remarks

Triggered seismicity at the Irazú-Turrialba volcanic complex adds to previous observations of volcanic activity induced by earthquakes. Since the complex is only 200 km from the Nicoya earthquake epicenter, this triggering sequence is one of the few examples of regional earthquakes triggering volcanic seismicity. It is noteworthy that the frequencies of the seismic waves are considerably higher than for the common observation of remote triggering by $M_w > 8$ teleseismic earthquakes. Triggering is usually due to Rayleigh or Love waves. Yet, in this case because of the comparably small distance to the epicenter triggering should be attributed mainly to S-waves that are about to evolve into surface waves.

The triggering of seismicity at the Irazú-Turrialba volcanic complex strengthens the observations of Prejean and Hill [2013]. Although Turrialba volcano was in an active phase at the time of the Nicoya earthquake, triggering occurred on Irazú which was at rest. Additionally, seismicity was triggered rather in the near-surface hydrothermal system adjacent to the volcano than at depth within the magmatic plumbing system. In the above study we propose a combination of dynamic triggering and co-seismic reduction of normal stress to cause the sudden increase in seismic activity with a duration of more than 24 hours. Linking our observations to the theories of earthquake-volcano interaction introduced in Chapter 2.3.2 also suggests unclogging of fractures as a possible mechanism to initiate the earthquake sequence. The mechanism may also apply to the short term effects of raised earthquake rate induced by the $M_w > 4$ Nicoya aftershocks that disturb the Omori decay of seismicity.

There is additional evidence for a dynamically triggered earthquake near Irazú volcano during the arrival of seismic waves from the Nicoya earthquake. The top of Figure 4.6 shows the waveforms of the Nicoya earthquake and the very first local event near Irazú volcano that marks the delayed onset of triggered seismicity. The spectrogram below reveals another local earthquake triggered during the phase of peak amplitudes from the Nicoya wave arrivals. It is identified as a high frequency (> 5 Hz) burst (similar to the later local event) on top of the lower frequencies (<5 Hz) that belong to the Nicoya earthquake seismic waves.

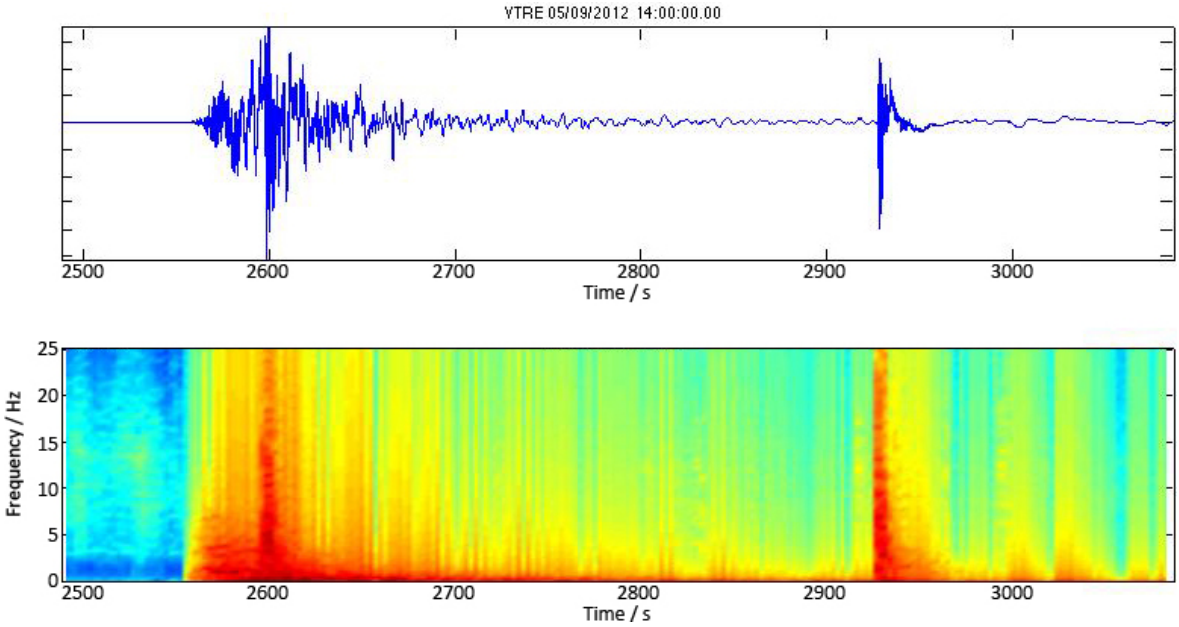

Figure 4.6: Top: Waveform of Nicoya earthquake (around 2550–2700 s) and a triggered local earthquake (after 2900 s) as recorded on station VTRE. Bottom: Spectrum of the above signal, revealing another triggered local earthquake during the peak amplitudes of the S-wave arrival (at 2600 s). The event is characterized by the same frequency content as the second local earthquake.

4.3 Earthquakes in the Larderello geothermal field

Searching for seismic activity worldwide dynamically triggered by the 2011 M_w 9.0 Tohoku earthquake, we discovered two potentially triggered earthquakes in the Larderello-Travale geothermal field, Italy. Data for three seismic stations (FROS, SASS, TRIF, see Figure 4.7) is publicly available at the European Intergrated Data Archive (EIDA). We used this 125 Hz sampling rate data to search for a response of the Larderello-Travale geothermal field to the passing surface waves from the 9800 km distant 2011 M_w 9.0 Tohoku earthquake. In Figure 4.8 the upper three traces show the unfiltered Tohoku waveforms. Late Rayleigh waves with periods of 40 s induced a vertical peak ground velocity of about 0.6 mm/s while early 107 s period Rayleigh waves caused the maximum vertical displacement of about 5.5 mm. Coinciding with this very first peak of the marked Rayleigh wave arrivals we record a local M_l 1.7 earthquake triggered during a temporary maximum of 0.4 mm/s ground velocity. A second local earthquake with M_l 1.6 occurs several minutes later at the end of the high amplitude Rayleigh wave coda. The epicenters of both earthquakes are marked in Figure 4.7 and are close to geothermal power plants. Both earthquakes are triggered a shallow 1–3 km depth. These earthquakes are not listed in the Istituto Nazionale di Geofisica e Vulcanologia (INGV) seismic database which is complete for magnitudes $M_l > 1.6$. However, we might have overestimated the magnitude of the potentially triggered earthquakes. Alternatively they may have failed to pass automatic detection because their signals were covered by the Tohoku seismic waves. Especially the first of the two earthquakes appears to be

dynamically triggered by the Tohoku Rayleigh waves because of the striking coincidence with the first peak of the Rayleigh wave arrivals. Compared to other triggering studies the ground velocity during triggering of this event is low (0.4 mm/s) and so is the associated dynamic stress $\sigma_d = G \times \mathrm{PGV}/v_s = 4$ kPa (using $G = 30$ GPa and $v_s = 3$ km/s [De Matteis et al., 2008]). The second event is triggered during the Rayleigh wave coda at ground velocities of approximately 0.6 mm/s (6 kPa dynamic stress). Dynamic triggering stresses that low would require near-lithostatic fluid pore pressures which seems possible in such a highly active geothermal area. In this case the observed earthquakes would nicely represent the fluid-driven Rayleigh wave triggering scenario from Hill [2012b] in Figure 2.12. Note that we cannot entirely rule out that the two earthquakes simply occurred as regular seismic activity in the Larderello geothermal field and accidentally coincided with the Tohoku Rayleigh waves. However, in the years 2009–2013 the INGV catalog lists approximately 0.2 earthquakes with $M_l > 1.0$ per day for the greater Larderello-Travale area. Hence, two earthquakes within 30 minutes and precisely during the Rayleigh waves of the Tohoku earthquake are very unlikely to occur naturally.

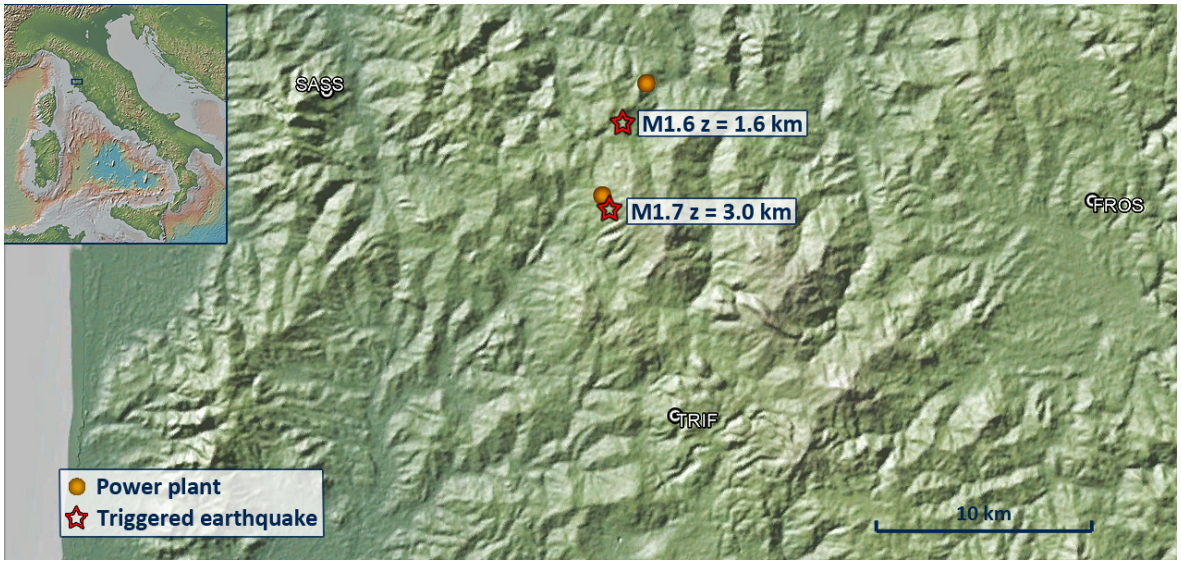

Figure 4.7: Map of Larderello-Travale geothermal field with triggered earthquakes. The mapped area is marked in the inset. The seismic stations used for the location are marked with station name. Red stars mark the epicenters of the two triggered earthquakes. They both fall near geothermal power plants which are marked as yellow circles.

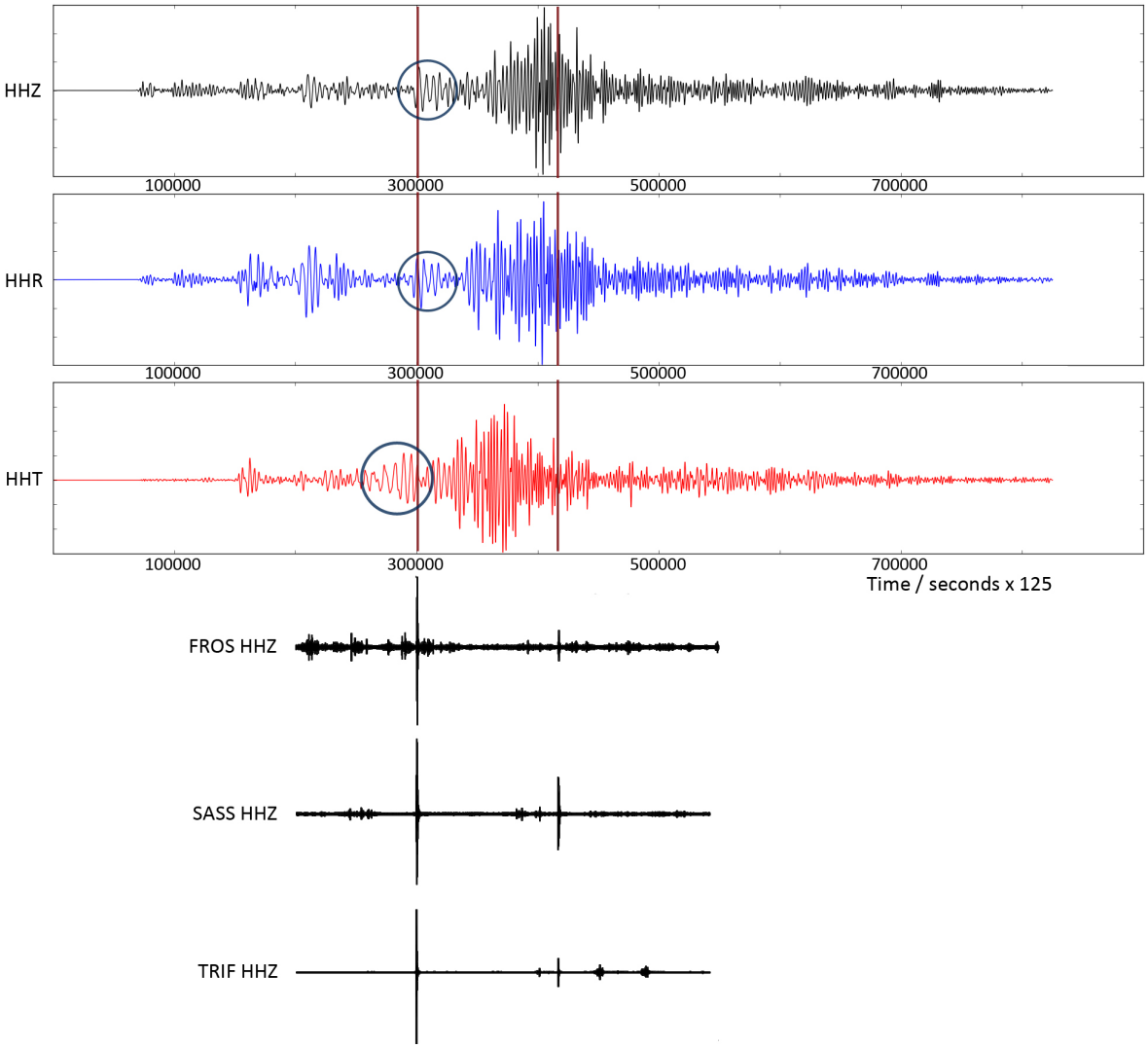

Figure 4.8: Triggered earthquakes at Larderello-Travale geothermal field. The upper three traces show ground velocity on the vertical (HHZ), radial (HHR) and transversal (HHT) components of the 2011 M_w 9.0 Tohoku earthquake measured on FROS. Circles mark the first arrivals of Rayleigh waves (HHZ and HHR) and Love waves (HHT). The red lines mark the timing of the two possibly triggered earthquakes that are identified in the lower three vertical traces from stations FROS, SASS and TRIF. To reveal the local earthquakes over the background Tohoku signals we applied a 5–15 Hz bandpass filter.

5 Triggering of tectonic tremor

Tectonic tremor is a poorly understood seismic phenomenon mainly observed on major plate boundary faults such as subduction zones [Aiken et al., 2013; Obara, 2012] and the San Andreas Fault [Gomberg et al., 2008]. The seismic signature of tectonic tremor resembles the characteristics of volcanic tremor as shown in Figure 2.17, yet the driving mechanisms of tectonic (or nonvolcanic) tremor are not well understood. Observations of tectonic tremor on subduction zones suggest that tremor accompanied by slow-slip may be an important part of the earthquake cycle [Beroza and Ide, 2011]. Thus, tremor could play a vital role in the estimation of seismic hazard on major plate boundary faults. Additionally, tectonic tremor is very susceptible to and repeatedly triggered by dynamic stresses from remote earthquakes and thus provides a tool to further understand dynamic triggering mechanisms. Tectonic tremor is observed on many subduction zones worldwide (see below), yet any new tremor discovery helps to further constrain the driving mechanisms. The following Section reports the first evidence of tectonic tremor along the Java subduction zone, Indonesia.

5.1 Non-volcanic tremor in Sumbawa, Indonesia

This Section is published as: F. Fuchs, M. Lupi and S. A. Miller (2014), Remotely triggered non-volcanic tremor in Sumbawa, Indonesia, *Geophysical Research Letters, 41*, 4185–4193.

Introduction

Non-volcanic tremor (NVT) provides important information about dynamics of plate boundaries, but the underlying mechanisms driving NVT are not understood. NVT is ubiquitous and observed worldwide, and to date this includes Alaska and Aleutians [Gomberg and Prejean, 2013], California [Chao et al., 2012b; Gomberg et al., 2008], Cascadia [Aiken et al., 2013], Chile [Gallego et al., 2013], Costa Rica [Walter et al., 2011], Cuba [Peng et al., 2013], Japan [Miyazawa and Brodsky, 2008; Obara, 2012], Mexico [Zigone et al., 2012], New Zealand [Fry et al., 2011] and Taiwan [Chao et al., 2012a]. In this paper, we expand this list to now include Sumbawa, Indonesia.

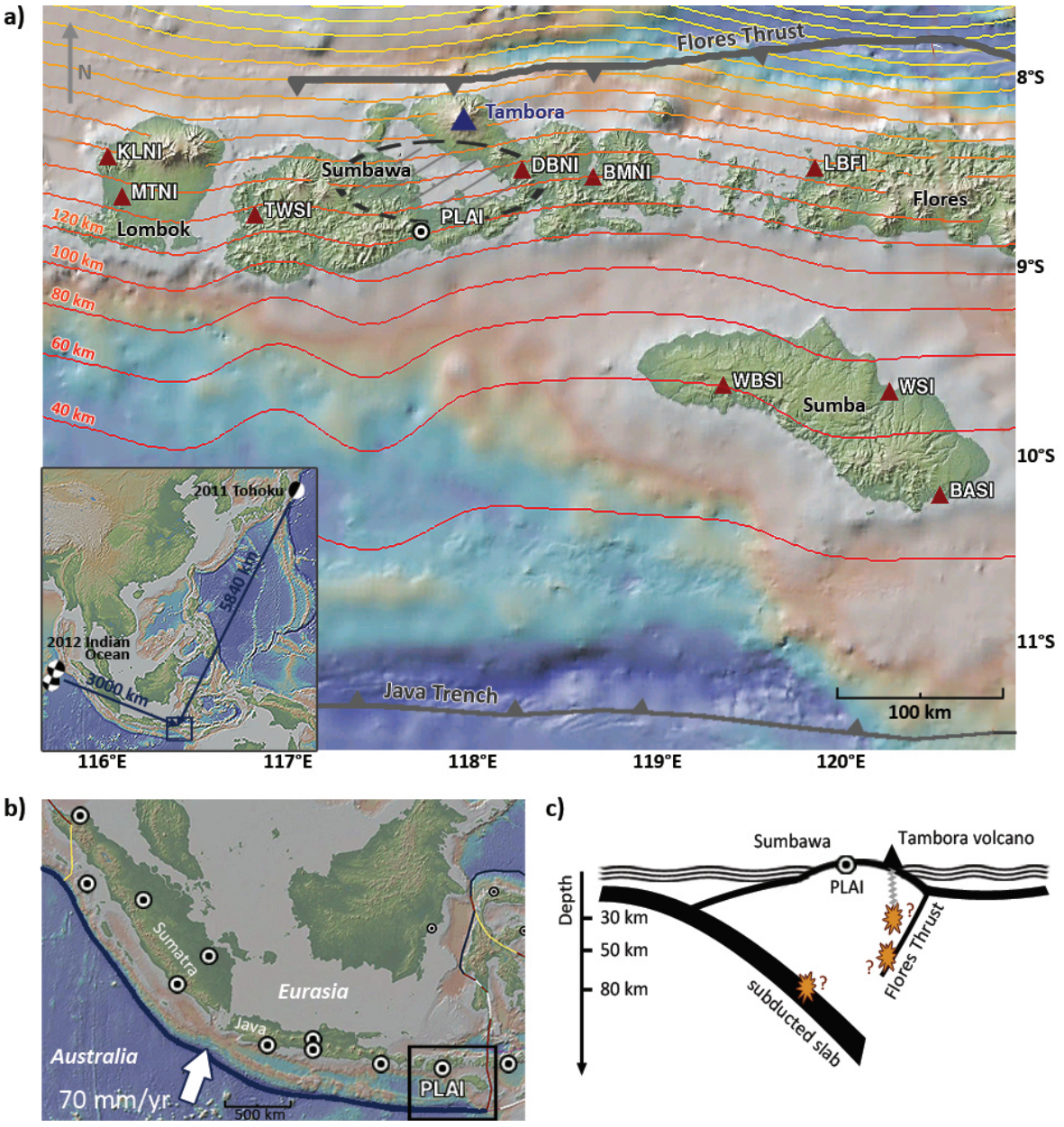

Figure 5.1: **a**) Map of Sumbawa, Indonesia. The mapped area and the distances to the triggering earthquakes are marked in the inset. Thin solid lines mark the extension of the subducted slab with depth which is indicated on the left [Hayes et al., 2012]. The circle denotes the location of the GEOFON station PLAI, triangles (except for Tambora volcano) mark seismic stations of the Indonesian BMG-Net. The encircled area in the middle represents a potential source area for triggered tremor on the Flores Thrust. **b**) Tectonic setting of Indonesia. The thick blue line marks the elongation of the Java Trench subduction zone. Thin lines represent continental margins. Circles denote the locations of seismic stations of the GEOFON network. The rectangle indicates the area mapped above. **c**) Sketch illustrating the three potential source regions for the triggered tectonic tremor. Tremor could be located at depth within the Tambora volcanic complex, below the locked zone of the Flores Thrust or on a deep section of the subducted slab. The sketch is not drawn to scale.

The characteristic seismic signature of tremor is emergent and irregular bursts of seismic energy depleted in high frequencies, and lasting from seconds to days. Naturally occurring tremor, termed ambient or background tremor, is distinguished from triggered tremor that is usually in phase with peak Love- or Rayleigh-wave amplitudes [Chao et al., 2012a,b; Guilhem et al., 2010] of remote or regional earthquakes. Body wave triggering of tremor is rare, but has been observed for both P and S waves [Ghosh et al., 2009; Hill et al., 2013; Shelly et al., 2011]. The threshold for tremor triggering is remarkably low, responding to transient stresses as low as 1 kPa [Guilhem et al., 2010], and some correlations are observed with tidal stressing [Gallego et al., 2013; Rubinstein et al., 2008; Thomas et al., 2013]. This has lead to a general acceptance that high pressure fluids are likely involved in their genesis [Beroza and Ide, 2011].

Among others, Shelly et al. [2007] suggest that tremor may result from a consecutive occurrence of small low-frequency earthquakes. Tremor typically originates from within the transition zone between locked and freely slipping parts of plate-boundary faults, at depth of 15–40 km down-dip [Rogers and Dragert, 2003; Shelly et al., 2006], and tremor is often associated with slow slip earthquake (termed episodic tremor and slip, ETS) [Bartlow et al., 2011; Beroza and Ide, 2011; Miller, 2013]. Understanding the mechanisms driving ETS presents an important challenge because it is likely a dominant aspect of the evolutionary processes leading to tsunamigenic, megathrust subduction zone earthquakes.

This study reports and analyzes, for the first time, the occurrence of triggered tremor beneath Sumbawa, Indonesia, following three teleseismic earthquakes since 2011.

Study area & data availability

The island of Sumbawa, Indonesia is part of the Lesser Sunda Group about 250 km north of the Australian/Eurasian plate collision at the Java Trench with a convergence rate of approximately 70 mm/yr [Tregoning et al., 1994]. The tectonic setting of Indonesia is shown in Figure 5.1b. Silver et al. [1983] and McCaffrey and Nabelek [1984] documented back-arc thrusting on the eastern Sunda Arc which is mapped as the Flores Thrust in Figure 5.1a that dips towards the south beneath Sumbawa.

Seismic stations around Sumbawa (see Figure 5.1a) include PLAI, which is part of the GEOFON global broadband seismic network [Hanka et al., 2010]. The other stations belong to the broadband BMG-Net operated by the Indonesian Agency for Meteorology, Climatology and Geophysics. The sampling rate for PLAI is 50 Hz or 100 Hz and data can thus be used in this study. Unfortunately, the BMG-Net data insufficiently samples at 20–25 Hz, and could not be used because of filtering limitations. Data were accessed via the European Integrated Data Archive and processed with ObsPy [Beyreuther et al., 2010]. Initially searching for remotely triggered tremor by the 2011 M_w 9.0 Tohoku earthquake we checked all Indonesian GEOFON stations (see Figure 5.1b) and ultimately found tremor only on PLAI. We thus searched station PLAI (installed in March 2011) for triggered tremor in response to teleseismic surface waves from several earthquakes larger than M_w 7 (see Table 5.1).

Triggered Tremor

We identify triggered tremor as an emergent seismic signal depleted of high frequencies that is modulated in amplitude by surface waves of teleseismic earthquakes. Of the 17 teleseismic events studied, three earthquakes triggered tremor beneath Sumbawa: the 2011 M_w 9.0 Tohoku earthquake, and the two 2012 M_w 8.6 and M_w 8.2 strike-slip earthquakes in the Indian Ocean offshore Sumatra. Measured on PLAI, Rayleigh waves of these events induced a peak ground velocity (PGV) of 1–3 mm/s and dynamic stresses between 8 kPa and 27 kPa. Love waves induced even larger PGVs of 2–7 mm/s and dynamic stresses between 17 kPa and 58 kPa. The 2012 M_w 7.6 Philippines event induced ground motions just slightly weaker (PGV 0.6 mm/s and 5 kPa) without triggering any tremor. For the triggering earthquakes Rayleigh wave periods are in the 45–65 seconds range and Love wave periods range from 65 s (M_w 8.6 and M_w 8.2 Indian Ocean) to 110 s (M_w 9.0 Tohoku). Both Love and Rayleigh wave periods are approximately 40 s for the non-triggering Philippines event.

Figure 5.2 shows triggered tremor signals recorded on the PLAI station. For the Tohoku event, tremor is triggered by Rayleigh waves, whereas for the two strike-slip events triggered tremor appears to be initiated during the Love wave train but but reaches maximum amplitudes within the Rayleigh waves. Note that triggering is mainly due to the Rayleigh waves although Love wave amplitudes are up to twice as large, especially for the M_w 8.2 Indian Ocean event. Generally the tremor signal is stronger on the horizontal components than on the vertical. On the horizontal components peak tremor amplitudes range from approximately 60 nm/s (M_w 8.2 Indian Ocean) to about 190 nm/s (M_w 8.6 Indian Ocean) and seem to correlate with the surface wave induced PGV - the larger the surface wave PGV, the larger the tremor peak amplitude.

For Figure 5.2 frequency filters were applied to show tremor signals that are not obscured by noise or body wave coda. However, the spectrum of the tremor shows slightly lower frequencies, ranging from 3–12 Hz while being strongest around 5–7 Hz as shown for the M_w 8.6 Indian Ocean event in Figure 5.3.

This evidence for tremor triggered by three different earthquakes is only observed on the PLAI station and thus the tremor cannot be located. Although several BMG-Net stations are near PLAI (the closest being 70 km from PLAI) the low sampling rate of

Figure 5.2 (facing page): PLAI recordings of tremor triggered by **a**) the 2011 M_w 9.0 Tohoku earthquake, **b**) the 2012 M_w 8.6 Indian Ocean strike-slip earthquake and **c**) the 2012 M_w 8.2 Indian Ocean event. All waveforms show ground velocity and no time-shifting was applied. The upper three traces show the unfiltered and rotated waveforms of the teleseismic event, respectively. The lower three traces display filtered and unrotated waveforms and show the triggered tremor signal along with body wave arrivals and codas. Love and Rayleigh wave trains are labeled and the dashed lines denote the center of clearly visible tremor spikes. The frequency filters have been chosen such that they yield a good SNR for plotting purposes. See Figure 5.3 for the complete frequency content of the tremor signal. The left column shows the entire teleseismic signal while the right part is a zoom-in on the surface waves only.

a) 2011 Mw 9.0 Tohoku

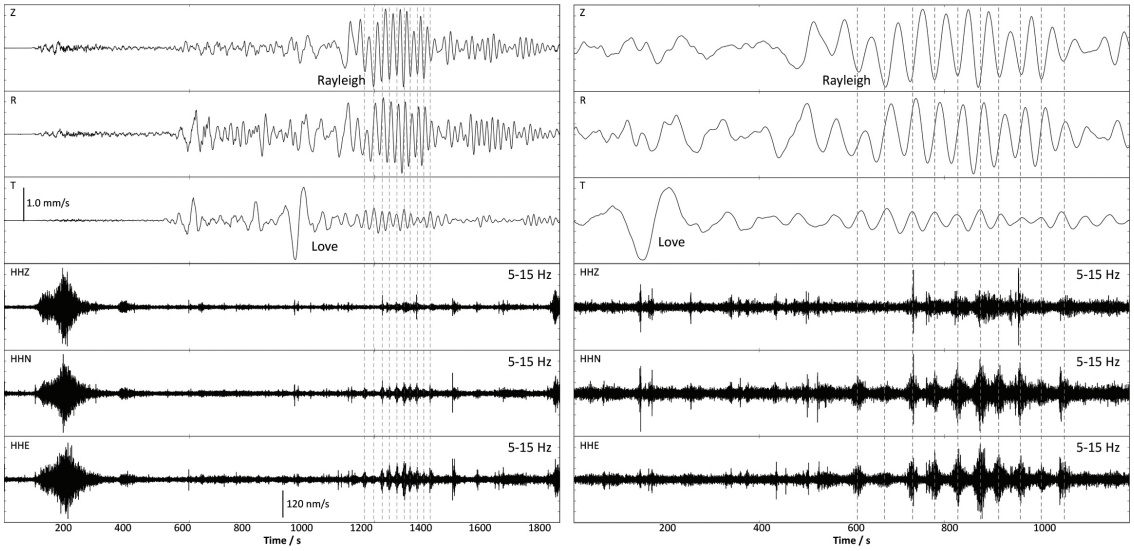

b) 2012 Mw 8.6 Indian Ocean

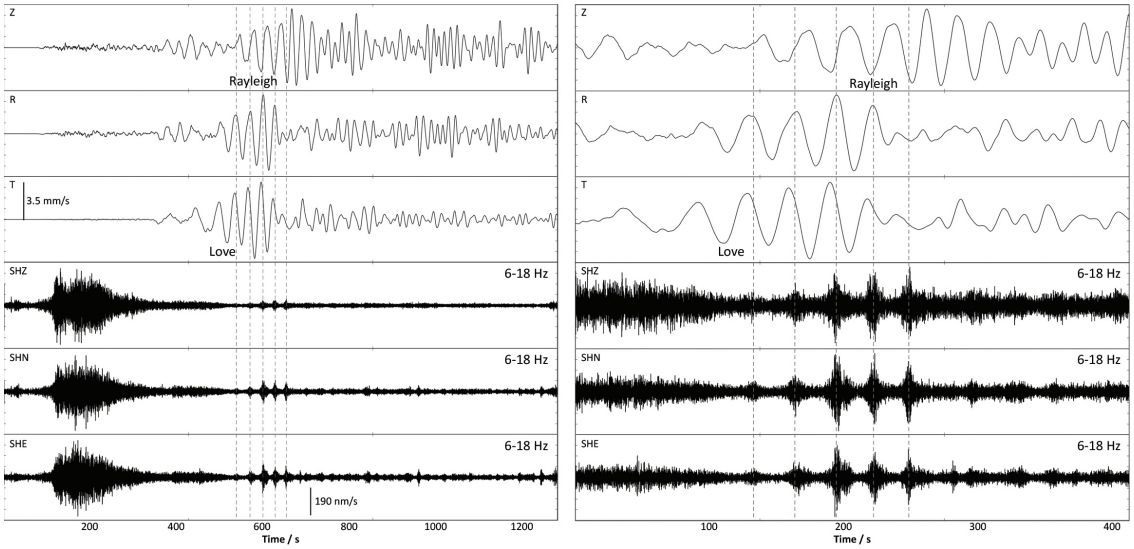

c) 2012 Mw 8.2 Indian Ocean

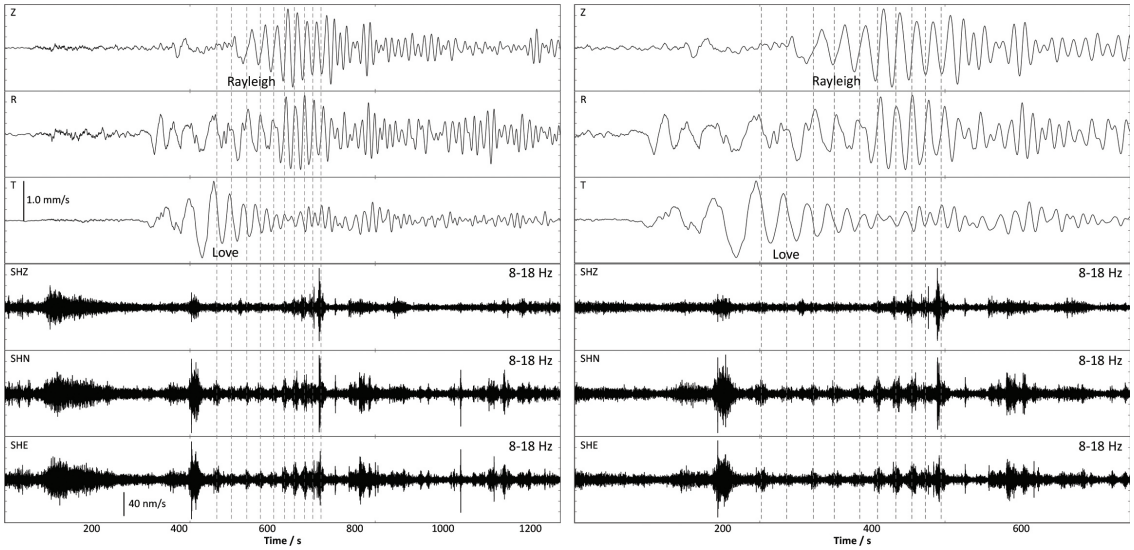

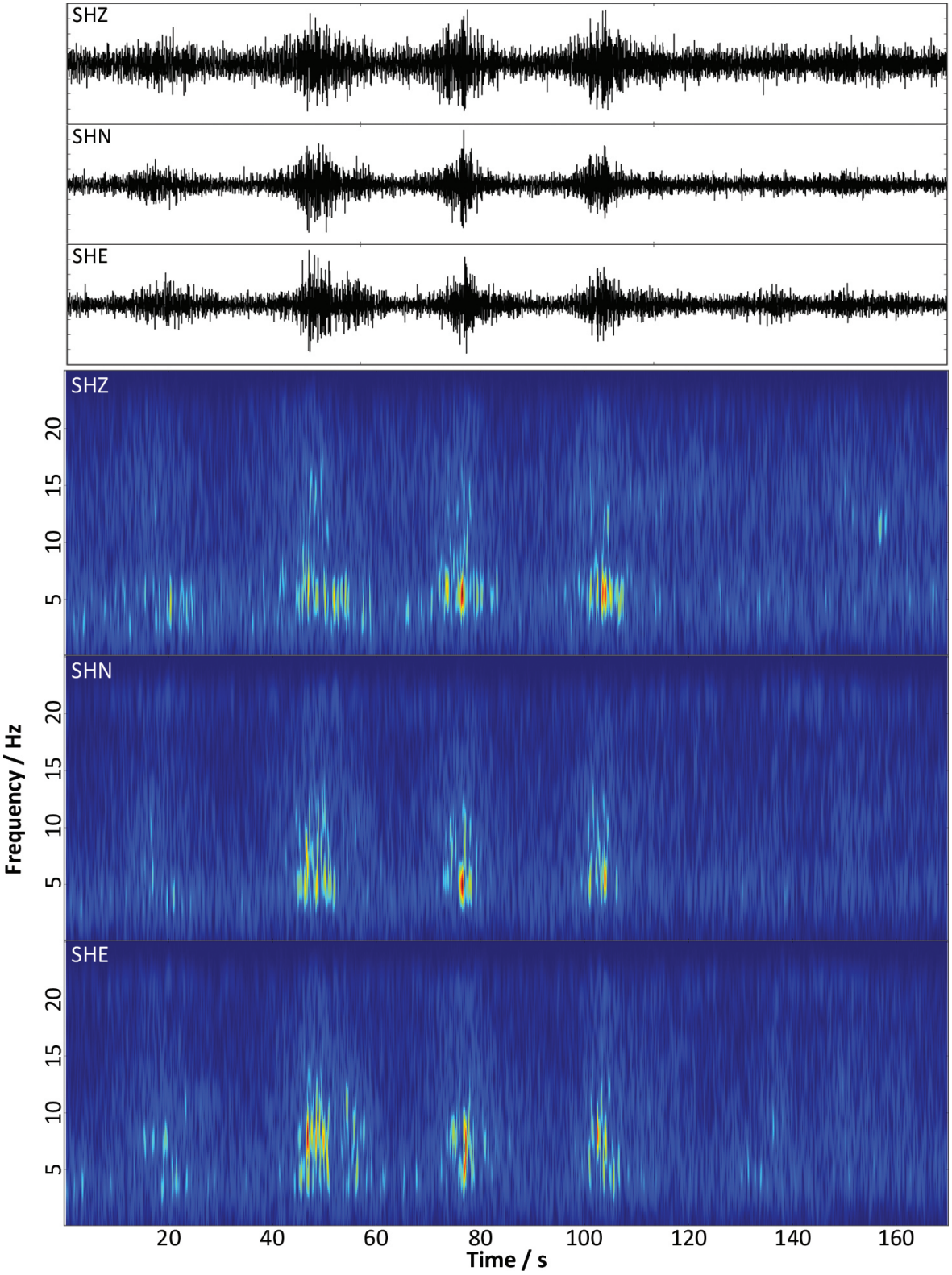

Figure 5.3: Spectrum of tremor spikes induced by the 2012 M_w 8.6 Indian Ocean event. Data was high-pass filtered for frequencies > 4 Hz such that the spectrum is not dominated by body wave codas. Frequencies of the tremor range up to 15 Hz while the signal is strongest in the 5-10 Hz region. Note that the signal might be composed of lower frequencies as well, which are lost due to the pre-filtering. The spectral content of tremor triggered by the M_w 8.2 Indian Ocean and M_w 9.0 Tohoku earthquakes is similar.

20–25 Hz (thus allowing filters lower than 10 Hz only) prevents application of a reliable filtering scheme in the frequency range (5–15 Hz) required to reveal the weak triggered tremor within the noise and teleseismic signals. Thus, no clear signal of triggered tremor could be found in the data of the close TWSI, DBNI or any BMG-Net stations. The closest neighboring GEOFON stations are 400–500 km distant and do not record signals similar to what is seen on PLAI.

Discussion

We find a strong correlation between teleseismic surface waves and the onset of emerging characteristics of the frequency content, indicative of triggered tremor. Tremors in Figure 5.2 are not perfectly in phase with the respective surface waves because the signal was not time shifted to resemble the correlation at the source volume. Still, periodicity and amplitude of the triggered tremor correlate very closely with those of the surface waves. The observed tremor is the first evidence for triggered tremor along the Sunda Arc, Indonesia.

Only one station (PLAI) provided suitable data to reliably pick up the tremor, so the source of the tremor can not be located.However, trying to match tremor bursts with cycles of surface wave ground motion we find that peak tremor amplitudes (on horizontal components) are delayed by approximately 10 s compared to peak Rayleigh wave ground motion, thus placing the tremor about 30–50 km from PLAI (assuming a shear wave velocity of 3–5 km/s). This result is not well-constrained and there could be substantial variation for the two Indian Ocean events. But since the 10 second delay between surface wave arrivals at PLAI and the onset of tremor applies to both the M_w 9.0 Tohoku and the M_w 8.2 Indian Ocean event (with different incidence angles), this suggests the tremor source generally resides beneath PLAI.

A depth of 30–50 km suggests an origin associated with the Flores thrust rather than the Java subduction zone interface. Non-volcanic tremor typically occurs down-dip at about 15–40 km depth [Rogers and Dragert, 2003; Shelly et al., 2006] on plate-boundary faults, but the PLAI station would be more than 120 km distant from the subduction interface, likely yielding less distinctive tremor signals and weaker correlation in time than observed. Additionally the Java subduction zone is older (150 Ma [Widiyantoro and van der Hilst, 1996]), and thus colder, than typical tremor generating subduction zones. The Sumbawa section of the Flores Thrust is seismically active and local earthquakes that fall near the marked area in Figure 5.1 (USGS ANSS Comprehensive Catalog) show thrust mechanisms and extend down to about 26 km, possibly indicating the depth of the locked zone. Hence, nearby earthquakes reveal that this southward dipping structure is in the typically tremor generating depth range of 15–40 km beneath PLAI. This would be the first observation of tectonic tremor on a non-subduction zone thrust fault.

However, Fry et al. [2011] report triggered tremor from depth of 50–60 km at New Zealand where the age of the subducted slab is 120 Ma [Ide, 2012]. Similarly, given the age of the subducted slab near Sumbawa, tremor might also be generated at a very

deep section of the Java subduction zone. This section would be close enough to PLAI (see Figure 5.1) to allow for the observed signal strength and correlations.

Another possibility for the tremor source is the Tambora volcano. We rule out that the observed signals show volcanic tremor since Tambora volcano was not in an erupting state or state of unrest at the time. However, it is possible that the tremor reflects triggering of volcanic-related low-frequency earthquakes from within the Tambora complex, as Obara [2012] suggests for tremor on Hokkaido, Japan. Yet, no information is available about the occurrence of low-frequency earthquakes at Tambora volcano and the interplay of tectonic and volcanic tremor at volcanic centers is unknown. Since we cannot rule out any of the aforementioned scenarios future targeted studies to refine the tremor source should be conducted. The three suggested scenarios for the origin of the tremor are illustrated in Figure 5.1c. Please note that the sketch is not drawn to scale.

For all earthquakes studied (see Table 5.1) Figure 5.4 shows induced dynamic stress and the incidence angle of the seismic waves with respect to (b) the Flores Thrust or (d) the Java trench (assuming both strike approximately E–W). The three triggering earthquakes induced recognizably greater peak ground velocity (PGV) and dynamic stresses on Sumbawa than all of the other earthquakes, the exception being the 2012 M_w 7.6 Philippines event. Although the Philippines event did not trigger any tremor, it is interesting because the incidence angle is almost identical to the M_w 9.0 Tohoku earthquake, which should favor Rayleigh wave triggering in both cases. Additionally, the Rayleigh wave period of the M_w 8.2 Indian Ocean earthquake and the M_w 7.6 Philippines earthquake is about 40 seconds, producing very similar seismic waves. However, the triggering earthquakes induced a PGV of at least 1 mm/s while the M_w 7.6 Philippines event induced a PGV of only 0.6 mm/s. We conclude that this places a triggering threshold for tremor beneath Sumbawa of about 1 mm/s PGV (or alternatively 8 kPa of dynamic stress), which is of the same order of magnitude as reported for Taiwan [Chao et al., 2012a].

Our results are consistent with triggering factors suggested elsewhere [Chao et al., 2012a; Guilhem et al., 2010; Peng et al., 2009] such as ground motion, incidence angle and surface wave periods. While Chao et al. [2012a] report triggering predominantly for intermediate periods (10–30 s), Guilhem et al. [2010] and references therein show that long-period (greater than 30 s) surface waves have a greater potential for triggering tremor. Here, we note that the Rayleigh waves triggering tremor are in the long-period 45–65 s range, while the (non-triggering) Love waves show periods from 55–110 s. In the specific case of the M_w 8.6 Indian Ocean event, triggered tremor emerges only towards the end of the dispersive Love-wave train, when periods are in the 50–60 s range, despite the fact that ground motion is already above the apparent 1 mm/s threshold. Thus, our observations suggest that long-period (45–65 s) surface waves are optimal for triggering tremor at Sumbawa.

To establish the triggering potential of the surface waves (following Hill [2012a], Chao et al. [2012a] and Chao et al. [2013]), we assume that tremor originates from a fault plane striking E-W, which approximates the Flores Thrust or the Java subduction zone. The observations (see Figure 5.2a) of Rayleigh wave triggering from the Tohoku earthquake is consistent with the calculated triggering potential on the Flores Thrust

(Figure 5.4b) and reasonable for the subduction zone scenario (Figure 5.4d). However, for the two 2012 Indian Ocean earthquakes, Love wave triggering potential is large and Love wave induced ground motion is more than twice that of the Rayleigh waves, yet tremor correlates better with the Rayleigh waves, especially for the M_w 8.2 event. This observation adds to other studies [Chao et al., 2012a; Miyazawa and Brodsky, 2008] that report Rayleigh wave favored triggered tremor for strike-parallel incidence in Nankai,

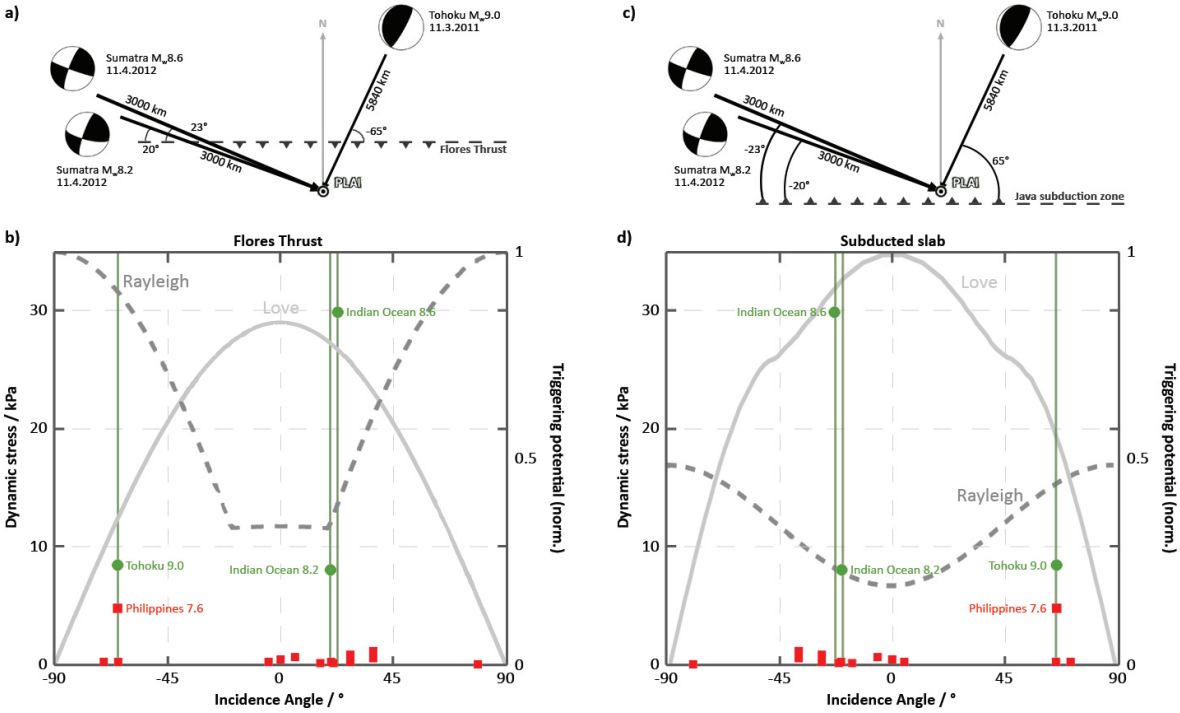

Figure 5.4: Analysis of the triggering potential. **a,c)** Illustration of the wave incidence angle for the three triggering earthquakes with respect to a hypothetical E-W striking fault plane that estimates either the Flores Thrust (a) or the Java subduction zone (c). Note the change in sign due to different dip orientation. **b,d)** Triggering potential for Love and Rayleigh waves on the Flores Thrust (b) and the subducted slab (d) compared to incidence angle and peak dynamic stress of all earthquakes that were studied. Parameters used: Reverse fault, 60° Dip for Flores Thrust, 25° Dip for Java subduction zone, μ^*=0.2, 20 s period waves at 20 km (Flores) and 45 km (subducted slab) depth (compare Chao et al. [2012a] and Chao et al. [2013]). Green dots represent the triggering events, red squares denote the non-triggering events. See the list in Table 5.1 for event details. Only four events induced dynamic stresses in the kPa range. The two markers at ±65° represent the 2011 Tohoku and the 2012 Philippines event (the latter did not trigger any tremor), the two markers at ±23° represent the 2012 strike-slip sequence in the Indian Ocean.

Japan and the Central Range, Taiwan. While Miyazawa and Brodsky [2008] and Chao et al. [2012a] favor tremor triggering by simple Coulomb shear failure promoted by the transient stresses, alternative explanations for the observed preferred Rayleigh wave triggering include higher frictional strength of the tremor hosting fault or mixed-mode failure by local fluid transport. In our case, the low triggering thresholds that we observe beneath Sumbawa implicate very low effective stresses and hence favor tremor

generation by a mechanism based of fluids which are likely associated with nearby arc volcanism.

Conclusions

We observed surface wave triggered tremor beneath Sumbawa, Indonesia induced by the 2011 M_w 9.0 Tohoku and the two 2012 M_w 8.6 and M_w 8.2 Indian Ocean strike-slip events. Tremor amplitudes scale with ground motion and peak at 180 nm/s ground velocity on the horizontal components. A comparison of ground motion of the three triggering events and a similar (non-triggering) 2012 M_w 7.6 Philippines event constrains an apparent triggering threshold of approximately 1 mm/s ground velocity or 8 kPa dynamic stress. Surface wave periods of 45–65 s appear optimal for triggering tremor at Sumbawa. Tremor is triggered predominantly by Rayleigh waves, even when Love waves produced higher ground motion and triggering potential. Rayleigh wave triggering, low triggering amplitudes, and the tectonic setting all favor a model of tremor generated by localized fluid transport.

Non-volcanic tremor is typically associated with low-frequency earthquakes and slow-slip events. Expanded broadband station coverage should be pursued in search of episodic tremor and slow-slip phenomena and this first-reported observation of triggered tremor beneath Sumbawa should initiate follow-on targeted studies of ETS in this important tectonic region of the Sunda Arc.

5.2 Remarks

Following the descriptions of Hill [2012b] in Chapter 2.3.1 prefered Rayleigh wave triggering may be an indicator of the tectonic setting at Sumbawa, Indonesia. According to Figure 2.12 large differential stresses on faults with a high friction coefficient or near-lithostatic pore pressure conditions can be responsible for Rayleigh wave induced dynamic Mohr-Coulomb triggering of tectonic tremor. Note, however that the given stress orbits are calculated for low-angle megathrust faults at 30 km depth and thus do not properly represent any of the possible tremor locations near Sumbawa. Without knowing the tremor location, the mechanism of triggered tremor generation at Sumbawa cannot be further investigated at this point. Locating the source of tremor near Sumbawa will require the installation of a seismic broadband network on Sumbawa and neighboring islands.

Table 5.1: List of teleseismic earthquakes used in this study. Only the upper three triggered tremor beneath Sumbawa. The distance is given from the epicenter to PLAI station. The angle denotes the angle of the incident seismic waves with respect to the Flores thrust or the Java Trench (with reversed sign). PGV was measured for the Rayleigh waves. Stress denotes the estimated peak dynamic stress on the surface imposed by the seismic waves, using the given PGV, S-wave velocity v_s=3.6 km/s [McCaffrey et al., 1985] and a shear modulus of 30 GPa.

Region	M_w	Date	Dist. [km]	Angle [°]	PGV [mm/s]	Stress [kPa]
Indian Ocean	8.6	11.04.2012	3000	23	3.20	27.0
Tohoku	9.0	11.03.2011	5840	-65	1.01	8.43
Indian Ocean	8.2	11.04.2012	3000	20	0.96	7.99
Philippines	7.6	31.08.2012	2380	-65	0.56	4.69
Pakistan	7.7	24.09.2013	6890	37	0.14	1.16
Kermadec	7.6	06.07.2011	7200	28	0.10	0.83
Solomon	8.0	06.02.2013	5200	6	0.08	0.68
Iran	7.7	16.04.2013	7250	37	0.06	0.49
New Guinea	7.1	14.12.2011	3200	0	0.05	0.39
Fiji	7.3	15.09.2011	6860	20	0.03	0.27
Kermadec	7.4	21.10.2011	7200	28	0.03	0.23
Tohoku	7.3	09.03.2011	5850	-65	0.02	0.20
Kamchatka	7.7	14.08.2012	7020	-71	0.02	0.18
Costa Rica	7.6	05.09.2012	17500	-5	0.02	0.17
Tonga	7.4	23.05.2013	7090	21	0.02	0.17
Vanuatu	7.1	02.02.2012	5530	16	0.02	0.16
Chile	7.1	25.03.2012	15000	79	0.01	0.03

6 Mud volcanoes and earthquakes

The devastating 2006 mud eruption in the district of Sidoarjo, Indonesia, caused great damage to the surrounding population. Named Lusi (Lumpur Sidoarjo), the expulsion of mud is ongoing until today and has forced displacement of ten thousands of Indonesians. Yet, the origin of the mud eruption is unclear and a topic of scientific debate, the two opposing theories being a drilling trigger by a nearby well-bore and a natural trigger by the 2006 M_w 6.3 Yogyakarta, Indonesia, earthquake. Since the site of the Lusi eruption is comparably far from the epicenter for a M_w 6.3 earthquake the natural trigger scenario would show that very little dynamic stresses may still promote dramatic effects at distance. The following section describes a numerical method to investigate if seismic waves of the Yogyakarta earthquake could have triggered the Lusi mud eruption. While triggering examples presented in the previous Sections report seismological observations of triggering, the following Section will introduce a conceptual idea how volcanic systems may be affected even by intermediate magnitude regional earthquakes.

Figure 6.1: Central vent of the Lusi mud eruption today. Embankments have been built to prevent further flooding of the surroundings. Unlike regular mud volcanos, the material erupted at Lusi is hot, thus producing the steam. Photograph taken from [Cheveralls, 2011].

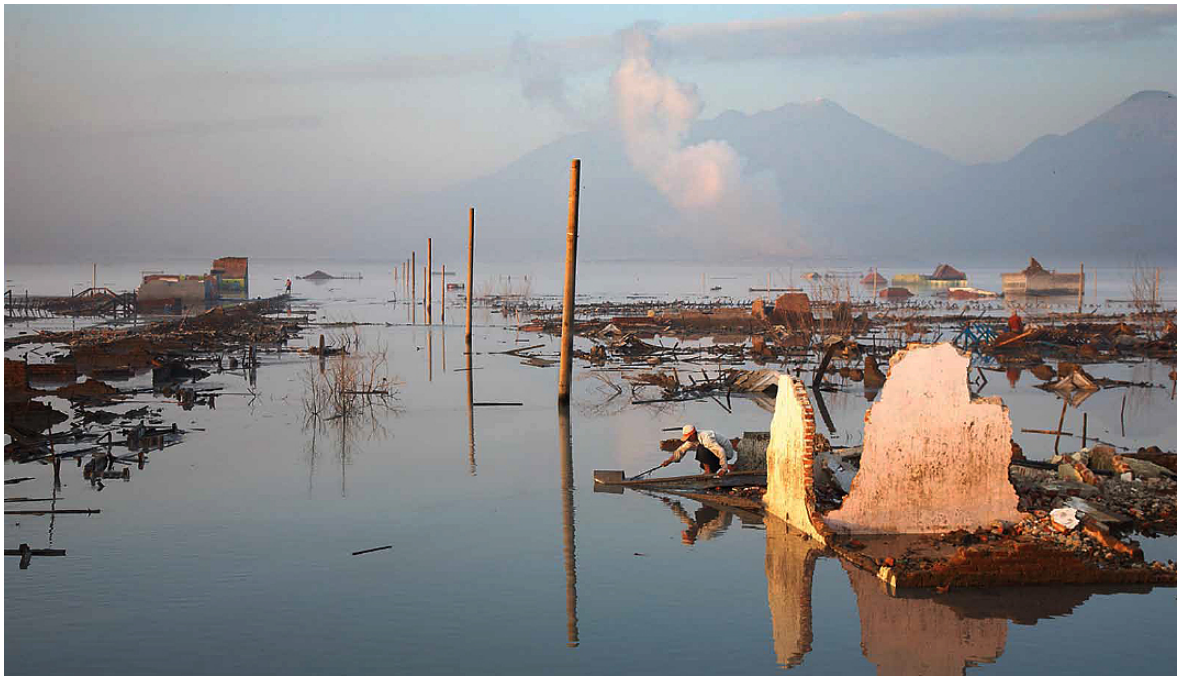

Figure 6.2: Village flooded by the Lusi mud eruption. Steam rising from the main vent in the background. The mountains behind form the neighboring and possibly connected Arjuno-Welirang volcanic complex. Photograph by [Axford, 2009].

6.1 Mud eruption triggered by seismic wave focusing

This Section is published as: M. Lupi, E. H. Saenger, F. Fuchs and S. A. Miller (2013), Lusi mud eruption triggered by geometric focusing of seismic waves, *Nature Geoscience, 6*, 642–646.

Numerical study on the triggering of the Lusi mud eruption

Mud volcanoes typically form in geological settings with high sedimentation rates such as compressional tectonic belts, submarine slopes and, as for Lusi, in inverted backarc basins [Manga et al., 2009; Tanikawa et al., 2010]. Fast sedimentation rates and high geothermal gradients dehydrate minerals faster than the fluid product can escape its low-permeability confines, resulting in overpressured and under-consolidated clay (mud) layers trapped at depth.

On 26 May 2006, 47 hours before the arrival of mud at the surface, a shallow (12 km deep) M_w 6.3 strike-slip earthquake occurred near Yogyakarta, Indonesia, approximately 250 km distant from the eruption site of Lusi (see Figure 6.3). The essence of the drilling trigger argument is that 250 km falls outside of the empirically determined distance range of volcanic triggering phenomena [Manga and Brodsky, 2006; Manga et al., 2009], and drilling with uncased sections of the borehole was underway about

200 m from the eruption site [Davies et al., 2008; Sawolo et al., 2009; Tingay et al., 2008]. Relevant here is that two volcanoes active at that time, Mount Merapi and Mount Semeru, at distances of about 50 and 300 km respectively, from the Yogyakarta epicenter (Figure 6.3), both showed a threefold increase in heat flow and erupted volume flux in response to that earthquake [Harris and Ripepe, 2007]. This indicates that the Yogyakarta earthquake produced sufficient seismic energy to provoke a response at distances similar to, and even exceeding, the distance to Lusi.

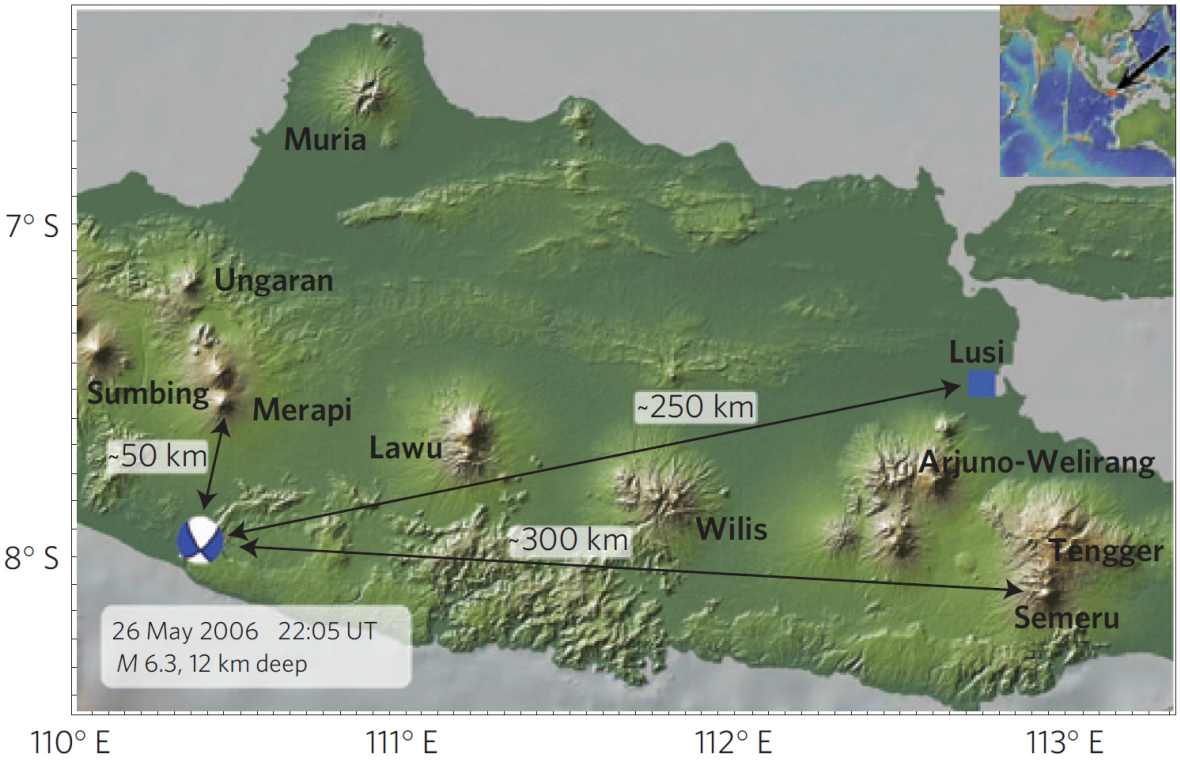

Figure 6.3: Map of Java with relevant distances from the Yogyakarta earthquake. The blue square marks the position of Lusi and arrows show the distance between the epicenter of the Yogyakarta earthquake and the systems that responded to that event.

Before the eruption, the mud layer at Lusi had sufficient shear strength as evidenced by the integrity of the uncased section before collapse [Davies et al., 2008; Sawolo et al., 2009]. Static stress changes ($\sigma_s \sim 10$ kPa) from the Yogyakarta earthquake at such a distance are irrelevant and dynamic stress changes, σ_d, assuming a shear velocity of 2500 m/s, were estimated at $\sigma_d \sim 21 + 33/-12$ kPa [Davies et al., 2008]. However, an analysis of the geological structure of Lusi by Istadi et al. [2009] shows strong variations of acoustic impedance with depth, indicating a potentially complicated wave field from incoming seismic energy (see Figure 6.4). To study the effect of varying acoustic impedances, we carried out high-resolution forward simulations [Saenger and Bohlen, 2004; Saenger et al., 2000] using a synthetic data set for elastic waves propagating through the known lithology of Lusi (for more details see Methods Section below).

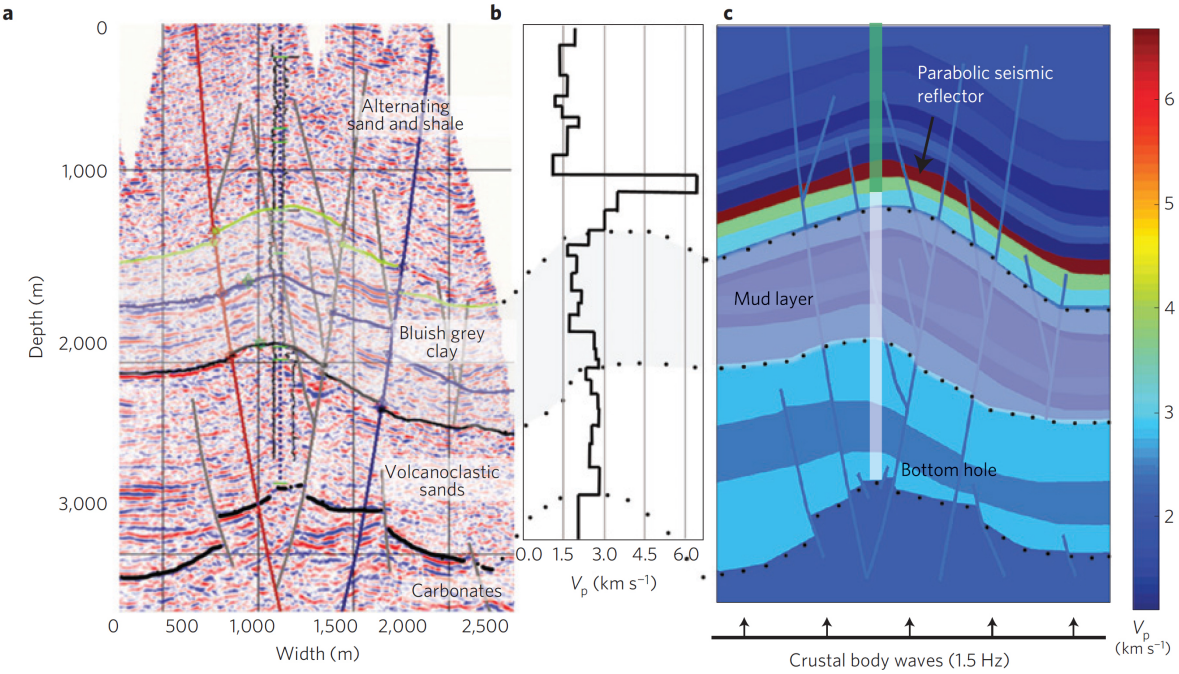

Figure 6.4: Geometry, v_p variations with depth and model of Lusi used in the numerical study. **a)** Seismic profile of the geological structures beneath Lusi used to reconstruct the geology of the model [Sawolo et al., 2009]. **b)** Vertical profile for v_p velocities used in the model [Istadi et al., 2009]. The acoustic impedance of faults is not known, so we assumed $\rho = 2000$ kg/m^3, $v_p = 2325$ m/s and $v_s = 1531$ m/s. **c)** Distribution of v_p velocities in the model domain. The mud layer is shaded grey, the cased and uncased well (not modeled) are shaded green and white, respectively.

We simulated frequencies from 0.5 to 1.5 Hz to explore synthetic crustal body waves propagating within Lusi and found that the high-velocity layer that seals the mud source (red level in Figure 6.4c) dominates the system. This parabolic-shaped high v_p layer reflects and geometrically focuses body wave energy arriving from below (see Figure A.2 for results of inclined incidence). We use the term *parabolic seismic reflector* for this phenomenon and the effect of this structure at Lusi was to focus and amplify substantial seismic energy into the overpressured mud layer. Although surface waves are not significant for crustal earthquakes at epicentral distances of 250 km [Kulhanek, 2002], we nevertheless simulated Rayleigh waves to determine how previous earthquakes (that is, M_w 9.2 and M_w 8.7 Sumatra events in 2004 and 2005) may have affected the system. The surface wave simulations (see Figure 6.7a) show that the high-velocity layer prevents any significant energy from penetrating to the depths of the mud layer, which may explain why Lusi did not respond to surface waves from more powerful, but more distant, earthquakes [Davies et al., 2008]. The focusing effect is frequency dependent in that the effect is reduced for wavelengths longer than the diameter of the reflecting structure, which in our case is about 3 km, resulting in a corner frequency of approximately 1 Hz for an assumed shear wave velocity of 3 km/s (see Figures 6.7b and 6.8 for simulations at 0.5 and 1.0 Hz). The simulation results for 1.5 Hz body waves (P- and S-waves) are plotted in Figure 6.5 using established criteria [Saenger, 2011] as maximum energy density, vertical displacement, dynamic stress and shear strain.

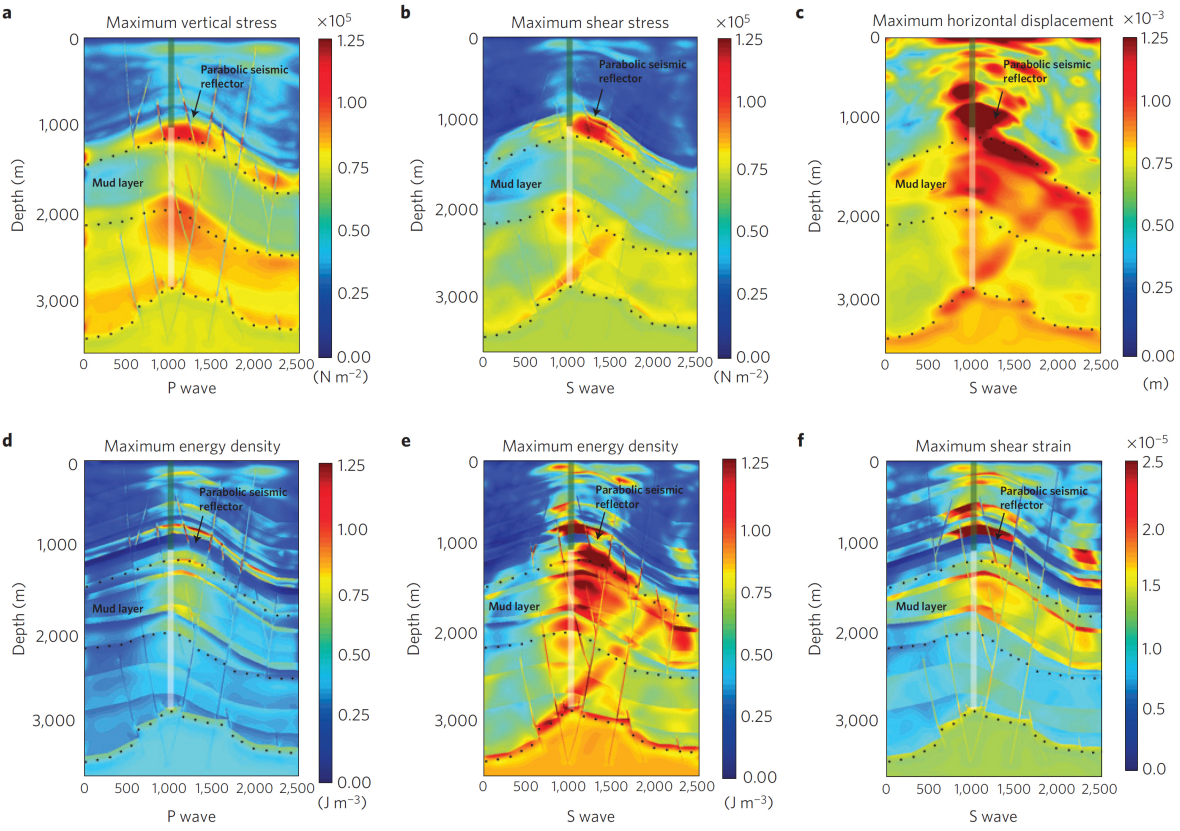

Figure 6.5: Simulation results for: **a**,**d** P-wave and **b**,**c**,**e**,**f**, S-wave at 1.5 Hz. **e)** Peak energy density of 1.25 J/m^3 is reached above the seismic reflector and in the mud layer, demonstrating how the domed structure geometrically focuses energy. Dynamic stress σ_{d} (**a**,**b**), vertical displacement (**c**) and shear strain ϵ (**f**) induced by wave propagation shows how the lithology affects their distribution. Peaks of σ_{d} of 0.25 MPa are observed immediately below the casing, whereas the induced dynamic stress in the mud layer is approximately 0.075 MPa with peaks of 0.1MPa in the deeper part. Vertical displacements of 1.25 mm occur in the mud layer, inducing peak strains of 20 $\mu\epsilon$.

Maximum energy densities induced by S-waves are more intense and widespread in comparison with the P-wave results, showing peaks of over 1 J/m^3 immediately above and below the parabolic seismic reflector and at the bottom of the wellbore where volcanoclastic sands overlay suspected overpressured carbonates hosting H_2S-rich fluids [Tingay et al., 2008]. Although the overpressured carbonates are essential to the drilling trigger argument, there is no evidence that this layer was breached, while the source of the H_2S could very well have been the shale-clay layer. Energy densities in this range are significant because mud volcanoes have been triggered by energy densities as low as 0.1 J/m^3 [Rudolph and Manga, 2012]. Furthermore, a peak dynamic shear stress of about 0.1 MPa and a maximum vertical displacement of approximately 1 mm occurred in the mud layer and at the bottom hole. Note that the results in Figure 6.5 show the values for an incoming wave of one cycle, but the Yogyakarta earthquake and its aftershocks produced wave trains into Lusi, subjecting the overpressured and underconsolidated mud layer to cyclic loading that further increased pore pressure with each additional cycle of applied shear stress [Yassir, 1989]. Increasing pore pressure reduces the shear modulus,

so each subsequent cycle propagated into an increasingly reducing shear modulus (that is, impedance), which would further amplify the focused energy. Our calculations for a single wave cycle show shear strains of up to 20 microstrain ($\mu\epsilon$) within the mud layer. Although it is not known what shear strain magnitude would induce liquefaction at the depths of Lusi, we note that this is within the range of the 10–100 $\mu\epsilon$ purported to have caused liquefaction of the San Francisco Marina Bay muds (albeit at shallower depths) in response to the 1989 M_w 7.1 Loma Prieta earthquake [Stewart and Hussein, 1992].

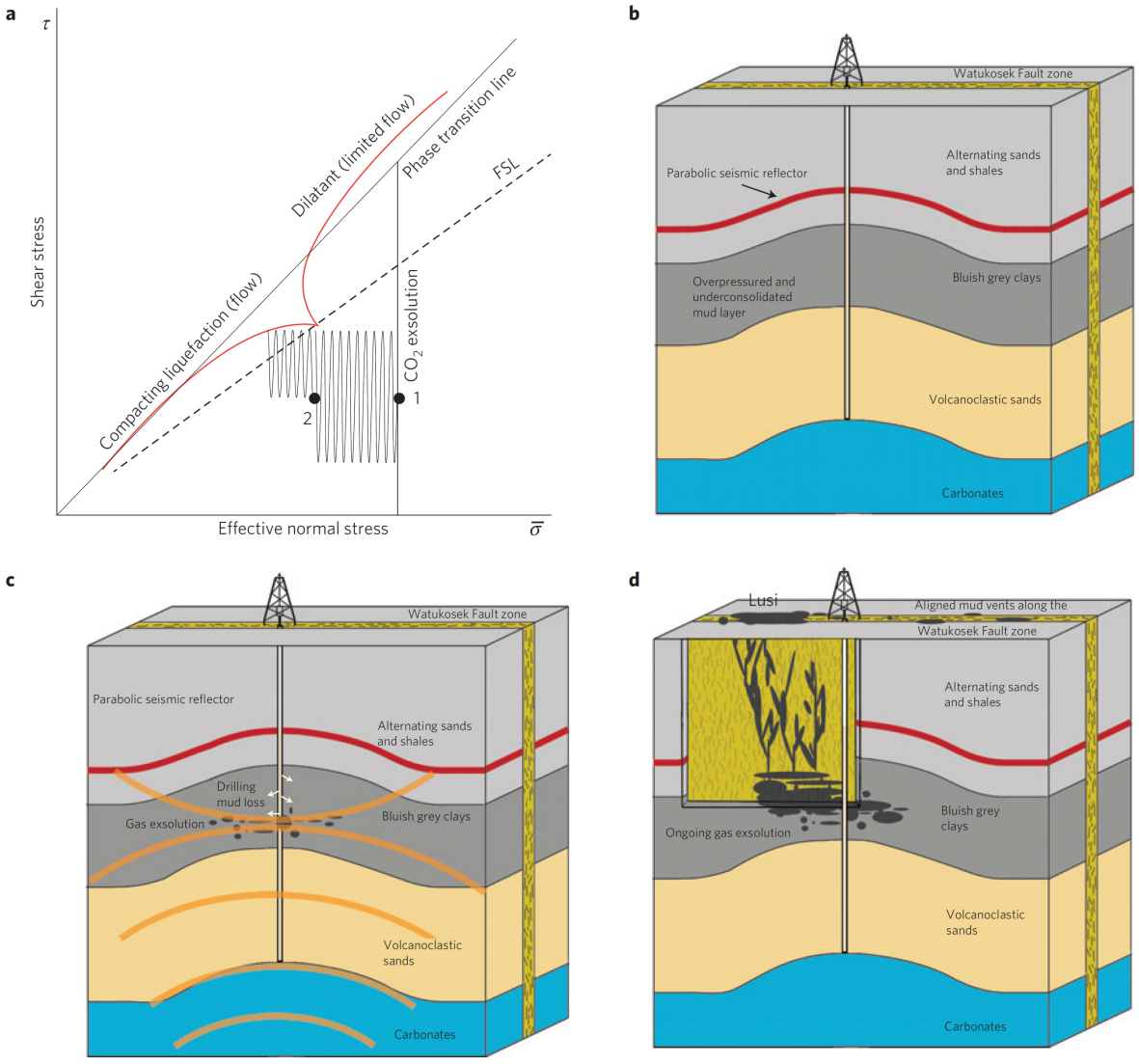

Figure 6.6: Conceptual stress path and proposed scenario for triggering the Lusi mud eruption. **a)** Amplified seismic energy perturbs the initial stress state (1), increasing pore pressure through cyclic shear stressing. Aftershocks (2) cyclically load the (impedance-reduced) mud layer, reaching the FSL. At the FSL, the mud layer either liquefied and lost strength (compacting), or strain hardened (dilatant). Fluid pressure reductions to below initial conditions trigger CO_2 exsolution, mobilizing the mixture of mud, gas and water. **b)** State of system before the Yogyakarta earthquake with high fluid pressures and a narrow drilling window [Tingay et al., 2008]. **c)** Liquefaction from Yogyakarta earthquake and aftershocks drew drilling mud into the layer. **d)** Liquefied mud layer injects and reactivates the pre-stressed Watukosek Fault system.

Our results support a scenario where lithology-controlled focusing of the incoming seismic waves into the mud layer resulted in liquefaction and disruption of an aquitard [Wang, 2007] see (Figure 6.6). This allowed the fluidized mud to inject into an incipient fault plane that set in motion the collapse of this metastable system. Slip on the fault facilitated hydraulic connectivity to a deeply rooted sediment-hosted hydrothermal system [Mazzini et al., 2007] that fed (and still feeds) the eruption with a substantial long-term fluid input. This scenario is supported by isotopic evidence of a significant mantle He fraction [Mazzini et al., 2012], high lithium concentrations and the observation that the well caved at a depth of 1275 m, consistent with calculated regions affected by the highest energy density and strain. Finally, large spatial scale liquefaction reconciles the long-known discrepancy between the site of the borehole and the first arrival of mud at five separate locations aligned with the Watukosek Fault between 200 and 1000 m from the well [Sawolo et al., 2009].

The behavior of the mud layer during the complex process of liquefaction [Ishihara et al., 1975; Tsukamoto et al., 2009] leads to two alternative scenarios, which can be simplified into two end-member states: compacting or dilating (Figure 6.6a). As fluid pressure increases with each loading cycle, compacting materials liquefy and flow when reaching the flow surface line (FSL). Dilatant materials strain-harden after reaching the FSL because dilatancy reduces pore pressure and flow is arrested. The liquefaction properties of the mud layer beneath Lusi are not known, but both behaviors have been observed in experiments on samples from various mud volcanoes [Yassir, 1989] and either behavior could have initiated Lusi. If the mud layer is compacting, then liquefaction reduced the shear strength to near zero and allowed the highly pressured and fluidized mud to inject into an incipient slip plane. If the mud layer is dilatant, flow would be limited from pore pressure reductions concomitant with dilatancy, but that same dilatancy would exsolve large quantities of CO_2 from the pore fluids when the fluid pressure reduced beneath its initial value to produce a mobile mud-fluid-gas mixture. CO_2 exsolution for Lusi was previously attributed to pressure reductions through flow into the fault zone, but this might also be appended to include large-scale CO_2 exsolution from dilatant liquefaction. In either case, cyclic loading from the Yogyakarta earthquake significantly increased pore pressure and loaded the system towards the FSL. High pore pressures were retained in the mud layer because of the very low permeability of the formation [Tanikawa et al., 2010] and when two powerful aftershocks renewed cyclic loading of this reduced impedance system, geometric amplification probably further liquefied the layer. This mechanism is also supported by drilling mud losses observed shortly after the Yogyakarta mainshock and the two powerful aftershocks. High strain rates in either compacting or dilating systems also substantially reduced the effective viscosity of the mud, thus making it more mobile [Mazzini et al., 2009].

Exonerating drilling as the primary trigger for Lusi requires an explanation for the observed mud loss and pressure kicks recorded at the borehole. Liquefaction of the mud layer would have drawn in drilling mud by either a complete loss of strength (compacting liquefaction), or by drawing in drilling mud from the dilatant volume increase and fluid pressure reduction of the mud layer (dilatant liquefaction). More than 21000 l of drilling mud were lost, translating into more than 200 m of mud column, or roughly 4 MPa assuming a mud loss depth of 1500 m. This significant pressure reduction allowed a

pressure pulse to propagate from deep in the borehole, perhaps from the overpressured carbonates, and through the borehole to provide the reported kick 26 hours after the earthquake. Hazardous drilling procedures [Tingay et al., 2008] and drawing fluids up (swabbing) when removing the drill string may have exacerbated the problem, but the borehole was responding only to liquefaction underway in the mud layer. Our results suggest that the borehole was a witness to, and not the perpetrator of, the initiation of Lusi.

The larger implication of our results is that most hydrothermal and volcanic systems host parabolic-shaped lithology with contrasting acoustic impedance [Paulatto et al., 2010] that can amplify incoming seismic energy [Davis et al., 2000]. If the energy focuses on fluid- or magma-rich reservoirs, substantial amplification of loading-unloading cycles can instigate or exacerbate proposed processes of rectified diffusion [Sturtevant et al., 1996], entrained gas exsolution, or liquefaction. Incoming seismic waves from distant earthquakes are reflected (refracted) by these parabolic seismic reflectors (refractors) that amplify and focus energy, thus triggering a response of the system that would have otherwise gone unperturbed. Because surface waves penetrate to depths that depend on the wavelength, this mechanism may apply to the recently observed correlation between Love wave stressing duration and long-distance earthquake triggering [Pollitz et al., 2012].

Our results indicate that Lusi is a natural disaster and a geological rarity of a newborn, tectonic-scale hydrothermal system. Lusi can thus be explored for deeper understanding of earthquake triggering, deep-rooted volcanic hydrogeology, degassing processes, reassessments of longevity and possibly a disaster-to-development opportunity through geothermal energy development and lithium mining of the deeply derived fluids.

Methods

The model is based on an interpreted two-dimensional seismic profile [Sawolo et al., 2009] and includes all of the relevant structures. The geological formations, their petrophysical properties and acoustic impedances are well constrained by the known density [Tanikawa et al., 2010] and P-wave velocity v_p [Istadi et al., 2009] (Figure 6.4b). We estimated shear wave velocities from the P-wave velocities by assuming bulk and shear moduli of 5.3 GPa and 30 GPa, respectively [Davies et al., 2008]. The detailed two-dimensional model (Figure 6.4c) measures 3.5 km$\times$ 2.5 km, with 21 geological layers and faults. The geometry was discretized into a rotated staggered finite-difference grid of 2.5×10^7 nodes with a grid spacing of 0.675 m. Periodic boundary conditions were applied along the sides of the model domain, a free surface at the top of the domain and a displacement boundary condition in the form of a plane wave was input at the bottom boundary. The amplitude of the incoming wave is constrained such that the average vertical displacement at the surface in the simulations is fixed at 1 mm to be consistent with the 1–2 mm vertical displacement observed at Lusi from the Yogyakarta earthquake [Davies et al., 2008; Nakano et al., 2006].

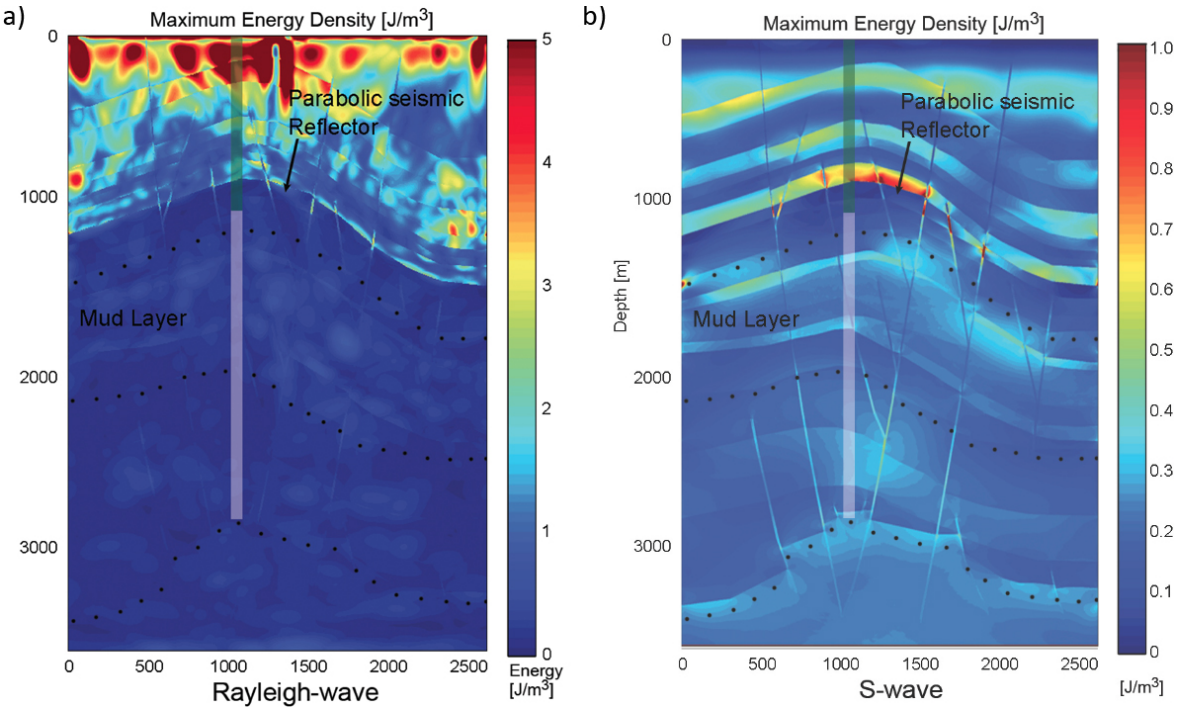

Figure 6.7: **a)** Numerical simulation results of Rayleigh-wave propagation. The Rayleigh-wave was input as a displacement boundary condition to the upper left side of the model domain. The high velocity layer shields the mud layer from any significant seismic energy. **b)** Maximum energy density for a 0.5 Hz plane S-wave applied at the bottom boundary. Focusing effects are reduced for frequencies below 1 Hz.

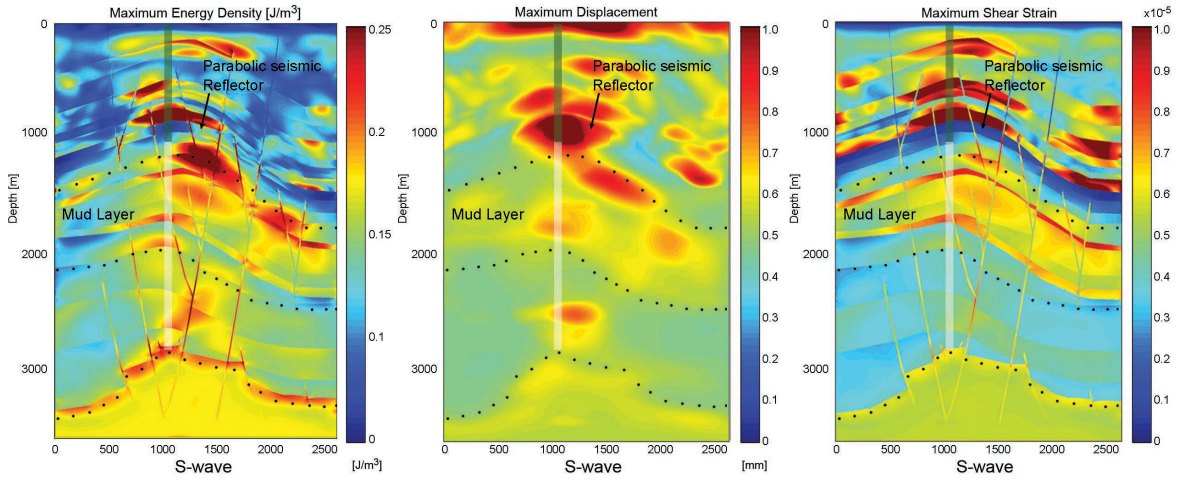

Figure 6.8: Results of the numerical study for a 1.0 Hz plane S-wave applied at the bottom boundary. Plotted from left to right os the maximum energy density, maximum shear strain, and maximum displacement, respectively. Focusing still occurs at 1 Hz but effects are reduced because the frequency dependence is controlled by the diameter of the seismic reflector relative to the wavelength. For the geometry of LUSI, this is about 1 Hz.

6.1.1 Ground motion analysis

One challenge within this study was to determine reliable input parameters such as ground displacement and seismic wave frequencies for the numerical simulation. Since no seismometers with digital data recordings were installed near Lusi at the time of the Yogyakarta earthquake, Davies et al. [2008] and Nakano et al. [2006] estimate the ground motion at Lusi by empirical attenuation relations to approximately 1–2 mm peak displacement. However, no information about the frequency content of the seismic waves at the site of Lusi is available. We used digital recordings of the station KRK of the BMG-Net operated by the Indonesian Agency for Meteorology, Climatology and Geophysics (see Figure 6.9). The station is 240 km far from the Yogyakarta epicenter, and thus approximately 30 km closer to the earthquake than Lusi. Station KRK is oriented at an back-azimuth of 98° from Yogyakarta as compared to 83° for Lusi. The waveforms in Figure 6.10 show the three component ground velocity recordings of the Yogyakarta earthquake at KRK station. Simulation results show that the focusing effect is reduced for seismic wave frequencies < 1 Hz so for determination of the ground motion we bandpass filtered the waveforms for frequencies in the 0.5–5 Hz range. In this range, the maximum ground motion is caused by S-waves (see horizontal components) with approximately 1 s period and and a peak ground velocity (PGV) of 1 mm/s. These values verify the 1 mm maximum surface displacement for 1 Hz body waves we used as input for the wave propagation simulation.

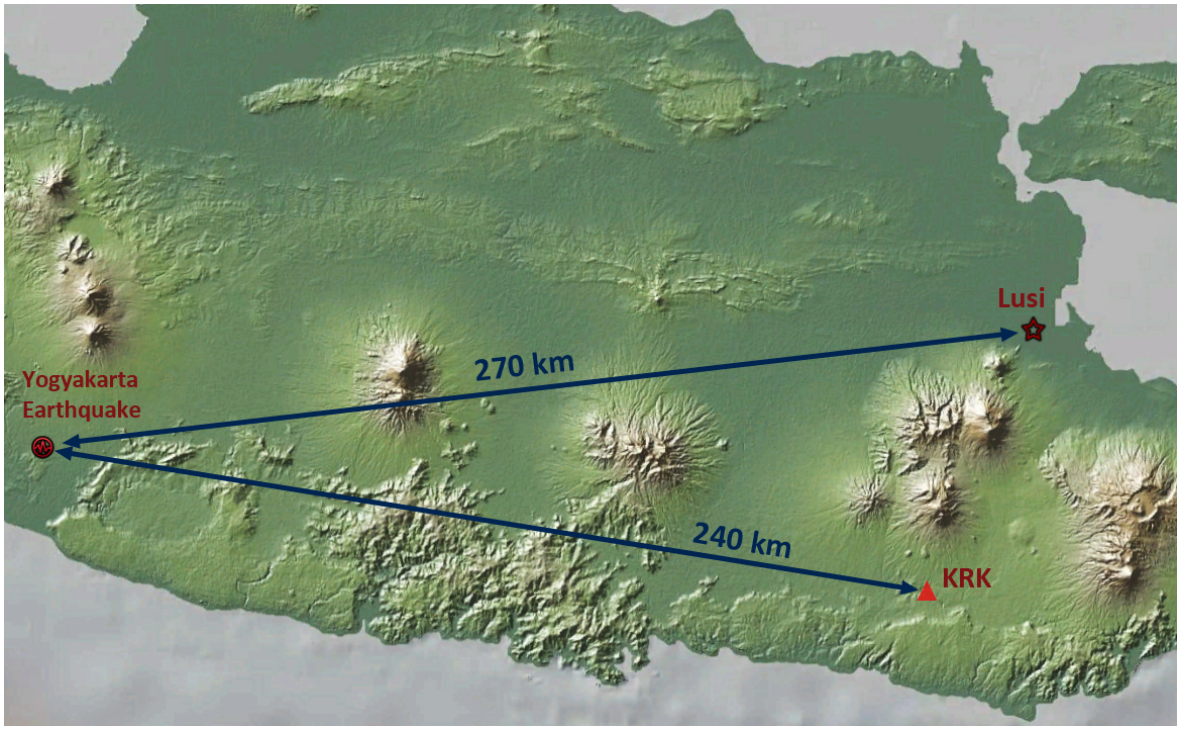

Figure 6.9: Distances of KRK seismic station and Lusi to the Yogyakarta epicenter.

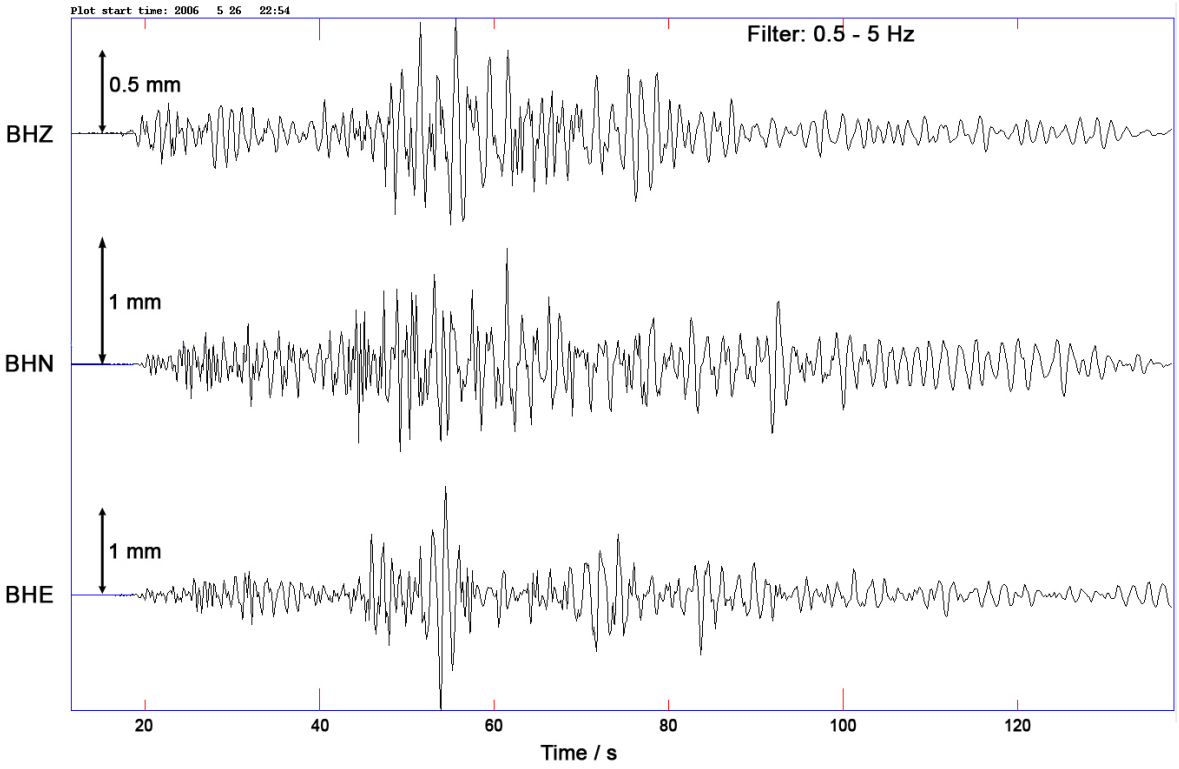

Figure 6.10: Waveforms of the Yogyakarta earthquake recorded on station KRK (240 km from Yogyakarta). The seismogram shows ground velocity and is filtered for frequencies between 0.5 – 5 Hz. S- waves with approximately 1 s period induced peak ground velocities (PGV) of about 1 mm/s.

6.1.2 Corrigendum

In the above section, we adopted a published velocity profile [Istadi et al., 2009] described as check-shot data, which we used as an input constraint for our numerical simulations. We were subsequently alerted to artifacts in that velocity profile, so below we present revised simulation results, based on additional data.

The seismic P-wave (v_p) and S-wave (v_s) velocity profiles measured in the BJP1 borehole (see Figure 6.12) show that the v_p profile extends from a depth of about 300 m to the bottom of the section. The S-wave and density profiles, however, were only determined from the depth of the casing (ca. 1100 m) to the bottom of the section. As we mentioned above, the system responds more vigorously to S-wave energy, but the critical information about the S-wave mechanical impedance (v_s multiplied by density ρ) for the first 1100 m of this section does not exist. Instead, we estimate an S-impedance profile above the mud layer by using the observed P-wave velocity profile and the observation that the S-wave velocity in the mud layer is as low as 380 m/s at 1100 m depth. This extremely low value reinforces what has been pointed out elsewhere [Istadi et al., 2009; Tanikawa et al., 2010], that the mud layer is a low-velocity zone representative of an over-pressured and under-consolidated sedimentary horizon. Such horizons are common throughout sedimentary basins in Southeast Asia.

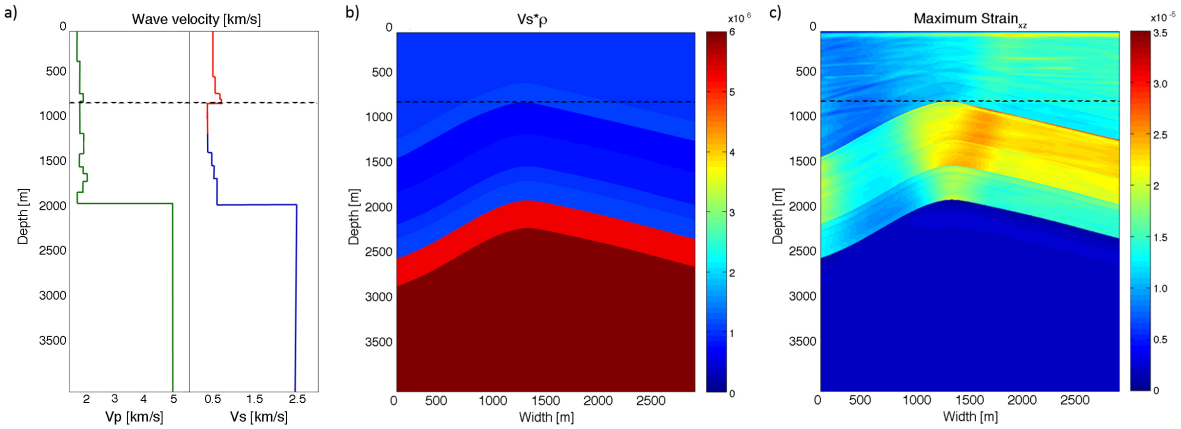

Figure 6.11: Revised numerical simulations. **a)** We estimate an S-wave velocity (red line) profile based on the measured P-wave (green line) and S-wave (blue line) velocity profiles. The model domain was discretized into 21 layers (with higher resolution for the first 2000 m) approximated from the measured and estimated profiles (Figures 6.12 and 6.13). Experimental data [Lee, 2010] suggest that v_s varies indirectly with v_p. That is, $v_p \sim A \times v_s$, where A varies depending on the shear modulus, pore pressure and effective pressure (Figure 6.13), hence v_s does not always correlate positively with v_p. The observation of v_p=2000 m/s directly above the mud layer (Figure 6.12b) implies from Figure 6.13 that v_s=750 m/s, while further observations of v_p=1600-1750 m/s in the mud layer are also consistent with the observation of v_s=380 m/s and v_p/v_s=4.5 in the mud layer (Figure 6.14). Therefore, there is little uncertainty about the magnitude of the impedance contrast, and small changes in these values will not significantly affect our results because the results scale with impedance contrast. **b)** We use the S-wave estimates (a) to construct an S-wave impedance profile. **c)** We use the S-wave impedance profile (b) in our numerical simulation, using the same input and boundary conditions as our original model simulation. The dashed line marks the top of the mud layer. The results from this simulation show that the inferred impedance contrast at Lusi is sufficient to focus seismic energy into the mud layer.

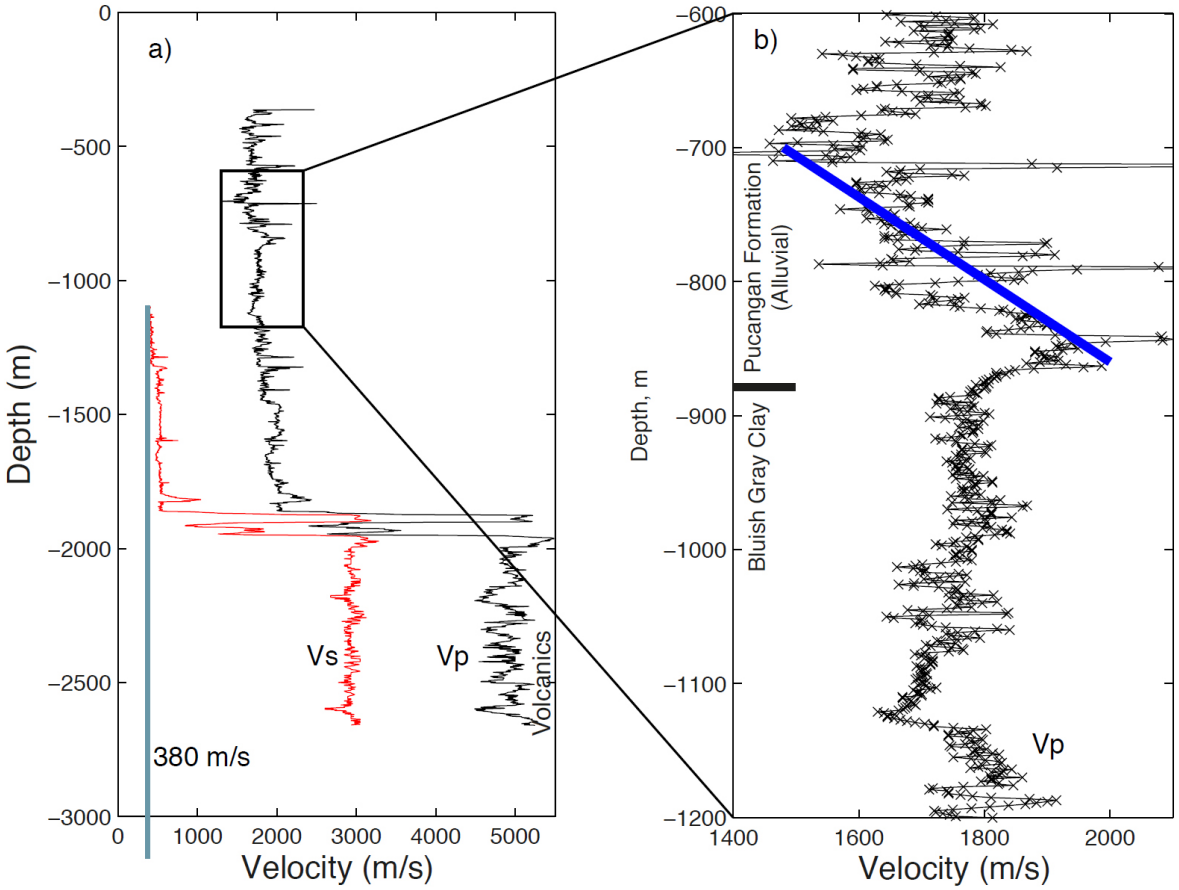

Figure 6.12: Measured v_p and v_s profiles (a) from the BJP-1 borehole. The v_p record extends to about 300 m depth, while the v_s record does not begin until the casing shoe at about 1100 m depth. Notice that v_s is about 380 m/s in the mud layer. A zoom-in of a portion of the record (b) shows increasing v_p with depth above the mud layer, between about 700 m and 875 m depth (blue line), indicative of a normally compacting horizon. A reduction in v_p at depths from 875 m to 1150 m indicates significantly reduced effective stress from the over-pressured and under-consolidated mud layer.

We estimate the S-wave velocity above the mud layer using experimental data (see Figure 6.13) showing the relationship between S-wave velocity and P-wave velocity, and v_p/v_s ratios, at low effective stress [Lee, 2010]. Although the P-wave velocity profile above the mud layer appears to not vary significantly (Figure 6.12a), a closer inspection (Figure 6.12b) shows that the P-wave velocity steadily increases just above the mud layer from about 1500 m/s to about 2000 m/s, between about 700 and 875 m depth. The steady increase in P-wave velocity with depth, typical of a normal compacting horizon, indicates lower fluid pressures relative to the fluid pressure in the underlying mud layer. We assume that the top of the mud layer corresponds to the observed drop in v_p at around 900m depth, which is consistent with the well log data. Using the recorded v_p constraint of 2000 m/s with a v_p/v_s ratio of about 2.7 (Figure 6.13), we estimate an S-wave velocity at the top boundary of the mud layer of about 750 m/s. We assume that the 380 m/s S-wave velocity recorded at 1100 m depth extends to the top of the mud layer because of the relatively constant and reduced P-wave velocity below

the compacting layer (Figure 6.12b). It should be emphasized that there is considerable uncertainty in v_s above the mud layer, but the observed reduction in v_p with depth (after a systematic increase of velocity with depth in the layer above) corresponds to a far greater reduction in v_s within the mud layer. Therefore, the interface between the mud layer and the compacting layer corresponds to an impedance contrast. This is evident in the elevated v_p/v_s ratios of about 4.5 within the mud layer (Figure 6.14), which again indicates low effective normal stress (Figure 6.13). At low effective stress, v_p and v_s are only weakly coupled whereby v_p remains relatively constant while v_s varies depending on the pore pressure. The effective stress dependence on v_p/v_s ratios occurs because v_s is solely dependent on the shear modulus while v_p is dominated by the bulk modulus. Since shear modulus varies strongly as a function of pore pressure, small changes in pore pressure at low effective stress generate large changes in v_s, with little influence on v_p. From the available experimental data in Figure 6.13, we can expect about a factor of two difference in v_p/v_s. Although the data [Lee, 2010] in Figure 6.13 are from a different lithology, the physics are lithology-independent.

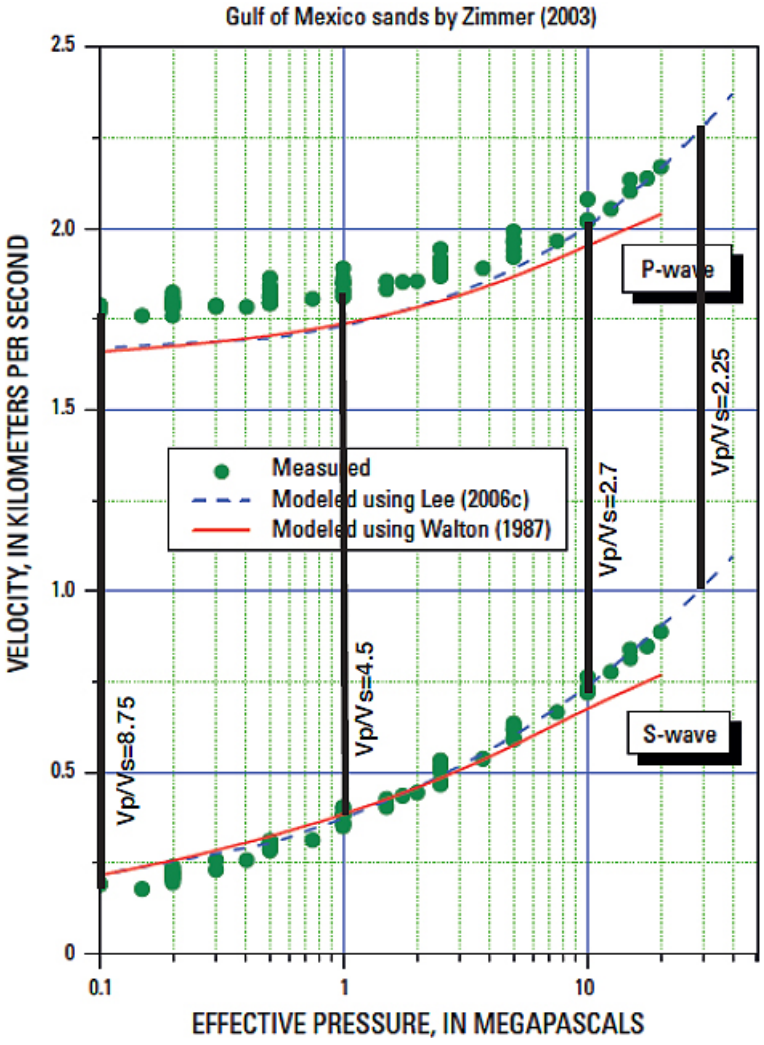

Figure 6.13: Experimental data showing large reductions in v_p/v_s ratios with increasing effective stress. We used the measured v_p of 2000 m/s at the top of the mud layer to estimate a v_s of about 750 m/s at this boundary. The recorded S-wave velocity of 380 m/s in the mud layer (v_p/v_s=4.5, Figure 6.14) indicates low effective stress representative of an under-consolidated and overpressured horizon, typically referred to as low-velocity zones. Modified from Lee [2010].

We multiply our estimated S-wave velocity profile (Figure 6.11a) with the measured density profile, using 1800 kg/m^3 where there is no data, to generate a new impedance profile (Figure 6.11b). We used this impedance profile as input for our numerical

simulation, using the same input and boundary conditions as described in the above section. For simplicity, the modeled faults in the previous simulations have been removed.

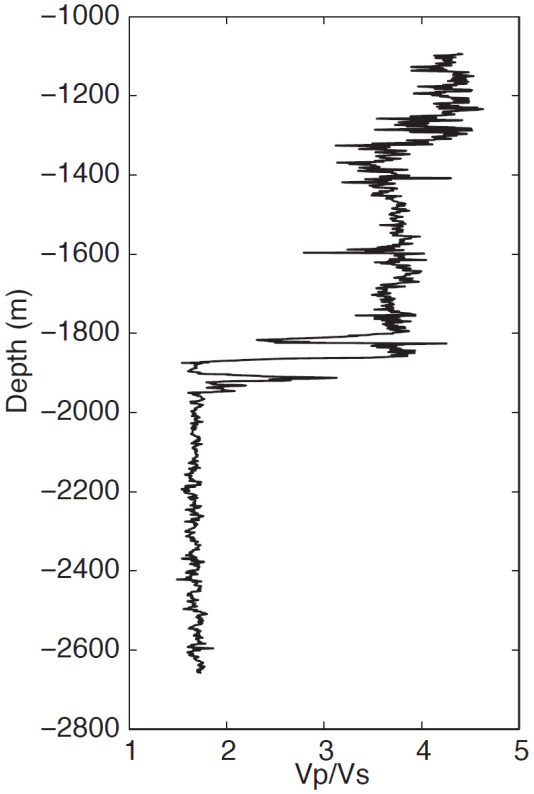

Figure 6.14: Measured v_p/v_s ratios showing persistently elevated ratios of about 4.5 within the mud layer indicative of a low effective stress (high pore pressure) environment.

The results from our revised simulations (Figure 6.11c) show that our estimated impedance contrast between the low-velocity mud layer and the compacting sediments above this layer produces a comparable focusing effect and maximum shear strain as the original simulations. Notably, our 2D simulations underestimate by a factor of five the additional amplification when the third dimension of this parabolic structure is considered [Davis, 2013]. The conclusions from Section 6.1 therefore remain unchanged.

6.1.3 Remarks

The Lusi mud eruption falls outside empirical magnitude-distance relationships established by Manga [2007]. However, studies of Delle Donne et al. [2010], Farias et al. [2014] and Hill and Prejean [2014] point out that simple magnitude to distance relations may not be suitable to capture the variety of earthquake induced activity on magmatic and mud volcanoes. To test distance relationships and to investigate earthquake mud-volcano interactions we deployed a Trillium 240s broadband seismometer on the Salse di Nirano mud volcanic field in Northern Italy. The mud volcanic complex experiences repeated shaking by aftershocks of the 2012 Emilia earthquake sequence and thus serving as a natural laboratory it allows to study the response of an active mud volcanic system to transient seismic waves. Section 6.2 presents first results from this study.

Whether or not the Lusi mud eruption was triggered by seismic wave induced liquefaction by geometric amplification may still be up for debate. Regardless, the results above present a new perspective on dynamic triggering by body waves in contrast to the common surface wave triggering of teleseismic earthquakes. The concept of seismic wave amplification by geometric focusing does not only apply to the case of Lusi. Since the dome shaped structure of the lithologies rather than a strong impedance contrast seems to be important for the focusing effect, we may have found a principle of relevance for body wave triggering in a variety of dome shaped lithologies. This could include focusing inside dome shaped magmatic volcanoes in general or more specifically focusing by the shape of the magma chamber. It may also apply to fluid filled caves or oil reservoirs. In general this could be an important aspect of dynamic triggering wherever intrusion or accumulation of material deforms the surrounding crust such that dome shaped lithologies are formed.

6.2 Seismic signals of the Salse di Nirano mud volcano

Figure 6.15: Salse di Nirano mud volcanic field near Modena, Northern Italy. The picture shows three of the four major mud extrusion locations where mud cones have formed.

The Nirano mud volcanic field Salse di Nirano is located south-west of Modena, Italy, and sits upon an anticline associated with the Pede-Apennines thrust [Bonini, 2008] (see Figure 6.16). The Nirano Mud volcanic Field responded to the Emilia seismic sequence [Manga and Bonini, 2012] that occurred in Northern Italy in May 2012, approximately

50 km distant from the Nirano mud volcanic field. To capture the response of the mud system to aftershocks of the Emilia sequence we deployed a Trillium 240s broadband seismometer in the Nirano mud volcanic field. The typical signal recorded by the seismic station consists of background noise below 2 s, sometimes interrupted by rhythmic high-frequency pulses that last from several minutes to hours. Each pulse lasts approximately 20 s and it is separated by intervals of low frequency noise lasting from 40 s to 180 s approximately (see Figure 6.17). We identify such a high frequency (drumbeat) signal irregularly throughout our dataset, with no distinction between day or night hours.

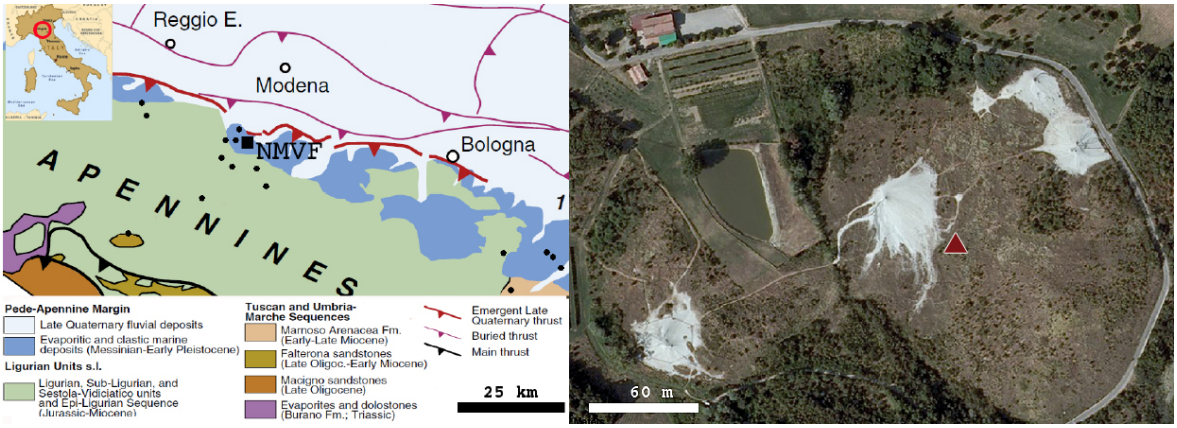

Figure 6.16: Geological map of the Pede-Apennine domain and aerial view of the Nirano mud volcanic field. Left: Black dots show the location of the mud extrusion occurring in the Pede-Apennine margin and the square points out the location of the Nirano mud volcanic field. The Pede-Apennine thrust is marked by the bold red line on the left [Tassi et al., 2012]. Right: Aerial view of the Nirano mud volcanic field showing the four main mud extrusion centers that form mud cones [Bing, 2014]. The red triangle marks the location of the seismometer.

Zoporowski and Miller [2009] simulated the drumbeat signal describing fluid expulsion from an underground reservoir through a conduit. The governing equations result in oscillatory behavior that is able to reproduce the drumbeat characteristics. However, the model of Zoporowski and Miller [2009] is a very simple one based on pressure build up and release only, disregarding any interplay between mud, gases and conduit geometry. The drumbeat signal that we observe may be associated to a slug flow similar to volcanic systems [Vergniolle and Jaupart, 1986] where deep fluids migrating through a high aspect ratio structure recharge the shallow mud-system. The slug flow maintains the pressure high enough to support mud volcanism and progressively reduces the fluid pressure at depth promoting the subsidence of the caldera.

We exclude any anthropic origin (i.e. factory- or pump-induced signal) due to the varying time window that separates each high-frequency peak throughout different pulsing events. In addition, the Salse di Nirano is a natural reserve and the closest (private) well would be more than 2 km far. The artificial lake located within the Nirano mud volcanic field did not use the pump when we identified the rhythmic signal.

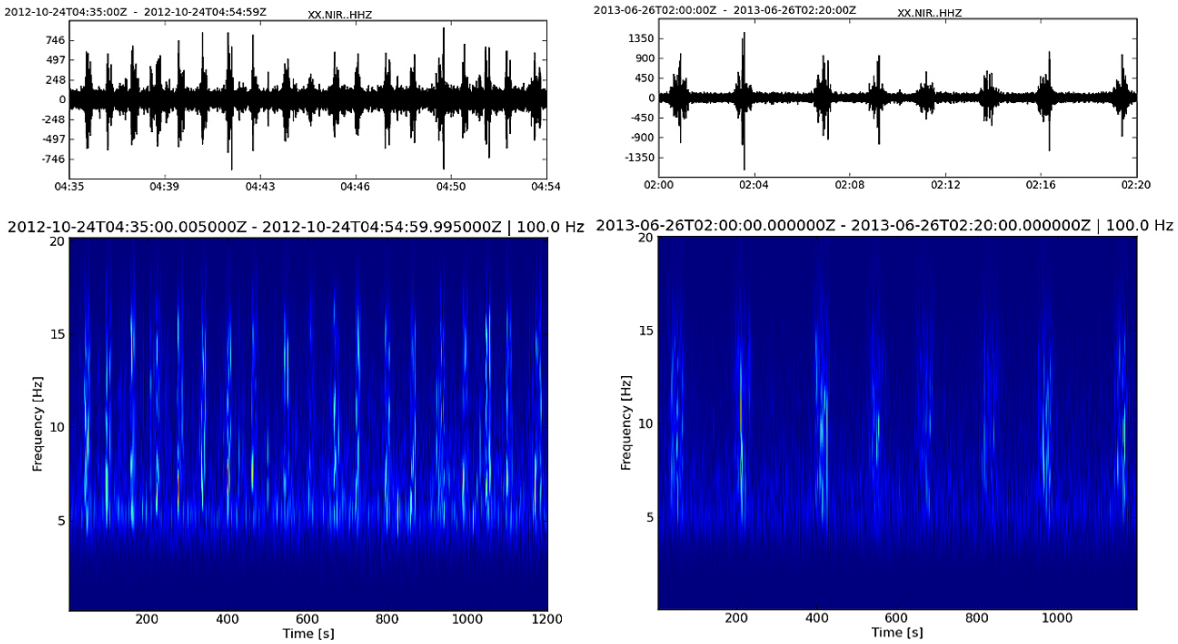

Figure 6.17: Drumbeat seismic signal and corresponding spectrogram recorded at Salse di Nirano on the 24th of October 2012 and 26th of June 2013. The signal of the vertical component was bandpassed between 5 Hz and 15 Hz and was present on each component.

7 Summary & Concluding remarks

This thesis compiles case studies of natural and triggered seismicity in volcanic and hydrothermal settings. During two seismic campaigns in the years 2011 and 2013 we discovered seismic activity beneath the Snæfellsjökull volcano in Western Iceland. In July–September 2011 we located 29 earthquakes with magnitudes $M_l < 1.1$ and frequencies in the 4–12 Hz range. Seismicity clusters closely around the Snæfellsjökull volcano at depths between 9–13 km. In May–October 2013 another 36 volcanic earthquakes ($M_l < 1.5$) were captured near the volcano at similar epicenters, depth and frequency content. The Snæfellsjökull was previously considered dormant and there are generally two possibilities to evaluate the volcanic seismicity at this volcano. The repeated occurrence of low-magnitude earthquakes may be due to magmatic fluids rising from depth and thus be a sign for increasing activity of the Snæfellsjökull. However, this conclusion is very speculative as there are no additional measures such as ground deformation that would supports this scenario. Additionally, although volcanism along the Snæfellsnes peninsula was active until 1050 BP the area should not be actively supplied with new magmatic material since it lies far from the Icelandic Plume or the Mid-Atlantic Ridge. Seismicity at the Snæfellsjökull may also be related to hydrothermal fluids circulating in the fracture network that likely surrounds the former magmatic plumbing system. Microseismicity at dormant volcanoes can also be the consequence of magma cooling inside the reservoir which leads to stress build-up [Hill et al., 2002] that releases in small earthquakes. Originally, the seismic campaigns on the Snæfellsnes were aiming to constrain potential faults [Sigurdsson, 1970] along the peninsula and investigate the unusual alignment of volcanic centers. The discovery of seismicity at Snæfellsjökull in 2011 changed the focus of the 2013 campaign to this volcano, yet future research on the Snæfellsnes should include the Lýsuhóll (or Helgrindur) and the Ljósufjöll volcanic complexes which are both elongated along the peninsula (see Figure 3.2). The installation of seismic networks on all three volcanic systems can yield information about the current state of volcanism along the entire Snæfellsnes and will allow to locate potential tectonic related earthquakes on the peninsula. Such project should be considered for future research as Snæfellsnes geology and volcanism remain unsolved topics in Icelandic geodynamics. Note that the installation of permanent seismic stations on the Snæfellsnes peninsula will also improve epicenter locations of events on the Mid-Atlantic Ridge, especially along the Reykjanes peninsula.

The Iceland studies reveal earthquake activity within resting volcanic complexes. There is compiling evidence [Hill and Prejean, 2014; Prejean and Hill, 2013] that resting volcanoes may be more susceptible to dynamic triggering by remote earthquakes as compared to those in an erupting phase. However, explanations for this behavior have yet to be found. This phenomenon may be related to closed conduits for the resting volcanoes (allowing for pressure build-up to near-critical conditions) in contrast to open

volcanic conduits during an ongoing eruption or active phase. Additionally, volcanic responses to earthquakes are often observed within the hydrothermal system rather than the magmatic part of the volcano [Farias et al., 2014; Prejean and Hill, 2013]. We did not observe any triggered activity on the Snæfellsjökull volcano which is likely because the volcano is not in a critical state and does not host a well-evolved hydrothermal system.

The Irazú-Turrialba volcanic complex in Central Costa Rica provides special conditions for dynamic triggering research as it consists of two neighboring volcanoes - the currently resting Irazú volcano and the Turrialba volcano that entered an erupting phase in 2010. After the 2012 M_w 7.6 Nicoya earthquake we observed a sudden increase in seismic activity on a fault near Irazú with more than 300 earthquakes within 36 hours after the passage of seismic waves from the 200 km distant Nicoya earthquake. Since events during this period predominantly fall onto a single fault plane we propose a combined mechanism of dynamic triggering and short-lived co-seismic relaxation to explain the elevated activity through fault reactivation. Interestingly, the response to the transient stresses is not within the active Turrialba volcano which adds to previous observations of triggered volcanic activity in systems at rest. Dynamic stresses induced by the M_w 7.6 Nicoya main shock are about 300 kPa and thus well above triggering thresholds in the low Kilopascal range that are reviewed by Hill and Prejean [2014]. It is, however, noteworthy that $\sim M_w$ 4.5 aftershocks of the Nicoya earthquake trigger a temporary increase on top of the Omori-like decay of seismicity. At 200 km distance such comparably low magnitude events are supposed to have negligible effects [Manga et al., 2009], yet our results indicate that such suggestions are wrong. Farias et al. [2014] (see Appendix) report similar triggered seismic activity in a hydrothermal system at the Nevados de Chillán volcanic complex in Central Chile after a 190 km distant M_w 6.1 earthquake, further suggesting that even low dynamic stresses may be capable of triggering at distances greater than suggested by Manga et al. [2009]. The issue of established magnitude-distance relationships for dynamic triggering will be further discussed below.

For the first time, we report triggered tectonic tremor along the Sunda Arc, Indonesia. The GEOFON seismic station PLAI recorded tremor signals triggered by surface waves from three teleseismic earthquakes with $M_w > 8.2$ in 2011 and 2012. Tremor was predominantly triggered by 45–63 s period Rayleigh waves and we establish an apparent triggering threshold of approximately 8 kPa which is in agreement with tremor observations elsewhere [Hill and Prejean, 2014]. Tremor could not be located, but may originate from the subducted plate at great depth [Fry et al., 2011] , from within the Tambora volcano as a results of low-frequency swarms [Obara, 2012] or from the Flores back-arc thrust located just north of Sumbawa. Tremor on the subducted slab or the Flores back-arc may be connected to slow-slip events, as observed on other subduction zones [Beroza and Ide, 2011]. Thus, our observations could be the first hint of slow-slip in the Sunda Arc and in particular the first report of tremor on a non-plate boundary back-arc thrust. In contrast to many observations where triggered tremor could be explained as clock-advanced Mohr-Coulomb slip by means of the Hill [2012b] triggering potential, tremor near Sumbawa is preferably triggered by Rayleigh waves, although the triggering potential of Love waves is higher. This suggests that high-pressure fluids are likely involved in the tremor generation at Sumbawa. However, any detailed analysis of

the triggering mechanism is obsolete until the tremor source is determined. Regions that show triggered tremor usually host ambient tremor as well [Chao et al., 2012a] and we therefore propose to install temporary networks of broadband seismometers on Sumbawa to search for both ambient and triggered tremor. Additionally, the dense Indonesian seismic BMG-Net may be utilized to detect and locate tectonic tremor near Sumbawa.

We performed a numerical wave propagation simulation study to evaluate the role of seismic waves in the triggering of the 2006 Lusi mudi eruption, Indonesia. Results indicate that the dome shaped lithologies with varying seismic impedance at depth can focus seismic energy. In case of the Lusi mud eruption, seismic energy was focused into a previously stable mud layer, leading to liquefaction and eventually resulting in the outburst of mud forming the Lusi eruption site. These results may not only explain the Lusi mud eruption but are also applicable to many other geologic settings that feature dome or parabolic shaped lithologies. When neighboring geologic layers of such formations show contrasting seismic impedance they can reflect and focus seismic energy so it reaches critical values for dynamic triggering. Still, the cause of the 2006 Lusi mud eruption is strongly debated. Davies et al. [2008] and Manga et al. [2009] favor a man-made drilling trigger and strongly refuse any natural impact on the Lusi mud eruption. A key argument is that Lusi falls outside an empirical magnitude-distance relation established by Manga [2007] and that claims 250 km to be too much of a distance for a magnitude M_w 6.3 earthquake to trigger a response in mud volcanoes. Many recent studies show, however, that magnitude-distance relations are oversimplifying the complex interaction of seismic waves and (mud-) volcanic systems.

Delle Donne et al. [2010] show that thermal anomalies can be induced at magmatic volcanoes by earthquakes much more distant or weaker than expected from Manga [2007]. Additionally, the work of Farias et al. [2014] (see Appendix) shows triggering effects of a Chilean M_w 6.1 earthquake at a volcanic complex 190 km away, thereby lowering the proposed magnitude-distance relation. Ultimately, the response of the Irazú volcano to $M_w \sim 4.5$ aftershocks at 160 km distance requires a reformulation of proposed magnitude-distance relations. In fact, it is common among earthquake and tremor triggering studies to establish parameters that may be key to the triggering mechanisms that go far beyond magnitude and distance [Hill and Prejean, 2014]. Indisputable, evaluation of the triggering capabilities of a given earthquake has to include ground motion. Ground motion (both displacement and ground velocity) have early been established as basic triggering parameters. Results from this work e.g. Nicoya aftershocks triggering temporarily elevated seismicity at Irazú volcano (Section 4.1), earthquake triggering in the Larderello-Travale geothermal field (Section 4.3), triggering of tectonic tremor on Sumbawa (Section 5.1) and the work of Farias et al. [2014] (Appendix) show that ground motion in the low Millimeter range can be sufficient for remote triggering. The respective dynamic stresses are as low as few Kilopascal in agreement with triggering thresholds reviewed by Hill and Prejean [2014]. Additionally, Hill [2012a] points out the importance of the incidence angle for remote triggering by dynamic Coulomb failure stress. Farias et al. [2014] highlight the role of particle motion during passage of seismic waves that may contribute to triggering. Surface wave periods and the triggering waves frequency content also seem to affect triggering,

although the effects vary among different regions worldwide [Hill and Prejean, 2014]. Thus, the question if a given earthquake may trigger a response at distance is far more complicated than can be captured in empirical magnitude-distance relations.

After 20 years of remote triggering research, many of the underlying mechanisms are still only vaguely known. Dynamic Coulomb failure as introduced in Chapter 2.3.1 has been successfully applied to many instances of dynamic earthquake and tremor triggering. It provides a reasonable explanation for both triggered earthquakes in near-critical conditions and triggered tremor as promoted slow-slip along the main slip direction on plate boundary faults such as the Cascadia and Nankai subduction zones [Enescu et al., 2012; Rubinstein et al., 2007]. However, when Rayleigh wave preferred triggering is observed - as we do for tremor near Sumbawa - the exact role of fluids and the dilatational stress components cannot be explained, yet. Earthquake-volcano interactions are still poorly understood. Mechanisms were proposed many years ago, such as rectified diffusion and advective overpressure, relaxing magma bodies, sinking crystal plumes, hydraulic surges, permeability pumping or fracture unclogging (see Section 2.3.2). However, attributing the variety of observed volcanic systems responding to seismic waves (eruptions, elevated seismicity, thermal anomalies) to a specific mechanism is complicated or speculative. Some highly idealized bubble based concepts such as advective overpressure and rectified diffusion do not hold under realistic parameters and natural conditions in volcanic areas. Since volcanic response to earthquakes is often observed within the hydrothermal system, fracture unclogging or hydraulic surges are promising candidates for dynamic earthquake-volcano interaction. They include delayed triggering and recharge time and may also apply to the earthquake triggering we observed at he Irazú-Turrialba complex and the Larderello-Travale geothermal field. Since one cannot probe the interior of volcanoes, laboratory experiments and numerical simulations may help to understand the applicability of proposed physical mechanisms to natural volcanic systems.

Volcanoes and earthquakes still pose threats to human population worldwide. Dynamic triggering studies may help to estimate seismic hazards by further understanding the earthquake cycle through tectonic tremor and by identifying near-critical conditions on faults through remotely triggered earthquakes. The interplay of Rayleigh waves and crustal fluids requires more research, especially to better understand earthquake-volcano interactions. A better understanding of remote triggering will help to describe the short-term processes that lead to slip nucleation and generation of earthquakes and thereby can potentially lead towards better techniques for earthquake prediction. Subduction zones repeatedly generate strong earthquakes which influence the neighboring volcanic arc. Research focusing on earthquake-volcano interaction will result in better knowledge of the conditions leading to triggered volcanic unrest and in the future may even allow to anticipate volcanic eruptions following large earthquakes.

Appendix

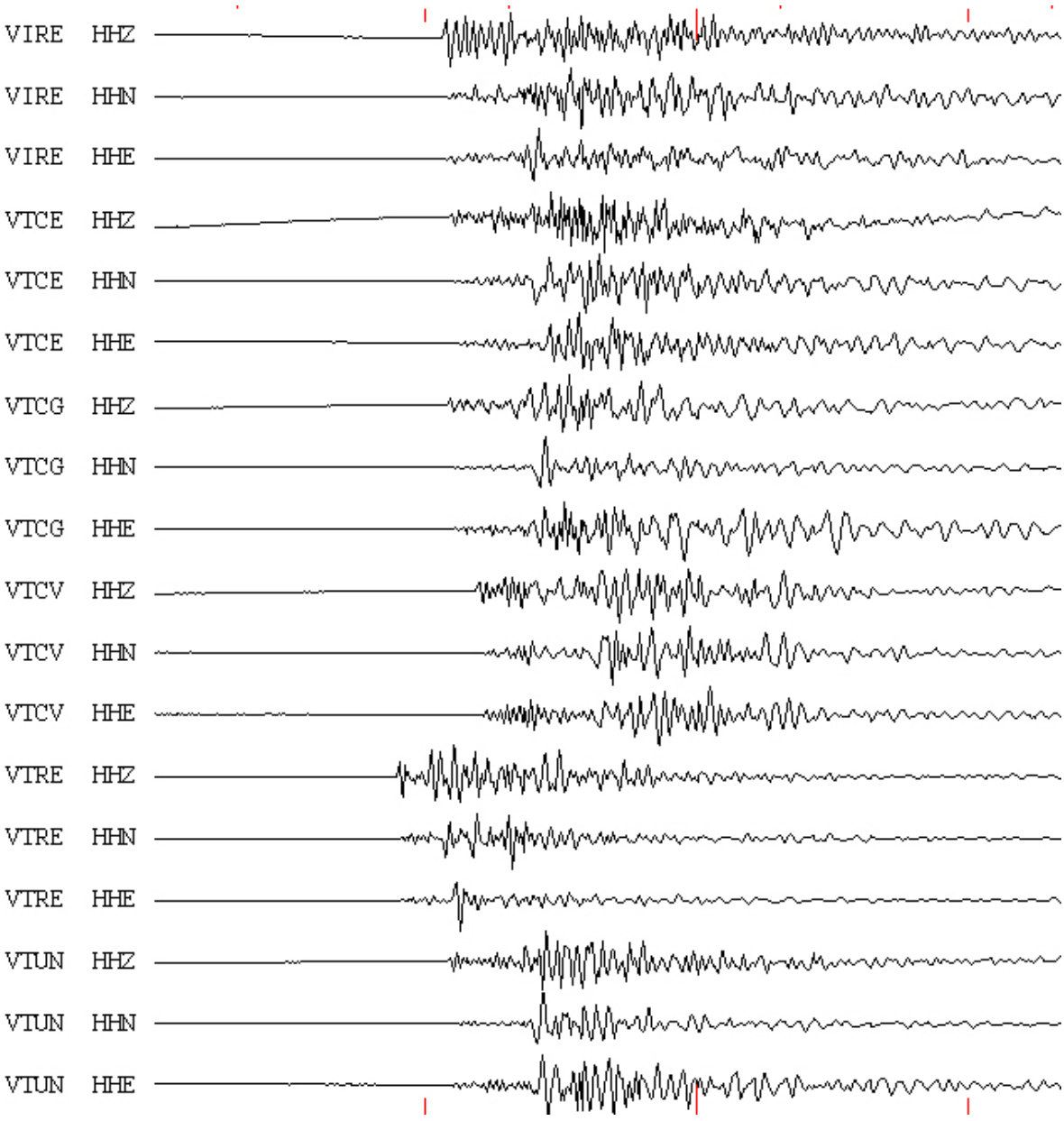

Figure A.1: Sample waveform of a volcano-tectonic earthquake within the earthquake sequence triggered at the Irazú-Turrialba volcanic complex, Costa Rica, by the 2012 M_w 7.6 Nicoya earthquake.

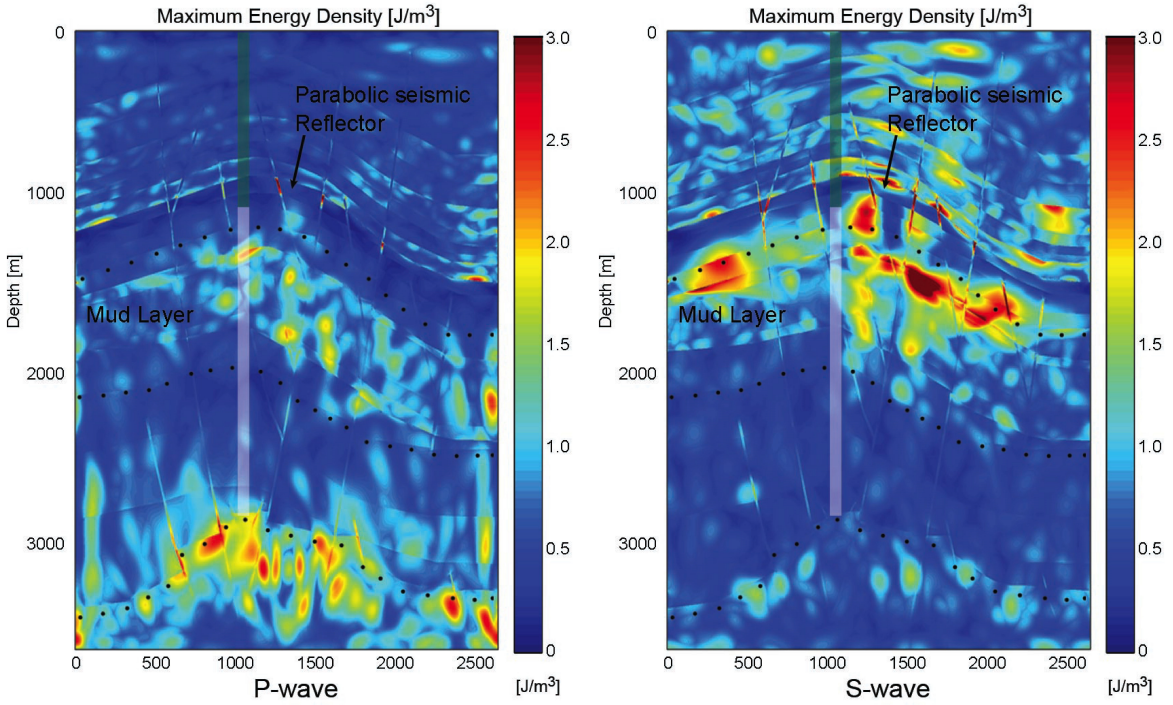

Figure A.2: Supplemental results for the Lusi mud eruption study (see Section 6.1). Maximum energy density for P-wave and S-waves arriving with an incidence angle of approximately 45° (non-planar source). The point source applied at the lower left corner of the computational domain in the vertical and horizontal directions approximates a P- and S-wave, respectively, producing a wave front that arrives at the overlying lithology at an incidence angle of approximately 45°. The focusing effect is maintained also for different incidence angles.

Date	Location Lat.–Lon. [°]	Err.Lt. [km]	Err.Ln. [km]	Depth [km]	Err.D. [km]	Mag. [M_l]
2013/06/12	64.789–23.391	0.9	1.6	19.4	0.8	–
2013/06/14	64.804–23.748	0.8	1.2	5.3	1.8	0.3
2013/06/16	64.699–23.633	1.7	2.4	19.1	1.1	1.1
2013/06/26	64.794–23.762	0.5	1.4	8.4	0.9	1.5
2013/06/29	64.808–23.763	0.0	1.1	9.8	0.0	0.9
2013/06/29	64.805–23.766	0.7	1.4	8.3	1.4	0.7
2013/07/02	64.792–23.753	0.8	1.2	7.6	1.3	0.7
2013/07/02	64.799–23.798	0.7	1.5	10.1	1.3	1.3
2013/07/02	64.791–23.777	0.8	1.0	14.2	0.8	1.5
2013/07/02	64.793–23.763	0.6	1.4	9.8	0.8	1.1
2013/07/03	64.795–23.790	0.6	1.1	10.5	0.9	0.4
2013/07/09	64.906–23.519	0.4	0.6	1.1	2.6	0.7
2013/07/12	64.797–23.774	1.0	1.9	9.2	1.7	1.0
2013/07/15	65.024–23.638	0.6	1.5	1.0	14.6	0.0
2013/07/15	64.744–23.121	1.8	2.1	29.3	1.3	1.1
2013/07/18	64.789–23.794	0.9	1.9	13.0	1.4	1.0
2013/07/18	64.782–23.825	1.2	1.3	15.2	1.0	0.7
2013/07/18	64.855–23.857	1.1	2.8	16.6	0.8	1.0
2013/07/21	64.811–23.780	0.3	1.0	1.0	3.3	0.9
2013/07/25	64.801–23.772	0.2	0.4	1.0	1.7	0.6
2013/07/28	64.785–23.787	0.7	1.6	12.2	1.3	0.6
2013/07/28	64.821–23.726	0.3	0.6	0.9	2.8	-0.2
2013/07/29	64.790–23.823	1.2	2.4	12.7	1.6	0.7
2013/08/01	64.837–23.811	0.6	1.6	18.8	0.5	1.1
2013/08/01	64.785–23.502	1.2	1.7	27.7	0.7	0.9
2013/08/01	64.739–23.688	1.3	2.1	7.9	1.6	–
2013/08/06	64.809–23.791	0.9	1.8	7.6	2.4	0.5
2013/08/12	64.821–23.752	0.7	2.0	10.7	1.3	0.9
2013/08/12	64.794–23.755	0.3	0.9	1.1	2.0	0.5
2013/08/17	64.754–23.842	2.7	0.6	12.1	0.7	0.5
2013/08/20	64.722–23.803	1.1	2.7	20.3	1.0	1.2
2013/08/25	64.796–23.778	0.5	1.1	6.9	1.1	1.2
2013/08/25	64.770–23.949	1.5	2.0	17.6	1.2	–
2013/09/09	64.796–23.700	0.2	0.9	1.1	2.1	1.3
2013/09/21	64.807–23.748	0.6	0.5	0.7	2.7	0.9
2013/09/23	64.798–23.786	0.3	0.6	5.5	0.9	0.8

Table A.1: List of earthquakes near Snæfellsjökull volcano, Iceland, in May–October 2013. Epicenter locations and errors are preliminary and may change upon future inspection. For some events no reliable magnitude could be determined.

Journal of Volcanology and Geothermal Research 283 (2014) 116–126

Contents lists available at ScienceDirect

Journal of Volcanology and Geothermal Research

journal homepage: www.elsevier.com/locate/jvolgeores

Seismic activity of the Nevados de Chillán volcanic complex after the 2010 Mw8.8 Maule, Chile, earthquake

Cristian Farías [a,*], Matteo Lupi [a,b], Florian Fuchs [a], Stephen A. Miller [a,c]

[a] Steinmann Institute Geophysics/Geodynamics, University of Bonn, Bonn, Germany
[b] Geological Institute, ETH, Zürich, Switzerland
[c] The Centre for Hydrogeology and Geothermics, University of Neuchatel, Neuchatel, Switzerland

ARTICLE INFO

Article history:
Received 30 August 2013
Accepted 24 June 2014
Available online 9 July 2014

Keywords:
Volcano
Seismicity
Earthquakes
Chile
Maule
Aftershocks

ABSTRACT

Couplings between large magnitude subduction zone earthquakes and the subsequent response of their respective volcanic arcs are generally accepted, but the mechanisms driving this coupling are not known. The 2010 Maule earthquake (Mw8.8) ruptured approximately 500 km along strike in the south-central part of Chile, and provides an opportunity to investigate earthquake–volcano interactions. In an exploratory campaign, we deployed four broadband seismometers atop and surrounding the Nevados de Chillán volcanic complex because it is located directly behind one of the two primary slip patches of the Maule Earthquake. The data recorded (from December 2011 to April 2012) shows significant seismic activity, characterized by numerous volcano tectonic events and tremor episodes occurring within the volcanic complex. We recorded two strong aftershocks of the Maule earthquake (Mw 6.1 in January 2012, and Mw 7.1 in April 2012) and investigated the response of the volcano to the incoming seismic energy. We find that volcanic tremor increased significantly upon arrival of the seismic waves from the Mw 6.1 event, which was then followed a few hours later by a significant increase in volcano-tectonic events when tremors subsided. This delay between tremor and volcano-tectonic events suggests that fluid and/or magma migration (manifested as tremor) readjusted the local stress state that then induced the volcano-tectonic events. The increased activity persisted during the subsequent two weeks. In contrast, the Mw 7.1 event, which occurred at a similar epicentral distance from the volcano, did not produce any significant seismic response of the volcanic complex. Analysis of the particle velocity records of the two events shows that the volcanic system was perturbed in different ways because of the incidence angle of the incoming energy, inducing a back-elliptical vertical and fault parallel motion for the Mw 6.1 and no clear directional dependence for the Mw 7.1. This suggests dilatation-induced fluid migration within the complex, and a kinematic mechanism of the perturbation rather than the perturbation amplitude. Our results demonstrate the importance for continued monitoring of the arc behind Maule, with an increased seismometer and GPS array density to determine the style of deformation currently occurring in the arc.

1. Introduction

The influence of large magnitude earthquakes on volcanic activity has been a long-standing topic in Earth sciences. Recent improvements of monitoring networks combined with accurate analyses of historical records may allow a better understanding of the mechanisms underlying earthquake–volcano interactions. Static and dynamic stress triggering have been proposed to explain why volcanic systems may react to remote earthquakes. However, the debate on the physical processes controlling such interaction is still on-going and large data sets are necessary to distinguish between existing ideas (Marzocchi et al., 2002; Eggert and Walter, 2009; Bebbington and Marzocchi, 2011).

Static and dynamic stress triggering operate at different time-scales and distances. Dynamic triggering is induced by immediate effects caused by the passage of seismic waves through a geological system at or near a critical state (Hill et al., 2002; Ichihara and Brodsky, 2006). Numerical studies suggest that the convex structure of folded and faulted geological layers in volcanic and hydrothermal systems can focus seismic energy enhancing local stress variations (Davis et al., 2000; Lupi et al., 2013). This affects the physical equilibrium of the system and promotes fluid pressure variations by suggested mechanisms of rectified diffusion (Brodsky et al., 1998), volatile exsolution (Sparks et al., 1977; Manga and Brodsky, 2006), and other manifestations of rising fluids (Hill et al., 2002). Dynamic stress triggering operates over short timescales (i.e. the immediate response to passing seismic waves), however, volcanic responses can occur up to several days after the earthquake because of the time required by the perturbed system to evolve. Brodsky and Prejean, (2005) and Hill (2008) show that dynamic stresses can

* Corresponding author. Tel.: +49 228 7360629.
E-mail address: cfarias@geo.uni-bonn.de (C. Farías).

http://dx.doi.org/10.1016/j.jvolgeores.2014.06.013
0377-0273/

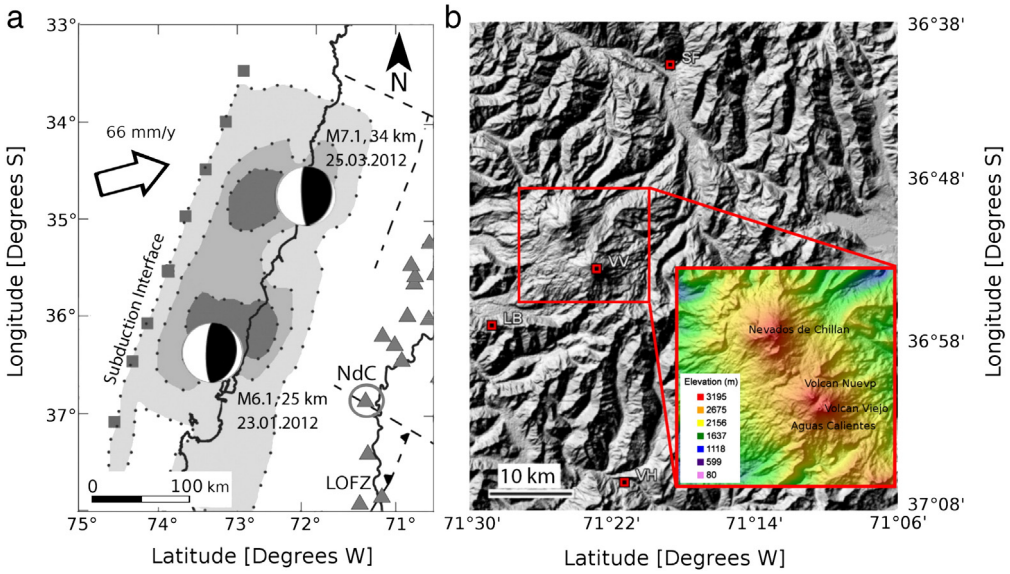

Fig. 1. a) Geodynamic setting of Chile between 33° and 38° and array distribution. The slip of the Maule earthquake is taken from USGS and dark gray indicates the maximum slip of 14 m which occurred at 35 km deep (Moreno et al., 2010). The southern and northern beach-balls mark the locations and focal mechanisms of the January 23rd, 2012, M6.1 and March 25th, 2012, M7.1 aftershocks, respectively. The northern portion of the Liquiñe–Ofqui fault zone (LOFZ) is also marked in the map. b) Topographic image of Nevados de Chillán volcanic complex. The red dotted squares indicate the location of the temporary stations and the inset shows the three main cones of the system. (For interpretation of the references to color in this figure legend, the reader is referred to the web version of this article.)

travel great distances as stress decays according to $1/R^{1.66}$, with R being the distance from the hypocenter. Heat flux variations (Harris and McNutt, 2007; Delle Donne et al., 2010), seismic swarms (Hill et al., 1995) and transient deformation Johnston et al., 1995 are among the most common effects induced by transient seismic waves in volcanic centers. Examples of volcanic activity triggered by dynamic stress fronts are the eruption of Cordón Caulle volcano, Chile, 38 h after the Mw9.5 Valdivia (1960) earthquake (Lara et al., 2004), swarming in the Long Valley Caldera, USA, few minutes after the Mw7.3 Landers (1992) earthquake (Hill et al., 1993), the increase of seismicity of the Uturuncu volcano, Bolivia, immediately after the arrival of the surface waves induced by the Mw8.8 Maule earthquake (Jay et al., 2011), and the sudden increase in volcano-tectonic (VT) seismic activity at Llaima volcano, Chile, after the Maule earthquake (Mora-Stock et al., 2012).

Table 1
Historic eruptions of NdC volcano and historic mega-thrust earthquakes that occurred within 500 km from the complex, since 1900 AD. Distance stands for the distance between the epicenter location and the NdC. the eruptive events always occurred at the Volcán Nuevo, except once (2nd of July 1935, Volcán Viejo). For several historical records both the exact date and the VEI of the eruption are not specified. Mega-thrust events are shaded in gray and under "eruptive characteristics" we list historic information about the eruptions: C stands for central emission, FV for flank vent emission, RF for radial fissure emission, E for explosive eruption, PF for pyroclastic flows, PH for phreatic eruption, LF for lava flow, D for dome creation, and MF for mud flow. Historic eruptions and mega-thrust events are taken from Siebert et al., (2012) and SSN (2013), respectively.

Date	Magnitude	Epicenter	Eruptive characteristics	Eruption VEI	Distance [km]
16.08.1906	8.2	Valparaíso	FV, E, LF, MF	2	420
–.–.1907	—	—	FV, E	1	—
29.01.1914	8.2	Constitución	E	2	250
–.–.1923	–	–	FV	2?	–
10.04.1927	–	–	E	2?	–
30.11.1928	8.2	Talca	FV, E	2?	210
17.01.1934	–	–	E	2?	–
02.07.1935	–	–	FV, LF, MF	2?	–
24.01.1939	8.2	Chillán	–	–	100
–.–.1945	–	–	–	–	–
–.–.1946	–	–	FV, E	2?	–
22.05.1960	9.5	Valdivia	–	–	350
–.–.1965	–	–	FV	–	–
–.–.1972	–	–	FV	–	–
–.07.1973	–	–	FV, E, PF, LF, D	2	–
03.03.1985	8.0	San Antonio	–	–	400
29.08.2003	–	–	C, RF, E, PH	1	–
21.01.2009	–	–	–	–	–
27.02.2010	8.8	Maule region	–	–	140

Static stress triggering mechanisms are proposed to explain marked increases of volcanic activity over longer time-scales (from months to decades). Static stress variations promoted by large magnitude earthquakes decay according to $1/R^3$ and are proposed to be caused by the post-seismic viscoelastic relaxation of the upper lithosphere (Walter and Amelung, 2007), or intermediate timescale changes in local kinematics (Lupi and Miller, 2014). Additionally, upwelling of deep fluids following mega-thrust earthquakes may be favored due to reduced normal stresses exerted on the volcanic plumbing system and that may modify the physical state of magmatic reservoirs. A new mechanism (Lupi and Miller, 2014) to explain the post-seismic increase of eruptive rates proposes that reductions of the horizontal principle stress ($\sigma_1 = \sigma_H$) induced by mega-thrust earthquake transforms the stress regime from a compressional environment to a strike slip faulting regime in the arc, which in turn favors the mobilization of magmas. This is in agreement with recent findings that show the coexistence of compressional and transpressional tectonic regimes over long time-scales in the Suban basin, Sumatra (Hennings et al., 2012), and with seismic activity occurring in volcanic arcs residing atop subduction zones recently affected by mega-thrust earthquakes (i.e. Sumatra, Chile, and Japan). The Mw9.5 Valdivia (1960) earthquake and its fore- and after-shocks (four foreshocks greater than Mw7.0, including a Mw7.9) induced large static stress variations in the volcanic arc. The geomechanical perturbation of this megathrust event may have induced the eruptions of Cordon Caulle and Copahue in 1960, Nevados de Chillan in 1965, and possibly Quizapu and Planchon Peteroa volcanoes in 1967. Static stress variations may last for decades as shown by cGPS measurements that indicate that the back-arc facing the 1960 Valdivia rupture zone is currently dominated by westwards displacements (Khazaradze et al., 2002; Brooks et al., 2011).

Central Chile is an ideal natural laboratory for investigating subduction zone earthquakes and the subsequent response of volcanic

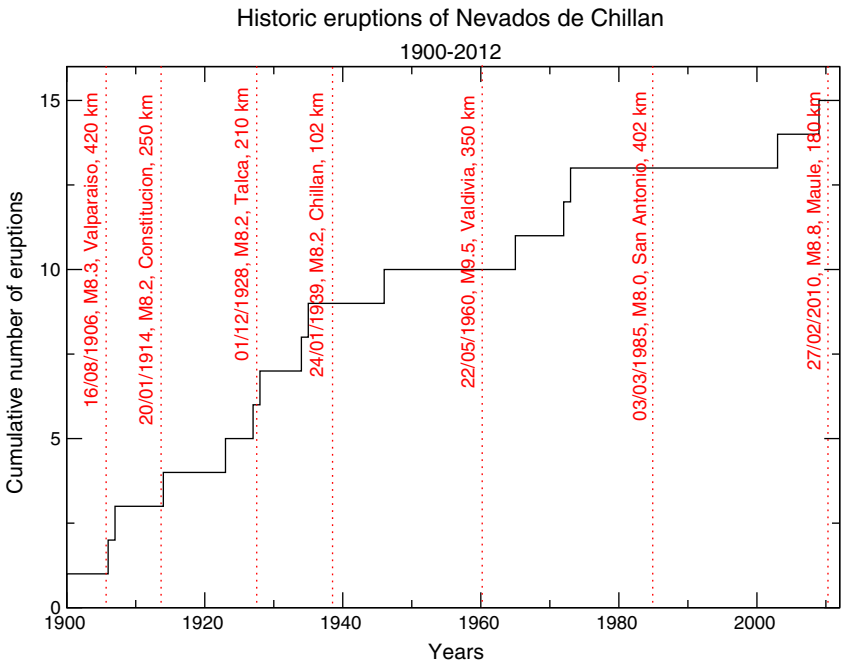

Fig. 2. Cumulative number of eruptions of Nevados de Chillán volcanic complex and mega-thrust events since 1900. Dotted vertical lines indicate mega-thrust earthquakes whose hypocenter was located less than 500 km from the volcano. Details on date, magnitude, and epicenter–volcano distance are shown in the vertical sentences. More information about eruptive behaviors can be found in Table 1. Note that the historic earthquake records may be affected by non systematic reporting.

arc because of the 2010 Mw 8.8 Maule earthquake and its rich aftershock sequence (including events as large as Mw 7.1). The area is extremely remote and rugged, and thus complicates the logistics of instrumentation, but this also offers a low-noise environment for seismic studies. It was observed in September 2010 that a Ml 5.2 earthquake at Planchón-Peteroa volcano was followed few hours later by a volcanic eruption, and our goal was to search for a similar behavior around the Nevados de Chillán volcano. We chose the Nevados de Chillán complex because it resides directly behind the high slip patch of the Maule earthquake, and has a geometrically intriguing feature of striking NW–SE that may be in part controlled by post-megathrust kinematics. In an exploratory campaign, we deployed four broadband stations from December 2011 to April 2012 around the Nevados de Chillán volcano, and recorded numerous volcano tectonic (VT) events, volcanic tremor, and background activity. We also recorded the response of the complex to two distant Maule aftershocks (Mw 6.1 at 192 km distance and Mw 7.1 at 200 km distance), and found different reactions of the volcano complex. The observed behavior provides insights into the mechanisms driving the triggered response of the volcano plumbing system.

Table 2
1. D velocity model used for NdC, with v_p and v_s being P-wave and S-wave velocities, respectively. This model is based on the work of Bohm et al. (2002) and it is currently in use by the Volcanologic Observatory of the Southern Andes (OVDAS, in Spanish) in Chile.

Depth [km]	v_p [km/s]	v_p/v_s
0	5.51	1.75
5	6.28	1.75
20	6.89	1.75
35	7.40	1.75
45	7.76	1.75
55	7.94	1.75
90	8.34	1.75

2. Geodynamic and geological setting of Central Chile

The tectonic setting of Chile from 33°S to 47°S is characterized by the oblique subduction of the Nazca plate underneath the South American plate (Fig. 1a).

Plate convergence of approximately 66 mm yr^{-1}, is accommodated by large-magnitude earthquakes along the length of the collision zone, and arc volcanism is ubiquitous. The most prominent geological feature of this part of Chile is the NNE–SSW striking Liquiñe–Ofqui fault, a right-lateral transpressional fault zone running from 38°S to 47°S. Monogenetic cones and basaltic to andesitic volcanoes (i.e. Villarrica, Llaima and Osorno) reside upon the Liquiñe–Ofqui fault, while more evolved volcanic systems (i.e. Nevados de Chillán and Copahue) reside along NW–SE striking lineaments, antithetic to the direction of the arc (Cembrano, 1992, 1996; Lavenu and Cembrano, 1999; Cembrano et al., 2000; Lange et al., 2008; Cembrano and Lara, 2009). Morphological evidence shows that the Liquiñe–Ofqui fault terminates approximately near the Copahue volcano (38°S) (Cembrano and Lara, 2009), but strike-slip moment tensor solutions of shallow seismic activity following the Maule earthquake document that strain partitioning extends in the arc also between 33°S and 38°S (Lupi and Miller, 2014). Nakamura (1977) suggests that the large scale distribution of volcanoes and their elongation can provide insights into the stress orientation at the regional scale. Lupi and Miller (2014) propose a 'bookshelf' mechanism to explain the occurrence of NW–SE trending lineaments across the Chilean and Argentinean border.

Table 3
Location of the four seismic stations deployed around Nevados de Chillán volcanic complex.

Location	Station	Latitude	Longitude	Elevation [m]
Las Bravas	LB	36.926 S	71.501 W	1799
Valle Hermoso	VH	37.078 S	71.340 W	1217
San Fabián	SF	36.670 S	71.287 W	824
Volcán Viejo	VV	36.872 S	71.370 W	3118

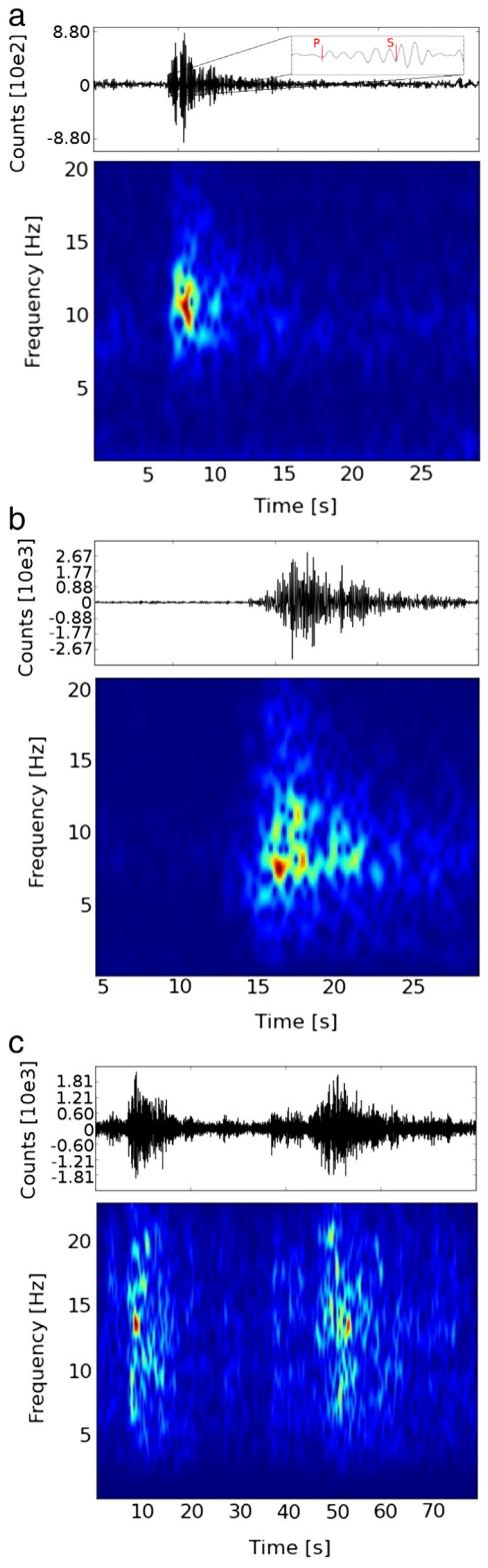

Fig. 3. Volcano tectonic events at the Nevados de Chillán. a) Deep VT, with an inlet with P- and S-wave arrivals marked in red, b) shallow VT, and c) high frequency swarm events found in the dataset for Nevados de Chillán from December 26th, 2011, to February 5th, 2012. (For interpretation of the references to color in this figure legend, the reader is referred to the web version of this article.)

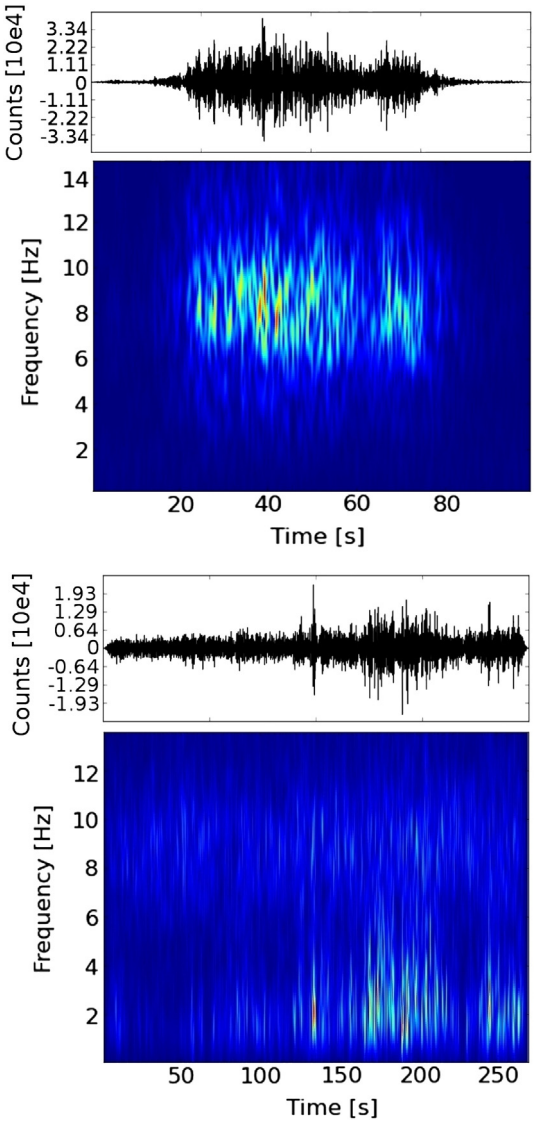

Fig. 4. Trace and spectrogram of tremor events. a) High frequency tremor event found throughout the normal activity of the volcano. b) Spasmodic volcanic tremor found in NdC complex after the swarm occurring on the 5th of January 2012.

Nevados de Chillán experienced significant static stress changes induced by the Maule earthquake (Lupi and Miller, 2014), which was one reason for choosing this site for investigation. Additionally, Dzierma and Wehrmann (2010) studied the (pre-Maule) probability of a VEI ≥ 2 eruption within the next ten years for ten Chilean volcanoes located between 33°S and 42°S. Their analyses showed that Llaima, Villarrica, and Nevados de Chillán volcanoes are the most likely candidates to erupt, followed by Puyehue and Calbuco volcanoes. From hereafter we will refer to the Nevados de Chillán volcanic complex as NdC.

The NdC volcanic complex (Fig. 1b) consists of 24 cones distributed along a 12 km long lineament striking approximately N290 (Fig. 1b) (Gonzalez-Ferrán, 1995). Volcán Nuevo, Volcán Viejo and Volcán Nevados are the three main volcanic centers. Volcán Nuevo resulted from the 1906 eruption that occurred immediately after the 1906 Valparaíso earthquake. Table 1 provides detailed information about the location of mega-thrust epicenters and the occurrence of volcanic activity at NdC. Due to the recent explosive activity of the Volcán Nuevo and to the rapid development of tourism in the area, the NdC is considered a high-risk volcano.

Fig. 2 shows the cumulative number of eruptions of the NdC during the past century and the occurrence of mega-thrust earthquakes nearby the NdC. Since the recorded VEI of many eruptions is similar, as showed in Table 1 the comparison of both time series can show interesting insights. It emerges that from 1900 to 1940 the volcano appeared more sensitive to external perturbations than in present the time, and only in three cases (1906, 1914, and 1928) the volcano entered in an eruptive

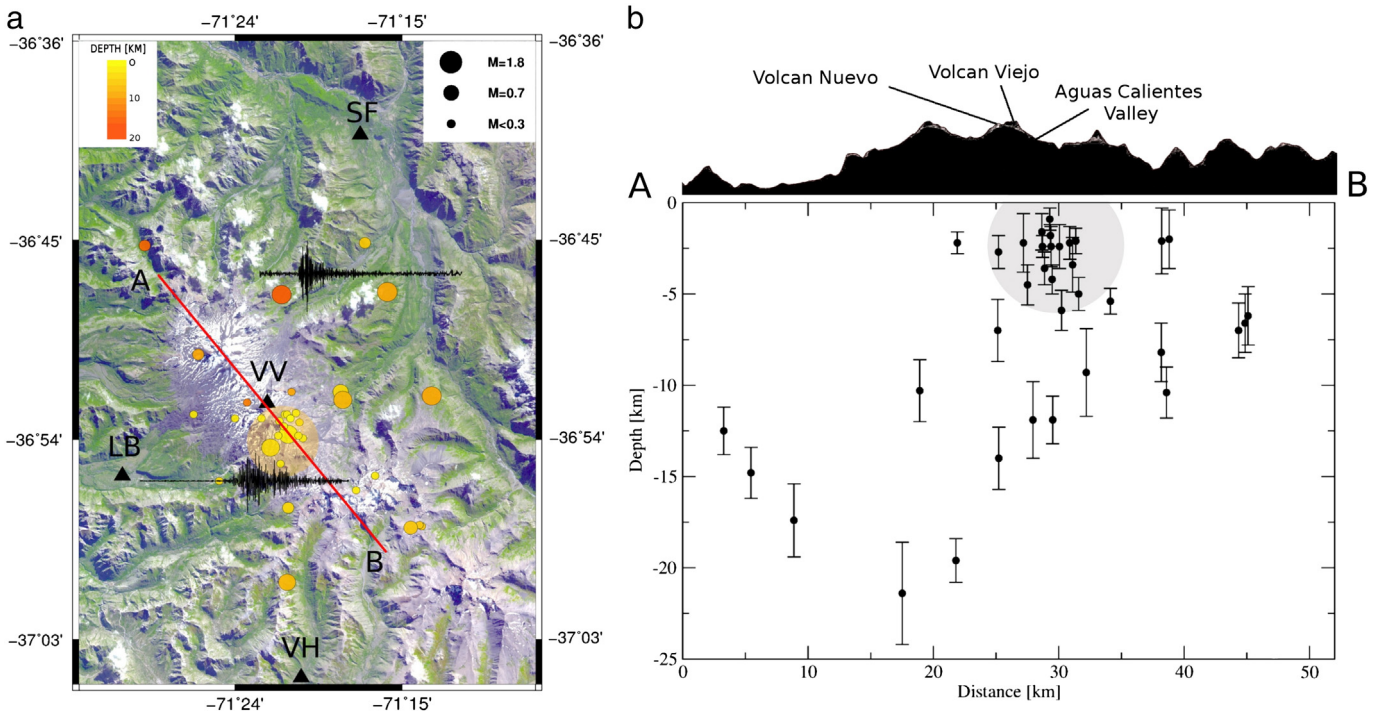

Fig. 5. a) Epicenter map of the seismic events within the Nevados de Chillán volcanic complex. Stations are marked as black triangles. Typical signals for shallow and deep VT events are drawn next to the location of the respective type of event. Note the difference of the waveform for both deep and shallow events. The orange circle marks the region where the non-locatable shallow events may be located. b) Locations of the events, from the perspective of the transverse cut marked by the red line in a), with A and B being the same points marked there. The error bars indicate the uncertainty of the locations in the vertical direction. Due to the geometry of the array, some extra uncertainty should be added in the left–right component of the locations in the cross section. The gray area is the projection along the line and the vertical direction of the yellow circle in a). Notice how most of the shallower events are located beneath the Aguas Calientes valley. (For interpretation of the references to color in this figure legend, the reader is referred to the web version of this article.)

phase almost immediately after the occurrence of a mega-thrust earthquake.

3. Seismic network and methods

We deployed four Trillium 240 broadband seismometers equipped with Reftek130 data loggers around and atop the NdC complex from December 2011 to April 2012. Data were continuously recorded at a sampling rate of 100 Hz. We used a STA/LTA triggering algorithm (Withers et al., 1998) to mark the events, which we inspected manually to determine P- and S-wave arrivals. We used SEISAN (Ottemöller et al., 2011) and the 1D velocity model reported in Table 2. Our temporary network consisted of one station (VV) atop the NdC volcano surrounded by three stations (LB, VH, and SF) (Fig. 1) approximately 20 km from VV station (Table 3). Sporadic technical problems resulted in some discontinuity in our dataset. The time window presented here (from December 26th, 2011 to February 5th, 2012) is continuous. Our array is the first ever to be used to study the NdC complex, but accessibility in this remote region resulted in a non-optimal geometry. Nevertheless, epicenter locations are well constrained north–south, but accuracy is limited in the east–west direction.

4. Results

We registered many different events during our experiment, with the vast majority recorded by station VV only and identified as volcano-tectonic (VT) earthquakes (McNutt, 2005; Wassermann, 2012), (Fig. 3), and tremor events (Fig. 4). In the first case, waveforms were 10 to 40 S long, with frequency content higher than 5 Hz. Among this type of event we defined three sub-categories: i) Events

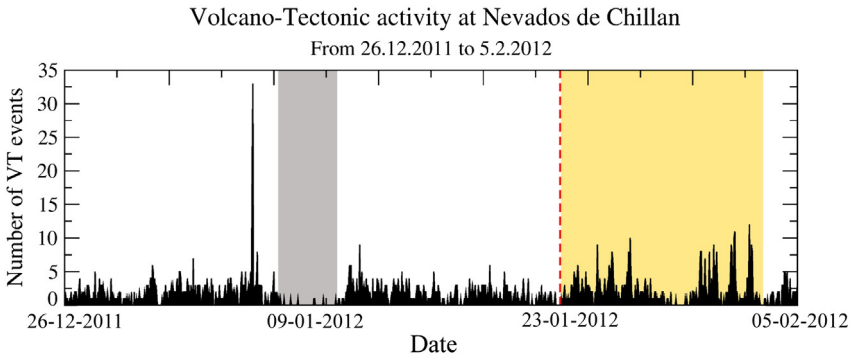

Fig. 6. Seismicity at Nevados de Chillán from December 26th, 2011, to February 5th, 2012. Gray and orange bands show periods of strong background tremor and triggered seismicity after a M6.1 regional earthquake, respectively. (For interpretation of the references to color in this figure legend, the reader is referred to the web version of this article.)

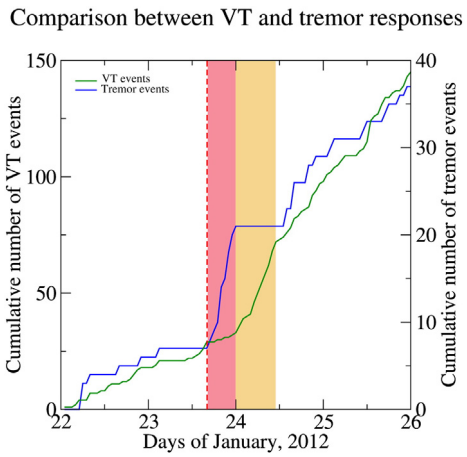

Fig. 7. Number of VT events per hour on Nevados de Chillán volcano before and after the M6.1 aftershock. The vertical dashed line marks the occurrence of the M6.1 and the red-shaded region highlights a strong increase of tremor events after the M6.1 earthquake. Next, tremor subsides and the number of VT events strongly increase (yellow-shaded area). (For interpretation of the references to color in this figure legend, the reader is referred to the web version of this article.)

characterized by clear P- and S-wave onsets, with a dominant band around 8 Hz. Our network allowed us to manually locate approximately 50 earthquakes, with magnitudes ranging from Ml 0.1 to Ml 1.8 and depths from 0.1 km to 30 km; ii) events lacking of a clear S-wave onset, with a lower frequency band, typically around 6 Hz, which are shallow VT events according to the literature (Wassermann, 2012); iii) swarm events dominated by frequencies from 13 to 15 Hz (Fig. 3), which occurred between 16:00 UTC and 19:00 UTC of January 5th, 2012.

Tremor events last approximately 60 S and can also be separated into two sub-categories according to the shapes of the waveform and their occurrence patterns. The most common tremor was characterized by an excitement of the 8 Hz band, and was recorded by station VV only. Similar events were recognized by Leet (1991) who described them as composite hydrothermal-magmatic tremor. Another possible source for this type of event is the superposition of several very shallow VT events. The second type of tremor occurred only between January 6th and January 8th, 20 h after the high frequency VT swarm (spike of Fig. 6). These signals were recorded by VV, LB, SF, and VH stations and were marked by clusters of high-amplitude signal dominated by 2 and 8 Hz frequencies (Fig. 4b).

4.1. Seismic activity

Fig. 5 shows the distribution of seismic events around the NdC. The NW–SE cross-section across the volcanic edifice shows that seismic activity clusters beneath the south-eastern flank of the cone Volcán Viejo, and more specifically below the Aguas Calientes valley, which is an area characterized by fumarolic activity and hot springs. We could not locate several VT events because they did not appear in all the stations of our array, and most of them were only registered by VV station. However, due to the lack of a clear S-wave onset in most of them, and the short time between the arrival of P and S-waves (generally separated by less than a second), it is likely that these events were originated at shallow depths, in the surrounding of Volcán Viejo cone (see shaded areas of Fig. 5). Deeper events are more dispersed and range from 10 to 25 km deep and fall outside the volcanic complex. Magnitudes of the shallow events range between Ml 0.1 to Ml 0.8 while the deeper events have somewhat larger magnitudes (the largest being a Ml 1.8 earthquake).

Fig. 6 shows the number of VT events per hour recorded at station VV from December 26th, 2011, through February 5th, 2012. The peak on the left-hand side of the chart highlights a seismic swarm that occurred on January 5th, 2012 at 17:00 UTC, and lasted for 2.5 h. During this interval VT events are marked by a higher frequency content (see Fig. 3c), with a dominant band around 13–15 Hz, and with a remarkably shorter coda compared to other VT earthquakes recorded during our seismic campaign. Twenty hours after this swarm, the VT event rate decreased down to approximately one event per hour and continuous tremor marked by clusters of high-amplitudes emerged.

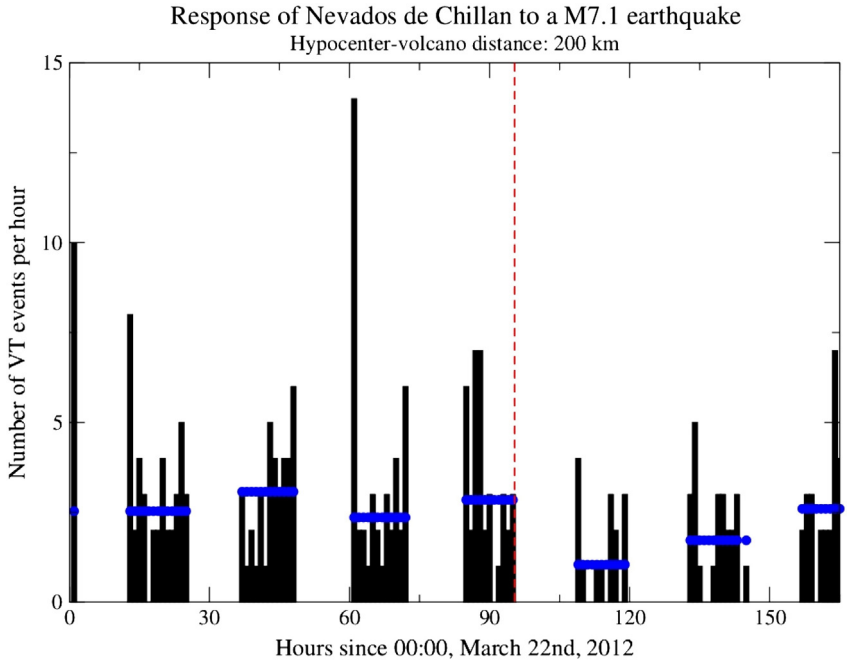

Fig. 8. Number of VT events per hour occurring at the Nevados de Chillán volcano before and after the M7.1 aftershock. The vertical dashed line marks the occurrence of the M6.1 and blue lines mark the average number of VT events per hour. (For interpretation of the references to color in this figure legend, the reader is referred to the web version of this article.)

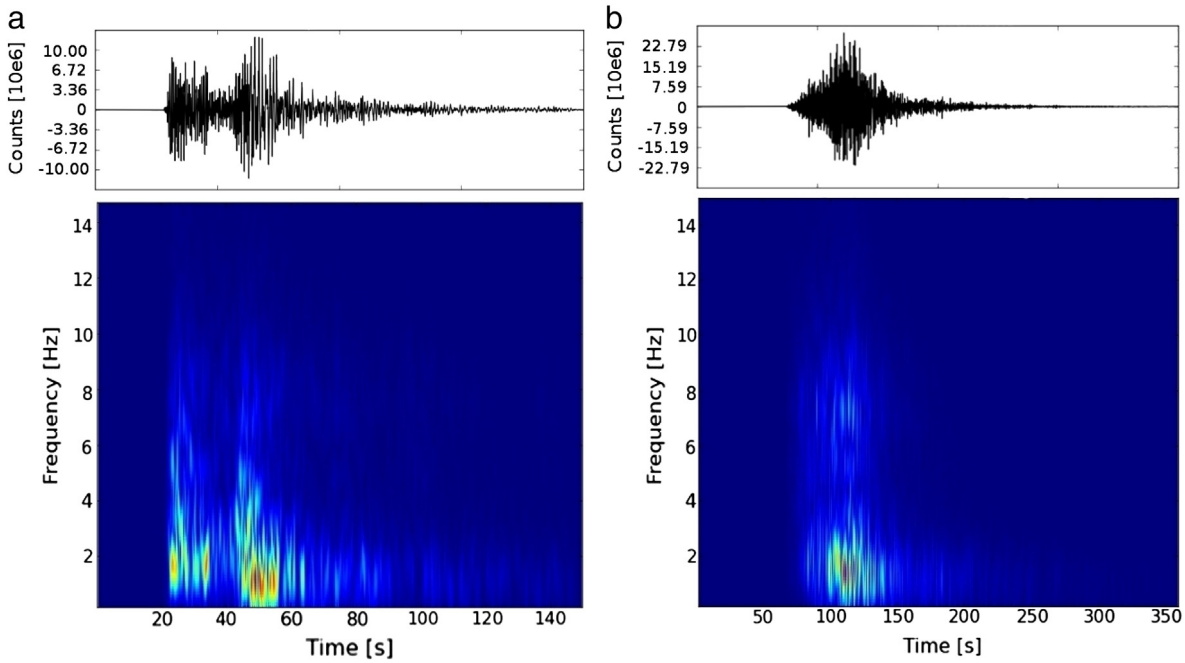

Fig. 9. Waveform and spectra for the M6.1 and M7.1 earthquakes.

4.2. Response to large regional earthquakes

On January 23rd, 2012, a Mw 6.1 aftershock occurred at the subduction interface (25 km deep, USGS), approximately 192 km from the NdC volcanic complex (Fig. 1). The volcanic activity at NdC before the event was low, with less than one event per hour. The Mw 6.1 earthquake occurred at 16:04 UTC, afterwards (17:04 UTC) tremor activity increased noticeably and lasted for approximately 9 h. When tremor stopped at 02:00 UTC, the VT event rate increased to an average of 3.5 events/h. Fig. 7 shows the total number of tremor and VT events before and after the occurrence of the Mw 6.1 earthquake, highlighting the onset of double-couple events after tremor subsided. A second large aftershock of the Maule mega-thrust earthquake occurred on March 25th, 2012, 200 km away (34 km deep, USGS) from the NdC complex (Fig. 1). At the time, station VV was suffering 12 hours of daily data loss due to energy-storage issues. Nevertheless, we captured the signal of the Mw 7.1 earthquake and analyzed the VT rate of the available data. Comparing the Mw 7.1 post-seismic records with the ones that followed

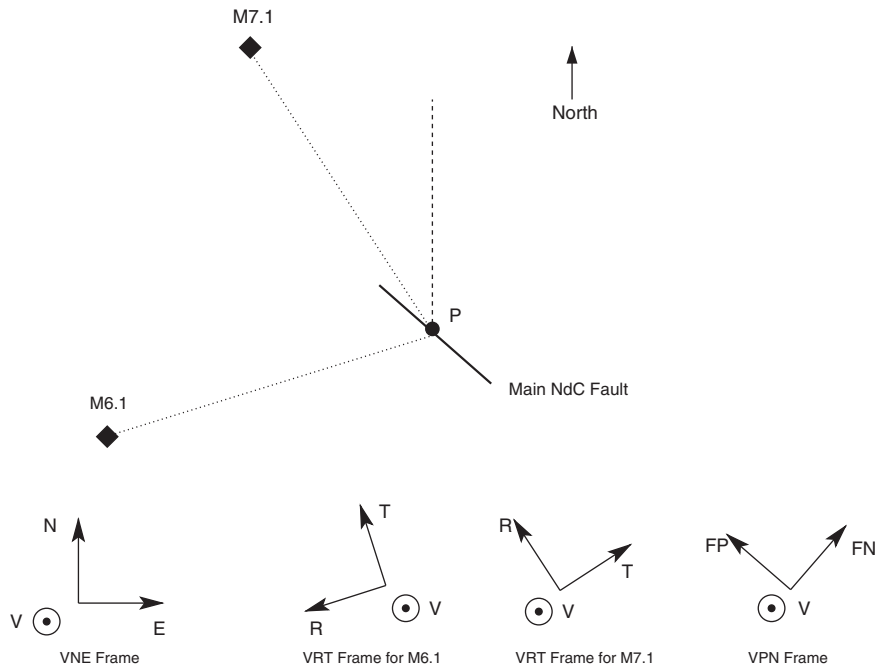

Fig. 10. Schematic representation of the relative location of the Mw6.1 and Mw7.1 events to the main lineament of the Nevados de Chillán volcanic complex, and the different coordinate frames used in our analysis. More detail on each one of the frames is given on the text.

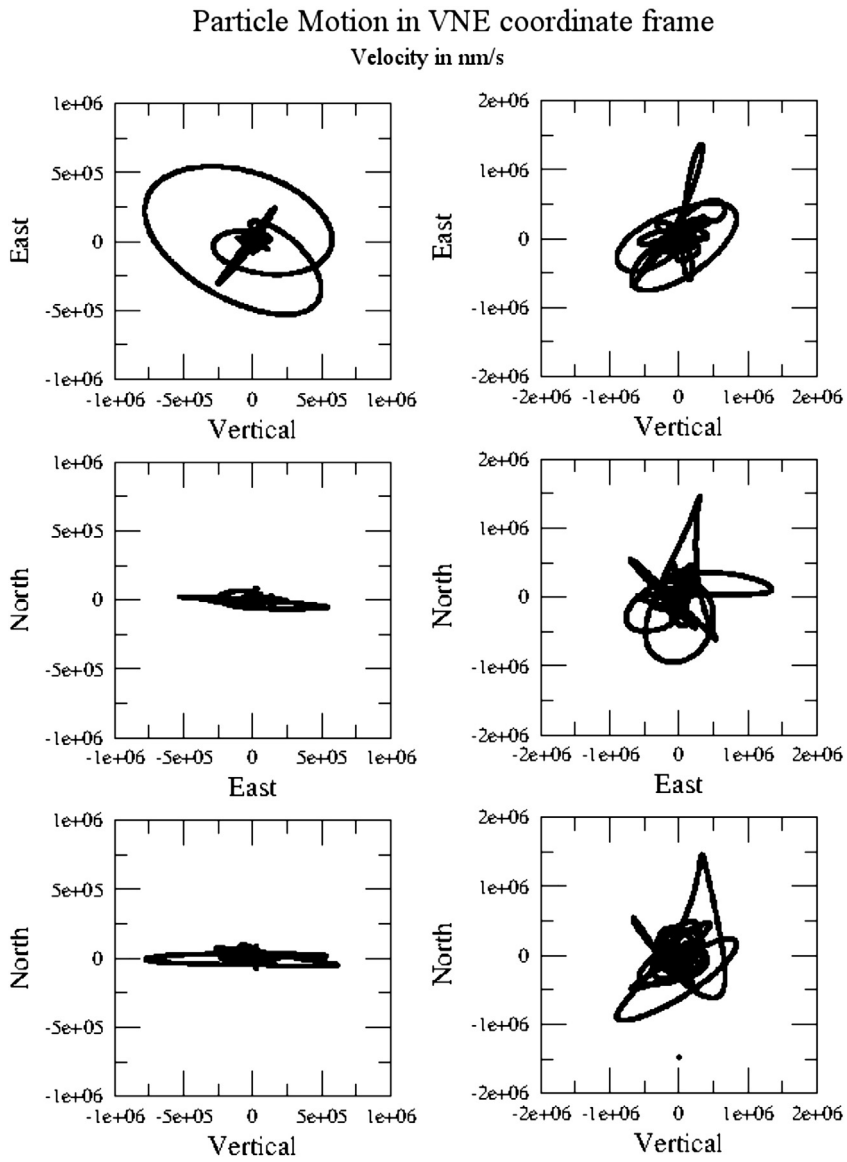

Fig. 11. Velocity particle motion plots in Volcan Viejo station for the Mw6.1 and Mw7.1 event in the VNE frame. The signal was filtered between 0.01 Hz and 0.1 Hz and the velocity is measured in nm/s. The N-V axes identify the north-vertical plane, E-V the east-vertical plane and the N-E axes identify the north-east plane. Note the dominant oscillatory behavior induced by the M6.1 earthquake on the N-Z and N-E planes in contrast to the motion induced by the M7.1.

the Mw 6.1 we found that before the Mw 7.1 earthquake the seismic activity was particularly intense with an average of three events per hour (Fig. 8). However, the available data show that the VT rate decreased to one event per hour after the earthquake. Although our analysis is biased by the lack of data, the reduction of the number of events per hour following the Mw 7.1 aftershock is clearly shown. This type of response is similar to that recorded for Mt. Wrangell and Mt. Veniaminof volcanoes after the 2002, Mw 7.9 Denali earthquake (Sanchez and McNutt, 2004).

5. Discussion

We investigated the seismic activity of the NdC complex after the Maule earthquake and found that seismic activity mainly occurs from 2 to 5 km deep beneath the region called Aguas Calientes, a valley known for its natural hot springs and fumaroles. Deeper events also occur below the volcanic complex down to approximately 20 km deep. We did not locate several low-magnitude seismic events because they did not appear on a sufficient number of stations. However, their waveforms are characteristic of shallow VT events. This points to a local origin that may be within the volcanic system, possibly beneath the Aguas Calientes valley. The location of this shallow seismicity plus the type of tremor events we recorded in our campaign suggest that the activity at the NdC has a strong hydrothermal component, thus making the volcano an active hydrothermal-magmatic system.

We observed different responses of the NdC to two large Maule aftershocks (Mw 6.1, Fig. 7 and Mw 7.1, (Fig. 8) originating at similar hypocentral distances from the NdC. We identified a triggered response of the NdC after the Mw 6.1 event but not after the Mw 7.1 event. Note that although data loss during the Mw 7.1 event introduces a bias, we registered a decrease in VT when compared to the behavior prior to the Mw 7.1 event (blue lines in Fig. 8 indicate the average rate). Fig. 9 shows the waveforms and spectra of the two aftershocks of the Maule earthquake. The maximum amplitudes in a ground motion seismograph of the two events are comparable and are on the order of 1 to 2 mm for the vertical component at station VV. Using particle motion plots, we investigated the effect of the incidence angle of the incoming seismic waves and

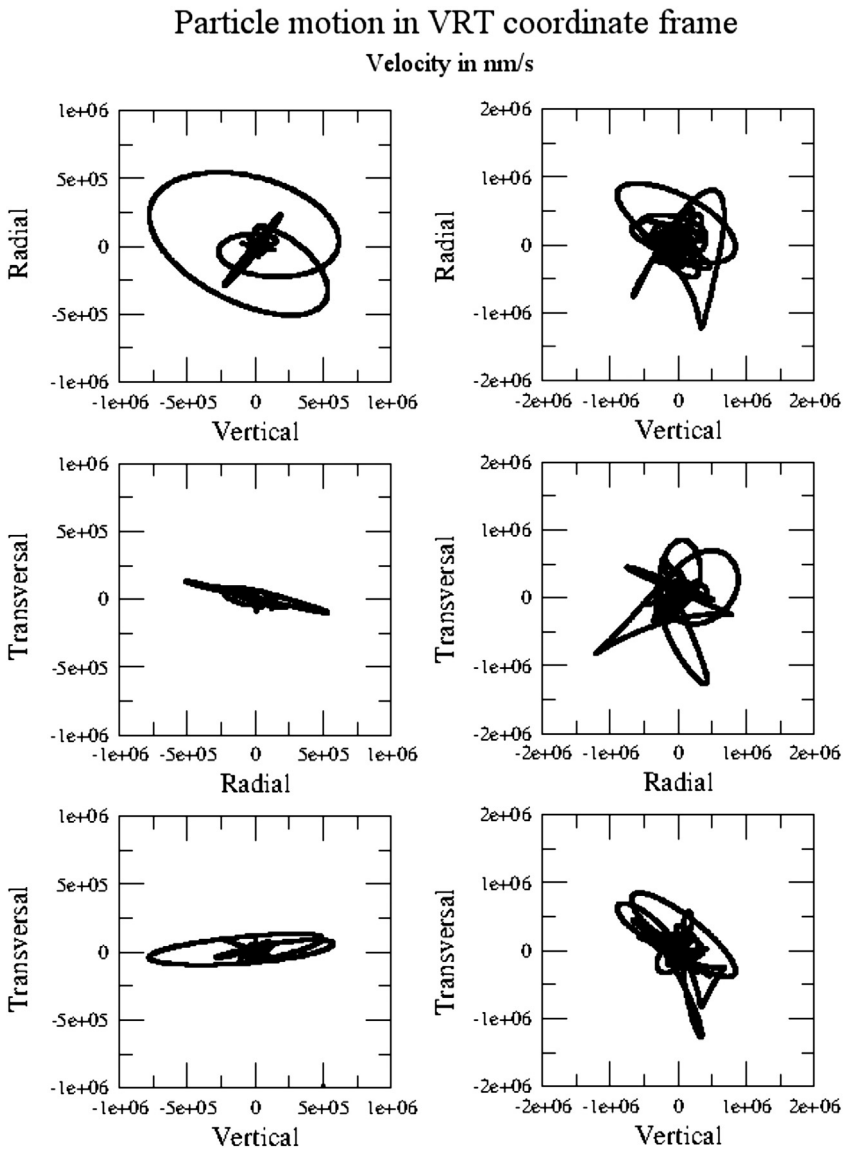

Fig. 12. Velocity particle motion plots in Volcan Viejo station for the Mw6.1 and Mw7.1 event, each one in a frame rotated to its backazimuth (VRT frame). The signal was filtered between 0.01 Hz and 0.1 Hz and the velocity is measured in nm/s. For each earthquake, the R-V axes identify the radial-vertical plane, T-Z the transverse-vertical plane and the T-R axes identify the transverse-radial plane.

found that the difference between the effect produced by the two events may lie there. Fig. 10 shows a scheme of the different coordinate frames used in the observation point given by the location of VV station. Figs. 11, 12, and 13 show particle velocity motion plots for both earthquakes in station VV, filtered between 0.01 Hz and 0.1 Hz, in different coordinate systems: vertical/north/east (VNE), vertical/radial/transversal (VRT) for both events, and vertical/NdC fault normal/NdC fault parallel (VNP). In the VNE frame the most noticeable feature is how the particle motion induced by the Mw6.1 event presents a dominant motion along the east and vertical directions, with amplitudes around 10 mm s^{-1}, while the Mw7.1 event induced velocities with maximum amplitudes on the order of 20 mm s^{-1}, but without any preferential orientation. The induced particle motion in the VRT frame shows how, for the Mw6.1 event, the transverse movement is significantly smaller than the radial one, suggesting that the wave train is mostly dominated by Rayleigh waves rather than Love waves. In the case of the Mw7.1 event, there is no clear dominance of either transverse or radial motion modes. Finally, on the VPP frame it can be appreciated how the Mw6.1 event induced a motion oblique to the main fault of the NdC complex, which may help to create a fault-parallel motion, thus enhancing a stress change along the main lineament of the system. On the other hand, the Mw7.1 does not show a preferred direction of motion.

The analysis of particle motion in the three different coordinate frames suggests that the Mw6.1 event may have induced a elliptical motion in the main fault of the NdC, with dominant fault-parallel and vertical components, thus promoting the creation of spaces for the fluids to arise and move along the lineament, as reflected by the important increase on seismicity right after the passage of the wave train. This indicates that the observed behavior of triggered tremor followed by VT events was controlled by dilatational processes due to the Rayleigh waves. This is consistent with other studies that report triggered tremor due to the passage of the Rayleigh waves in regions like Japan after the 2004 Sumatra–Andean earthquake (Miyazawa and Mori, 2005, 2006). In a more general work frame, our observations are also consistent with other studies showing permeability increases correlating with passing seismic waves (Kitagawa et al., 2002; Elkhoury et al., 2006).

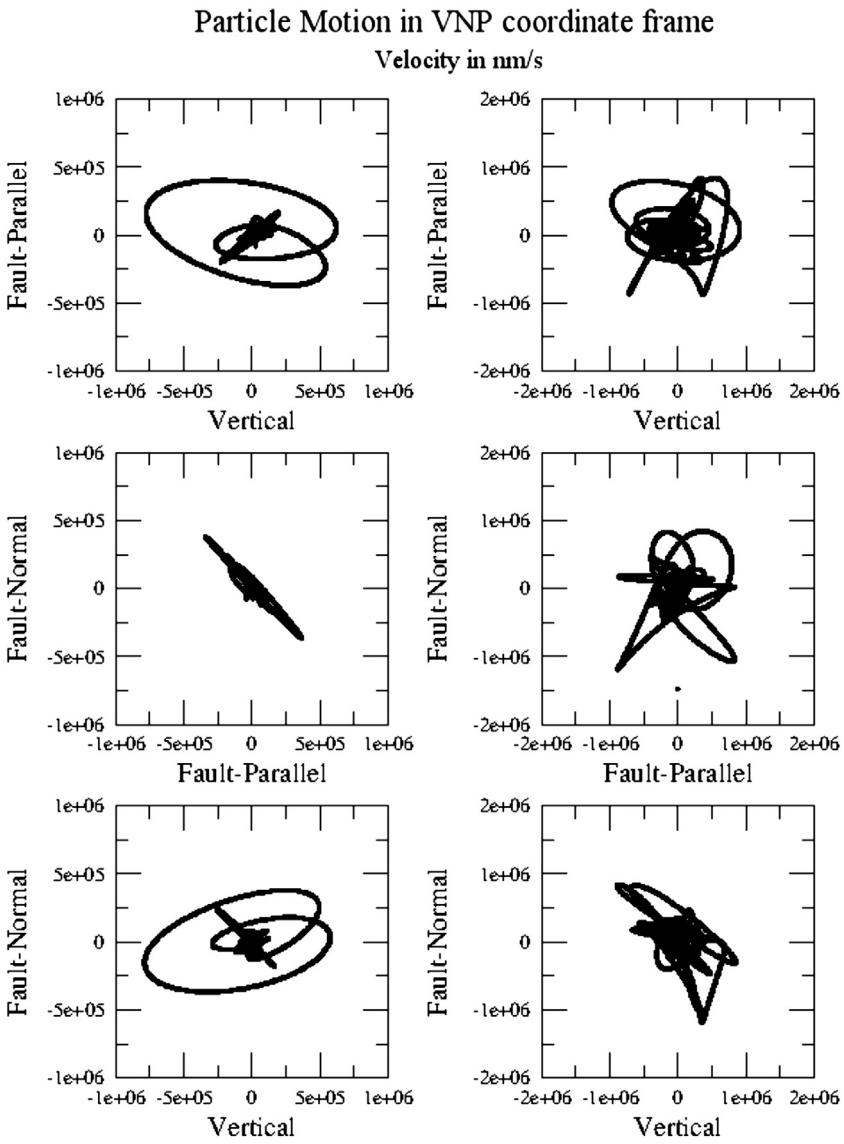

Fig. 13. Velocity particle motion plots in Volcan Viejo station for the Mw6.1 and Mw7.1 event, in the VNP coordinate frame. The signal was filtered between 0.01 Hz and 0.1 Hz and the velocity is measured in nm/s. The FP-Z axes identify the fault-parallel/vertical plane, FN-Z the fault-normal/vertical plane and the FP-FN axes identify the fault-parallel/fault-normal plane.

6. Conclusions

We presented data from a seismic campaign that took place from December 2011 to April 2012 around the Nevados de Chillán (NdC) volcanic complex, in Central-Southern Chile. We recorded numerous volcano-tectonic (VT) and tremor events within the volcanic complex. The majority of the events was shallower than 5 km deep and occurred beneath the south-east flank of the volcano. Two major aftershocks (Mw 6.1 and Mw 7.1) of the 2010 Maule earthquake, at similar distances for the NdC elicited different responses. The response to the Mw6.1 event was characterized by an increase of tremor activity 1 h after the earthquake, followed by a marked increase of VT events when the tremor subsided. This strongly suggests a fluid driven mechanism induced by the passage of the seismic waves. In contrast, the Mw 7.1 event did not trigger a response of NdC. We propose that this difference in behavior is a result of the incidence angle of incoming energy, where the Mw 6.1 showed predominantly EW (arc-oblique) particle motion and the Mw 7.1 showed no particular oscillatory path. An alternative explanation could be that the response to the Mw 6.1 event relaxed the system and therefore was not perturbed sufficiently to induce a response from the Mw 7.1. Future seismic campaigns with a higher density array will allow triggered responses to be constrained with better accuracy.

The volcanic arc behind the Maule earthquake is an excellent natural laboratory for investigating earthquake–volcano interactions, and should be instrumented in the future to better understand earthquake–volcano interactions and the internal dynamics of perturbed arc systems.

Acknowledgments

Cristian Farias thanks the Becas Chile Scholarship Program (72120406) for supporting his work. Humanitus Sidoarjo fund is thanked for supporting Matteo Lupi. Matteo Lupi was also partially supported by the ETH Zurich Postdoctoral fellowship. Daniel Basualto from Observatorio Volcanológico de los Andes del Sur (OVDAS) is acknowledged for providing us the 1-D velocity model. Cristian Sepulveda and Gustavo Aldea are acknowledged for their help in the field and logistical support.

References

Bebbington, M., Marzocchi, W., 2011. Stochastic models for earthquake triggering of volcanic eruptions. J. Geophys. Res. B 116.

Bohm, M., Lüth, S., Echtler, H., Asch, G., Bataille, K., Bruhn, C., Rietbrock, A., Wigger, P., 2002. The Southern Andes between 36 and 40°S latitude: seismicity and average seismic velocities. Tectonophysics 356, 275–289.

Brodsky, E., Prejean, S., 2005. New constrains on mechanism of remotely triggered seismicity at Long Valley Caldera. J. Geophys. Res. B 110.

Brodsky, E., Sturtevant, B., Kanamori, H., 1998. Earthquakes, volcanoes, and rectified diffusion. J. Geophys. Res. 103, 23827–23838.

Brooks, B., Bevis, M., Whipple, K., Arrowsmith, J., Foster, J., Zapata, T., Kendrick, E., Minaya, E., Echalar, A., Blanco, M., Euillades, P., Sandoval, M., Smalley, R., 2011. Orogenic-wedge deoformation and potential for great earthquakes in the central andean backarc. Nat. Geosci. 4, 380–383.

Cembrano, J., 1992. The Liquiñe–Ofqui Fault Zone (LOFZ) in the Province of Palena: Field and Microstructural Evidence of a Ductile-Brittle Dextral Shear Zone. Universidad de Chile, Departamento de Geología, Comunicaciones.

Cembrano, J., Lara, L., 2009. The link between volcanism and tectonics in the southern volcanic zone of the Chilean Andes: a review. Tectonophysics 471, 96–113.

Cembrano, J., Hervé, F., Lavenu, A., 1996. The Liquiñe Ofqui fault zone: a long-lived intra-arc fault system in Southern Chile. Tectonophysics 259, 55–66.

Cembrano, J., Schermer, E., Lavenu, A., Sanhueza, A., 2000. Contrasting nature of deformation along an intraarc shear zone, the Liquiñe–Ofqui fault zone, Southern Chilean Andes. Tectonophysics 319, 129–149.

Davis, P., Rubinstein, J., Liu, K., Gao, S., Knopoff, L., 2000. Northridge earthquake damage caused by geologic focusing of seismic waves. Science 289, 1746–1750.

Delle Donne, d, Harris, A., Ripepe, M., Wright, R., 2010. Earthquake-induced thermal anomalies at active volcanoes. Geology 38, 771–774.

Dzierma, Y., Wehrmann, H., 2010. Eruption time series statistically examined: probabilities of future eruptions at Villarrica and Llaima volcanoes, southern volcanic zone, Chile. J. Volcanol. Geotherm. Res. 193, 82–92.

Eggert, S., Walter, T., 2009. Volcanic activity before and after large tectonic earthquakes: observations and statistical significance. Tectonophysics 471, 14–26.

Elkhoury, J.E., Brodsky, E.E., Agnew, D.C., 2006. Seismic waves increase permeability. Nature 441, 1135–1138.

Gonzalez-Ferrán, O., 1995. Volcanes de Chile. Instituto Geográfico Militar, Chile.

Harris, R.N., McNutt, M.K., 2007. Heat flow on hot spot swells: evidence for fluid flow. J. Geophys. Res. B 112.

Hennings, P., Allwardt, P., Paul, P., Zahm, C., Alley, H., Kirschner, R., Lee, B., Hough, E., 2012. Relationship between fractures, fault zones, stress, and reservoir productivity in the Suban gas field, Sumatra, Indonesia. Am. Assoc. Pet. Geol. Bull. 96, 753–772.

Hill, D., 2008. Dynamic stresses, coulomb failure, and remote triggering. Bull. Seism. Soc. Am. 102, 2313–2336.

Hill, D., Reasenberg, A., Michael, A., Arabaz, W., Beroza, G., Brumbaugh, D., Brune, J., Castro, R., Davis, S., dePolo, D., Ellsworth, W., Gomberg, J., Harmsen, S., House, L., Jackson, S., Johnston, J., Jones, L., Keller, R., Malone, S., Munguia, L., Nava, S., Pechmann, J., Sanford, A., Simpson, R., Smith, R., Stark, M., Stickney, M., Vidal, A., Walter, S., Wong, V., Zollweg, J., 1993. Seismicity remotely triggered by the magnitude 7.3 Landers, California, earthquake. Science 260, 1617–1623.

Hill, D., Johnston, M., Langbein, J., Bilham, R., 1995. Response of Long Valley Caldera to the m = 7.3 Landers, California, earthquake. Geophys. Res. Lett. 100, 12985–13005.

Hill, D., Pollitz, P., Newhall, C., 2002. Earthquake–volcano interactions. Phys. Today 55, 41–47.

Ichihara, M., Brodsky, E., 2006. A limit on the effect of rectified diffusion in volcanic systems. Geophys. Res. Lett. 32.

Jay, J., Pritchard, M., West, M., Christensen, D., Haney, M., Minaya, E., Sunagua, M., McNutt, S., Zabala, M., 2011. Shallow seismicity, triggered seismicity, and ambient noise tomography at the long-dormant Uturuncu Volcano, Bolivia. Bull. Volcanol. 74, 817–837.

Johnston, M., Hill, D., Langbein, J., Bilham, R., 1995. Transient deformation during triggered seismicity from the 28 June 1992 $m_w = 7.3$ Landers earthquake at Long Valley Volcanic Caldera, California. Bull. Seism. Soc. Am. 85, 787–795.

Khazaradze, G., Wang, K., Klotz, J., Hu, Y., He, J., 2002. Prolonged post-seismic deformation of the 1960 great Chile earthquake and implications for mantle rheology. Geophys. Res. Lett. 29, 2050.

Kitagawa, Y., Fujimori, K., Koizumi, N., 2002. Temporal change in permeability of the rock estimated from repeated water injection experiments near the Nojima fault in Awaji Island, Japan. Geophys. Res. Lett. 29, 1483.

Lange, D., Cembrano, J., Rietbrock, A., Haberland, C., Dahm, T., Bataille, K., 2008. First seismic record for intra-arc strike-slip tectonics along the Liquiñe–Ofqui fault zone at the obliquely convergent plate margin of the Southern Andes. Tectonophysics 455, 14–24.

Lara, L., Naranjo, J., Moreno, H., 2004. Rhyodacitic fissure eruption in Southern Andes (Cordón Caulle; 40.5°S) after the 1960 (mw: 9.5) Chilean earthquake: a structural interpretation. J. Volcanol. Geotherm. Res. 138, 127–138.

Lavenu, A., Cembrano, J., 1999. Compressional and transpressional stress pattern for pliocene and quaternary brittle deformation in forearc and intra-arc zones (Andes of Central and Southern Chile). J. Struct. Geol. 21, 1669–1691.

Leet, R., 1991. Investigation of Hydrothermal Boiling and Steam Quenching as Possible Sources of Volcanic Tremor and Geothermal NoisePh.D. thesis University of Washington.

Lupi, M., Miller, S., 2014. Short-lived tectonic switch mechanism for long-term pulses of volcanic activity after mega-thrust earthquakes. Solid Earth 5, 13–24.

Lupi, M., Saenger, H., Fuchs, F., Miller, S., 2013. Lusi mud eruption triggered by geometric focusing of seismic waves. Nat. Geosci. http://dx.doi.org/10.1038/ngeo1884.

Manga, M., Brodsky, E., 2006. Seismic triggering of eruptions in the far field: volcanoes and geysers. Annu. Rev. Earth Planet. Sci. 34, 263–291.

Marzocchi, W., Casarotti, E., Piersanti, A., 2002. Modeling the stress variations induced by great earthquakes on the largest volcanic eruptions of the 20th century. J. Geophys. Res. 107.

McNutt, S., 2005. Volcanic seismology. Annu. Rev. Earth Planet. Sci. 32, 461–491.

Miyazawa, M., Mori, J., 2005. Detection of triggered deep low-frequency events from the 2003 Tokachi-oki earthquake. Geophys. Res. Lett. 32.

Miyazawa, M., Mori, J., 2006. Evidence suggesting fluid flow beneath Japan due to periodic seismic triggering from the 2004 Sumatra–Andaman earthquake. Geophys. Res. Lett. 33.

Mora-Stock, C., Thorwart, M., Wunderlich, T., Bredemeyer, S., Hansteen, T., Rabbel, W., 2012. Comparison of seismic activity for Llaima And Villarrica volcanoes prior to and after the Maule 2010 earthquake. Int. J. Earth Sci. 1–14.

Moreno, M., Rosenau, M., Oncken, O., 2010. 2010 Maule earthquake slip correlates with pre-seismic locking of Andean subduction zone. Nature 467, 198–202.

Nakamura, K., 1977. Volcanoes as possible indicators of tectonic stress orientation: principle and proposal. J. Volcanol. Geotherm. Res. 2, 1–16.

Ottemöller, L., Voss, P., Havskov, J., 2011. Seisan Earthquake Analysis Software for Windows, Solaris, Linux, and Macosx.

Sanchez, J., McNutt, S., 2004. Intermediate-term declines in seismicity at Mt. Wrangell and Mt. Veniaminof volcanoes, Alaska, following the 3 November 2002 m_w 7.9 Denali fault earthquake. Bull. Seism. Soc. Am. 94.

Siebert, L., Simkin, T., Kimberly, P., 2012. Volcanoes of the World. University of California Press, USA.

Sparks, R., Sigurdsson, J., Wilson, L., 1977. Magma mixing: a mechanism for triggering acid explosive eruptions. Nature 267, 315–318.

SSN, 2013. http://www.sismologia.cl/links/terremotos/index.html Technical Report. Chilean Seismological Service.

Walter, T., Amelung, F., 2007. Volcanic eruptions following m ≥ 9 megathrust earthquakes: implications for the Sumatra–Andaman volcanoes. Geology 35, 539–542.

Wassermann, J., 2012. Volcano Seismology, IASPEI New Manual of Seismological Observatory Practice 2. Deutsches GeoForschungsZentrum GFZ, Potsdam.

Withers, M., Aster, R., Young, C., Beiriger, J., Harris, M., Moore, S., Trujillo, J., 1998. A comparison of select trigger algorithm for automated global seismic phase and event detection. Bull. Seism. Soc. Am. 88, 95–106.

Bibliography

Aiken, C., Z. Peng, and K. Chao (2013), Tremors along the Queen Charlotte margin triggered by large teleseismic earthquakes, *Geophysical Research Letters*, *40*, 829–834.

Allen, R. M., et al. (2002), Plume-driven plumbing and crustal formation in Iceland, *Journal of Geophysical Research*, *107*, 2163.

Alvarado, G. E., M. J. Carr, B. D. Turrin, C. C. Swisher, H. Schmincke, and K. W. Hudnut (2006), Recent volcanic history of Irazú volcano, Costa Rica: Alternation and mixing of two magma batches, and pervasive mixing, *Geological Society of Ameria Special Paper*, *412*, 259–276.

Árnadóttir, T., B. Lund, W. Jiang, H. Geirsson, H. Björnsson, P. Einarsson, and T. Sigurdsson (2009), Glacial rebound and plate spreading: Results from the first countrywide GPS observations in Iceland, *Geophysical Journal International*, *177*, 691–716.

Axford, S. (2009), Photograph taken by Steve Axford, http://steveaxford.smugmug.com/.

Baer, G., Y. Hamiel, G. Shamir, and R. Nof (2008), Evolution of magma-driven earthquake swarm and triggering of the nearby Oldoinyo Lengai eruption, as resolved by InSAR, ground observations and elastic modeling, East African Rift, 2007, *Earth and Planetary Science Letters*, *272*, 339–352.

Bamler, R., and P. Hartl (1998), Synthetic aperture radar interferometry, *Inverse Problems*, *14*, R1–R54.

Bar-Sinai, Y., R. Spatschek, E. A. Brener, and E. Bouchbinder (2013), Instabilities at frictional interfaces: Creep patches, nucleation, and rupture fronts, *Physical Review E*, *88*, 060403.

Bartlow, N. M., S. Miyazaki, A. M. Bradley, and P. Segall (2011), Space-time correlation of slow slip and tremor during the 2009 Cascadia slow slip event, *Geophysical Research Letters*, *38*, L18309.

Beeler, N. M., R. W. Simpson, S. H. Hickman, and D. A. Lockner (2000), Pore fluid pressure, apparent friction, and Coulomb failure, *Journal of Geophysical Research*, *105*, 25,533–25,542.

Berberian, M., et al. (2001), The 1998 March 14 Fandoqa earthquake (M-w 6.6) in Kerman province, southeast Iran: re-rupture of the 1981 Sirch earthquake fault, triggering of slip on adjacent thrusts and the active tectonics of the Gowk fault zone, *Geophysical Journal International*, *146*, 371–398.

Beroza, G. C., and S. Ide (2011), Slow earthquakes and nonvolcanic tremor, *Annual Review of Earth and Planetary Sciences*, *39*, 271–296.

Berry, J. P. (1960), Some kinetic considerations of the Griffith criterion for fracture (1) Equations of motion at constant force, *Journal of the Mechanics and Physics of Solids*, *8*, 194–206.

Beyreuther, M., R. Barsch, L. Kirscher, T. Megies, Y. Behr, and J. Wassermann (2010), ObsPy: A python toolbox for seismology, *Seismological Research Letters*, *81*, 530–533.

Bing (2014), Microsoft Bing Maps, http://www.bing.com/maps.

Bjarnason, I. T., and H. Schmeling (2009), The lithosphere and asthenosphere of the Iceland hotspot from surface waves, *Geophysical Journal International*, *178*, 394–418.

Bonali, F. L. (2013), Earthquake-induced static stress change on magma pathway in promoting the 2012 Copahue eruption, *Tectonophysics*, *608*, 127–137.

Bonini, M. (2008), Elliptical mud volcano caldera as stress indicator in an active compressional setting (Nirano, Pede-Apennine margin, northern Italy), *Geology*, *36*, 131–134.

Brandsdóttir, B., and W. H. Menke (2008), The seismic structure of Iceland, *Jökull*, *58*, 17–34.

Brodsky, E. E. (2006), Long-range triggered earthquakes that continue after the wave train passes, *Geophysical Research Letters*, *33*, L15313.

Brodsky, E. E., and S. G. Prejean (2005), New constraints on mechanisms of remotely triggered seismicity at Long Valley Caldera, *Journal of Geophysical Research*, *110*, B04302.

Brodsky, E. E., B. Sturtevant, and H. Kanamori (1998), Earthquakes, volcanoes and rectified diffusion, *Journal of Geophysical Research*, *103*, 23,827–23,838.

Brodsky, E. E., E. Roeloffs, D. Woodcock, I. Gall, and M. Manga (2003), A mechanism for sustained groundwater pressure changes induced by distant earthquakes, *Journal of Geophysical Research*, *108*, 2390.

Chao, K., Z. Peng, C. Wu, C. C. Tang, and C. H. Lin (2012a), Remote triggering of non-volcanic tremor around Taiwan, *Geophysical Journal International*, *188*, 301–324.

Chao, K., Z. Peng, A. Fabian, and L. Ojha (2012b), Comparisons of triggered tremor in California, *Bulletin of the Seismological Society of America*, *102*, 900–908.

Chao, K., Z. Peng, H. Gonzalez-Huizar, C. Aiken, B. Enescu, H. Kao, A. A. Velasco, K. Obara, and T. Matsuzawa (2013), A global search for triggered tremor following the 2011 Mw 9.0 Tohoku earthquake, *Bulletin of the Seismological Society of America*, *103*, 1551–1571.

Cheveralls, K. (2011), Drowning in mud, *Berkeley Science Review*, *Spring Issue*, 26–43.

Chouet, B. A. (1996), Long-period volcano seismicity: its source and use in eruption forecasting, *Nature*, *380*, 309–316.

Cochran, E. S., J. E. Vidale, and S. Tanaka (2004), Earth tides can trigger shallow thrust fault earthquakes, *Science*, *306*, 1164–1166.

Corti, G., E. Carminati, F. Mazzarini, and M. O. Garcia (2005), Active strike-slip faulting in El Salvador, Central America, *Geology*, *33*, 989–992.

Coulomb, C. A. (1776), Sur une application des regles maximis et minimis a quelques problems de statique, relatives a l'architecture, *Mémoires de mathématique et de physique*, *7*, 343–382.

Dadson, S. J., et al. (2004), Earthquake-triggered increase in sediment delivery from an active mountain belt, *Geoloy*, *32*, 733–736.

Darbyshire, F. A., R. S. White, and K. F. Priestly (2000), Structure of the crust and uppermost mantle of Iceland from a combined seismic and gravity study, *Earth and Planetary Science Letters*, *181*, 409–428.

Davies, R. J., M. Brumm, M. Manga, R. Rubiandini, R. Swarbrick, and M. Tingay (2008), The east Java mud volcano (2006 to present): An earthquake or drilling trigger?, *Earth and Planetary Science Letters*, *272*, 627–638.

Davis, P. (2013), Triggered mud eruption?, *Nature Geoscience*, *6*, 592–593.

Davis, P. M., J. L. Rubinstein, K. H. Lui, S. S. Gao, and L. Knoppoff (2000), Northridge earthquake damage caused by geologic focusing of seismic waves, *Science*, *289*, 1746–1750.

De Matteis, R., T. Vanorio, S. Zollo A. Ciuffi, A. Fiordelisi, and E. Spinelli (2008), Three-dimensional tomography and rock properties of the Larderello-Travale geothermal area, Italy, *Physics of the Earth and Planetary Interiors*, *168*, 37–48.

Delle Donne, D., A. J. Harris, M. Ripepe, and R. Wright (2010), Earthquake-induced thermal anomalies at active volcanoes, *Geology*, *38*, 771–774.

Di Toro, G., R. Han, T. Hirose, N. de Paola, S. Nielsen, K. Mizoguchi, F. Ferri, M. Cocco, and T. Shimamoto (2011), Fault lubrication during earthquakes, *Nature*, *471*, 494–498.

Dickinson, W. R., and T. Hatherton (1967), Andesitic volcanism and seismicity around the Pacific, *Science*, *157*, 801–803.

Dieterich, J. (1994), A constitutive law for rate of earthquake production and its application to earthquake clustering, *Journal of Geophysical Research*, *99*, 2601–2618.

Diez, M., P. C. La Femina, C. B. Connor, W. Strauch, and V. Tenorio (2005), Evidence for static stress changes triggering the 1999 eruption of Cerro Negro Volcano, Nicaragua and regional aftershock sequences, *Geophysical Research Letters*, *32*, L04309.

Du, Z., et al. (2002), Crustal structure beneath western and eastern Iceland from surface waves and receiver functions, *Geophysical Journal International*, *149*, 349–363.

Dziak, R. P., W. W. Chadwick, C. G. Fox, and R. W. Embley (2003), Hydrothermal temperature changes at the southern Juan de Fuca ridge associated with Mw 6.2 Blanco transform earthquake, *Geology*, *31*, 119–122.

Dzurisin, D., and Z. Lu (2006), Interferometric synthetic-aperture radar (InSAR), in *Volcano Deformation*, chap. 5, pp. 153–194, Springer Berlin Heidelberg.

Eggert, S., and T. Walter (2009), Volcanic activity before and after large tectonic earthquakes: Observations and statistical significance, *Tectonophysics*, *471*, 14–26.

Einarsson, P. (2008), Plate boundaries, rifts and transforms in Iceland, *Jökull*, *58*, 35–58.

Elkhoury, J. E., A. Niemeijer, E. Brodsky, and C. Marone (2011), Laboratory observations of permeability enhancement by fluid pressure oscillations of an in situ fractured rock, *Journal of Geophysical Research*, *116*, B02311.

Enescu, B., et al. (2012), Love wave triggering of non-volcanic tremor in the Nankai region, southwest Japan: Observations and physical interpretation, *AGU Fall Meeting*, Abstract S33B-2550.

Farias, C., M. Lupi, F. Fuchs, and S. A. Miller (2014), Seismic activity of the Nevados de Chillán volcanic complex after the 2010 Mw8.8 Maule, Chile, earthquake, *Journal of Volcanology and Geothermal Research*, *283*, 116–126.

Flude, S., R. Burgess, and D. W. McGravie (2008), Silicic volcanism at Ljósofjöll, Iceland: Insights into evolution and eruptive history from Ar-Ar dating, *Journal Volcanology and Geothermal Research*, *169*, 154–175.

Foster, J. H., A. R. Lowry, and B. A. Brooks (2013), Fault frictional parameters and material properties revealed by slow slip events at Kilauea volcano, Hawaii, *Geophysical Research Letters*, *40*, 6059–6063.

Fournier, R. O. (1999), Hydrothermal processes related to movement of fluid from plastic to brittle rock in the magmatic-epithermal environment, *Economic Geology*, *94*, 1193–1211.

Fry, B., K. Chao, S. Bannister, Z. Peng, and L. Wallace (2011), Deep tremor in New Zealand triggered by the 2010 Mw8.8 Chile earthquake, *Geophysical Research Letters*, *38*, L15306.

Gallego, A., R. M. Russo, D. Comte, V. Mocanu, R. E. Murdie, and J. V. van Decar (2013), Tidal modulation of continuous nonvolcanic seismic tremor in the Chile triple junction region, *Geochemistry, Geophysics, Geosystems*, *14*, 851–863.

Gerstenberger, M. C., S. Wiemer, L. M. Jones, and P. A. Reasenberg (2005), Real-time forecasts of tomorrow's earthquakes in California, *Nature*, *435*, 328–331.

Ghosh, A., J. E. Vidale, Z. Peng, K. C. Creager, and H. Houston (2009), Complex nonvolcanic tremor near Parkfield, California, triggered by the great 2004 Sumatra earthquake, *Journal of Geophysical Research*, *114*, B00A15.

Gomberg, J., and S. Prejean (2013), Triggered tremor sweet spots in Alaska, *Journal of Geophysical Research: Solid Earth*, *118*, 6203–6218.

Gomberg, J., J. L. Rubinstein, Z. Peng, K. C. Creager, J. E. Vidale, and P. Bodin (2008), Widespread triggering of nonvolcanic tremor in California, *Science*, *319*, 173.

Gonzalez, P. J., K. F. Tiampo, M. Palano, F. Cannavo, and J. Fernandez (2012), The 2011 Lorca earthquake slip distribution controlled by groundwater crustal unloading, *Nature Geoscience*, *5*, 821–825.

Guilhem, A., Z. Peng, and R. M. Nadeau (2010), High-frequency identification of non-volcanic tremor triggered by regional earthquakes, *Geophysical Research Letters*, *37*, L16309.

Gupta, H. K. (2002), A review of recent studies of triggered earthquakes by artificial water reservoirs with special emphasis on earthquakes in Koyna, India, *Earth-Science Reviews*, *58*, 279–310.

Gutenberg, B., and C. F. Richter (2010), Magnitude and energy of earthquakes, *Annals of Geophysics*, *53*, 7–12.

Handin, J. (1969), On the Coulomb-Mohr failure criterion, *Journal of Geophysical Research*, *74*, 5343–5348.

Hanka, W., J. Saul, B. Weber, J. Becker, P. Harjadi, and Fauzi and GITEWS Seismology Group (2010), Real-time earthquake monitoring for tsunami warning in the Indian Ocean and beyond, *Natural Hazards and Earth System Sciences*, *10*, 2611–2622.

Hardarsson, B. S., and J. G. Fitton (1991), Increased mantle melting beneath the Snæfellsjökull volcano during Late Pleistocene deglaciation, *Nature*, *353*, 62–64.

Harris, A. J. L., and M. Ripepe (2007), Regional earthquake as a trigger for enhanced volcanic activity: Evidence from MODIS thermal data, *Geophysical Research Letters*, *34*, L02304.

Havskov, J., and L. Ottemoller (1999), Seisan earthquake analysis software, *Seismological Research Letters*, *70*, 532–534.

Hayes, G. P., D. J. Wald, and R. L. Johnson (2012), Slab1.0: A three-dimensional model of global subduction zone geometries, *Journal of Geophysical Research*, *117*, B01302.

Hellweg, M. (2000), Physical models for the source of Lascar's harmonic tremor, *Journal of Volcanology and Geothermal Research*, *101*, 183–198.

Hill, D. P. (2008), Dynamic stresses, Coulomb failure, and Remote triggering, *Bulletin of the Seismological Society of America*, *98*, 66–92.

Hill, D. P. (2010), Surface-wave potential for triggering tectonic (nonvolcanic) tremor, *Bulletin of the Seismological Society of America*, *100*, 1859–1878.

Hill, D. P. (2012a), Dynamic Stresses, Coulomb Failure, and Remote Triggering – Corrected, *Bulletin of the Seismological Society of America*, *102*, 2313–2336.

Hill, D. P. (2012b), Surface-wave potential for triggering tectonic (nonvolcanic) tremor – corrected, *Bulletin of the Seismological Society of America*, *102*, 2337–2355.

Hill, D. P., and S. Prejean (2007), Dynamic triggering, *Treatise on Geophysics*, *4*, 257–291.

Hill, D. P., and S. G. Prejean (2014), Dynamic Triggering, for publication in *Treatise on Geophysics, 2nd Edition* (G. Schubert, ed.), Volume 4, "Earthquake Seismology" (H. Kanamori, ed.).

Hill, D. P., M. J. S. Johnston, J. O. Langbein, and R. Bilham (1995), Response of Long Valley Caldera to the Mw = 7.3 Landers, California, earthquake, *Journal of Geophysical Research*, *100*, 12,985–13,005.

Hill, D. P., F. F. Pollitz, and C. Newhall (2002), Earthquake-volcano interactions, *Physics Today*, *55*, 41–47.

Hill, D. P., Z. Peng, D. R. Shelly, and C. Aiken (2013), S-Wave triggering of tremor beneath the Parkfield, California, section of the San Andreas fault by the 2011 Tohoku, Japan, earthquake: Observations and theory, *Bulletin of the Seismological Society of America*, *103*, 1541–1550.

Hill, D. P., et al. (1993), Seismicity remotely triggered by the magnitude 7.3 Landers, California, earthquake, *Science*, *260*, 1617–1623.

Husen, S., S. Wiemer, and R. B. Smith (2004a), Remotely triggered seismicity in the Yellowstone national park region by the 2002 Mw 7.9 Denali fault earthquake, Alaska, *Bulletin of the Seismological Society of America*, *94*, 317–331.

Husen, S., R. Taylor, R. B. Smith, and H. Healser (2004b), Changes in geyser eruption behavior and remotely triggered seismicity in Yellowstone National Park produced by the 2002 M 7.9 Denali fault earthquake, Alaska, *Geology*, *32*, 537–540.

Ichihara, M., and E. E. Brodsky (2006), A limit on the effect of rectified diffusion in volcanic systems, *Geophysical Research Letters*, *33*, L02316.

Ide, S. (2012), Variety and spatial heterogeneity of tectonic tremor worldwide, *Journal of Geophysical Research*, *117*, B03302.

Ikuta, R., M. Satomura, A. Fujita, S. Shimada, and M. Ando (2012), A small persistent locked area associated with the 2011 Mw9. 0 Tohoku-Oki earthquake deduced from GPS data, *Journal of Geophysical Research*, *117*, B11408.

Ishihara, K. (1993), Liquefaction and flow failure during earthquakes, *Geotechnique*, *43*, 351–415.

Ishihara, K., F. Tatsuoka, and S. Yasuda (1975), Undrained deformation and liquefaction of sand under cyclic stresses, *Soils and Foundations*, *15*, 29–44.

Istadi, B. P., G. H. Pramono, P. Sumintadireja, and S. Alam (2009), Modeling study of growth and potential geohazard for Lusi mud volcano: East Java, Indonesia, *Marine and Petroleum Geology*, *26*, 1724–1739.

Jakobsdóttir, S. S. (2008), Seismicity in Iceland: 1994-2007, *Jökull*, *58*, 75–100.

Jóhannesson, H. (1980), Stratigraphy and evolution of axial rift zones in western Iceland, *Náttúrufrædingurinn*, *50*, 13–31.

Jóhannesson, H. (1982a), Quaternary volcanism in west Iceland, *Sögufélag*, pp. 129–137.

Jóhannesson, H. (1982b), Overview of the geology of Snæfellsnes, *Ferdafélag Íslands*, pp. 151–174.

Jóhannesson, H., R. M. Flores, and J. Jónsson (1981), A short account of the Holocene tephrochronology of the Snæfellsjökull central volcano, western Iceland, *Jökull*, *9*, 23–30.

Johnson, H. P., M. Hutnak, R. P. Dziak, C. G. Fox, I. Urcuyo, J. P. Cowen, J. Nabelek, and C. Fisher (2000), Earthquake-induced changes in a hydrothermal system on the Juan de Fuca mid-ocean ridge, *Nature*, *407*, 174–177.

Jousset, P., and J. Rohmer (2012), Evidence for remotely triggered microearthquakes during salt cavern collapse, *Geophysical Journal International*, *191*, 207–223.

Kawakatsu, H., et al. (2000), Aso94: Aso seismic observation with broadband instruments, *Journal of Volcanology and Geothermal Research*, *101*, 129–154.

Keefer, D. K. (2002), Investigating landslides caused by earthquakes - a historical review, *Surveys in Geophysics*, *23*, 473–510.

King, C. Y. (1986), Gas geochemistry applied to earthquake prediction - an overview, *Journal of Geophysical Research*, *91*, 2269–2281.

King, G. C. P., R. S. Stein, and J. Lin (1994), Static stress changes and the triggering of earthquakes, *Bulletin of the Seismological Society of America*, *84*, 935–953.

Kokfelt, T. K., K. Hoernle, C. Lundstrom, F. Hauff, and C. v.d. Boogard (2009), Time-scales for magmatic differentiation at the Snæfellsjökull central volcano, western Iceland: Constraints from U-Th-Pa-Ra disequilibria in post-glacial lavas, *Geochimica et Cosmochimica Acta*, *73*, 1120–1144.

Kulhanek, O. (2002), The structure and interpretation of seismograms, in *International Handbook of Earthquake and Engineering Seismology*, edited by W. H. K. Lee, P. Jenning, C. Kisslinger, and H. Kanamori, Academic Press.

Lee, M. W. (2010), Predicting S-Wave velocities for unconsolidated sediments at low effective pressure, *USGS Scientific Investigations Report*, *5138*.

Lewis, J. C., A. C. Boozer, A. López, and W. Montero (2008), Collision versus sliver transport in the hanging wall at the Middle America subduction zone: Constraints from background seismicity in central Costa Rica, *Geochemistry, Geophysics, Geosystems*, *9*, Q07S06.

Liechavicius, C. (2013), Photograph taken by Claudia Liechavicius, http://www.viajarpelomundo.com/2013/06/os-incriveis-vulcoes-da-costa-rica.html.

Lienert, B. R. E., and J. Havskov (1995), A computer program for locating earthquakes both locally and globally, *Seismological Research Letters*, *66*, 26–36.

Linde, A. T., and I. S. Sacks (1998), Triggering of volcanic eruptions, *Nature*, *395*, 888–890.

Linde, A. T., I. S. Sacks, M. J. S. Johnston, D. P. Hill, and R. G. Billham (1994), Increased pressure from rising bubbles as a mechanism for remotely triggered seismicity, *Nature*, *371*, 408–410.

Linkimer, L., I. G. Arroyo, P. Montero, K. Walter, and O. H. Lücke (2013), Upper-Plate Earthquake Swarms Remotely Triggered by the 2012 Mw 7.6 Nicoya Earthquake, Costa Rica, *AGU Fall Meeting*, Abstract 1799571.

Lockner, D. A., and N. M. Beeler (2003), Stress-induced anisotropic poroelasticity response in sandstone, in *Electronic Proceedings of the 16th ASCE Engineering Mechanics Conference*, pp. 1–13, University of Washington, Seattle, Washington.

Lupi, M., and S. A. Miller (2014), Short-lived tectonic switch mechanism for long-term pulses of volcanic activity after mega-thrust earthquakes, *Solid Earth*, *5*, 13–24.

Lupi, M., S. Geiger, and C. Graham (2011), Numerical simulations of seismicity-induced fluid flow in the Tjörnes Fracture Zone, Iceland, *Journal of Geophysical Research*, B07101.

Lupi, M., E. H. Saenger, F. Fuchs, and S. A. Miller (2013), Lusi mud eruption triggered by geometric focusing of seismic waves, *Nature Geoscience*, *61*, 642–646.

Main, I. (1996), Statistical physics, seismogenesis, and seismic hazard, *Reviews of Geophysics*, *34*, 433–462.

Manga, M. (2007), Did an earthquake trigger the May 2006 eruption of the Lusi mud volcano?, *Eos*, *88*, 201.

Manga, M., and M. Bonini (2012), Large historical eruptions at subaerial mud volcanoes, Italy, *Natural Hazards and Earth System Sciences*, *12*, 3377–3386.

Manga, M., and E. Brodsky (2006), Seismic triggering of eruptions in the far field: Volcanoes and geysers, *Annual Review of Earth and Planetary Sciences*, *34*, 263–291.

Manga, M., M. Brumm, and M. L. Rudolph (2009), Earthquake triggering of mud volcanoes, *Marine and Petroleum Geology*, *26*, 1785–1798.

Martin, E., and O. Sigmarsson (2010), Thriteen million years of silicic magma production in Iceland: Links between petrogenesis and tectonic settings, *Lithos*, *116*, 129–144.

Martin, E., J. L. Paquette, V. Bosse, G. Ruffet, M. Tiepolo, and O. Sigmarsson (2011), Geodynamics of rift-plume interaction in Iceland as constrained by new $^{40}Ar/^{39}Ar$ and in situ U-Pb zircon ages, *Earth and Planetary Science Letters*, *311*, 28–38.

Marzocchi, W. (2002a), Remote seismic influence on large explosive eruptions, *Journal of Geophysical Research*, *107*, 2018.

Marzocchi, W., E. Casarotti, and A. Piersanti (2002b), Modeling the stress variations induced by great earthquakes on the largest volcanic eruptions of the 20th century, *Journal of Geophysical Research*, *107*, 2320.

Matsumoto, N., G. Kitagawa, and E. Roeloffs (2003), Hydrological response to earthquakes in the Haibara well, Central Japan: Groundwater level changes revealed using state space decomposition of atmospheric pressure, rainfall and tidal responses, *Geophysical Journal International*, *155*, 885–898.

Mazzini, A., H. Svensen, G. G. Akhmanov, G. Aloisi, S. Planke, A. Malthe-Sørenssen, and B. P. Istadi (2007), Triggering and dynamic evolution of the Lusi mud volcano, Indonesia, *Earth and Planetary Science Letters*, *261*, 375–388.

Mazzini, A., A. Nermoen, M. Krotkiewski, Y. Podladchikov, S. Planke, and H. Svensen (2009), Strike-slip faulting as a trigger mechanism for overpressure release through piercement structures. Implications for the Lusi mud volcano, Indonesia, *Marine and Petroleum Geology*, *26*, 1751–1765.

Mazzini, A., G. Etiope, and H. Svensen (2012), A new hydrothermal scenario for the 2006 Lusi eruption, Indonesia. Insights from gas geochemistry, *Earth and Planetary Science Letters*, *317*, 305–318.

McCaffrey, R., and J. Nabelek (1984), The geometry of back arc thrusting along the eastern Sunda Arc, Indonesia: Constraints from earthquake and gravity data, *Journal of Geophysical Research*, *89*, 6171–6179.

McCaffrey, R., P. Molnar, and S. W. Roecker (1985), Microearthquake seismicity and fault plane solutions related to arc-continent collision in the eastern Sunda Arc, Indonesia, *Journal of Geophysical Research*, *90*, 4511–4528.

Miller, S. A. (2008), Note on rain-triggered earthquakes and their dependence on karst geology, *Geophysical Journal International*, *173*, 334–338.

Miller, S. A. (2012), Shaken and stirred: Chilling the crust with earthquakes, *Geology*, *40*, 191–192.

Miller, S. A. (2013), The role of fluids in tectonic and earthquake processes, *Advances in Geophysics*, *54*, 1–46.

Mitchell, M. A., R. S. White, S. Roecker, and T. Greenfield (2013), Tomographic image of melt storage beneath Askja volcano, Iceland using local microseismicity, *Geophysical Research Letters*, *40*, 5040–5046.

Miyazawa, M., and E. E. Brodsky (2008), Deep low-frequency tremor that correlates with passing surface waves, *Journal of Geophysical Research*, *113*, B01307.

Mjelde, R., A. J. Breivik, T. Raum, E. Mittelstaedt, G. Ito, and J. I. Faleide (2008), Magmatic and tectonic evolution of the north Atlantic, *Journal of the Geological Society*, *165*, 31–42.

Mohr, O. (1900), Welche Umstände bedingen die Elastizitätsgrenze und den Bruch eines Materials?, *Zeitschrift des Vereins Deutscher Ingenieure*, *44*, 1524–1530.

Montero, P. W., J. C. Lewis, J. S. Marshall, S. Kruse, and P. Wetmore (2013), Neotectonic faulting and forearc sliver motion along the Atirro-Río Sucio fault system, Costa Rica, Central America, *Geological Society of America Bulletin*, *125*, 857–876.

Nakano, M., H. Kumagai, K. Miyakawa, T. Yamashina, H. Inoue, M. Ishida, S. Aoi, N. Morikawa, and P. Harjadi (2006), Source estimates of the May 2006 Java earthquake, *Eos Transactions AGU*, *87*, 493–494.

Nishenko, S. P., and R. Buland (1987), A generic recurrence interval distribution for earthquake forecasting, *Bulletin of the Seismological Society of America*, *77*, 1382–1399.

Nostro, C., R. S. Stein, M. Cocco, M. E. Belardinelli, and W. Marzocchi (1998), Two-way coupling between Vesuvius eruptions and southern Apennine earthquakes, Italy, by elastic stress transfer, *Journal of Geophysical Research*, *103*, 24,487–24,424.

Obara, K. (2012), New detection of tremor triggered in Hokkaido, northern Japan by the 2004 Sumatra-Andaman earthquake, *Geophysical Research Letters*, *39*, L20305.

Pallister, J. S., et al. (2010), Broad accomodation of rift-related extension recorded by dyke intrusion in Saudi Arabia, *Nature Geoscience*, *10*, 705–712.

Paulatto, M., et al. (2010), Upper crustal structure of an active volcano from refraction/reflection tomography, Montserrat, Lesser Antilles, *Geophysical Journal International*, *180*, 685–696.

Pedersen, R., and F. Sigmundsson (2006), Temporal development of the 1999 intrusive episode in the Eyjafjallajökull volcano, Iceland, derived from InSAR images, *Bulletin of Volcanology*, *68*, 377–393.

Peng, Z., J. E. Vidale, A. G. Wech, R. M. Nadeau, and K. C. Creager (2009), Remote triggering of tremor along the San Andreas Fault in central California, *Journal of Geophysical Research*, *114*, B00A06.

Peng, Z., C. Wu, and C. Aiken (2011), Delayed triggering of microearthquakes by multiple surface waves circling the Earth, *Geophysical Research Letters*, *38*, L04306.

Peng, Z., H. Gonzalez-Huizar, K. Chao, C. Aiken, B. Moreno, and G. Armstrong (2013), Tectonic tremor beneath Cuba triggered by the Mw 8.8 Maule and Mw 9.0 Tohoku-Oki earthquakes, *Bulletin of the Seismological Society of America*, *103*, 595–600.

Pollitz, F. F., R. Stein, S. Volkan, and R. Burgmann (2012), The 11 April 2012 east Indian Ocean earthquake triggered large aftershocks worldwide, *Nature*, *490*, 250–253.

Power, J. A., S. C. Moran, S. R. McNutt, S. D. Stihler, and J. J. Sanchez (2001), Seismic response of the Katmai volcanoes to the 6 December 1999 magnitude 7.0 Karluk Lake earthquake, Alaska, *Bulletin of the Seismological Society of America*, *91*, 57–63.

Prejean, S., and D. P. Hill (2013), Where do we stand after twenty years of dynamic triggering studies?, *AGU Fall Meeting*, Abstract 1811598.

Pritchard, M., J. Jay, F. Aron, S. Henderson, and L. Lara (2013), Subsidence at southern Andes volcanoes induced by the 2010 Maule, Chile earthquake, *Nature Geoscience*, *6*, 632–636.

Protti, M., et al. (2014), Nicoya earthquake rupture anticipated by geodetic measurement of the locked plate interface, *Nature Geoscience*, *2014*, 117–121.

Quintero, R., and E. Kissling (2001), An improved p-wave velocity reference model for Costa Rica, *Geofisica Internacional - Mexico*, *40*, 3–20.

Roeloffs, E. A. (1998), Persistent water level changes in a well near Parkfield, California, due to local and distant earthquakes, *Journal of Geophysical Research*, *103*, 869–889.

Rogers, G., and H. Dragert (2003), Episodic tremor and slip on the Cascadia subduction zone: The chatter of silent slip, *Science*, *300*, 1942–1943.

Rubinstein, J. L., J. E. Vidale, J. Gomberg, P. Bodin, K. C. Creager, and S. Malone (2007), Non-volcanic tremor driven by large transient shear stresses, *Nature*, *448*, 579–582.

Rubinstein, J. L., M. la Rocca, J. E. Vidale, K. C. Creager, and A. G. Wech (2008), Tidal modulation of nonvolcanic tremor, *Science*, *319*, 186–189.

Rudolph, M. L., and M. Manga (2012), Frequency dependence of mud volcano response to earthquakes, *Geophysical Research Letters*, *39*, L14303.

Rutledge, J. T., W. S. Phillips, and B. K. Schuessler (1998), Reservoir characterization using oil-production-induced microseismicity, Clinton County, Kentucky, *Tectonophysics*, *289*, 129–152.

Ryan, W. B. F., et al. (2009), Global Multi-resolution Topography synthesis, *Geochemistr*, *10*, Q03014.

Saccorotti, G., D. Piccinini, F. Mazzarini, and M. Zupo (2013), Remotely triggered micro-earthquakes in the Larderello-Travale geothermal field (Italy) following the 2012 May 20, Mw 5.9 Po-plain earthquake, *Geophysical Research Letters*, *40*, 835–840.

Saenger, E. H. (2011), Time reverse characterization of sources in heterogeneous media, *NDT&E International*, *44*, 751–759.

Saenger, E. H., and T. Bohlen (2004), Finite-difference modelling of viscoelastic and anisotropic wave propagation using the rotated staggered grid, *Geophysics*, *69*, 583–591.

Saenger, E. H., N. Gold, and S. A. Shapiro (2000), Modeling the propagation of elastic waves using a modified finite-difference grid, *Wave Motion*, *31*, 77–92.

Sawolo, N., E. Sutriono, B. P. Istadi, and A. B. Darmoyo (2009), The Lusi mud volcano triggering controversy: Was it caused by drilling?, *Marine and Petroleum Geology*, *26*, 1766–1784.

Schön, J. H. (2011), *Physical properties of rock: A workbook*, Elsevier.

Segall, P., and S. D. Fitzgerald (1998), A note on induced stress changes in hydrocarbon and geothermal reservoirs, *Tectonophysics*, *289*, 117–128.

Shaw, H. R., and B. Chouet (1991), Fractal hierarchies of magma transport in Hawaii and critical self-organization of tremor, *Journal of Geophysical Research*, *96*, 10,191–10,207.

Shelly, D. R., G. C. Beroza, S. Ide, and S. Nakamula (2006), Low-frequency earthquakes in Shikoku, Japan and their relationship to episodic tremor and slip, *Nature*, *442*, 188–191.

Shelly, D. R., G. C. Beroza, and S. Ide (2007), Non-volcanic tremor and low-frequency earthquake swarms, *Nature*, *446*, 305–307.

Shelly, D. R., Z. Peng, D. P. Hill, and C. Aiken (2011), Triggered creep as a possible mechanism for delayed dynamic triggering of tremor and earthquakes, *Nature Geoscience*, *4*, 384–388.

Sibson, R. H. (1981), Controls on low-stress hydro-fracture dilatancy in thrust, wrench and normal fault terrains, *Nature*, *289*, 665–667.

Sigurdsson, H. (1970), Structural origin and plate tectonics of the Snæfellsnes Volcanic Zone, western Iceland, *Earth and Planetary Science Letters*, *100*, 129–135.

Silver, E. A., D. Reed, and R. McCaffrey (1983), Backarc thrusting in the eastern Sunda Arc, Indonesia: A consequence of arc-continent collision, *Journal of Geophysical Research*, *88*, 7429–7448.

Soosalu, H. J., J. Key, R. S. White, C. Knox, P. Einarsson, and S. S. Jakobsdóttir (2009), Lower-crustal earthquakes caused by magma movement beneath Askja volcano on the north Iceland rift, *Bulletin of Volcanology*, *72*, 55–62.

Stefánsson, R., G. B. Gudmundsson, and M. J. Roberts (2006), Long-term and short-term earthquake warnings based on seismic information in the SISZ, *Vedurstofa Íslands*, Report 06006.

Stefánsson, R., G. B. Gudmundsson, and P. Halldorsson (2008), Tjörnes fracture zone. New and old seismic evidences for the link between the north Iceland rift zone and the Mid-Atlantic ridge, *Tectonophysics*, *447*, 117–126.

Stefánsson, R., et al. (1993), Earthquake prediction research in the South Icelandic Seismic Zone and the SIL project, *Bulletin of the Seismological Society of America*, *83*, 696–716.

Stein, R. S., A. A. Barka, and J. H. Dieterich (1997), Progressive failure on the North Anatolian fault since 1939 by earthquake stress triggering, *Geophysical Journal International*, *128*, 594–604.

Steinthorsson, S. (1967), Two new C-14 dates of peat samples below tephra layers of Snæfellsjökull central volcano (in Icelandic with an English summary), *Náttúrufræðingurinn*, *37*, 236–238.

Stewart, H. E., and A. K. Hussein (1992), The Loma Prieta, California, earthquake of October 17, 1989–Marina District, in *Professional Paper 1551-F*, edited by T. D. O' Rourke, US Geological Survey.

Sturtevant, B., H. Kanamori, and E. Brodsky (1996), Seismic triggering by rectified diffusion in geothermal systems, *Journal of Geophysical Research*, *101*, 25,269–25,282.

Tackley, P. J. (2000), Mantle convection and plate tectonics: Toward an integrated physical and chemical theory, *Science*, *288*, 2002–2007.

Takada, Y., and Y. Fukushima (2013), Volcanic subsidence triggered by the 2011 Tohoku earthquake in Japan, *Nature Geoscience*, *6*, 637–641.

Tanikawa, W., M. Sakaguchi, H. T. Wibowo, T. Shimamoto, and O. Tadai (2010), Fluid transport properties and estimation of overpressure at the Lusi mud volcano, East Java Basin, *Engineering Geology*, *116*, 73–85.

Tarasewicz, J., R. S. White, B. Brandsdóttir, and B. Thorbjarnardóttir (2011), Location accuracy of earthquake hypocentres beneath Eyjafjallajökull, Iceland, prior to the 2010 eruptions, *Jökull*, *61*, 33–50.

Tarasewicz, J., B. Brandsdóttir, R. S. White, M. Hensch, and B. Thorbjarnardóttir (2012), Using microearthquakes to track repeated magma intrusions beneath the Eyjafjallajökull stratovolcano, Iceland, *Journal of Geophysical Research*, *117*, B00C06.

Tassi, F., M. Bonini, G. Montegrossi, F. Capecchiacci, B. Capaccioni, and O. Vaselli (2012), Origin of light hydrocarbons in gases from mud volcanoes and CH_4-rich emissions, *Chemical Geology*, *294*, 113–126.

Terakawa, T., S. A. Miller, and N. Deichmann (2012), High fluid pressure and triggered earthquakes in the enhanced geothermal system in Basel, Switzerland, *Journal of Geophysical Research*, *117*, B07305.

Terzaghi, K. (1943), *Theoretical Soil Mechanics*, John Wiley & Sons.

Thomas, T. W., J. E. Vidale, H. Houston, K. C. Creager, J. R. Sweet, and A. Ghosh (2013), Evidence for tidal triggering of high-amplitude rapid tremor reversals and tremor streaks in northern Cascadia, *Geophysical Research Letters*, *40*, 4254–4259.

Tingay, M., O. Heidbach, R. J. Davies, and R. Swarbrick (2008), Triggering of the Lusi mud eruption: Earthquake versus drilling initiation, *Geology*, *36*, 639–642.

Tobin, D. G., and L. R. Sykes (1968), Seismicity and tectonics of the northeast Pacific Ocean, *Journal of Geophysical Research*, *73*, 3821–3845.

Toda, S., R. S. Stein, K. Richards-Dinger, and S. B. Bozkurt (2005), Forecasting the evolution of seismicity in Southern California: Animations built on earthquake stress transfer, *Journal of Geophysical Research*, *110*, B05S16.

Toda, S., R. S. Stein, V. Sevilgen, and J. Lin (2011), Coulomb 3.3 Graphic-rich deformation and stress-change software for earthquake, tectonic, and volcano research and teaching–user guide, *USGS Open-File Report*, *1060*, 63.

Tregoning, P., F. K. Brunner, Y. Bock, S. S. O. Puntodewo, R. McCaffrey, J. F. Genrich, E. Calais, J. Rais, and C. Subarya (1994), First geodetic measurement of convergence across the Java Trench, *Geophysical Research Letters*, *21*, 2135–2138.

Tsukamoto, Y., K. Ishihara, and K. Harada (2009), Evaluation of undrained shear strength of soils from field penetration tests, *Soils and Foundations*, *49*, 11–23.

Utsu, T. (1961), A statistical study on the occurrence of aftershocks, *Geophysical Magazine*, *30*, 521–605.

Utsu, T., Y. Ogata, and R. S. Matsuura (1995), The centenary of the Omori formula for a decay law of aftershock activity, *Journal of Physics of the Earth*, *43*, 1–33.

van der Elst, N. J., H. M. Savage, K. M. Keranen, and G. A. Abers (2013), Enhanced remote earthquake triggering at fluid-injection sites in the midwestern united states, *Science*, *341*, 164–167.

Varostos, P., and M. Lazaridou (1991), Latest aspects of earthquake prediction in Greece based on seismic electric signals, *Tectonophysics*, *188*, 321–347.

Vartanyan, G., S. Stazhilo-Alekseev, and E. Zaltsberg (2014), Hydrogeodeformation monitoring: Prospects of earthquake prediction, *Environmental Earth Sciences*, *71*, 3039–3047.

Vergniolle, S., and C. Jaupart (1986), Separated two-phase flow and basaltic eruptions, *Journal of Geophysical Research*, *91*, 12,842–12,860.

Vigny, C., et al. (2011), The 2010 Mw 8.8 Maule megathrust earthquake of Central Chile, monitored by GPS, *Science*, *332*, 1417–1421.

Violay, M., S. Nielsen, B. Gibert, E. Spagnuolo, A. Cavallo, P. Azais, S. Vinciguerra, and G. di Toro (2014), Effect of water on the frictional behavior of cohesive rocks during earthquakes, *Geology*, *42*, 27–30.

Visini, F., and B. Pace (2014), Insights on a key parameter of earthquake forecasting, the coefficient of variation of the recurrence time, using a simple earthquake simulator, *Seismological Research Letters*, *85*, 703–713.

Waldhauser, F., and W. L. Ellsworth (2000), A double-difference earthquake location algorithm: Method and application to the northern Hayward fault, California, *Bulletin of the Seismological Society of America*, *90*, 1353–1368.

Walter, J. I., S. Y. Schwartz, J. M. Protti, and V. Gonzalez (2011), Persistent tremor within the northern Costa Rica seismogenic zone, *Geophysical Research Letters*, *38*, L01307.

Walter, T., R. Wang, M. Zimmer, H. Grosser, B. Lühr, and A. Ratdomopurbo (2007), Volcanic activity influenced by tectonic earthquakes: static and dynamic stress triggering at Mt. Merapi, *Geophysical Research Letters*, *34*, L05304.

Wang, C. Y. (2007), Liquefaction beyond the near field, *Seismological Research Letters*, *78*, 512–517.

Wang, C. Y., and M. Manga (2010), Hydrologic responses to earthquakes and a general metric, *Geofluids*, *10*, 206–216.

Wassermann, J. (2012), Volcano seismology, in *New Manual of Seismological Observatory Practice 2*, edited by P. Bormann, GFZ Potsdam.

Weatherley, D. K., and R. W. Henley (2013), Flash vaporization during earthquakes evidenced by gold deposits, *Nature Geoscience*, *6*, 294–298.

Weingarten, M., and S. Ge (2014), Insights into water level response to seismic waves: A 24 year high-fidelity record of global seismicity at Devils Hole, *Geophysical Research Letters*, *41*, 74–80.

West, M., J. J. Sánchez, and S. R. McNutt (2005), Periodically triggered seismicity at Mount Wrangell, Alaska, after the Sumatra earthquake, *Science*, *308*, 1144–1146.

White, R. S., J. Drew, H. R. Martens, J. Key, H. J. Soosalu, and S. Jakobsdóttir (2011), Dynamics of dyke intrusion in the mid-crust of Iceland, *Earth and Planetary Science Letters*, *304*, 300–312.

Widiyantoro, S., and R. van der Hilst (1996), Structure and evolution of lithospheric slab beneath the Sunda Arc, Indonesia, *Science*, *271*, 1566–1570.

Withers, M., R. Aster, C. Young, J. Beiriger, M. Harris, S. Moore, and J. Trujillo (1998), A Comparison of Select Trigger Algorithms for Automated Global Seismic Phase and Event Detection, *Bulletin of the Seismological Society of America*, *88*, 95–106.

Yang, T., and Y. Shen (2005), P-wave velocity structure of the crust and uppermost mantle beneath Iceland from local earthquake tomography, *Earth and Planetary Science Letters*, *235*, 597–609.

Yassir, N. (1989), Mud volcanoes and the behaviour of overpressured clays and silts, Ph.D. thesis, University of London.

Yue, H., T. Lay, S. Y. Schwartz, L. Rivera, M. Protti, T. H. Dixon, S. Owen, and A. V. Newman (2013), The 5 september 2012 Nicoya, Costa Rica Mw 7.6 earthquake rupture process from joint inversion of high-rate GPS, strong-motion, and teleseismic p-wave data and its relationship to adjacent plate boundary interface properties, *Journal of Geophysical Research*, *118*, 5453–5466.

Zigone, D., et al. (2012), Triggering of tremors and slow slip event in Guerrero, Mexico, by the 2010 Mw 8.8 Maule, Chile, earthquake, *Journal of Geophysical Research*, *117*, B09304.

Zoporowski, A. (2011), Dynamical and Mechanistic Effects of High Pressure Fluids in the Earth's Crust, Ph.D. thesis, University of Bonn.

Zoporowski, A., and S. A. Miller (2009), Modelling eruption cycles and decay of mud volcanoes, *Marine and Petroleum Geology*, *26*, 1879–1887.

All background images used for maps in this thesis were created with GeoMapApp: http://www.geomapapp.org and utilize the GMT basemap image by Ryan et al. [2009].

Acknowledgments

Steve
Matteo
Cristian
Thomas
Gunnar
Julia
Sebastian
Sjonni
Wenbin
Sighvatur
Richard
Johannes
Stefan

Katja

Eidesstattliche Erklärung

Hiermit versichere ich an Eides statt, dass die vorgelegte Arbeit persönlich, selbständig, ohne fremde Hilfe und ohne Benutzung anderer als der angegebenen Hilfsmittel angefertigt wurde und die aus anderen Quellen direkt oder indirekt übernommenen Daten und Konzepte unter Angabe der Quelle kenntlich gemacht sind. Die vorgelegte Arbeit oder ähnliche Arbeiten sind nicht bereits anderweitig als Dissertation eingereicht worden und es wurde kein früherer Promotionsversuch an dieser oder einer anderen Universität unternommen.

Bonn, 20. August 2014